eman ta zabal zazu

Universidad del País Vasco
Euskal Herriko Unibertsitatea

UNIVERSIDAD DEL PAÍS VASCO
EUSKAL HERRIKO UNIBERTSITATEA
PHD THESIS

Heterogeneous catalysis on curved crystals: CO oxidation on Pt and Rh

Fernando García Martínez

supervised by
Dr. Frederik M. Schiller
Prof. J. Enrique Ortega Conejero

February 2022

A meus avós e a Piay.

Table of contents

Preface

Acknowledgements

Han pasado cuatro años, (casi) una pandemia y una cambiante melena desde que empecé la tesis en Donosti. Durante este largo tiempo han pasado un sinfín de cosas buenas, así que ¡gracias a todos por ellas!

Primero de todo, quiero agradecer a mis supervisores Kike y Fred por estos 4 años de doctorado, discusiones científicas (y de fittings), beamtimes... y especialmente por meterle caña a la corrección de la tesis estos últimos meses. Siempre que tenía un problema o una duda, eramos capaces de solucionarlo entre todos. Parece que eso no es lo estándar, así que vielen dank y eskerrik asko! Espero que sigamos colaborando en el futuro y que os vaya todo muy bien a los dos. Muchas gracias también a los demás integrantes del grupo: Laura, Max, Martina, Dimas, Celia, Rodrigo...

Non podo seguir sen agradecerlle á miña familia todo o seu apoio incondicional durante todos estes anos, especialmente a meus pais e a miña irmá. Moitas grazas por estar ahí sempre, nos bós e malos momentos, e aturar os meus cambios de humor. E tamén aos meus avós, por preocuparse tanto por se como ben e por como vai o traballo no “colexio” (ao que sigo indo con 27 anos). E of course que lle teño que mandar máis bicos enormes a miña outra familia de Pontevedra (Lau, Kiki, Eli, Gorge, Carla, Mariña, Sara, Moi, Mónica, Carlitos...) e Santiago (Sara, Adri, Alba(s)...). Querovos moitíííísimo a todes, e aínda que marche pa Alemaña, as cañas cando volva de visita que non nolas quite nin Dios nin a pandemia de turno!

To continue with, ahora le toca al equipo de Donosti. No voy a mencionar los nombres de las siguientes personas por miedo a represalias físicas. La Madrastra, la bruja de la Sirenita, la amiga cercana de Rodrigo Cuevas, la chica que grita mucho, el que está divorciado pero prefiere no hablar de ello, y la chica a la que cierta alcaldesa le puso un flamante puente nuevo en la bahía y ahora no le pasan los blablacars por el puente que esta cerca de su mansión en primera línea de playa: os quiero un montonazo, me encanta estar con vosotros e ir al Dabadaba por motivos lírico-festivos. Aunque estemos cada uno en un rincón distinto, hay vínculos que nunca se rompen, y siempre nos quedara Donosti! Y esto también se aplica a los demás: Txemikel, Idoia, Sabine, Ana, Carlos, Antonella, Raoni, Jon, Martin, Nodar, Paul, Cris, Jorge, Edurne, Sofi, Thomas, Joseba, Alaa... Si me olvido de alguien sorry, es que sois muchos!

I cannot end this part without thanking my big small sister Khadiza, future head of the Mumbai University. You are my favourite companion for the shifts of the beamtimes and the siderhouses. Now that I am moving to Germany, we can meet in Denmark so you can complain about me not eating the food you've prepared for me and also practice some Spanish.

To finish with, I would also like to thank all my coworkers who made this Thesis possible. Edvin and Johan, it was really nice to go to Lund to do experiments, it was a great opportunity to learn new things and go abroad during the pandemic! And of course, thanks Lisa, Sabrina, Sebastian and Alfred for taking me out for beers! I enjoyed it a lot. Also, thanks Nacho and Virginia for the support at ALBA, and of course Ira, Andrew, Adrian an Juan Pablo for the support at the experiments in NSLS-II. I enjoyed a lot my travels there. It was cool to go to the States, work there and taste the largest hamburger I have ever seen!

Muchas gracias a todos, tanto a los que estáis y a los que ya no, por hacer estos 4 añitos algo mas llevaderos!

List of publications

Articles in preparation as a result of this Thesis are not included.

- **CO Chemisorption on Vicinal Rh(111) Surfaces Studied with a Curved Crystal**
  Fernando García-Martínez, Frederik Schiller, Sara Blomberg, Mikhail Shipilin, Lindsay R. Merte, Johan Gustafson, Edvin Lundgren, J. Enrique Ortega
  J. Phys. Chem. C **124** (2020), 9305–9313
  DOI: 10.1021/acs.jpcc.0c00039

  I contributed by analyzing all data and writing the paper.

- **Catalytic Oxidation of CO on a Curved Pt(111) Surface: Simultaneous Ignition at All Facets through a Transient CO-O Complex**
  Fernando García-Martínez, Carlos García-Fernández, Juan Pablo Simonovis, Adrian Hunt, Andrew Walter, Iradwikanari Waluyo, Florian Bertram, Lindsay R.Merte, Mikhail Shipilin, Sebastian Pfaff, Sara Blomberg, Johan Zetterberg, Johan Gustafson, Edvin Lundgren, Daniel Sánchez-Portal, Frederik Schiller, J. Enrique Ortega
  Angewandte Chemie International Edition **59** (2020), 20037-20043
  DOI: 10.1002/anie.202007195

  I contributed by designing the plan and performing the NAP-XPS experiments. I analyzed the UHV- and NAP-XPS data and wrote the photoemission part of the paper.

The following paper was not included in this Thesis, yet it comprises information relevant for the CO oxidation on Pd vicinal surfaces.

- **Reduced Carbon Monoxide Saturation Coverage on Vicinal Palladium Surfaces: the Importance of the Adsorption Site**
  Fernando García-Martínez, Elisabeth Dietze, Frederik Schiller, Dorotea Gajdek, Lindsay R. Merte, Sabrina M. Gericke, Johan Zetterberg, Stefano Albertin, Edvin Lundgren, Henrik Grönbeck, J. Enrique Ortega
  The Journal of Physical Chemistry Letters **12** (2021), 9508-9515
  DOI: 10.1021/acs.jpclett.1c02639

  I contributed by designing the XPS experimental plan. I analyzed the XPS data and wrote the photoemission part of the paper.

Abstract

It is undeniable that catalysis is one of the pillars of modern society, since almost all processes occurring in the industry and combustion vehicles are based on such phenomenon. Within this context, the catalytic carbon monoxide (CO) oxidation is one of the most studied topics. This is not surprising, since we must understand this reaction in order to improve the performance of catalytic converters and other processes in the petrochemical industry involving CO. In addition, this reaction is a pillar for investigating more complex catalytic processes, from which we can cement the knowledge for tailoring new and efficient catalysts.

Rhodium (Rh), Platinum (Pt) and Palladium (Pd) are among the best CO oxidation catalysts. Typically, particles of these metals are placed in the catalytic converter of combustion cars to oxidize the dangerous CO to the less harmful carbon dioxide (CO_2), among other processes. Since the reaction takes place at the surface of such nanoparticles, we must explore how these behave under reaction conditions. With the aid of Surface Science, we may study the composition and/or structure of well-defined surfaces when exposed to both reactants, namely CO and oxygen (O_2). Thereafter, we may extend such investigations to stepped surfaces and eventually to nanoparticles.

The catalytic CO oxidation requires, at least at low pressures, the coadsorption of both reactants, in order for them to collide and form CO_2. In the case of O_2, the molecule will dissociate on the surface to form atomic oxygen (O), which will later react with coadsorbed CO. The resulting CO_2 molecule will readily desorb from the surface of the catalyst. On one hand, chemisorbed CO will quench the O_2 adsorption, and will prevent the reaction. Therefore, the CO-covered surface is called poisoned stage (no/low CO_2 production). On the other hand, chemisorbed O does not hinder the CO adsorption. Typically, O-covered surfaces usually feature a large catalytic CO_2 turnover, for which O-covered surfaces are classified as active. The transition between these two stages occurs at the temperature at which the CO leaves the surface, which is called ignition (or ligth-off) temperature T_i.

In this Thesis, we carried out an investigation of the influence of surface sites with different atomic coordination (steps, terraces, kinks) on the CO oxidation reaction. For such purpose, we have employed curved crystals. These are cylindrical sections of single crystals that expose a smooth sequence of crystal planes away from a high symmetry direction, and hence possess a varying distribution of steps and kinks sites across their curved surface. This enables to selectively probe different surfaces in gas surface reactions under the very same experimental conditions.

Three curved samples were employed throughout this Thesis. Two of them have the (111) plane located at the center, and an increasing density of either A-type ({100} microfacets, square) or B-type ({111} microfacets, triangular) straight steps as one departs from the position of the (111) surface at the apex of the crystal. These are the c-Pt(111) and c-Rh(111) samples, and their design is ideal for studying A-B asymmetries. The other sample has the kinked Pt(645) plane at the center of the crystal [k-Pt(645)]. At kinked surfaces, steps feature alternating {111} and {100} microfacets. On the k-Pt(645) sample, the (111) plane is located between the center and one of the edges, enabling to probe Pt vicinal surfaces with kinked steps up to the densely stepped (312) plane.

The following Chapters comprise three different, well-distinguished sets of experiments. First of all, the bare CO chemisorption was investigated in Ultra-High Vacuum (UHV) with X-Ray Photoemission Spectroscopy (XPS), in order to have a proper reference to characterize the CO-poisoning layer found at higher pressures. Later, the very same systems were studied under reaction conditions at several temperatures to study their composition and CO_2 turnover. These CO oxidation experiments were conducted close to *operando* conditions, in order to mimic the environment to which real catalysts are submitted. Working with curved substrates demands for sufficient spatial resolution (< 0.5 mm) to probe the different facets across the curved surface. During this Thesis, two different techniques conducted at relatively high pressures (millibar range) were employed. On one hand, Planar Laser-Induced Fluorescence (PLIF) allowed probing the $CO_{2(g)}$ cloud arising from the CO oxidation all over the curved sample simultaneously. This enabled to easily track differences in the CO ignition across the curved sample. However, since this technique provides only information about the gas phase above the sample, we resorted to Near-Ambient Pressure XPS (NAP-XPS) to gain information on the chemical composition of the surface. Since this technique permits to simultaneously probe the surface chemical species and the gas phase close to the catalyst, we could correlate the chemical state of the surface with the CO_2 production at selected points across the curved surface. In addition, a comparison with the UHV experiments helps characterizing and quantifying these surface chemical species. By merging these different measurements, we were able to obtain significant insights on the CO oxidation at Pt(111) and Rh(111) vicinal surfaces.

For the Pt crystals with either close-packed and kinked steps, PLIF revealed a surprising simultaneous ignition of the stepped surfaces: the CO_2 production explodes at the same time across the curved surface. The NAP-XPS measurements point to CO-depleted terraces while the steps remain CO-saturated prior to the ligth-off of the reaction. The consistent analysis of the XPS spectra during a slow ignition cycle at the (111) surface points towards the existence of an additional, unresolved oxygen species prior to ligth-off. With the aid of theoretical calculations, we postulate that such species is subsurface oxygen that builds up before ignition, and vanishes afterwards. This subsurface oxygen would increase the adsorption energy of CO anchored at terraces to values close to its step analogous, explaining the simultaneous ignition at Pt vicinals.

PLIF measurements on the c-Rh(111) sample showed that, as compared to its A-type analogous, the B-steps ignite at lower temperature. Therefore, the ignition at A- and B-type Rh vicinal surfaces is asymmetric around the (111) plane. Complementary NAP-XPS measurements showed that both A- and B-steps are CO-saturated after exposing them to high CO pressures and room temperature, away from the ignition temperature. However, as the light-off approaches the B-steps become partially CO-depleted and covered by chemisorbed O, while the A-steps remain CO-saturated. We believe that this is the reason for the asymmetry in the ignition, since coexistence of CO and O at the B-steps would tentatively increase the catalytic CO_2 production.

For the c-Rh(111) surface we examined the active stage in more detail. We found markedly different oxygen-related species for the (111) plane and the A- and B-type microfacets. While trilayers of RhO_2 readily form in the A-steps after the surface transits to the active stage, an increase in the temperature is needed to develop the oxide also at the (111) plane. We did not observe the formation of RhO_2 in the B-steps until the CO was pumped from the chamber. This, together with the fact that a pure RhO_2 trilayer is reported to be inactive towards the CO oxidation, may indicate that Rh B-steps are more reactive than its A-type analogous during the CO oxidation.

List of acronyms and terms

- **1D**: 1-dimensional
- **2D**: 2-dimensional
- E_{ac}: Activation Energy
- E_{ads}: Adsorption Energy
- **AP**: Ambient-Pressure
- **ChemO**: Chemisorbed atomic oxygen
- **ER**: Eley-Rideal mechanism
- **HK**: Harris-Kasemo mechanism
- **HP-STM**: High-Pressure Scanning Tunneling Microscopy
- **HV**: High Vacuum
- **LEED**: Low Energy Electron Diffraction
- **LH**: Langmuir-Hinshelwood mathematical mechanism
- **ML**: Monolayer
- **MvK**: Mars-van Krevelen mechanism
- **NAP**: Near Ambient-Pressure
- **NAP-XPS**: Near Ambient-Pressure X-ray Photoemission Spectroscopy
- $\mathbf{O_{Terr}}$: Chemisorbed atomic O at terraces
- $\mathbf{O_{Step}}$: Chemisorbed atomic O at steps
- **PLIF**: Planar Laser-Induced Fluorescence
- $\mathbf{S_B}$: Step-Brigde
- $\mathbf{S_H}$: Step-Hollow
- $\mathbf{S_S}$: Step-Square
- $\mathbf{S_T}$: Step-Top

- **SFG**: Sum-Frequency Generation
- **STM**: Scanning Tunneling Microscopy
- **SXRF**: Surface X-Ray Diffraction
- $\mathbf{T_B}$: Terrace-Bridge
- T_c: CO Cooling Temperature
- T_i: CO Ignition Temperature
- $\mathbf{T_H}$: Terrace-Top
- $\mathbf{T_T}$: Terrace-Top
- **UHV**: Ultra-High Vacuum
- **XPS**: X-ray Photoemission Spectroscopy

Chapter 1

Introduction

1.1 Catalysis and gas-surface reactions

The speed of a chemical reaction at a given temperature is determined by the activation energy, E_{ac}: "*the minimum energy needed for reaction to occur in an encounter between reactants*" [1]. Typically, E_{ac} is reflected in the temperature needed for the reaction, following the Arrhenius law. A chemical transformation with large E_{ac} is unlikely, unless a significant amount of energy required is provided. This, e.g., is the case of the CO oxidation: $CO_{2(g)}$ will not be produced by simply mixing $CO_{(g)}$ and $O_{2(g)}$. However, introducing a warm Pt filament in such mixture will dramatically increase the CO_2 turnover [2]. It is then said that Pt is a catalyst: "*a substance that accelerates a reaction but undergoes no net chemical change*" [1].

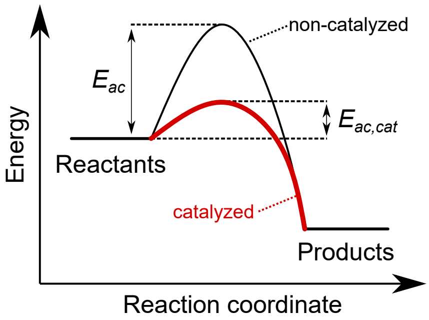

Figure 1.1: Energy diagram of a chemical reaction.
Energy variation during a chemical transformation as a function of the reaction coordinate. The activation energy of the bare chemical reaction (E_{ac}) is larger than one taking place with a catalyst ($E_{ac,cat}$). Therefore, a lower energy is required to start the reaction if a catalyst is present.

The role of a catalyst is to provide an alternative reaction path that lowers E_{ac}, leading to a faster reaction rate and saving energy. Their nature is diverse: proteins (i.e. enzymes) catalyze the biochemical processes occurring in cells [3], supported particles in catalytic converters turn the exhaust gases into less harmful ones [4], and dry yeast dissociates hydrogen peroxide in the *elephant's toothpaste* experiment [5].

Knowing how the catalyst alters the reaction is of key importance to improve the process in terms of activity (reaction rate), selectivity (formation of selected byproducts) and lifetime (time until deactivation). Depending on how its elements aggregate, we may classify a catalytic reaction in two large groups: homogeneous (same state) or heterogeneous (dissimilar state). Since the CO oxidation occurs on metallic surfaces, we will exclusively focus on gas-solid reactions. Gerhard Ertl extensively studied several of such processes, in particular CO oxidation, in the late twentieth century. He received the Chemistry Nobel Prize in 2007 "*for his studies of chemical processes on solid surfaces*" [6].

We shall also briefly define the concept of a *surface*, i.e. the boundary of a material that describes its interface with either the vacuum, a gas or a liquid. As a consequence of such termination, surface atoms have fewer coordination (lower neighbouring atoms) than those located at the bulk material. The resulting interaction of reactants and the surface radically alters the properties of both [7]. Adsorbed gas molecules form a chemical bond with the surface (*chemisorption*), often enabling an alternative reaction path that accelerates the reaction rate as compared to the sole gases [8].

Adsorbed molecules/atoms (*adsorbates*) will anchor to the surface at selected positions, resembling (in the eyes of Langmuir) to chess pieces in a checkerboard [9]. In many cases they will adopt ordered structures above the metal lattice, called *superstructures* [10]. However, surfaces may exhibit atomic sites with different coordination, namely terraces (atoms located at the same height), steps (atoms separating terraces of various heights), and defects (dislocations, missing atoms). One would expect a different catalytic activity at each of these sites [11], as we will discuss in Section 2.1.

The strength of the bond between the adsorbate and the surface is defined by the adsorption energy, E_{ad}, which significantly influences the reaction. According to Sabatier's principle [12], this interaction must be "*just right*" for the reaction to happen. On one hand, a strong bonding stabilizes the adsorbate, hence the formation of products will not be favourable. On the other hand, a weak bonding prevents a sizeable gas-solid interaction, and with it the catalysis from initiating.

One of the most important concepts of a chemical reaction is its reaction mechanism (or path). It consists on all elementary steps involved in the full catalytic cycle, from the first interaction of the reactant(s) with the catalyst, to the release of the product(s) [12]. A surface reaction may undergo several pathways, described in detail in Appendix A1. Briefly:

- **Langmuir-Hinshelwood**, LH [13, 14]. The coadsorbed reactants collide on the surface to form a readily desorbing product.
- **Eley-Rideal**, ER [15, 16]. An adsorbed reactant is attacked by a gas molecule. This yields the product, which promptly desorbs.
- **Mars-van Krevelen**, MvK [17, 18]. One of the reactants exhibits a compound on the catalyst surface, e.g., an oxide. Such structure may be partially consumed by impinging molecules of other reactants to turnover the desired product. The compound is readily renewed by gas molecules of the former reactant, leaving the catalyst intact.

Despite this variety, the most common process is the LH mechanism [9]; the ER is seldom observed [7]. However, the MvK may be relevant at large pressures due to formation of additional species, such as oxides [19].

We must introduce two key concepts in the investigation of gas-solid reactions in the Surface Science approach: the pressure and materials gap [20], both sketched in Figure 1.2. The *pressure gap* refers to the large difference between Ultra-High Vacuum laboratory measurements (UHV, $p < 10^{-9}$ mbar), necessary for achieving a clean and controlled surface, and the conditions to which catalysts are submitted at industrial facilities [(N)AP, (Near-)Ambient Pressures, $p \geqslant 1$ (m)bar] [21, 22]. This tremendous gap may induce dissimilarities between UHV and (N)AP experiments [23], such as different reaction mechanisms [19], saturation superstructures [24] or oxidation states [25], among others [see Figure 1.2a)]. However this gap may not occur for certain conditions and substrates [22, 26, 27].

The *materials gap* refers to the inherent difficulty to study real catalysts, as mentioned by Langmuir in 1922 [13]. Industrial catalysts, such as metallic nanoparticles [28] or nanowire arrays [29], may undergo several of the complex processes described above, making it difficult exact studies. Hence, we should resort to relatively simple systems, such as flat or vicinal surfaces, to cement the basis of further essays on more complicated systems, such as zeolites, metal-oxide or bi-metallic nanoparticles and nano-structured materials. Catalysts with different complexities are illustrated in Figure 1.2b).

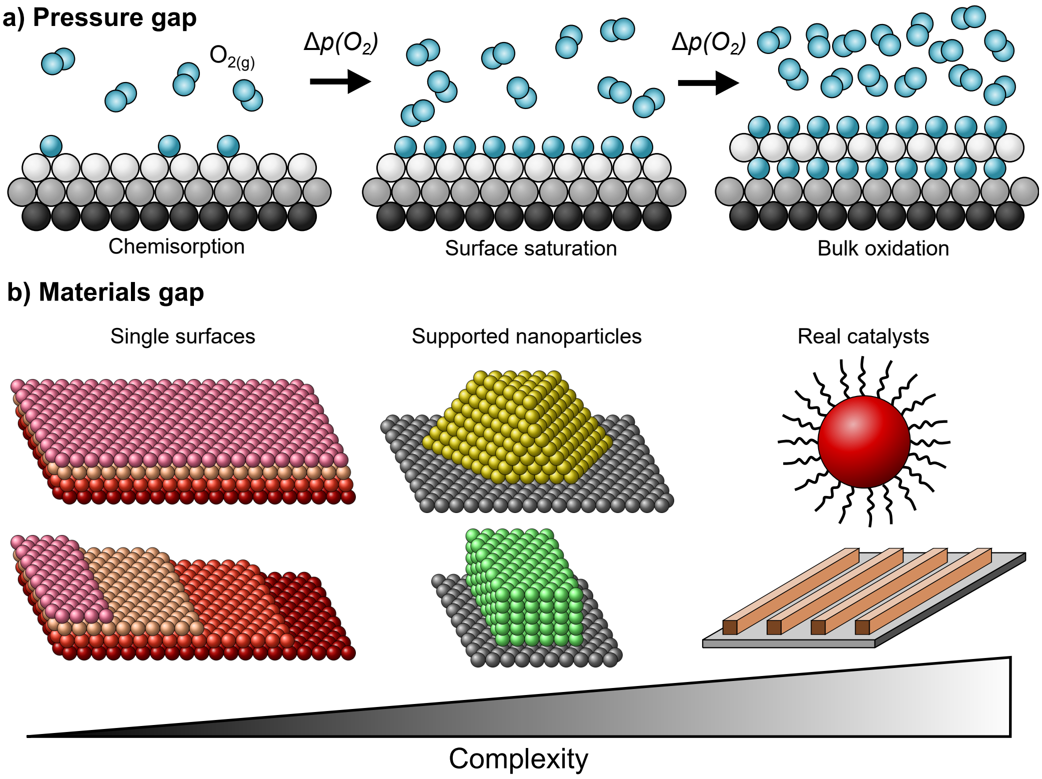

Figure 1.2: Pressure and materials gap in gas-solid reactions.
a) Pressure gap on the example of oxygen exposure: as the oxygen pressure rises [$\Delta p(O_2)$], the surface transitions from single chemisorbed O atoms towards a fully saturated surface. For even higher oxygen pressure, additional oxidation states may appear [30]. **b)** Materials gap. Complexity chart of different catalysts, from single flat/stepped surfaces and supported nanoparticles, to nano-structures and functionalized nanoparticles. Many other catalysts not included here, such as bimetallic alloys, metal-oxide nanoparticles and zeolites are employed in industry [29].

Typical Surface Science techniques, such as X-Ray Photoemission Spectroscopy (XPS), cannot operate at high pressures (in this case due to the scattering of electrons with the high pressure gas). Therefore, the study of catalytic surfaces was restricted to *ex-situ* (after the reaction at high pressure) or *in-situ* (during the reaction in UHV) essays. *Operando* experiments (under industrial conditions) [23] were not feasible. However, nowadays a large variety of setups allow to work at (N)AP conditions, enabling the study of catalysts under more realistic conditions. Among these techniques we find High-Pressure Scanning Tunneling Microscopy (HP-STM [25]), Infrared-Reflection Adsorption Spectroscopy (IRAS [31]), Sum-Frequency Generation (SFG [32]), Surface X-Ray Diffraction (SXRD [33]), Near-Ambient Pressure XPS (NAP-XPS [34], see also Section 2.2) and Planar Laser-Induced Fluorescence (PLIF [35], see Section 2.3).

In the study of gas-solid reactions catalyzed by a metal surface, important questions arise: which of the different surface planes of a metal catalyst is more active towards the reaction of interest? What is the role and interplay of different surface sites (terraces, steps, defects...) during a catalytic reaction? The answer to both questions is hindered in most studies. On one hand, metallic nanoparticles feature a multitude of different surfaces in the close proximity, for which their individual activity cannot be separately investigated with spectroscopic techniques. On the other hand, traditional Surface Science works use separate and more simple samples, which are not submitted to the very same reaction conditions and hence the interplay between different facets is significantly difficult to simulate. Nonetheless, we will discuss in Section 2.1 how curved crystals may be a reasonable model system to bridge nanoparticle catalysts with Surface Science studies on single crystal samples, and hence an appropriate way to answer all such questions.

1.2 The CO oxidation on metal surfaces

The CO oxidation reaction has been mater of theoretical and experimental discussion since several decades, due to both its (apparent) simplicity and its value as a model reaction for other catalytic processes. Furthermore, there is an urgent need to improve the efficiency of the petrochemical industry and the catalytic converters of combustion cars, in order to emit less dangerous gases to the environment [36]. The chemical reaction proceeds as follows:

$$2CO_{(g)} + O_{2(g)} \xrightarrow{\Delta,Cat} 2CO_{2(g)} \tag{1.1}$$

However, the reaction is not spontaneous at room temperature: we need to expose both gases to a catalyst (Cat) and heat (Δ) [2] in order to observe a significant CO_2 production rate. It typically follows a LH mechanism at low pressures [9]: O_2 molecules impinging the metallic surface will dissociate on it to form atomic O. This O can then collide with coadsorbed CO to form a readily desorbing CO_2 molecule. However, several factors may alter this seemingly simple oxidation reaction:

- **Catalyst**. It is evident that not all metals catalyze the reaction efficiently. Among others, Ru or Ir are good catalysts for this reaction [37, 38]. They both belong to the platinum-like metals, which also include the Pt itself, Pd and Rh. Modern catalytic converters employing metals are loaded with nanoparticles of the latter materials (Pt, Pd, Rh) in order to turn the toxic CO, nitrogen oxides (NO_x) and hydrocarbons (C_xH_y) coming from the fuel combustion to the less dangerous CO_2, nitrogen (N_2) and water (H_2O) [4].

- **Temperature**. The state of the surface, and hence its reactivity, heavily depends on the temperature. At low temperature, the surface of the mentioned metals will be covered by CO and no reaction will take place. Heating the catalyst yields a partial desorption of chemisorbed CO molecules, vacating surface sites and allowing an steadily increasing amount of O_2 to stick, dissociate and start the reaction. This will eventually lead to the *ignition* (or *ligth-off*) of the reaction: an exothermic process accompanied by a large boost of the reaction rate [39]. We shall discuss this phenomenon in the following paragraphs.

- **Total pressure**. If the reactants ratio is kept constant, an exponential growth of the total pressure linearly increments the ignition temperature [22]. Naively, the reason for this is a CO poisoning layer that becomes harder to overcome as the partial CO pressure grows.

- **Partial pressures**. Lowering the CO partial pressure decreases the ignition temperature, while the opposite is observed for O_2. We will elaborate later how CO self-poisons its own oxidation [2].
- **Flux**. Since two CO molecules per O_2 equivalent are consumed during the reaction, the production of CO_2 turns the gas mixture into more oxidative, lowering its light-off temperature. Therefore, refreshing the gases of the chamber gives rise to larger ignition temperatures [22].

The temperature controls the surface composition, and with it the reactivity of the metal. Let us discuss how the catalyst and the CO_2 production evolves during a typical CO oxidation experiment [39–41]. If we simultaneously expose our surface to CO and O_2 at room temperature, no CO_2 production will occur: we refer to this as the poisoned stage of the reaction. This is due to CO-poisoning: the surface will be coated with CO, which blocks the O_2 dissociative adsorption and quenches the reaction [42]. In fact, is has been shown that the O_2 dissociation barrier increases with the CO coverage [43]. Moreover, chemisorbed O does not hinder the CO adsorption: this effect is called *asymmetric inhibition* [44].

Increasing the temperature will cause some CO molecules to abandon the surface and empty adsorption sites. O_2 can now dissociate at these free patches and react with coadsorbed CO to form CO_2. However, as long as the CO dominates the surface, it will quench the dissociative O_2 adsorption and hence the CO_2 production [2]. We therefore need to further raise the temperature of the catalyst to liberate more surface sites and speed up the reaction kinetics. The CO oxidation is exothermic, hence an steadily growing amount of heat will be released as an increasing amount of CO_2 is produced.

This freed energy will warm the surface, causing a progressive desorption of more CO molecules, boosting at the same time the O_2 dissociative adsorption and the reaction rate. These processes will self-accelerate until an explosive boost in the CO desorption (and hence CO_2 production) is observed: the ignition (or light-off) of the CO oxidation has occurred [39].

After the ignition, the CO_2 turnover is maximum: we have reached the active stage of the CO oxidation. As discussed later, its nature is largely variable, although it is always characterized by a large CO_2 production and a typically CO-depleted surface. Most of the CO molecules have desorbed during the ignition, and typically oxygen-related species are observed on the surface. We will individually asses the active stage of Pt and Rh surfaces in the following sections.

In summary, the CO oxidation will be quenched at low temperature due to the poisoning of the surface by adsorbed CO molecules that block the dissociative adsorption of O_2. Since there is none or low CO_2 production, we talk about the poisoned stage of the reaction. Heating the catalyst will desorb some CO and vacate surface sites, steadily increasing the reaction rate. Further increase of the temperature will cause a dramatic growth in the CO_2 production, releasing a huge amount of heat and desorbing most the CO from the surface. This is the so-called ignition, and marks the transition towards the active stage. The latter is characterized by a vanishing amount of CO adsorbed on the surface and a large CO_2 production. It is usually accompanied by the formation of oxygen-related species.

A typical CO oxidation essay is sketched in Figure 1.3. A Pt(111) surface was exposed to both CO and O_2 (total pressure of 1.0 mbar, 1:4 CO:O_2 gas mixture) at room temperature, and subsequently heated to ignite the reaction. On one hand, we monitored the local gas composition by the use of a Quadrupole Mass Spectrometer (QMS) [45]. On the other hand, we analyzed both the catalyst surface and gas phase close to it by NAP-XPS. The fundamentals and setup of this technique are discussed in Section 2.2. Briefly, it allows to correlate the CO_2 turnover with the surface species.

In Figure 1.3a) we show a cascade plot of the C 1s region obtained at different temperatures. Starting the experiment at 300 K, different signals from graphitic carbon ("C"), chemisorbed CO (ChemCO) and gas phase CO are distinguished in the NAP-XPS. All CO-related features slightly decrease with the temperature, until they suddenly vanish from the spectrum at around 550 K. Simultaneously, $CO_{(g)}$ disappears from the QMS and $CO_{2(g)}$ appears in both techniques. These signals are sketched in Figure 1.3b) as a function of temperature and time, showing the expected parallelism. On one hand, CO slightly decreases as T_i approaches, and rapidly vanishes afterwards. On the other hand, CO_2 is small at low temperature, steadily grows when approaching the ignition, and explosively rises after it.

Choosing an adequate heater is also mandatory for a proper study of the CO oxidation. Using a Pt filament for heating will consume a fraction of the reactants, namely the double amount of CO as compared with O_2. This leads to a stronger reduction of the CO pressure and hence to a more oxidizing atmosphere, which causes a decay of T_i. If instead of the Pt filament heating, an inert pyrolytic boron nitride (BN) heater is employed, the gas phase will remain unchanged by the heater, and T_i will not be altered.

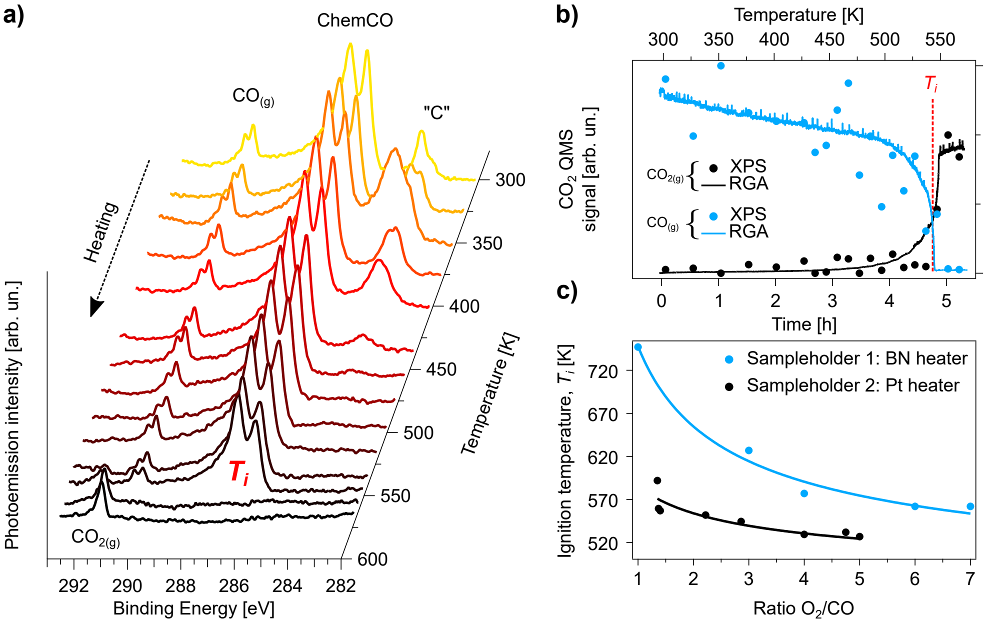

Figure 1.3: CO oxidation model experiment on Pt(111).
a) Waterfall plot of the C 1*s* region during a heating cycle of a Pt(111) sample under reaction conditions. The experiments were carried out at 1.0 mbar, 1:4 CO:O_2 gas mixture and 650 eV of photon energy. The labels "C" and ChemCO refer to graphitic carbon and chemisorbed CO on the surface, while $CO_{(g)}$ and $CO_{2(g)}$ allude to the gas phase photoemission lines of those molecules, respectively. **b)** Evolution of $CO_{(g)}$ and $CO_{2(g)}$ during the heating ramp as extracted from the QMS and XPS. The ignition temperature, T_i, is illustrated with a dashed red line at 550 K. **c)** Observed T_i at different CO:O_2 ratios (total pressure varied between 0.5-1.0 mbar). Data correspond to samples annealed with two different heaters, i.e. a Pt filament and a boron nitride-covered filament (BN). See the text for more details.

As mentioned before, the CO:O_2 ratio heavily alters T_i. Since adsorbed CO poisons the catalyst, a larger CO partial pressure will increase the light-off temperature significantly [2, 39]. This is nicely reflected in Figure 1.3c). Since the total pressure was kept constant in the 0.5-1.0 mbar range, we expect the differences in T_i to depend mainly on the CO:O_2 ratio [22].

To end with, there is a complex contribution in Figure 1.3a), corresponding to graphitic carbon ("C"). Adsorption of residual hydrocarbons from the chamber may lead to such signal. However, its increase with the temperature points towards the CO dissociation (or *CO cracking*) as its origin, since heating the sample will enhance the CO cracking rate [46]. Parallel to the "C" growth, a decrease of ChemCO may be observed (significant for Rh surfaces, see Appendix D3), indicating its dissociation. In addition, surface "C" can also be oxidized to CO_2 by surrounding oxygen [47]. This process is also named as *carbon burning*, resembling the diamond burning experiments performed by the Lavoisiers some 250 years ago [48].

With this information, we can now easily explain the "C" variation with the temperature. Up to 350 K, CO cracks and "C" is accumulated on the surface. Above 350 K, the "C" burning speeds-up, consuming the surface "C" until no more is detected at 450 K. To end with, we observed no appreciable increase in the CO_2 signal, excluding the "C" burning as a relevant pathway for the CO_2 production at these temperatures and conditions.

We have emphasized that there is a large CO_2 production during the active stage of the reaction: typically all CO molecules impinging the surface react. This tremendous activity might induce a reactants-depleted region close to the surface: the arrival of CO/O_2 molecules to the surface will be diffusion-limited, causing the reaction rate to be in the *Mass Transfer Limit* (MTL) regime [49]. In fact, this is the case for all active stages presented here: the $CO_{(g)}$ signal vanishes from the NAP-XPS, indicating low CO pressure close to the sample. This will also turn the gas mixture into strongly oxidizing (see Appendix B2), possibly inducing new O-rich structures [50].

The MTL is a big problem in catalysis, demanding for high-flux/pumping setups to properly study reactions such as the CO oxidation [21]. This is the case of the PLIF setup, characterized by a small chamber with a high pumping speed. However, in most NAP-XPS setups, large vacuum chambers are used and often the pumping rate is strongly limited. This translates to a nearly static gas regime only with pumping through the electron analyzer aperture, clearly affecting the nature of the active stage of the CO oxidation.

After introducing most of the key concepts of the CO oxidation and catalysis in general, in the following we will focus on the CO oxidation on flat and stepped Rh and Pt surfaces. For such purpose, we will review the effect of both CO and O_2, first individually and then together, on these surfaces.

1.3 CO oxidation on Platinum surfaces

There is a vast knowledge on the CO oxidation reaction on Pt surfaces, which is summarized in Appendix A2. Here, we will only introduce some aspects that are related to the present subject, i.e. the interaction of separated and combined CO and O_2 with Pt(111) and its vicinal surfaces.

1.3.1 CO adsorption

Exposing a Pt(111) surface to CO at low temperature and pressure will give rise to a rich variety of adsorbate arrangements [51, 52]. The coverage of these superstructures will be expressed in terms of *monolayers* (ML, i.e. adsorbed particles per substrate atoms). The maximum CO coverage corresponds to an hexagonal superstructure at 0.68 ML and 170 K [51], while a 0.5 ML, $c(4\times2)$-4CO arrangement develops at room temperature [53]. This is caused by the temperature-dependent decrease of the adsorption energy [51]. The room temperature superstructure consists of an equally populated layer of CO molecules anchored in top (terminal, on top of a Pt atom) and bridge (two-fold, between two Pt atoms) sites at terraces [54–56], named as $\mathrm{T_T}$ and $\mathrm{T_B}$, respectively. However, if the pressure is increased, the original hexagonal 0.68 ML arrangement may be recovered. This structure is complex, and it is described as a $(\sqrt{19}\times\sqrt{19})\mathrm{R}23.4°$-13CO superstructure with $7\mathrm{T_T}$:$6\mathrm{T_B}$ [19, 24, 57, 58]. Both CO saturation structures are shown in Figures 1.4a,b). They represent the canonical CO-poisoning layers on Pt(111).

CO molecules adsorbed at either close-packed or kinked steps feature a larger E_{ad} than their analogous at terraces. Therefore, they exhibit a higher desorption temperature [59]. Also, a larger reactivity is predicted [60]. CO is known to adsorb on top sites at the upper edge ($\mathrm{S_T}$) of the {111} microfacet of Pt B-steps [61–63], while both $\mathrm{S_T}$ and bridge positions ($\mathrm{S_B}$) coexist on Pt steps with {100} microfacets (A-steps) [64–67]. We illustrate these adsorption sites in Figure 1.4c). Early works on the CO adsorption on kinked surfaces report $\mathrm{S_T}$ as the preferential site at the zigzag arrays, however a small amount of $\mathrm{S_B}$ may also be present on the kinks [68].

Experiments conducted at high pressures revealed that both A- and B-type Pt steps restructure upon bare CO adsorption. On one hand, CO adsorbed on the A-type Pt(557) will develop triangular clusters accompanied with step doubling [69, 70]. On the other hand, the B-type Pt(332) features parallelogram-like structures after CO adsorption, although no step doubling was observed [70]. We will see later in Chapter 3 that there are some differences in CO coverage between the UHV [63, 64, 67] and NAP [70] studies.

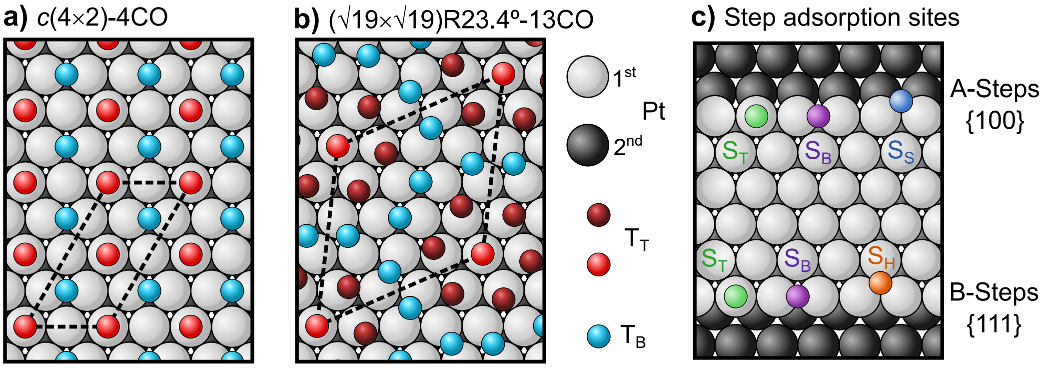

Figure 1.4: CO adsorption on Pt(111) and step edges.
a) $c(4{\times}2)$-4CO and **b)** $(\sqrt{19}\times\sqrt{19})$R23.4°-13CO superstructures at Pt(111). **c)** Relevant adsorption positions at A- and B-type straight steps. Pure (red) or tilted (garnet) T_T and T_B (cyan) correspond to Terrace-Top and Terrace-Bridge sites. S_T (green), S_B (purple), S_H (orange) and S_S (blue) refer to Step-Top Step-Bridge, Step-Hollow and Step-Square sites, respectively.

1.3.2 Oxygen adsorption

The oxidation of Pt is more complicated, since oxygen does not necessarily form ordered structures and it might also incorporate below the surface. If a Pt(111) surface is exposed to O_2 above 150 K, a layer of atomic O will develop, exhibiting a (2×2) Low-Energy Electron Diffraction (LEED) pattern [71–73]. This corresponds to a 0.25 ML, $p(2{\times}2)$-O superstructure with O atoms occupying fcc hollow sites [74–76], i.e. the three-fold configuration without any Pt atom in the second layer [see Figure 1.5a)]. Further increase in the coverage at room temperature is not observed due to kinetic limitations and the lack of sites for O_2 to dissociate [77]. Higher O_2 pressures [78] or stronger oxidizers are required to develop denser O phases [79–82].

STM images in the 0.25-0.5 ML regime show that O arranges in $p(2{\times}1)$ stripped chains [83]. As sketched in Figure 1.5b), the O atoms remain anchored on fcc sites [84]. As the O coverage approaches 0.5 ML, the $p(2{\times}1)$ domains start to pack parallel, forming 1D oxide chains [83]. DFT calculations show that these oxide stripes are formed by Pt surface atoms linked to 4 oxygen atoms [85], hence the "4O" name. This "4O" oxide is formed by PtO_4 motifs separated by Pt rows, as shown in Figure 1.5c). These streaks linearly extend with the coverage, eventually interconnecting as the oxygen coverage approaches of 0.75 ML [83]. Similar 1D chains were also reported for Pt(110) surfaces [86, 87]. The formation of subsurface O species may be observed if the coverage is further increased [84, 88, 89].

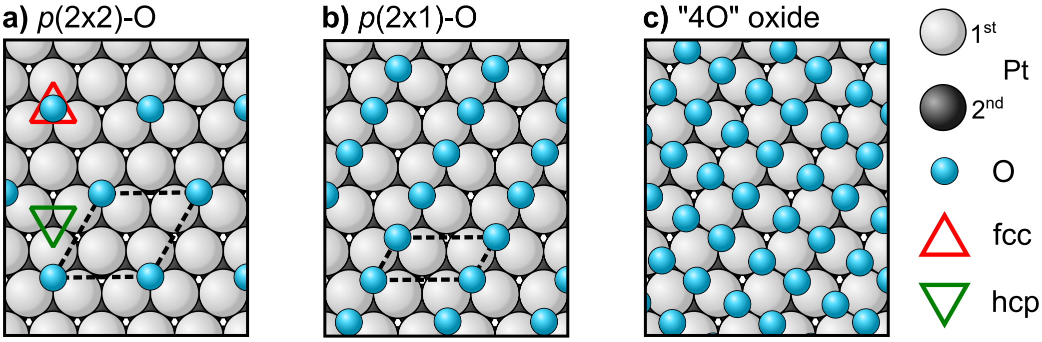

Figure 1.5: Relevant arrangements of O on Pt(111).
Top view of **a)** $p(2\times2)$ (0.25 ML), **b)** $p(2\times1)$ (0.5 ML) and **c)** "4O" oxide (1 ML) superstructures. Hollow hcp and fcc sites are sketched with green and red triangles, while O and Pt atoms in the first and second layer are coloured as cyan, light grey and dark grey, respectively.

Pt(111) oxidation experiments at high pressures by Miller *et al.* [30] reported the formation of the "4O" oxide stripes as the coverages reaches 0.6 ML (0.7 mbar O_2, 520 K). As the O coverage approaches 1 ML (620 K), they bunch to develop a complete "4O" layer. Only by increasing both the temperature and pressure (7 mbar, 720 K) one is able to further oxidize Pt(111) and form α-PtO_2 trilayers on the surface.

A STM work at bar O_2 pressures reported similar 1D oxide chains [25]. The STM images show how such stripes interconnect with each other to form complex "spoke-wheel" and close-packed, parallel structures, having a lattice constant that is similar to that of bulk α-PtO_2. The latter was not observed in this work, revealing that even at ambient O_2 pressures, the oxidation of Pt(111) is kinetically limited [82, 90, 91]. Surface roughening [79, 80, 82] and a large variety of different Pt oxides [91–95] may also coexist with the aforementioned species, making it difficult the study of Pt oxidation.

Regarding stepped surfaces, it is clear that the dissociative O_2 adsorption is favoured at the Pt steps over the flat terraces [96–99]. In addition, step doubling [100–103] and both larger O coverages [104] and desorption temperatures (i.e. E_{ad}) as compared to their flat analogous [96, 105] are observed. A STM and theoretical work by Feibelman and coworkers reported that atomic O is anchored at bridge sites at {100} steps (S_B, A-type), while it occupies the hollow fcc position close to the edge at {111}-oriented steps (S_H, B-type) [97] (see Figure 1.4). This was later corroborated by other studies [106, 107].

Wang *et al.* [96] observed the preferential oxidation of Pt steps as compared to terraces. Exposing a Pt(332) surface to O_2 yields the formation of 1D oxides chains of PtO_4 motifs at the edges, similarly to other works on Pt stepped surfaces [108, 109]. In addition, the step exposes the subsurface region of the higher terrace, easing the incorporation of O atoms [89].

Oxidation experiments conducted at large pressures on Pt(557) (A-steps) [110] lead to configurations similar to those in UHV. The nucleation of the oxides starts at the steps rather than the terraces, since it is kinetically limited for the latter. The oxides extend towards the terrace forming step-oriented triangular clusters, pointing to the step 1D stripe as their precursor. Increasing the pressure leads to the formation of a 2D, disordered oxide phase which is unstable after pumping the O_2 from the chamber.

The works on kinked surfaces are scarce at UHV conditions, and nonexistent at high pressures. While it is clear that O binds stronger on the kinks as compared to terraces, the nature of the adsorbed species remains unclear [111–113]. A XPS study by Held *et al.* in Pt(531) [114] reported three different species after annealing the surface in low O_2 pressure: a chemisorbed state (lower desorption temperature) and two oxide clusters *on the surface* (larger desorption temperature), different from both PtO and PtO_2.

1.3.3 CO oxidation

We will now explore how Pt behaves under CO oxidation conditions, i.e. when simultaneously exposed to CO and O_2. We will mainly focus on the composition of the active stage (oxides, roughening, step doubling...). At low pressures, the reaction occurs via a LH mechanism [41], and clear evidences of surface oscillations (temporally and spatially periodic variations of the surface composition) have been observed [44, 115].

In Pt(111) and low pressures, the activation energy of the CO oxidation decreases (increases) with the O (CO) coverage [116]. This reflects again how the CO poisons the O_2 dissociative adsorption, quenching the CO_2 formation. Early work by Gland *et al.* on Pt(111) [117] showed no preferential oxidation of bridge (T_B) sites, even though their adsorption energy is lower and one would expect their desorption prior to top CO (T_T). More importantly, they suggest that the reaction may occur between domain boundaries of the O islands, similarly to Kinne *et al.* [118]. Such hypoThesis was confirmed by Wintterlin and coworkers [119]. They followed the reaction of CO with a pre-adsorbed $p(2\times2)$-O layer (ChemO) by STM. They observed how the boundaries of the oxygen patches are steadily consumed by CO, which covers the vacant surface sites forming $c(4\times2)$-4CO domains.

Albeit the scenario seems simple until now, a general trend is hindered in Pt(111) at large pressures and temperatures, reasonably due to both the variety of Pt oxides and the several hours required for their formation [120]. The reaction is also reported to undergo via LH mechanism at high pressures [121], possibly occurring at defects during the CO-depleted active stage [122].

Miller *et al.* [123] studied the reactivity of several Pt(111)-O species, revealing that the oxidation state decreases the reactivity of Pt(111) for the CO oxidation. Additionally, a full trilayer of α-PtO_2 was found inactive towards CO oxidation [91, 95]. The chemical species observed under reaction conditions are similar for Pt nanoparticles and Pt(111), reflecting the utility of well-defined surfaces as basis for more complex systems [123].

A NAP-XPS essay on the CO oxidation on Pt(111) revealed only ChemO on the surface during the active stage at oxidizing conditions [38]. However, the absence of Pt-O species at both oxidizing and reducing conditions was reported by Krick Calderón and coworkers using the same technique [124], in clear contradiction with the first work. In addition, Farkas *et al.* [125] observed the oxidation of Pt(111) by SXRD in slightly O_2-rich conditions, reporting how the oxidized surface could be readily reduced by CO. Similarly, Pt nanoparticles may remain partially oxidized [126] or metallic [127] during the active stage of the reaction. A common trend is not found, possibly due to the experimental differences between these studies.

Pt(110) gave rise to an interesting debate on the reactivity of ChemO and Pt oxides. On one hand, Frenken and coworkers reported oxide formation during reaction conditions with HP-STM and SXRD [128, 129]. It is clearly seen that the oxide roughens the surface, and they claimed both a larger reactivity [than ChemO on metallic Pt(110)] and a MvK mechanism [128]. Ackermann *et al.* [129] could alter the composition of the active surface by tuning with the CO:O_2 ratio, observing different oxides. Only one of them could be stabilized under reaction conditions. In this line, Butcher and coworkers reported a similar reactivity of ChemO and the surface oxide on Pt(110) [130]. An additional Pt oxide, in this case Pt_3O_4, is predicted to be highly active [91]. On the other hand, Goodman and coworkers [27, 31, 131] reported no oxidation of Pt(110). The reaction is argued to follow a LH pathway during the active stage, yet the reason for this activity is a CO-depleted surface partially covered by ChemO. This would agree with the larger reactivity of ChemO observed by Miller *et al.* [123]. Furthermore, another NAP-XPS work on Pt(110) also reported no oxide formation and a LH mechanism [132]. As a comment, the existence of subsurface oxygen below the topmost Pt layer does not affect the overall activity either [133].

Regarding the CO oxidation essays at Pt(111) vicinals, works using a full cylindrical sample showed an increasing O sticking and decreasing CO oxidation probabilities at the steps, where the role of the steps on the CO oxidation depends on the CO:O_2 ratio [134]. Another work with a Pt(557) surface mimics these results: the steps are more reactive at low temperatures, while the terraces dominate the situation at higher temperatures, more relevant for real catalytic processes [135]. This agrees with several CO oxidation reports on close-packed and kinked Pt surfaces: the CO at terraces is more reactive (i.e. reacts faster) than that anchored at the steps [136–139]. The steps would act as O_2 dissociation centers, where diffusing CO molecules (O atoms lack of mobility [140]) may collide to form CO_2 [139]. Two different CO_2 molecules may be produced: hyperthermal (terraces, higher velocity) and thermal (steps, lower velocity) [141], since CO_2 is briefly trapped at the step edges after its formation [142]. The 1D oxide stripes formed at Pt(332) are more reactive than the oxygen located at the terraces [96]. The cluster oxides of Pt(531) also readily react with CO [114], pointing to a large reactivity as compared to the oxide located at terraces.

At higher pressures, sum-frequency generation studies by McCrea *et al.* [46, 47] reported that while the CO cracking occurs at lower temperature for Pt(557) than for Pt(111) (550 *vs* 570 K), T_i has the opposite tendency: the (111) surface ignites at 620 K, 20 K lower than the (557) plane (640 K), pointing to a more complex role of terraces during the CO oxidation.

To end with this Section, we must discuss two interesting CO oxidation studies at high pressures by Balmes and coworkers [143, 144]. They probed both the Pt(779) (A-steps) and Pt(997) (B-steps) surfaces with SXRD at reaction conditions. The Pt(779) [143] surface is faceted and consists on flat (111) areas and stepped (779) regions. No step doubling was detected. The relative ratio of (111) and (779) areas can be tuned with the CO:O_2 ratio. In a stoichiometric mixture, the amount of (779) areas, and also the reactivity towards CO oxidation, was found to be maximum. Departure from stoichiometry induced a reversible decay of the (779) areas [larger (111) facets] and CO_2 production. On the other hand, the measurements conducted on the Pt(997) sample [144] revealed that the surface can reversibly change from mono- (CO-rich) to double- (O_2-rich) atomic steps depending on the CO:O_2 ratio. This is expected, since oxygen-induced step doubling was already observed in UHV conditions [100–102, 104]. The CO_2 turnover of double steps is around 3 times bigger than their monoatomic analogous, and the reaction seems to follow a LH mechanism at these high pressures [144]. Mimicking these close-packed surfaces, the kinked Pt(210) also reconstructs both during reaction conditions and upon O_2 exposure [145].

1.4 CO oxidation on Rhodium surfaces

In the following the CO oxidation on Rh, the other substrate material of this Thesis, will be discussed. The bibliography is not as extensive as for Pt, and there is a larger agreement among different works.

1.4.1 CO adsorption

Initially, some controversy arouse regarding the adsorption geometry of CO at Rh(111). Early investigations reported that the Rh(111) CO saturation structure comprises both top and bridge sites [146, 147], although later reports found that CO anchors at top and hollow positions [148–150]. In general, Rh(111) will develop a rich variety of structural arrangements upon CO chemisorption, as discussed by Beutler and coworkers [151]. Up to 1/3 ML and at low temperature, CO will adopt top geometry (T_T) forming a $(\sqrt{3} \times \sqrt{3})$R30°-CO superstructure. T_T sites will further populate up to 1/2 ML, and at the same time the adsorption in hollow configuration (T_H) will also become visible in the spectra. A (4×4) LEED pattern is observed, yet the surface is significantly disordered. As the coverage grows, CO molecules will continue to adsorb in T_H sites, and a fraction of T_T molecules will also shift towards T_H configuration, reaching a saturation coverage of 0.75 ML at 95 K. At this point, a (2×2) LEED pattern is observed, which corresponds to an equally populated arrangement of CO molecules in top, hollow fcc and hollow hcp sites (0.25 ML each, $c(2 \times 2)$-3CO superstructure). As one would expect, the coverage limit decreases when the temperature approaches 300 K. At this temperature, the maximum coverage is ≈0.6 ML, pointing towards a stronger repulsive interaction of CO molecules within the $c(2 \times 2)$-3CO arrangement. All of these superstructures are sketched in Figure 1.6.

B-type [152–155] and kinked [156] Rh(111) vicinals have also been subject to investigations. CO will start to adsorb on top sites at the stepped arrays (S_T), similarly as on Pt. Nonetheless, as the coverage increases, the preferential position after/close to the saturation of S_T it is not clear. Two possibilities arise, either bridge geometry at stepped array (S_B) or T_T [152, 155]. However, both works confirm the ultimate adsorption at T_H positions. No absorption sites are reported for kinked vicinals, but such surfaces were found to enhance the CO dissociation [156]. A similar situation was observed for the B-type Rh(553) surface [152]. To our knowledge, there are no works concerning A-type vicinals.

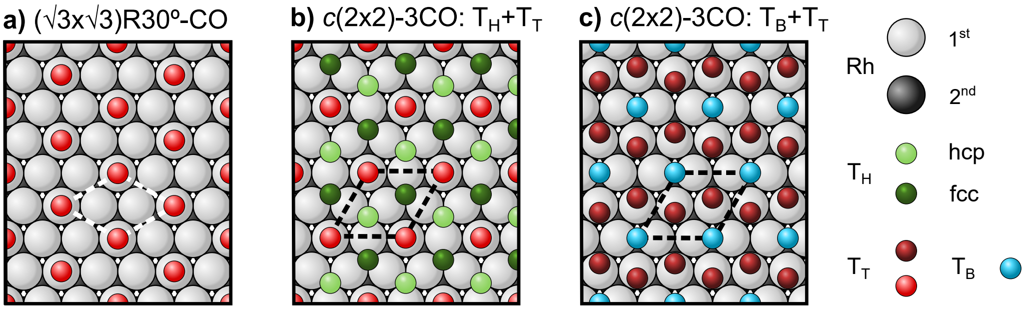

Figure 1.6: CO-induced superstructures on Rh(111).
a) $(\sqrt{3}\times\sqrt{3})$R30°-CO [151] and **b,c)** both $c(2{\times}2)$-3CO arrangements. CO adsorption in hollow positions is considered in b) [148–150], while it anchors at bridge sites in c) [146, 147]. The latter structure is nowadays accepted. CO molecules in top (T_T), bridge (T_B), hollow hcp and fcc sites are sketched as red (tilted T_T as garnet), blue and light and dark green, respectively.

1.4.2 Oxygen adsorption

O atoms are known to occupy hollow fcc sites on Rh(111), forming a $p(2{\times}2)$-O superstructure at 0.25 ML, and $p(2{\times}1)$-O stripes at 0.5 ML [157, 158]. This mimics Pt(111), as sketched in Figures 1.5a,b). Larger O_2 pressures may increase the oxygen coverage to 2/3 ML, forming $(2\sqrt{3}\times 2\sqrt{3})30°$ arrangement combining both hcp and fcc hollow sites {see Figure 1.7a) and Ref. [159]}. Even larger coverages are achieved at higher pressures (0.5 bar O_2) and temperatures (900 K) [160]. At these conditions, O will migrate into the subsurface, further oxidizing the Rh(111) surface and developing the Rh surface oxide. It consists on O-Rh-O trilayers in a (9×9) superstructure, resembling the trilayers of surface α-PtO_2 [30]. It is sketched in Figure 1.7b). Further bulk oxidation towards Rh_2O_3 may be observed, yet extreme pressures and temperature are required to overcome the kinetic hindrance [160].

Gustafson *et al.* [161] studied the structure of the B-stepped Rh(553) under a pure O_2 environment. On one hand, at low O_2 pressure, the surface undergoes a *step bunching* process: the intermediately stepped Rh(553) surface facets towards large (111) terraces separated by highly stepped (331)-oriented areas. The terraces feature a combination of both the (9×9) surface oxide and $p(2{\times}1)$-O stripes. The steps consist of a periodic structure where 1 out of 5 Rh atoms are ejected, while the remaining step atoms are coordinated to 4 O atoms. The distance Rh-O is close to that of Rh_2O_3, which may point to the fact that the steps promote bulk oxidation.

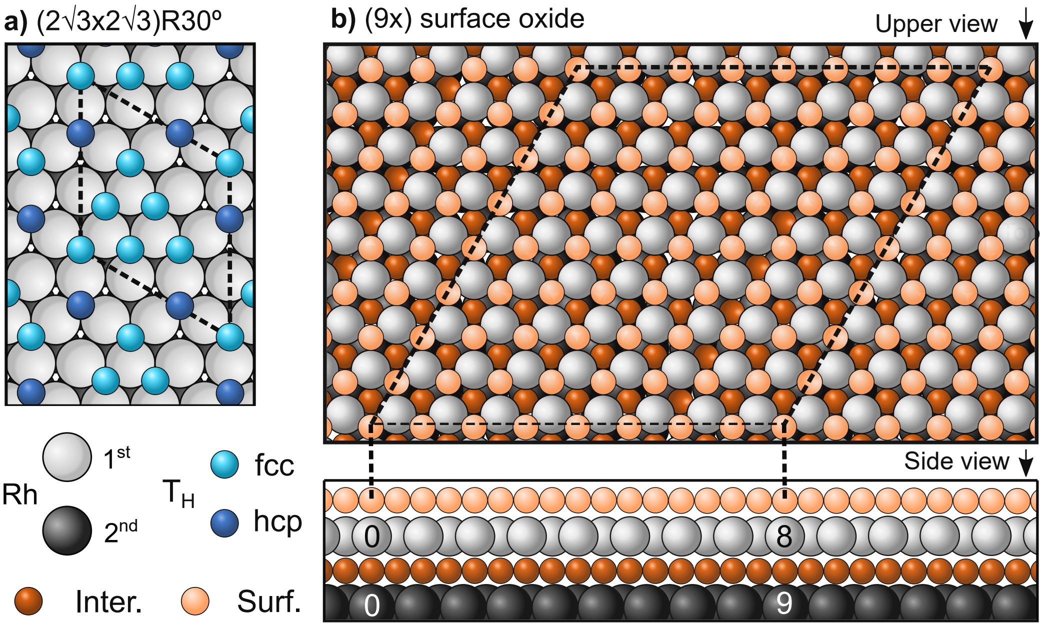

Figure 1.7: Relevant arrangements of oxygen on Rh(111).
a) Top view of the $(2\sqrt{3} \times 2\sqrt{3})R30^\circ$ superstructure [159]. **b)** Upper (top) and side (bottom) views of the (9×9) surface oxide [160]. Both unit cells are sketched are dashed black lines. In a), Rh atoms are colored as light (top layer) and dark (bottom layer) grey, while O atoms in hollow fcc and hcp sites are sketched with light and dark blue, respectively. In b), interfacial (below the first Rh layer) and surface (above the topmost Rh layer) O atoms of the surface oxide are depicted as dark and light orange. For the surface oxide, the size of surface Rh atoms was decreased to better illustrate the complex composition of the RhO_2 trilayers.

However, after exposure to near mbar O_2 pressures, the Rh(553) surface exposes a LEED (9×9) pattern similar to that observed in Rh(111). The SXRD measurements point to large {111} facets and the disappearance of the (331) regions, which reflects that the step bunching is maximized and the surface consists on large, flat terraces of the surface oxide. These RhO_2 trilayers have been observed/predicted in a significant variety of additional Rh surfaces [162–167], for which Gustafson and coworkers suggested that "*specific Rh crystal planes exposed during catalysis will not directly influence the reactivity*" [168]. We will discuss this point in Chapter 5 with our curved Rh(111) crystal.

1.4.3 CO oxidation

Lundgren *et al.* [169] compared the reactivity of the $p(2\times1)$-O stripes and the surface oxide in Rh(111) by exposing each of them to CO in UHV. Interestingly, CO does not adsorb on the perfect (9×9) oxide, therefore the stripes react remarkably faster than the oxide. A LH mechanism is prohibited for the latter, since both reactants cannot coadsorb. Therefore, the reduction of the oxide occurs at a larger time scale. The reaction initiation is believed to occur at oxide defects, where CO does adsorb. These chemisorbed CO molecules would react with neighbouring O atoms from the RhO_2 trilayer, creating more metallic Rh patches. Hence, larger areas would become available for the CO to adsorb, diffuse and form CO_2, increasing at the same time the reaction rate. This seems compatible with the reaction occurring at the metal-oxide interface, as reported by Farber and coworkers [162]. As expected, the reduction of the topmost layer of the surface O is observed prior to capture of interfacial O due to a lack of accessibility of subsurface O atoms [169]. The surface oxide has less Rh surface atoms than Rh(111), hence its reduction by CO produces a roughened metallic surface.

The surface oxide may also be observed in Rh(111) during CO oxidation experiments at realistic pressures [168, 170]. Similarly to Pt(110), there was a discrepancy on the nature of the active phase during CO oxidation [171–173]. In all of these experiments, it was observed that the surface oxide is present during the active stage of the reaction. However, it is difficult to directly assess its reactivity. Nevertheless, the authors that claimed a larger reactivity of the oxide later reported that the O-covered Rh metallic surface is more reactive than the RhO_2 trilayer oxide [39]. Bulk Rh_2O_3 poisons the reaction in a Rh(111) surface [165], as well as in a PtRh alloyed catalyst [170, 163], which points to a decrease in the activity towards the CO oxidation as the Rh oxidation state increases, mimicking Pt.

Zhang and coworkers studied the reaction of CO with preadsorbed O on Rh(553) (B-steps) [174], and observed that the reaction occurs faster on the stepped surface compared to the flat Rh(111) plane. This is what one would expect, since vicinal surfaces are believed to be more reactive than their high-symmetry analogous. However, the reaction does not take place at the very step edge, but at the upper terrace in the vicinity of the step. This reflects how not only the number of active sites, but the possibility to diffuse towards them during catalysis plays a major role during chemical reactions.

Finally, Zhang *et al.* conducted another interesting work on Rh(553) [175]. They exposed it to CO oxidation conditions at realistic pressures, and they monitored by SXRD the surface structure. They varied the CO:O_2 ratio at a constant temperature of 520 K, in order to alter the surface composition/structure. The following was observed:

- CO excess (10:2 CO:O_2): at these reductive conditions, the surface features CO-covered (111) and (110) facets. No significant CO_2 turnover was observed, for which the surface is assumed to be poisoned. Interestingly, the (110) faceting was not observed before on this Rh(553) surface, and theoretical calculations suggest that such effect happens due to the high CO coverage achieved at these pressures.

- Almost stoichiometric conditions (5:2 CO:O_2): only diffraction arising from the (553) plane was observed, hence the surface does not reconstruct under this reactants ratio. The CO_2 signal appears in the mass spectrometer, indicating the transition towards the active stage. This nicely reflects how the surface composition and ignition temperature can be triggered by simply tuning the gas mixture.

- Slightly oxidizing conditions (3.5:2 CO:O_2): the surface undergoes the step bunching process described in Ref. [161], where the surface exposes flat (111) and densely stepped (331) facets covered by oxygen during the active stage of the reaction.

- O_2 excess (2:2 CO:O_2): only the (9×9) oxide signal was observed in the SXRD. The Rh(553) sample is oxidized forming RhO_2 trilayers, and large hill-and-valley (111) and $(11\bar{1})$ regions coexist: the surface does not exhibit any steps anymore.

As expected, the surface structure heavily depends on the CO:O_2 ratio. An extreme case is reached at oxidizing conditions, under which hill-and-valley (111) and $(11\bar{1})$ facets covered with RhO_2 trilayers appear on the surface. Since the faceting is related to the formation of the surface oxide, and this develops in several Rh surfaces including Rh(100) [162–167], one would naively expect a similar situation for A-Stepped ({100} microfacet) Rh surfaces, although no studies exist to our knowledge. However, this still does not mean that the formation of the trilayer oxide would happen at the same temperature or the same pressure conditions for different Rh surfaces. This issue shall be also discussed further in Chapter 5 based on our observations at Rh(111) vicinals of the c-Rh crystal.

Chapter 2

Technical details

2.1 The curved crystal approach

Catalysis, as well as other physical or chemical processes, happens at the surface of metals or nanoparticles. Such surfaces have locally a crystalline structure, being formed by different facets with defects, steps, *etc.* However, investigations on these *real* systems are difficult, since different processes occur on each of the facets at the same time, and probing them in a separate way is challenging. Accordingly, most basic studies are carried out on *macroscopically flat* surfaces with a well-defined crystal symmetry direction. For an easier understanding we will focus on the example of a face-centered cubic (fcc) lattice, which is the one adopted by Platinum (Pt) and Rhodium (Rh) [176], the two substrates studied throughout this work. Cutting a 3-dimensional crystal gives rise to atomically well-defined surfaces that are characterized by the Miller indices (*hkl*) [176]. The most simple cases are the high-symmetry (or low index) planes, i.e. the (111), (110) and (100) surfaces. As depicted in Figure 2.1, all of surface atoms feature the same coordination at each of the planes. They respectively feature hexagonal, rectangular and square geometry [176], whereby a different reactivity is expected [7].

Away from high symmetry directions we find the low-symmetry (or high-Miller-index) surfaces [176], which may be viewed as an atomic staircase. In these surfaces, high-symmetry flat *terraces* are separated by atomic *steps*, hence the name stepped surfaces. They are also called vicinal surfaces, because they are close to a high symmetry direction in the average orientation of the surface. Since we will only explore (111) vicinal surfaces [or (111) vicinals] during the course of this Thesis, we will exclude those of the (110) and (100) planes in order to ease the discussion.

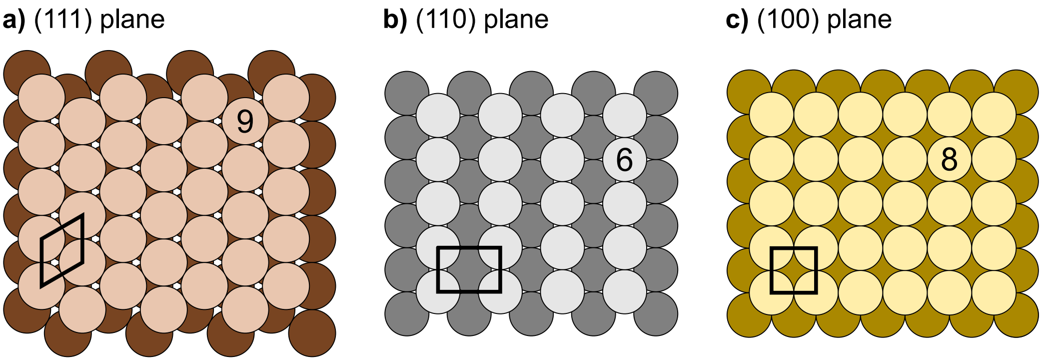

Figure 2.1: Sketches of the high symmetry fcc surfaces.
First (light) and second (dark) layers of fcc low index planes featuring hexagonal [**a)**, brown, (111)], rectangular [**b)**, grey, (110)] and square [**c)**, yellow, (100)] plane symmetries, respectively. The unit cell and surface coordination are illustrated with lines and numbers, respectively.

In Figure 2.2a) we sketch two (111) terraces at different heights. The atomic arrangement of the step atom in the upper terrace with respect to the atomic lattice in the lower terrace gives rise to different step types, each of them with unique properties. Depending on the surface orientation and the direction of the passage, the geometry and coordination number of the step (or edge) atom and the atom just below the step (understep or corner atom) will differ. On one hand, the step atoms will develop a straight line if we cut the upper terrace in the vertical direction: these are called *close-packed steps*, and can feature square [A-steps, {100} microfacet, Figure 2.2b)] or triangular [B-steps, {111} microfacet, Figure 2.2c)] geometry. On the other hand, the horizontal cut gives rise to a transition with a zig-zag structure [alternating {111} and {100} microfacets, Figure 2.2d)]. They are denoted as *kinked steps*, or just *kinks*. Strictly talking, they should be referred as fully kinked steps, since they feature one {111} per {100} microfacet. If we cut the terrace in any direction distinct from purely horizontal or vertical, kinks with a different combinations of A- and B-steps may arise [177].

Another important concept is the distance between atomic rows, since this defines the atomic terrace length on a vicinal surface. In close-packed surfaces, terraces are formed by piling single atomic rows in the direction perpendicular to the step. The width of such rows is then defined by $a_\perp$. In kinked surfaces, the atoms pack in successive rows in 1/2 intervals (see below). In this case, the width of each of these rows is defined by $a_\parallel/2$, the distance between rows in the direction perpendicular to the kinked steps (and hence in the direction parallel to straight steps). Both distances are shown in Figures 2.2b-d). In summary:

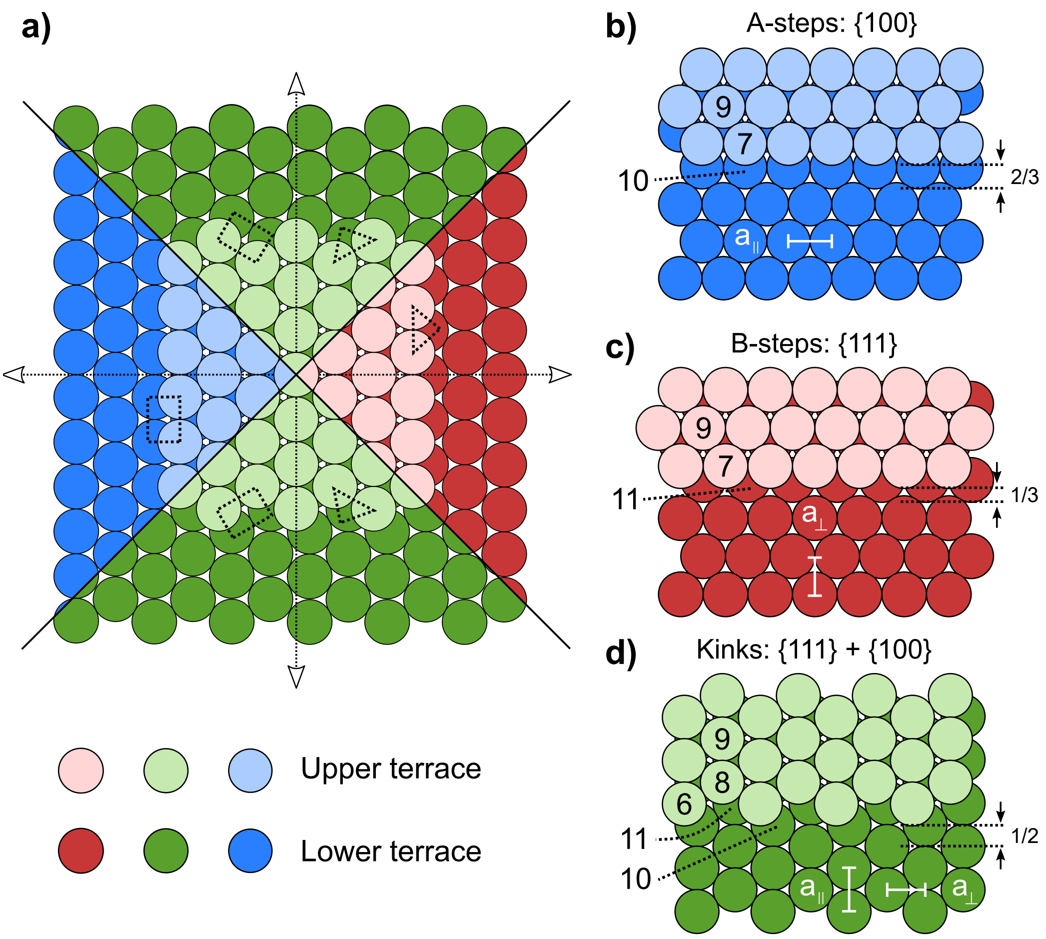

Figure 2.2: Types of steps in (111) vicinal surfaces.
a) Two (111) terraces at different heights, sketching the possible transition from the upper towards the lower terrace. Sketches of the different (111) steps, featuring square (**b)**, A-type, blue), triangular (**c)**, B-type, red) or zig-zag (**d)**, fully kinked, green) shape. The coordination of each of the relevant atoms is indicated, as well as the distances parallel ($a_{\parallel}$) and perpendicular ($a_{\perp}$) to a straight step.

- **A-steps** [Figure 2.2b)] have close-packed geometry along the $[1\bar{1}0]$ direction. The step-understep unit cell represents a square that is locally a {100}-oriented microfacet. Vicinal surfaces formed by such a step type are characterized by (hhk) Miller indices with $k > h$ or $(h, h, h{+}1)$. The atomic coordination of the step edge is 7, while that of the corner is 10. The step extends 1/3 of an atomic row ($a_{\perp}$) over the lower terrace, hence 2/3 of it is exposed.

- The **B-steps** [Figure 2.2c)] also have close-packed geometry along the $[1\bar{1}0]$ direction, but here the step-understep unit cell is a rhomboid (often called triangular shape) corresponding to a $\{111\}$ microfacet. The Miller indices of a vicinal surface of this type are (hhk) with $k < h$ or $(h, h, h-1)$. Again, the coordination of the step atoms is 7, but for the corner atoms is 11. The step expands $2/3\ a_{\perp}$ above the lower terrace, hence 1/3 remains uncovered.

- A fully **kinked step** results from steps running along the $[11\bar{2}]$ direction (perpendicular to $[1\bar{1}0]$), giving rise to the mentioned zig-zag, kinked appearance of the step. As can be observed in Figure 2.2d) one gets an alternation of square and rhomboidal microfacets, $\{100\}$ and $\{111\}$, respectively. Miller indices of vicinal surfaces of this type are generally characterized by $(h+1, h-1, h)$. The atomic coordination is 6 (first row) and 8 (second row) in the upper region, and 10 (first row) and 11 (second row) for corner atoms. The step extends 1/2 of an atomic row, which is this case corresponds to $\mathrm{a}_{||}$ (note the 90° rotation mentioned above), leaving the other 1/2 exposed.

Close-packed steps can be superimposed with their mirror images (they have an improper rotation axis at step atoms), hence they are achiral. However, kinked surfaces do not possess such axis: their mirror images are different, hence they are chiral surfaces [1]. Accordingly, kinks play a major role in surface chiral synthesis [178]. The properties of each step type are summarized in Table 2.1, and they are further described in Appendix A3.

	Step / Corner	Geometry	Microfacet	Symmetry	Miller indices
A-steps	7 / 10	Square	$\{100\}$	Achiral	$(h, h, h+1)$
B-steps	7 / 11	Triangular	$\{111\}$	Achiral	$(h, h, h-1)$
Kinks	6, 8 / 10, 11	Both	Both	Chiral	$(h+1, h-1, h)$

Table 2.1: Step properties in (111) vicinals.
Atomic coordination of step and corner sites (first and second row are indicated for kinked steps), together with the macroscopic step geometry, corresponding microfacet, symmetry and Miller (hkl) indices for A-, B- and Kinked steps.

Why are these steps important? Supported nanoparticles, such as those sketched in Figure 2.3, feature a complex combination of high- and low-index planes, often subjected to structural changes during chemical reactions [179–182]. The nanoparticle distribution of terraces and steps will result into a variable E_{ads} across its surface, maximum at the steps and minimum at the terraces, translating into a different reactivity depending on where the reaction takes place [60]. It is challenging to isolate the effect of each of the facets and keep track of the active atoms during catalysis. In addition, the relative density of the different types of surface atoms may change during catalysis: effects such as faceting [175], step doubling [144] and surface roughening [46, 47] are concomitant to catalysis. However, we must elucidate the role of each of the sites during the reaction in order to enhance their performance and tailor new and efficient catalysts.

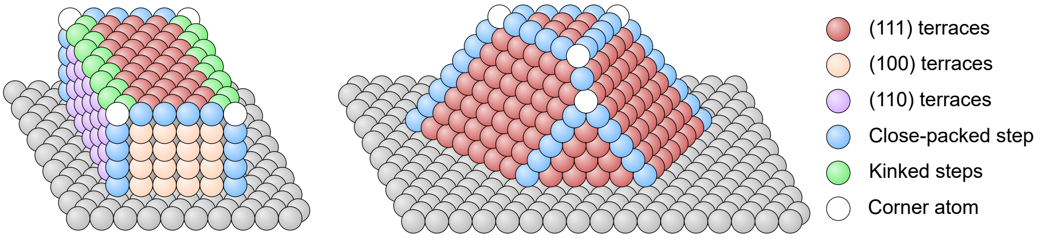

Figure 2.3: Different facets of supported nanoparticles.
Models of supported nanoparticles, showing examples of the possible configuration of the surface atoms. Atoms are colored according to their geometry, while the grey atoms represent the support. Note the different geometry of (111), (110) and (100) steps.

One methodology to asses this problem is to use substrates that allow to selectively probe different facets in one single sample. Curved crystals are an excellent approach to do so, allowing to easily compare flat and stepped surfaces at the very same experimental conditions. A review of the topic was recently presented by Auras *et al.* [183]. Curved crystals come in several forms, such as domes, full cylinders or cones. Despite these surfaces are typically difficult to employ, they have been used in the Surface Science community since almost 100 years. They were used for purely Physics experiments at the beginning, but researchers started soon to use them as substrates for catalytic essays, since they allow to easily compare different facets during a surface chemical reaction. Such approach has proven extremely useful, revealing, e.g., significant differences in reactivity and faceting during the CO oxidation reaction for different vicinal surfaces.

The novelty of this Thesis is not to study the well known catalytic CO oxidation reaction, but to assess the role of different undercoodinated sites on such reaction using curved single crystals. These feature a non-homogeneous density of various step types, enabling to probe different facets under the very same experimental conditions. In this work, we have used sections of cylindrical samples that are easily adapted to regular sampleholders, in order to facilitate the experiments. These curved crystals posses a smooth variation of the crystal orientation across the curved surface thanks to their cylindrical shape. Therefore, they feature a varying distribution of undercoodinated sites: depending on the position across the curved surface, the density of terraces and steps will differ. In other words, one can selectively probe several planes with a different distribution of steps and terraces using one single sample. This is ideal to investigate different facets of a material during physicochemical processes. Beyond surface chemistry and catalysis, they are also useful to, e.g., investigate film growth [184] or to explore surface electron scattering [185].

The scheme of a crystal curved around the (111) surface featuring straight steps is illustrated in Figure 2.4. It corresponds to the samples used for the experiments of Chapters 3 and 5. The cylinder axis is parallel to the $[1\bar{1}0]$ direction and the (111) surface is located at the center of the crystal. *On one side* of the crystal one has A-type steps, while B-type steps are found *on the other side*. The step density increases when moving away from the (111) plane at the center. This situation is illustrated in Figure 2.4a). Vicinal surfaces up to the (223) and (553) planes can be probed at each of the sides of the crystal, and several planes with smaller step density (larger terraces) can be probed in between (see Appendix A3).

The (111) plane [Figure 2.1a)] is located in the apex of the curved crystal, hence the naming c-M(111). In an ideal picture of a flat (111) surface, its step density equals 0. However, as one departs from the center (towards the edges), the situation changes. Approximately at halfway *on one side* we find the (445) plane, which features 8-atom-wide terraces separated by single atomic steps with {100} microfacets (A-steps). If we further approach the edge, we will reach the (223) surface, where the terraces are now 4-atoms wide. Therefore, a smooth increase of the step density is observed as one leaves the center of the sample. A similar situation applies when approaching the *other edge*: we find the (997) and (553) planes, with 8- and 4-atom-wide terraces, respectively. However, here the (111) terraces are separated by steps with {111} microfacets (B-steps). Hence, this particular design is ideal for studying differences between square and triangular A- and B-type steps.

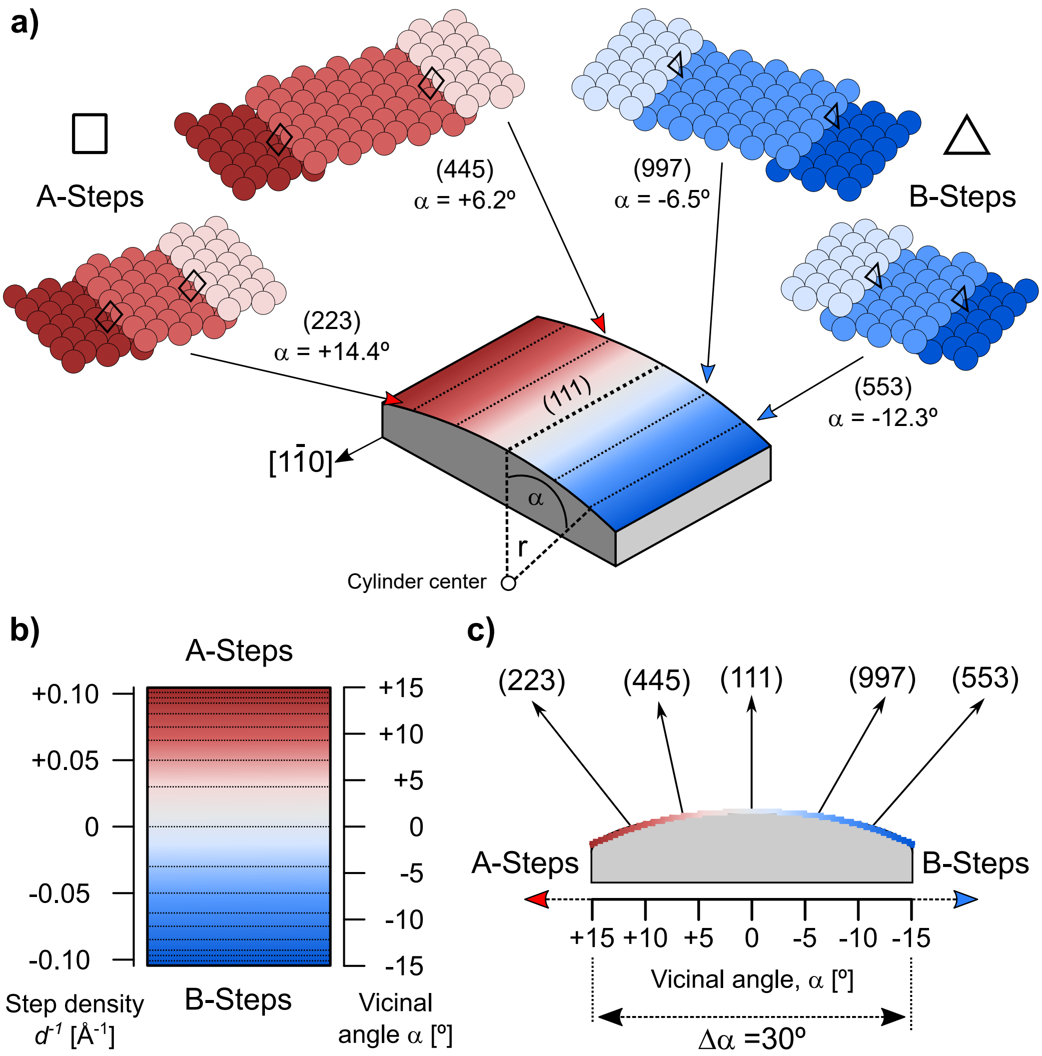

Figure 2.4: Curved (111) crystal with straight A- and B-steps.
a) Sketch of a curved crystal with close-packed steps, with selected A- and B-stepped surfaces and their correspondent atomic terrace length. α and r refer to the vicinal angle and the cylinder radius, respectively. **b)** Vertical view of the sample, with step density d^{-1} and vicinal angle α scales across the curved surface. **c)** Lateral view of the crystal with the position of selected surfaces, showing the overall vicinal angle range $\Delta\alpha = 30°$.

One key parameter in stepped surfaces is the vicinal angle α. As sketched in Figure 2.4a), it corresponds to the angle between the vectors normal to the high-symmetry surface and the chosen plane [176]. In other words, if we refer to a (111) vicinal, α corresponds to the angle between the latter and the considered (hkl) plane. The total interval of α that can be probed in a curved crystal ($\Delta\alpha$) is defined by its length (L) and radius (r), and it establishes the planes present on the curved surface. In the case of the sample of Figure 2.4, we deal with a crystal that has $r = 16$ mm and $L = 9$ mm. On the borders we would reach $\alpha = \pm 16.3°$. Since these borders maybe damaged from the polishing process we usually do not measure at these extreme points but focus in a range of $\alpha = \pm 15°$ ($\Delta\alpha = 30°$). Through this work we will use $\alpha > 0$ for A-steps, while $\alpha < 0$ for B-steps.

The macroscopic magnitude α is of utmost importance: it holds information about the nanoscopic distance between two different steps (d), and hence the frequency at which steps appear on a surface, i.e. the step density d^{-1}. In addition, α is irremediably connected to the average terrace length, l: larger terraces immediately lead to smaller d^{-1}, since the distance between steps d grows. As explained in Appendix A3, d and α are related by:

$$sin(\alpha) = \frac{h}{d} \tag{2.1}$$

where h is the step height. Therefore, in addition to the type of the step, we may in-distinctively define a surface by its step density or vicinal angle.

The (111) plane, located at the center of the crystal, features (ideally) no steps, hence α equals 0. As we approach either of the edges, the terraces become narrower as the density of steps rises, hence $|\alpha|$ steadily grows. This is illustrated in Figures 2.4b,c).

Using experimental techniques that allows one to probe only a small region of the curved sample, e.g., a tip of a scanning tunnelling microscope or a small light spot for a spectroscopic analysis, we will be able to study a full sequence of vicinal surfaces, each of them featuring a different α. In order to show the variation of a given property over the curved surface, data can be displayed a surface (or curvature) map. These are called α-scans, since each point features a different α (and hence step density d^{-1}), and they are unique to the curved crystal approach. Examples are shown in Appendix D1. For example, through α-scans one may obtain the evolution of terrace and step adsorbates as a function of the step density. Specially during chemical reactions, this has important implications for elucidating the role of such during catalysis. In order to extract the extension of these steps and the structure of the adsorbates anchored on them, we have derived the W-model.

2.1.1 The *W*-model

The interruption of a terrace by a step does not only have an influence at the edge position itself, but it may often affect some of the neighboring atoms/adsorbates close to the step, specially at the understep. Thus, one may define a theoretical lateral step extension W, in order to account for such "region of influence" of the step. It is obvious that the overall coverage of adsorbed species at the terraces $[\Theta_T(\alpha)]$ and the steps $[\Theta_S(\alpha)]$ depends on α due to the increasing step density. However, if we assume that locally each terrace and step feature a constant coverage of a certain chemical species [see Figure 2.5a)], then we can calculate $\Theta_T(\alpha)$ and $\Theta_S(\alpha)$ as:

$$\Theta_T(\alpha) = \Theta_T^0 \left[1 - W \cdot d^{-1}\right] = \Theta_T^0 \left[1 - W \cdot \frac{\sin(|\alpha|)}{h}\right] \tag{2.2}$$

$$\Theta_S(\alpha) = \Theta_S^0 \cdot W \cdot d^{-1} = \Theta_S^0 \cdot W \cdot \frac{\sin(|\alpha|)}{h} \tag{2.3}$$

As shown in Figure 2.5a), both Θ_T^0 and Θ_S^0 represent the local coverage of terraces and the effective step area (W-region), respectively. As sketched in Figure 2.5b), they do not to depend on α in this model. Is is important not to confuse them with the overall terrace and step coverage [$\Theta_T(\alpha)$ and $\Theta_S(\alpha)$], which may be derived after the evaluation of Equations 2.2 and 2.3 at a given α. The latter equations simply reflect that as α increases, the space (and hence the coverage of adsorbates) occupied by the terraces-steps is respectively reduced-increased by the size of the steps, times the frequency at which they appear ($W \cdot d^{-1}$). Hence, $\Theta_T(\alpha)$-$\Theta_S(\alpha)$ is maximum-minimum at the (111) plane (largest terraces), and then decreases-increases as the terraces narrow. The rate at which this occurs is determined by the effective step size W, which marks the fictitious terrace-step transition. Bigger W implies that each step region (both edge and corner) extends more into the lower terrace, consuming a larger portion of it. Accordingly, $\Theta_T(\alpha)$-$\Theta_S(\alpha)$ decreases-increases faster with α. However, smaller W leads to a narrower influence region of the steps at the lower terrace, which yields a slower $\Theta_T(\alpha)$-$\Theta_S(\alpha)$ decay-growth. Steps with different W are illustrated in Figure 2.5c).

Θ_T^0 can be readily identified as the coverage of the (111) plane, while Θ_S^0 accounts for the coverage of the *whole* W-region, i.e. both step and understep area. Θ_S^0 depends then on the effective size of the step W, and holds the information on how many adsorbates are found in this W-region. If we multiply Θ_S^0 by W, we obtain the amount of adsorbates per W-region. We can convert this to the more appealing adsorbate atoms/molecules per edge row if we divide it then by the size of an atomic step row ($a_\perp$ or $a_\parallel$ for straight or kinked steps, respectively, as sketched in Figure 2.2).

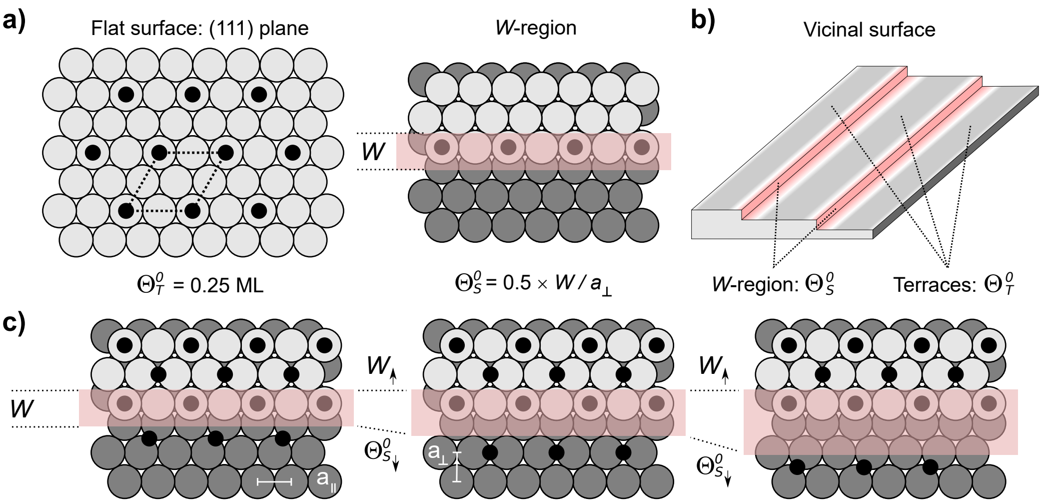

Figure 2.5: Further details of the *W*-model.
a) Coverage of a flat surface [(111) plane] and a W-region, represented by Θ^0_T and Θ^0_S, respectively. The effective step size W is sketched as a light red rectangle at the stepped surface. In **b)** we illustrate a vicinal surface featuring different terraces (light grey) and steps (light red). Individual terraces and W-region have a constant coverage of adsorbates Θ^0_T and Θ^0_S, respectively, that do not depend on the step density. **c)** Sketch of three step regions for an A-type (111) vicinal with increasing step size W. As W increases, Θ^0_S decreases, since the amount of adsorbates at the step-edge fixed and the first row of terrace adsorbates do not enter the step influence region [186, 187]. Note that the structure of the step and the upper terrace remain unaltered.

As we just mentioned, the W-model allows to extract the effective step width and adsorbate structure at the stepped edges. For instance, if we apply this model after CO saturation, we may be able to derive how the CO molecules are anchored at the stepped array. Interestingly, the obtained W also reflects the extension of the CO-depleted understep area. CO predominately adsorbs at the step edge, often leaving the understep region free of adsorbates [186, 187]. In reality, W represents the *imaginary* terrace-step transition: the smaller W is, the shorter the understep area becomes, and the closer to the understep row CO molecules adsorb [see Figure 2.5b)]. This turns into a less marked decay of the terrace coverage with α [188]. However, if W increases, the CO molecules will adsorb further away from the understep. Therefore, the terrace coverage will decay significantly faster with α, *a priori* largely affecting the total coverage as well [187].

2.2 X-ray Photoemission Spectroscopy

X-ray photoemission spectroscopy (XPS) is the commonly used terminology of the Electron Spectroscopy for Chemical Analysis (ESCA) technique. It was invented by Kai M. Siegbahn, for which he got awarded the Nobel price in 1981 [189]. XPS is based on the photoelectric effect, whose study earned Albert Einstein another Nobel Prize in 1921 [190].

According to the photoelectric effect, illuminating a material with sufficiently energetic light will cause some of its electrons to escape to vacuum. The basis of XPS is to record the intensity of these outgoing electrons (*photoelectrons*) as a function of their kinetic energy, i.e. the energy at which they reach the detector. Their kinetic energy (E_K) is described by:

$$E_K = h\nu - E_B - \phi_A \tag{2.4}$$

with $h\nu$ being the energy of the impinging photon, ϕ_A the work function of the analyzer and E_B the binding energy of the excited electron, i.e. the strength of the electron-nuclei bond. The addition of the term ϕ_A is discussed in Appendix A4. E_B describes the strength of the electron-nuclei bond. The analyzer provides the intensity as a function of E_K, hence the values of E_B can be derived from Equation 2.4. E_B is both element- and species-specific, for which it is normally used as the horizontal axis for the sake of comparison. Nonetheless, its scale is inverted (increases towards the left) in order to mimic the increase of E_K (see Figure 1.3). E_B is usually referred to the Fermi level in metals (E_F, highest occupied orbital at 0 K), more seldom to the vacuum level E_V, the lowest possible energy of a free electron [191]. As discussed later, the formation of a chemical bond leads to changes in the atomic energy levels, which we can probe by XPS to characterize them.

A photoemission process, together with a simulated spectra, is sketched in Figures 2.6a,b). A real spectra is discussed in Appendix A4. If $h\nu$ is sufficient, the photon impinging the sample will eject one electron, leaving a positive charge (hole, h^+) on the metal. By XPS we measure this final state, since the electron excitation/release and hole formation readily alters the initial electronic levels of the atom, shifting them [191].

We may estimate the XPS intensity I of a certain electron emission by:

$$I = J \cdot \rho \cdot \sigma \cdot K \cdot \lambda \tag{2.5}$$

where J is the photon flux of the X-ray source, ρ is the atomic density of the material and σ is the photoionization cross-section. K is an instrument-dependent factor, and λ is the electron escape depth (strongly related to the inelastic mean free path of the electron) [194].

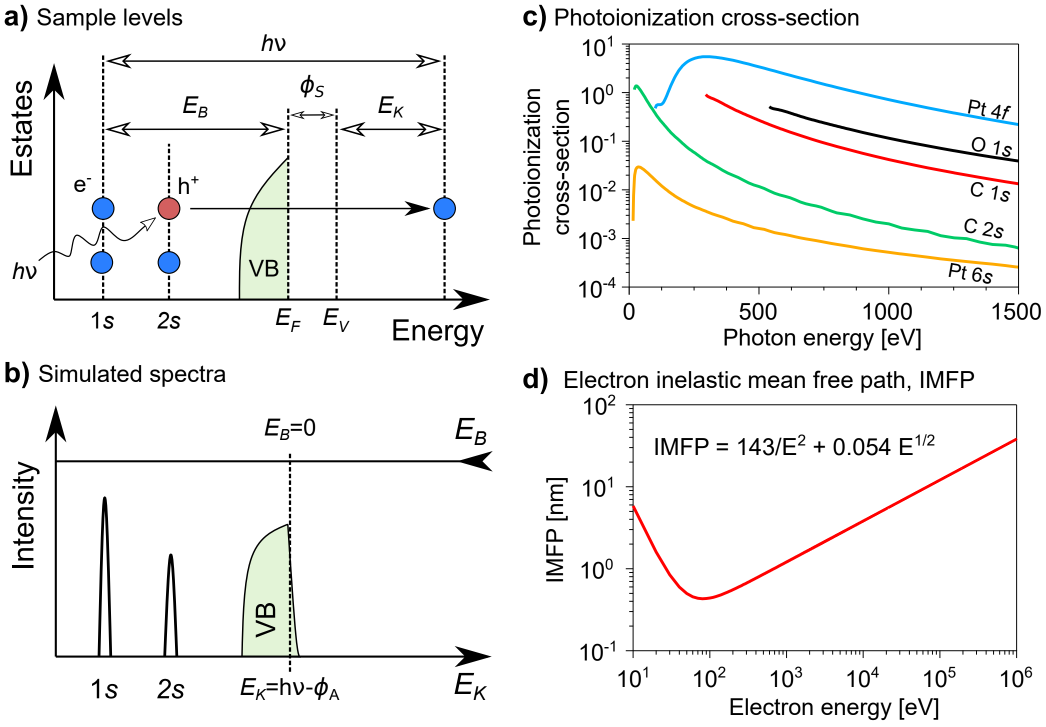

Figure 2.6: Additional details on XPS.
a) Simulated sample energy levels (states) and **b)** corresponding spectrum for a metallic sample (see Appendix A4). Impinging light ($h\nu$) causes the ejection of a photoelectron (e^-), leaving a positive hole (h^+) on the orbital. In b) we sketch both the kinetic (E_K) and binding (E_B) energy scales, which are inverted. E_V and E_F stand for vacuum and Fermi energies, while VB, ϕ_A and ϕ_S correspond to the valence band and the work-functions of analyzer and sample, respectively. The E_B scale is referred to E_F, hence it equals 0 at the former. **c)** Photoionization cross-sections of several core levels as a function of the impinging photon energy [192]. **d)** Universal electron Inelastic Mean Free Path (IMFP) as a function of the electron energy [193].

The I-dependence on both J and ρ is clear: if we shine our sample with more photons, or if more electrons are available in the energy level, I will intuitively increase. K encompasses parameters such as the efficiency and transmission of the detector, or the angle between incoming light and detector entrance. Nonetheless, we have brought Equation 2.5 to discuss the two remaining parameters, λ and σ, and their evolution with E_K. On one hand, λ defines the probing depth of the measurement. It increases with E_K (for $E_K > 50$ eV), since the electrons can travel deeper into the sample before getting scattered by the metal lattice.

On the other hand, σ defines the probability of the electronic transition. As sketched in Figure 2.6c), it depends on the element, orbital and photon energy, and it usually decreases with $h\nu$ [192]. Therefore, σ and λ have opposite behaviours with respect to $h\nu$. At low E_K, σ is usually large and λ is small, meaning that we are only probing few Å of the sample surface (we are *surface sensitive*). However, if we want to study bulk properties, we must increase $h\nu$ so as the probing depth is the adequate, typically loosing a significant intensity due to the decaying σ.

In our case, we will perform XPS in the mbar range of pressures. This means that the electrons have to travel through an atmosphere where most of them will get lost by collisions with gas molecules and only a small percentage will pass towards the analyzer. Therefore one should aim for very high XPS intensity and if possible a quite high surface sensitivity. For example, for a C $1s$ core level emission ($E_B \approx 284$ eV) we would then need $h\nu$ of approximately the C $1s$ binding energy plus the energy corresponding to the minimum of the electron mean free path on the material surface, $E_B \approx 50$ eV. However, some analyzers do not work well at such low kinetic energies but only from 100 eV. Therefore, one would then use photon energies between 320 eV and 370 eV to measure the C $1s$ region with good surface sensitivity.

Finally, we must discuss one of the most important feature of XPS, the chemical shift [191]. Let us imagine that we measure the XPS of two different samples, metallic and oxidized lithium (Li and Li_2O). In the case of the metal, the Li $2s^1$ electrons are forming the conduction band. However, this band is empty ($2s^0$) in the oxide, since the electrons are donated to the O $2p^4$ orbitals in order to fill the p shell. Therefore, the Li $1s$ electrons in Li_2O are less screened (stronger attached to the nuclei), exhibiting a larger E_B than Li metal. As a general trend, an increase in the oxidation state usually yields a shift towards larger values of E_B (see Figure 2.7).

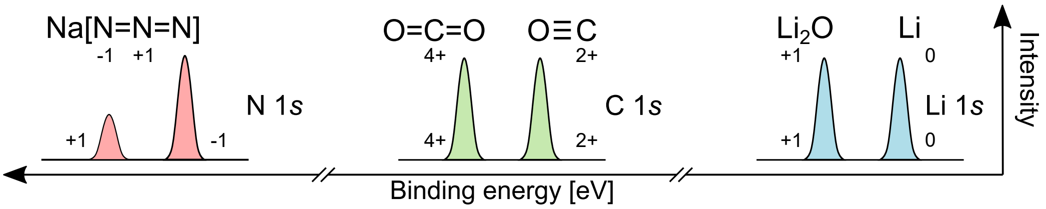

Figure 2.7: Chemical shift of different chemicals measured by XPS. Simulated spectrum for sodium azide, carbon dioxide, carbon monoxide, lithium (I) oxide and metallic Li (NaN_3, CO_2, CO, Li_2O and Li, respectively), showing peaks at different binding energies (E_B) due to the chemical shift. Note that the ratio N^-/N^+ in NaN_3 is 2, reflecting its chemical structure.

The chemical shift has proven extremely useful for distinguishing surface species, such as different CO adsorption sites [55], chemisorbed O and oxides [30], or even step and terrace species [63]. Tracking the chemical species is mandatory for understanding surface catalysis, and accordingly XPS has emerged as a powerful probing tool for conducting such studies [195].

As mentioned earlier, catalytic studies should be carried out as close as possible to *operando* in order to work at industrially relevant conditions (see Chapter 1). However, this is not straightforward. If we employ a lab source that often use Al K_α radiation of $h\nu = 1486$ eV to perform NAP-XPS, the intensity of both the light and photoelectrons will be scarce due at high pressure due to gas scattering, lower cross-section σ and low surface sensitivity (larger λ). However, synchrotrons provide extremely focused and brilliant photon beams [196, 197], well suited for high-pressure experiments.

A photoelectron detector must operate below 10^{-8} mbar [194], hence working at realistic pressures seems *a priori* incompatible with a regular XPS analyzer. However, it is possible to acquire data at higher *sample pressures* with some modifications to the setup. A review on this topic was presented by Starr *et al.* [198]. The main difficulty to perform (N)AP-XPS resides in how to produce a pressure gradient between sample and detector, so that only the latter operates in UHV. This can be achieved by diferentially pumping the set of lenses located between sample and analyzer: the pressure is sequentially decreased at each pumping stage, so UHV conditions are reached at the analyzer while the sample is at (m)bar pressures.

A small aperture (cone or nozzle, few hundreds of μm) is placed close to the sample ($< 100\mu m$) in typical (N)AP-XPS setups. On one hand, such opening is extremely small to prevent large amounts of gases to enter the differential pumping stage of the analyzer, hence keeping the pressure in adequate values. On the other hand, the entrance to the differential pumping stage is located near the position where the beam is impinging the sample, therefore the photoelectrons will enter the pumping stage without loosing a significant amount of intensity due to scattering with the gas. We illustrate the experimental NAP-XPS setup in Figure 2.8.

With XPS, we probe the surface of our material: impinging photons may eject photoelectrons, which we analyze with the detector. However, since we are working in a relatively high-pressure environment, a significant amount of gas phase molecules/atom will also be excited by the X-rays, emitting electrons. This is an unique feature of (N)AP-XPS: we can simultaneously measure the gas phase and the surface species, hence we may simultaneously track reactants, products and surface species in a reaction.

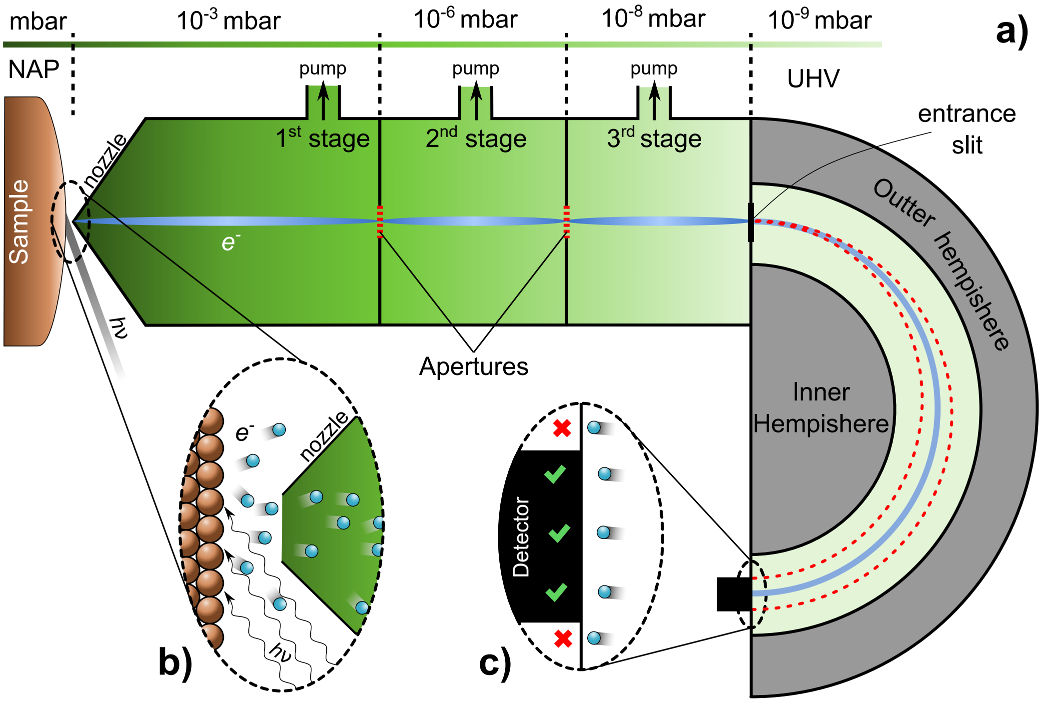

Figure 2.8: NAP-XPS setup using a curved crystal.
a) Sketch of a typical NAP-XPS experiment. Impinging light ($h\nu$) on the sample (brown) may eject photoelectrons (e^-, blue balls). As illustrated in **b)**, some of these electrons may enter the nozzle in the appropriate direction, being then directed to the entrance slit of the analyzer. The sample pressure is typically in the mbar range, while that of the analyzer is $\approx 10^{-9}$ mbar. In order to reach UHV in the electron detector, different pumping stages are placed between it and the sample, which sequentially decrease the pressure. Once in the analyzer, the electrons are selected according to E_K by applying a voltage difference between the inner and outer hemisphere (see Appendix A4). As depicted in **c)**, only electrons with the desired energy will be detected by the analyzer; the others will collide with the walls.

In soft X-rays beamlines ($<$ 5 keV), such as those of MaxIV, NSLS-II or ALBA synchrotrons [199–201], the low photon energy provides small λ, and hence good surface sensitivity. However, these instruments cannot work at pressures higher than a few mbar, since the light transmission is bad at these energies. This can be overcome by working with hard X-rays, yet σ will largely decay in important levels such as the O 1s or C 1s. In addition, we will no longer be surface sensitive. However, we may overcome this by using grazing incident photons: the Polaris instrument at the Petra III synchrotron operates in this mode, enabling real AP-XPS measurements [202].

2.3 Planar Laser-Induced Fluorescence

The other technique used throughout this Thesis is Infrared Planar Laser-Induced Fluorescence (IR-PLIF). These measurements were conducted at Lund University, in Sweden. We will employ IR-PLIF (or just PLIF) to probe the $CO_{2(g)}$ cloud formed above the sample during the CO oxidation above millibar pressures. The name is very descriptive: a sheet-shaped laser beam illuminates the area right above the sample. The laser beam has a specific photon energy, in order to excite the target gas molecule (CO_2 in this case). These excited molecules may in turn decay via a fluorescence event, which is then detected by an IR camera. PLIF allows to acquire 2D snapshots with great lateral spatial (up to 50 μm, depending on the optics and laser configuration) and temporal resolution [203–205]. This enables to precisely monitor the $CO_{2(g)}$ distribution above the catalyst, providing relevant insights into the CO ignition temperature, T_i (see Section 1.2).

Figure 2.9 shows a typical PLIF experiment using a curved c-M(111) crystal, on which the viewpoint coincides with that of the camera (i.e. perpendicular to the crystal curvature). As illustrated in Figure 2.4, such sample features the flat (111) plane at the center, and a smooth increase of *either* A- of B-type straight steps as one departures from the center towards the right or left edges. The laser beam ($\lambda = 2.7\mu$m) enters from the right side, and excites electrons in the ($0^0$00)-($10^0$01) combination band of the $CO_{2(g)}$ molecule, which has the same energy as the laser [35]. Some of the electrons may decay via a fluorescence process. The most probable transition (i.e. larger amount of emitted photons) is at $\lambda = 4.3\mu$m. The IR camera has an interference filter at this wavelength, hence only photons with this energy will enter the camera, allowing to spatially detect the $CO_{2(g)}$ cloud above the sample. Additional PLIF details may be found in Refs. [203, 204].

PLIF allows to selectively probe the $CO_{2(g)}$ production above the sample: T_i can be extracted by simply measuring the $CO_{2(g)}$ signal as a function of the temperature. Furthermore, we show in Figure 2.9 how the good spatial resolution of PLIF enables to detect T_i asymmetries in curved crystals, since we can easily visualize differences in the light-off of each of the sides of the sample [203]. If one of these regions ignites prior to the other, a significant gradient in the $CO_{2(g)}$ pressure will be created between both edges [see Figure 2.9a)], exhibiting a remarkable difference in the fluorescence signal. We show this in Figure 2.9b), contrary to the homogeneous $CO_{2(g)}$ production reported by Zetterberg *et al.* in flat samples [204]. Although one would naively expect an asymmetric ignition as long as the distribution of undercoordinated sites is not homogeneous on the surface, as observed for a c-Pd(111) crystal [203], this may not necessarily be the general trend.

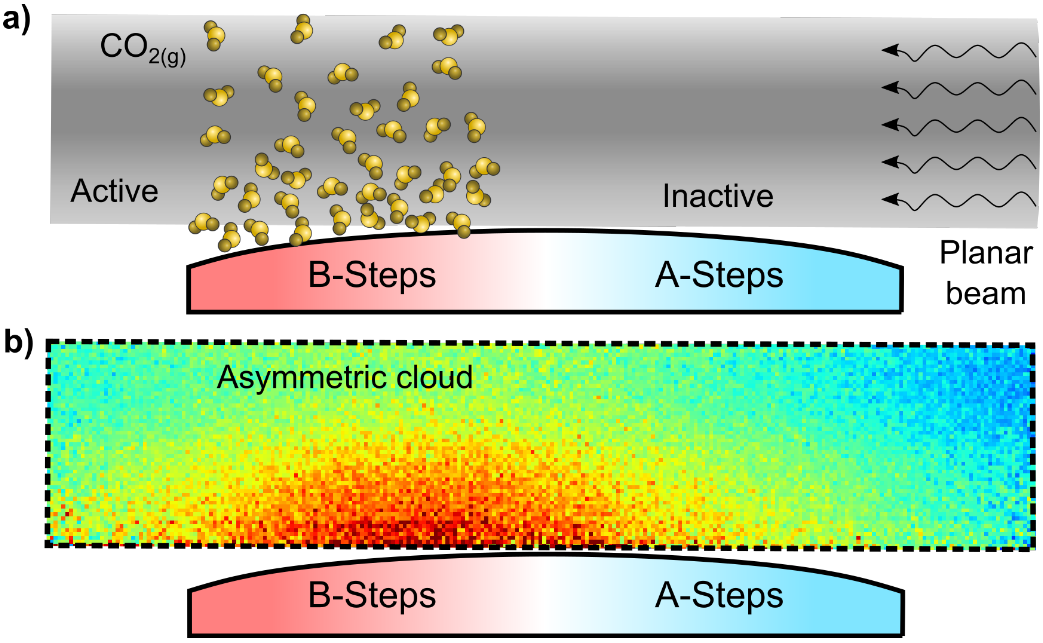

Figure 2.9: General PLIF setup using a curved crystal.
a) Simplified illustration of a PLIF experiment. The planar beam (light grey, $\lambda = 2.7\mu$m) is directed over the sample to excite $CO_{2(g)}$ molecules, of which a portion will decay via a fluorescence event. This radiation which will then be detected by a camera perpendicular to the laser sheet with an interference filter at $\lambda = 4.3\mu$m. **b)** PLIF 2D image acquired during a CO ignition cycle using a curved c-M(111) sample with A- and B-steps (see Figure 2.4), showing a dissimilar $CO_{2(g)}$ production depending on the step type.

The fluorescence intensity detected by the camera is proportional to the $CO_{2(g)}$ pressure. However, a reference (calibration) experiment is mandatory for quantification. Typically, two measurements are required to properly analyze a PLIF experiment. One of them consists on heating the sample while continuously recording PLIF in reaction conditions. With this sole information we must rely on the mass spectrometer, located in the outlet of the chamber, to detect the *macroscopic* ignition. A second heating cycle, in this case with only $CO_{2(g)}$, is needed to calibrate the PLIF signal. Since we work at a known $CO_{2(g)}$ pressure, it is possible to extract a $CO_{2(g)}$ PLIF-pressure conversion factor. This enables to extract the $CO_{2(g)}$ intensity of the real experiment, providing 2D images of the $CO_{2(g)}$ cloud at different temperatures. After this, we may finely locate T_i with spatial resolution at high pressures. Even though this technique gives very valuable information about the gas phase, no information about the catalyst surface is obtained. Hence, combining PLIF with NAP-XPS (surface sensitive, Section 2.2) provides highly valuable information in catalytic investigations [188].

Chapter 3

CO oxidation on Pt(111) vicinals with A- and B-steps

This first CO oxidation experiments were conducted on a Pt crystal curved around the (111) plane [c-Pt(111)]. As described in Figure 2.4, this sample features either A- or B-type vicinals with straight steps at each of the sides of the sample, and the (111) plane in the apex of the crystal.

We will focus on the ignition temperature (light-off) of the CO oxidation reaction. The light-off across the curved surface will be studied by PLIF and NAP-XPS. Next, a more profound analysis of the ignition is presented, where UHV reference measurements and complementary theoretical calculations are used to characterize the poisoned stage. Finally, we will briefly assess the chemical species involved in the active stage of the reaction. The results discussed here have been published already by us in Ref. [188]. Information on the experimental setup and procedures is given in Appendix B.

3.1 Symmetric ignition at A-B Pt vicinals

As a first approach to compare the CO ignition at (111) and A- and B-type Pt vicinals, we performed Planar Laser-Induced Fluorescence (PLIF, Section 2.3) experiments in order to probe the CO_2 production over the entire c-Pt(111) crystal at the same time. This is depicted in Figure 3.1.

The c-Pt(111) sample was exposed to a 150 mbar gas mixture of 4:4:92, CO:O_2:Ar ml/min flow ratio. The sample was heated to 510 K in order to speed up the experiment and afterwards its temperature was subsequently increased to 620 K during 1000 s (0.11 K/s) while continuously taking PLIF snapshots during the heating ramp. A Quadrupole Mass Spectrometer (QMS) located in the outlet of the chamber allowed to probe gases.

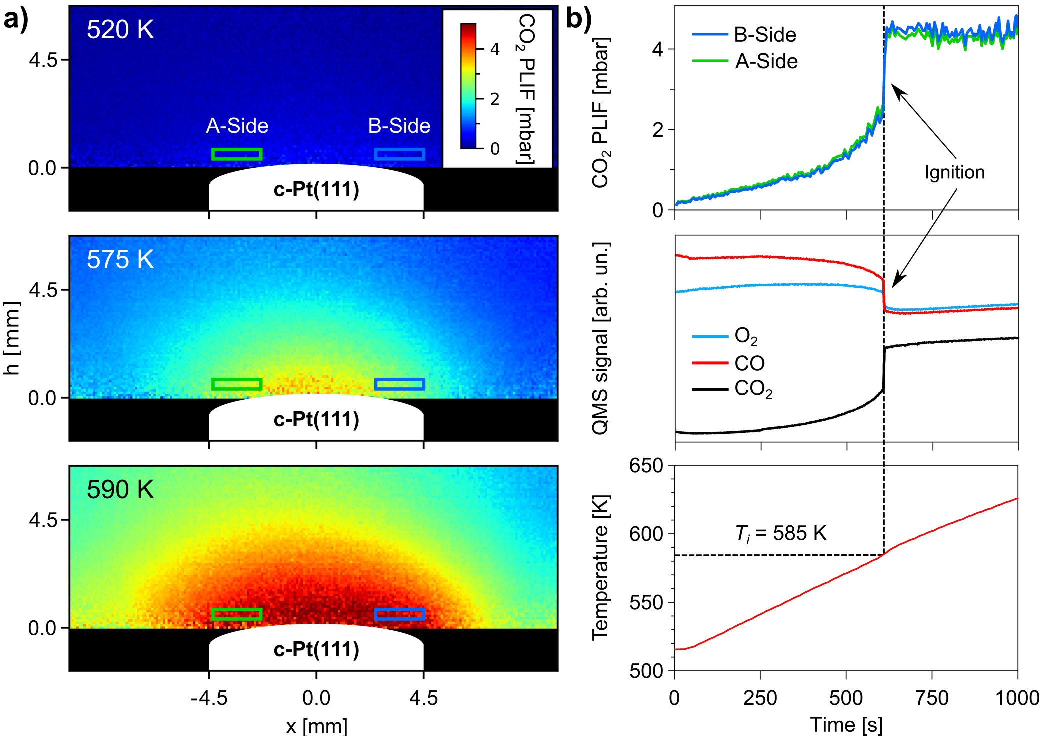

Figure 3.1: PLIF measurements at 1:1 CO:O_2 flow ratio.
a) 2D CO_2 PLIF images acquired in a 150 mbar gas mixture of 4:4:92, CO:O_2:Ar ml/min flow ratio. Individual snapshots far from (520 K, bottom), close to (575 K, middle) and after (590 K, top) the CO ignition are shown. **b)** Experiment variables as a function of time. The top panel shows the integrated intensity within the the green (A-side) and blue (B-side) rectangles sketched in a). O_2, CO and CO_2 QMS signals are shown in the middle graph, while the temperature is plotted in the bottom panel.

In Figure 3.1a) we show three characteristic PLIF images obtained during the CO oxidation experiment, which nicely reflect the power of the technique. At low temperature (520 K, bottom), there is no significant CO_2 signal, since the surface is poisoned. The CO_2 production steadily increases with the sample temperature, although timidly and mainly at the center of the crystal [(111) terraces, 575 K, middle]. However, at around 590 K (top), a large CO_2 cloud shows up above the sample, indicating that the reaction has ignited. The CO_2 cloud emerges and appears to extend homogeneously over the c-Pt(111) sample, in contrast to the case of c-Pd(111) [203], where a clear asymmetry is observed around the (111) center. This points to a simultaneous CO ignition at A- and B-type Pt(111) vicinals.

The experimental variables during the CO oxidation experiment are depicted in Figure 3.1b). On the top panel, we show the integrated intensity in the green and blue rectangles sketched in Figure 3.1a). They show the behaviour described above: the CO_2 production mildly increases as T_i approaches, until it suddenly explodes at 585 K in both sides of the sample. The O_2, CO and CO_2 signals in the QMS are shown in the middle panel. That of the CO_2 continuously grows with the temperature until it abruptly boosts also around 585 K. At the same time, those of the CO and O_2 rapidly decay, marking the light-off of the process. The temperature during the measurement is shown in the bottom graph, allowing us to correlate the time with the temperature. It exhibits one small bump right about T_i due to the exothermic nature of the CO oxidation. This also heats the sample, giving rise to a temporarily faster enhancement of the sample temperature.

Although PLIF experiments suggest that the ignition is symmetric, we will corroborate this observation by studying the chemical composition of the surface during the ignition process. For this purpose, we performed additional Near Ambient-Pressure X-Ray Photoemission Spectroscopy (NAP-XPS, see Section 2.2). In order to do so, we exposed the sample to a 0.7 mbar, 1:6 $CO:O_2$ gas ratio mixture, which means that we are working in O_2 excess. Afterwards, we subsequently measured at different temperatures three characteristic surfaces of the c-Pt(111) sample, namely the (111), (223) and (553) planes. They feature flat terraces, A- and B-type close-packed steps, respectively. The sample was heated in 5 K increments, and the O 1s and C 1s regions were acquired at the aforementioned positions at the curved crystal at each of the temperatures (average slope of 5.5 K/h).

The O 1s ramp is depicted in Figure 3.2, while the C 1s is discussed in Appendix B1. The ignition can be tracked in both regions, yet the C 1s does not give any information about the oxidation state of the surface. A detailed description of surface species will be deeply addressed later in this Chapter. A boron nitride (BN) heater was employed for these experiments. When a Pt filament is used, this ignites the reaction prior to the proper Pt sample and, as a result, the gas mixture is altered (see Section 1.2).

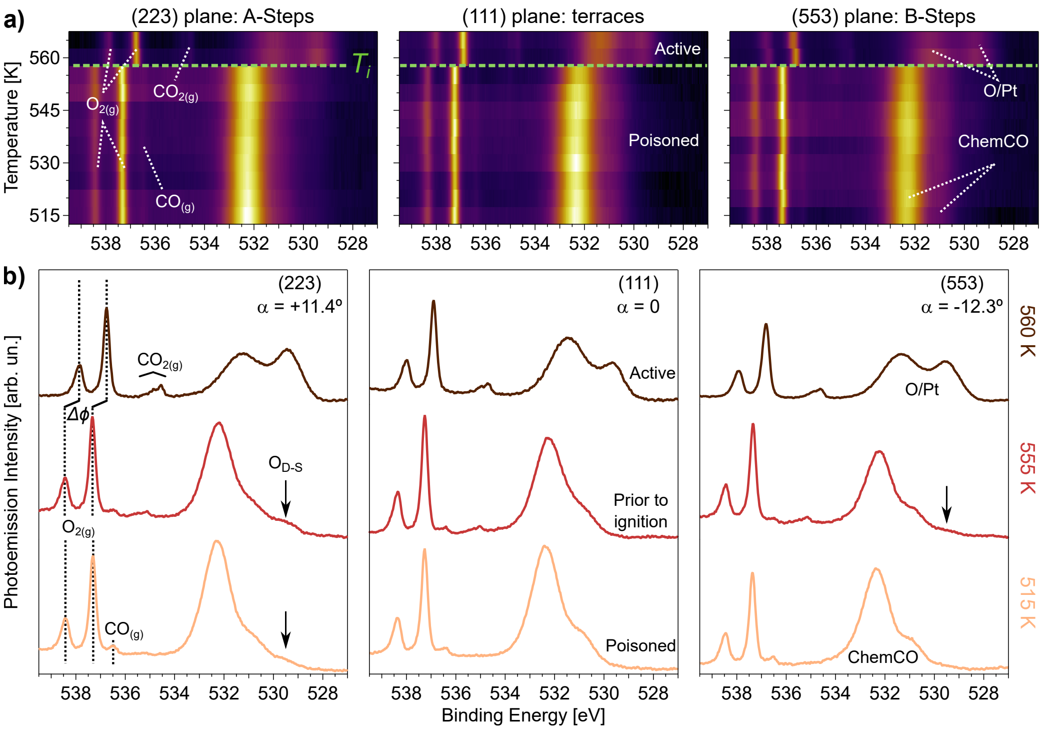

Figure 3.2: Ignition cycle in 1:6 CO:O_2 gas ratio.
a) O 1*s* photoemission intensity *vs* temperature as color plots for the (223), (111) and (553) planes, located at the left ($\alpha = 11.4°$), center ($\alpha = 0$) and right ($\alpha = -12.3°$) columns of the figure, respectively. Dashed green lines mark the ignition, occurring at $T_i = 560$ K. The labels "Active" and "Poisoned" refer to each of the stages of the CO oxidation reaction (see Section 1.2). **b)** Spectra far from (515 K, bottom), close to (555 K, middle) and after (560 K, top) ignition are shown for each of the surfaces. ChemCO and Pt/O refer to chemisorbed CO and oxygen-related species on the Pt surface, while $CO_{2(g)}$, $CO_{(g)}$ and $O_{2(g)}$ allude to the gas phase peaks of each of the molecules. Minor amounts of oxygen ($O_{D\text{-}S}$, Section 3.4) during the poisoned stage are indicated with vertical arrows. The spectra were acquired with a photon energy of 650 eV, under 0.7 mbar of total pressure in a 1:6 CO:O_2 gas mixture (average slope of 5.5 K/h). Gas phase peaks will shift towards lower binding energy due to a change in the work-function of the surface ($\Delta\phi$) after ignition. This is illustrated for $O_{2(g)}$ at the (223) plane, although it is observed at all vicinal surfaces and gases [38].

The spectra at the beginning of the heating ramp [515 K, bottom row of Figure 3.2b)] are similar for the three surfaces: they all consist on a large peak at around 532.5 eV and a smaller one at 531 eV; both are related to different chemisorbed CO (ChemCO) species [52, 63]. A residual contribution, emphasized by a vertical arrow, is observed around 529.5 eV but only on the (223) plane ($O_{D\text{-}S}$, refer to Section 3.4). At the relatively large working pressures, one can also detect gas phase peaks in the spectrum. The characteristic doublet of $O_{2(g)}$ is observed around 537 and 538 eV (1.1 eV splitting), while the small emission at 536.5 eV is related to $CO_{(g)}$ [38]. It is remarkably smaller than $O_{2(g)}$, reflecting the excess of the later in the gas mixture. ChemCO is the predominant surface species and there is no sizeable $CO_{2(g)}$ production according to neither the QMS (located in the second pumping stage of the electron analyzer [45]) nor the XPS.

At around 555 K [middle row of Figure 3.2b)], the spectra resemble those of 515 K, although ChemCO has decreased as its desorption has started. In addition, $O_{D\text{-}S}$ is now easily detectable at the (223) plane, and weakly appears at the (553) surface. This reveals minors amounts of oxygen located only at the stepped surfaces, which is discussed in Section 3.4. As observed in both the QMS and XPS, the $CO_{2(g)}$ signal slightly increases while that of $CO_{(g)}$ and $O_{2(g)}$ decrease, indicating that the reaction is occurring, yet at a reduced rate. Since a large amount of ChemCO and $CO_{(g)}$ is still observed, we further increased the temperature to depart from the poisoned stage.

Right after heating to 560 K, an abrupt boost (decay) of the CO_2 (CO, O_2) signal(s) is observed in the RGA and XPS. We measured again the three aforementioned surfaces [top row of Figure 3.2b)], which are radically different from those at low temperature. Two new peaks clearly dominate the spectrum. They are ascribed to oxygen-related Pt species (529.5 and 531.5 eV, O/Pt), and are further described in Section 3.5. Both ChemCO and $CO_{(g)}$ have vanished from the spectrum at this temperature, marking the transition to the active stage. This is of course also reflected in the C 1*s* shown in Appendix B1. More importantly, the spectra of the three planes have changed simultaneously at 560 K, therefore the ignition of A-B Pt vicinals also appears symmetric in the NAP-XPS measurements, again in contrast with the Pd case [206]. It is easily seen that the species change across the different surfaces, although this will be addressed later in the manuscript. In Appendix B2 we describe a complete reaction cycle, showing also a symmetric cooling of the CO oxidation.

3.2 Evolution of the CO-poisoning layer

Both PLIF and NAP-XPS revealed a simultaneous ignition of Pt A-B vicinals. We will now explore the CO layer of the poisoned stage prior to the light-off of the CO oxidation. The data acquired during reaction conditions will be compared with UHV CO chemisorption experiments, in order to quantify such species. Characteristic spectra are shown in Figure 3.3, while fitting details and coverage calibration are further described in Appendix B.

We shall start with the UHV experiments [top row of Figures 3.3a,b)]. The sample was exposed to 10 L CO at room temperature and subsequently cooled down to 90 K in order to reduce the vibrational broadening. Afterwards, the curved surface was scanned by means of XPS. Two well-defined peaks appear in the C 1*s* region at the (111) plane [middle column of Figure 3.3b)]. These contributions, located at 286.6 and 285.9 eV, are ascribed to CO molecules anchored at Terrace-Top (T_T) and Terrace-Bridge (T_B) sites [52, 55]. Assuming saturation, this corresponds to a $c(4\times2)$-4CO superstructure of 0.5 ML [53], where CO molecules equally occupy T_T and T_B positions [55]. The intensity ratio T_T:T_B obtained in our experiment is 1.4, close to the ideal ratio of 1; differences may arise due to Photoelectron Diffraction (PED) effects [55]. As explained in Appendix B, contributions accounting for vibrational excitations only of T_T molecules ($\sim$287.0 eV) were added to the fitting routine in order to finely evaluate the spectra.

As stated in Subsection 1.3.1, exposure to CO in UHV conditions does not promote step doubling or step bunching, hence we expect monoatomic steps. Probing the A- and B-stepped (223) and (553) surfaces [left and right columns of Figures 3.3a,b), respectively] after the 10 L CO dose reveals significant changes in the C 1*s* region. A new feature emerges at 286.2 eV, which we attribute to CO adsorption at Step-Top (S_T) positions [63, 67, 207]. Since the terraces narrow with α, the occupation of both T_T and T_B sites by CO molecules decreases as compared to the (111) surface. However, there is a larger amount of CO at T_B sites at the (553) plane, while adsorption on T_T is larger than at T_B positions at the (223) surface. We attribute such dissimilarities to the unique geometry and electronic configuration of {111} and {100} steps, which may yield a different lateral intermolecular interactions around the step edges [67]. As we illustrate in Figure 3.3c), this may lead to preferred CO adsorption in T_B (T_T) sites around the {111} ({100}) edges, explaining the differences in coverage.

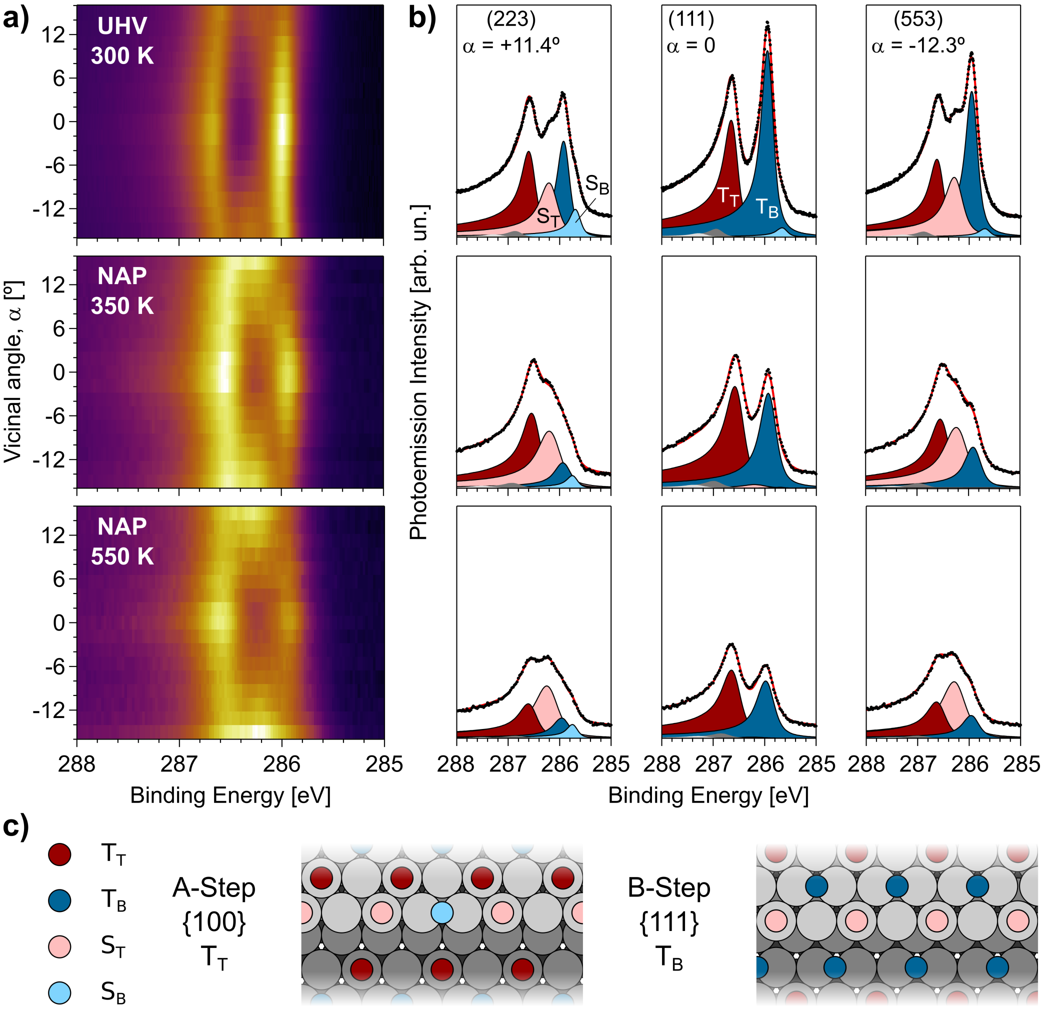

Figure 3.3: Poisoned stage variation across the curved crystal. **a)** C 1*s* surface maps across the c-Pt(111) sample after exposure to 10 L CO at room temperature (UHV 300 K, top), and under a 0.7 mbar, 1:6 CO:O_2 gas ratio mixture at 350 K (NAP 350 K, middle) and 550 K (NAP 550 K, bottom). The photon energy was 400 and 650 eV for UHV and NAP experiments, respectively. **b)** Selected spectra at the (223), (111) and (553) positions at the aforementioned conditions. They respectively feature A-steps, terraces and B-type steps. The conditions of each row correspond to those indicated in a). **c)** Preferred CO adsorption site around A- (T_T) and B- (T_B) close-packed steps. Steps feature 1 CO molecules per two Pt step atoms, yielding the 0.5 ML step coverage (50 % filling), as described later in the text. Terrace-Top, Terrace-Bridge, Step-Top and Step-Bridge CO molecules are named as T_T, T_B, S_T and S_B, respectively.

An additional photoemission peak may be perceived after CO saturation at 285.7 eV. This residual contribution is identical at the (111) and (553) planes, yet it slightly increases at the (223) plane. The growth of the peak at 285.7 eV at the latter surface is related to CO molecules anchored at Step-Bridge (S_B) sites in the {100} microfacets, as reported before [67]. However, since it remains constant (within experimental error) from the (111) surface towards the (553) plane, we attribute such feature to CO adsorbed at defects at these surfaces [63], concomitant to all samples [61, 122, 208, 209]. Accordingly, we subtracted this constant amount of defects from the overall S_B intensity variation as a function of α presented in the following paragraphs in order to adequately describe the behaviour of S_B across the α-scan.

After the characterization of the CO saturation species, we can now properly asses the CO-poisoning layer found during the CO oxidation [middle and bottom rows of Figures 3.3a,b)]. The spectra at NAP feature the same peaks as in UHV, although some changes are observed. Both S_T and S_B remain nearly constant at 350 and 550 K, whereas T_T and T_B progressively decrease. This observation is expected, since CO adsorbed at the terraces has lower adsorption energy compared to its analogous at steps [59, 61, 68]. The maximum amount of T_T and T_B is found at the (111) plane, hence their decay at elevated temperatures is more pronounced at terraces. If we compare the spectra of each of the surfaces at different temperatures, it is easily seen that CO adsorbed at T_T and T_B sites desorb while that chemisorbed at S_T and S_B positions is little altered as the temperature increases. To shortly summarize, the CO at steps remains adsorbed while the terraces steadily become CO-depleted prior to the CO ignition. Thus, the steps are CO-poisoned, and an earlier light off at these regions is hindered.

As mentioned above, photoemission spectra were acquired at many points across the curved surface after CO saturation and during reaction conditions at different temperatures. We call these photoemission intensity maps α-scans, and they are shown in Figure 3.3a). Each spectrum in the α-scan was systematically fitted, and the intensity of individual species at each of the points were converted into coverage. UHV and NAP coverages are depicted in Figure 3.4 as a function of α. The conversion is simple in UHV, since the spectrum at the (111) plane corresponds to 0.25 ML of both T_T and T_B sites [55]. However, we lack absolute coverage references at reaction conditions to calibrate those spectra. Nonetheless, both S_T and S_B remain almost constant while T_T and T_B decrease as the temperature increases and the ignition approaches. Therefore, supposing that the step coverages at UHV and during CO oxidation at 350 K are the same, we can derive a coverage calibration factor for the NAP spectra. More details on the coverage calibration of NAP experiments are given in Appendix B.

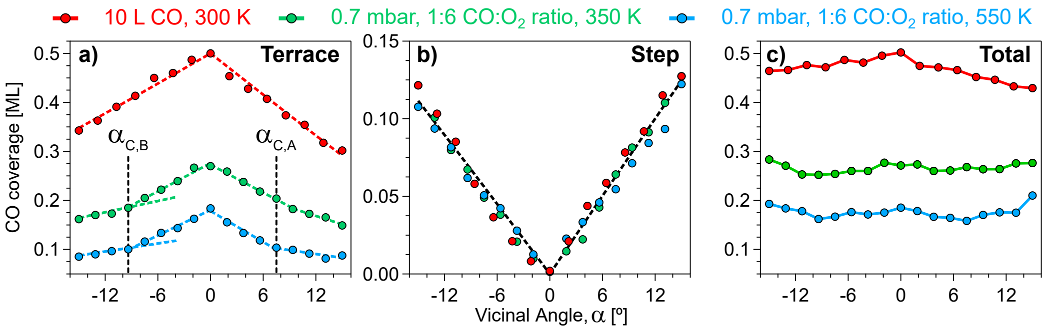

Figure 3.4: Evolution CO species with the vicinal angle. Coverage of CO anchored at **a)** terraces ($\mathrm{T_T}$+$\mathrm{T_B}$), **b)** steps ($\mathrm{S_T}$+$\mathrm{S_B}$) and **c)** in total as a function of α at each of the indicated experimental conditions, extracted from the systematic fit of the α-scans shown in Figure 3.3. Dashed lines are fits to the W-model described in Subsection 2.1.1. $\alpha_{C,A}$ and $\alpha_{C,B}$ reflect a change of the slope of the terrace curves, which we have extended at the B-side of the crystal ($\alpha < 0$) to illustrate such effect. The black dashed line in b) corresponds to the fitting of the CO anchored at steps to the W-model. As explained in Appendix B, it was used for coverage calibration of the NAP experiments.

The α-scans allow to evaluate terrace and step species as a function of the step density. Thus, we can apply the W-model described in Subsection 2.1.1 to extract the effective width of the steps, i.e. the averaged region of influence of the step on nearby terraces. We can also evaluate Θ_T^0 and Θ_S^0, which respectively correspond to the coverage of a flat surface [in this case the (111) plane], and the whole "W-region". As mentioned earlier, the W-region corresponds to an *imaginary* surface with no terraces.

We will start describing how the CO anchored at terraces evolves with the temperature [Figure 3.4a)]. It is easily perceived that the evolution of terrace-CO coverage as a function of α [$\Theta_T(\alpha)$] continuously decreases with the temperature, revealing the progressive desorption of the CO anchored at the terraces. By fitting $\Theta_T(\alpha)$ to Equation 2.2 at different temperatures, we can extract Θ_T^0, which again corresponds to coverage at a flat terrace (i.e. $\alpha = 0$). Θ_T^0 corresponds to 0.5 ML [CO saturation coverage at Pt(111) [53]] in UHV, and it progressively reduces to 0.28 and 0.18 ML at 350 and 550 K in the NAP regime, respectively. Similarly as earlier, CO adsorbed at (111) terraces steadily desorbs as the ignition approaches.

Prior to further analysis, we have drawn two vertical lines in Figure 3.4a). These represent a change of slope in $\Theta_T(\alpha)$ during reaction conditions and at high temperature, which will be further discussed in Section 3.4.

The effective width of the steps W, representing how much the step extends to the lower terrace, may also be derived from this analysis. By fitting $\Theta_T(\alpha)$ in UHV to Equation 2.2, one can obtain W for A- and B-steps (W_A, W_B) after CO saturation. In this case, they are 3.7 and 2.7 Å, respectively. The distance between atomic rows in the perpendicular direction of the close-packed step ($a_\perp$, see Section 2.1) corresponds to 2.40 Å in Pt(111). Therefore, the area of influence of A-steps exceeds over 50 % of $a_\perp$ (likely in the lower terrace), while for its B-type analogous does so only a 10 % of $a_\perp$. This is also reflected by a smaller Terrace-CO coverage at the former type of steps, since a larger extension of the steps automatically reduces the terrace area, and hence the available regions for CO to adsorb. The opposite behaviour (larger terrace coverage for A-steps) was reported during CO chemisorption experiments at 200 K for Pt(553) and Pt(223). However, the terrace (step) CO coverage of the former surface significantly decreases (increases) as the sample is heated [67], explaining the discrepancies with our data.

The same fitting procedure under reaction conditions yields $W = 4.4$ Å for both steps at 350 K. However, this symmetry breaks at 550 K, as $W_A = 7.5$ Å and $W_B = 6.1$ Å. At this high temperature, the situation is similar to the UHV case, where $W_A > W_B$. At 550 K, both W significantly exceed $a_\perp$, reflecting a faster decay of $\Theta_T(\alpha)$ as the temperature increases.

The evolution of the Step-CO coverage with α [$\Theta_S(\alpha)$] is depicted in Figure 3.4b). An ideal (111) surface has a negligible amount of steps ($\alpha = 0$), therefore $\Theta_S(\alpha)$ vanishes at it. As one departs from the (111) plane, α increases, and with it the amount of CO anchored to steps. $\Theta_S(\alpha)$ is very similar at 350 and 550 K, indicating that chemisorbed CO remains anchored at steps sites prior to ignition. Only a residual decrease of $\Theta_S(\alpha)$ after heating to 550 K, very close to the CO ignition, is observed. At our conditions, the large NAP coverages reported by Tao *et al.* were not achieved [70]; our coverages agree more with the experiments performed in UHV [63, 64, 67].

Inserting W_A and W_B in Equation 2.3 allows to extract Θ_S^0 for both step types. This is the coverage of the W-region, an imaginary surface with no terraces, only the effective step size W. We may convert Θ_S^0 to CO molecules per step row by multiplying it by $W/a_\perp$ (see Subsection 2.1.1). After CO saturation, we find values of 0.49 and 0.42 ML for A- and B- steps, respectively. This indicates that there are almost 1 out of 2 CO molecules per Pt edge atom (50 % filling, 0.5 ML) at saturation. By using the UHV data as calibration, we will force the same filling at 350 K in NAP conditions. Then a slight decay to 41 and 38 % (A- and B-type) is observed at 550 K. The 0.5 ML coverage of step edges is sketched in Figure 3.3c).

The Total-CO coverage is the sum of both step and terrace CO species [$\Theta_T(\alpha) + \Theta_S(\alpha)$, Figure 3.4c)]. At UHV saturation, the maximum coverage is found at the (111) plane. Away from the (111) surface, the Total-CO coverage decreases steadily with α. It decays faster at the A-side of the crystal, reflecting that despite A- and B-steps feature a similar coverage, $\Theta_T(\alpha)$ is smaller for A-type vicinals. During CO oxidation conditions, the tendency is rather complex. At 350 K, the total coverage initially decreases slightly away from the (111) plane, although it increases again at large step densities. At 550 K this effect is stronger. This is explained due to a progressive reduction of $\Theta_T(\alpha)$ that causes the decay of the Total-CO coverage near the (111) plane. However, $\Theta_S(\alpha)$ grows with the step density, allowing to counterbalance the decrease of $\Theta_T(\alpha)$ at densely stepped surfaces, yielding a minute, yet noticeable, growth of the Total-CO coverage at large α.

3.3 Subsurface oxygen at the (111) plane

We have seen that CO anchored at terraces steadily desorbs while that at steps remains prior to the symmetric ignition of the CO oxidation. In order to further delve into this phenomenon, we performed a more precise ignition cycle (0.25 K/min, 2.5 K steps) at oxidizing conditions (total pressure of 1.1 mbar, 1:7 CO:O_2 gas ratio). We will focus on the (111) surface, where the terraces are largest, in order to detect additional species at the CO-depleted terraces prior to the light-off. The results are shown in Figure 3.5.

Both the O 1*s* and C 1*s* regions were monitored during the heating ramp [see Figure 3.5a)]. We sketch three characteristic stages of the CO oxidation at different temperatures, namely the poisoned (bottom, far from light-off), “transient” (middle, close to ignition) and active (top, after light-off) stages, at the respective temperatures of 350, 555, 570 K. CO molecules anchored at T_T (532.7 and 286.6 eV) and T_B (530.9 and 286.0 eV) sites are detected in both the O 1*s* and C 1*s* regions [52, 55]. The small amount of graphitic “C” oxidizes [47] and the CO leaves the terraces as the temperature increases. However, the peak in principle assigned to T_T-CO progressively shifts towards lower binding energy in the O 1*s* as we approach the ignition. Such displacement was not observed during a CO desorption cycle performed in UHV conditions (Appendix C2), for which we believe this shift is related to the CO oxidation itself. Furthermore, as depicted in the top panel of Figure 3.5b), the ratio between the ChemCO intensity at the O 1*s* and C 1*s* remains constant at low temperatures, yet rapidly boosts prior to the transition towards the active stage around 560 K. We postulate that both the shift and the increase of the O 1*s*/C 1*s* ratio point to an additional oxygen species arising just before ignition, and overlapping with the T_T-CO peak.

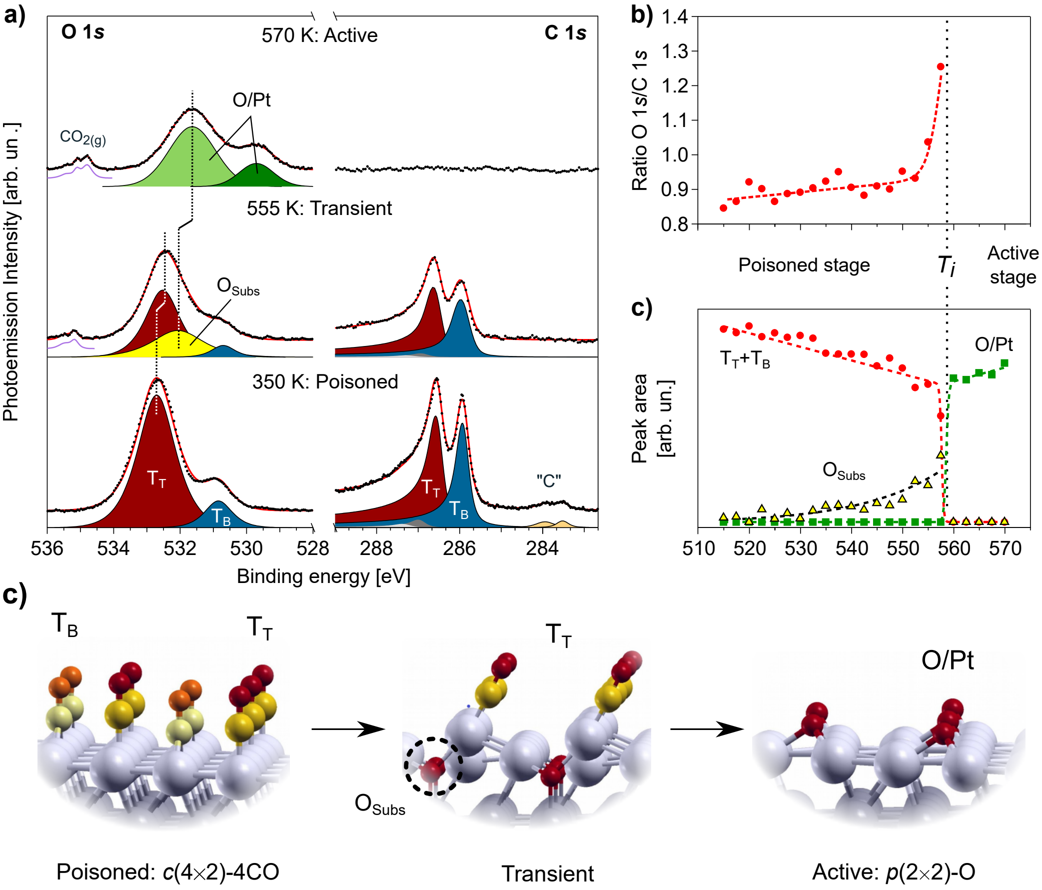

Figure 3.5: XPS evolution during a slow ramp at the (111) surface. **a)** O 1*s* (left) and C 1*s* (right) at three characteristic temperatures during a slow and precise heating ramp (0.25 K/min, 2.5 K steps) at the (111) plane. The sample was exposed to a 1.1 mbar, 1:7 CO:O_2 gas ratio mixture, while the photon energy was 650 eV. At the poisoned stage (350 K, bottom) no CO_2 is detected. However, a sizeable production is observed at the transient regime (555 K, middle), prior to the full ignition and the maximum CO_2 production occurring as the surface passages to the active stage (570 K, top). T_T, T_B, “C”, O/Pt and O_{Subs} refer to Terrace-Top and Terrace-Bridge CO molecules, graphitic carbon, O-related species and subsurface O, respectively. Vertical dashed white and black lines illustrate the shift of the photoemission peaks at the different temperatures. **b)** O 1*s*/C 1*s* ratio and **c)** ChemCO (T_T+T_B), O/Pt and O_{Subs} peak areas, as extracted from the fitting of each spectrum of the heating ramp. T_i marks the ignition temperature at 557.5 K. **c)** Theoretical structures used for the calculations of the poisoned, transient and active stages of the CO oxidation.

In order to extract this possible unresolved species, we performed a consistent peak fitting procedure. At 350 K, far from ignition, one would expect only chemisorbed CO (ChemCO, i.e. T_T and T_B) species in the O 1*s* region. Since these can be easily distinguished in the C 1*s*, one can derive O 1*s*-C 1*s* conversion factors to extract the expected O 1*s* intensity of T_T and T_B from their well-defined peaks in the C 1*s* region. It must be noted that PED effects may arise at the (111) plane in the O 1*s*, altering the real T_T/T_B ratio [24]. Therefore, individual O 1*s*-C 1*s* conversion factors for T_T and T_B must be derived. By fitting the C 1*s* at different temperatures and applying the O 1*s*-C 1*s* conversion factors obtained from the fit at 350 K, one can extract the expected intensity in the O 1*s* for T_T and T_B at each of the temperatures. Hence, if species other than ChemCO contribute to the O 1*s* total intensity, an extra intensity will be required to properly fit the O 1*s*.

Far away from ignition, the O 1*s*/C 1*s* ratio is virtually constant. However, this relationship significantly grows at 555 K, when the ignition is close. Therefore, the intensity calculated from the C 1*s* does not produce an adequate fit of the O 1*s* region, and one needs to add an additional feature in the fitting routine in order to account for this missing intensity. The position of such feature is 532.1 eV, as derived from the fitting. As discussed in the following paragraphs, we have named it O_{Subs}. It is residual at low temperature, but it rapidly increases when approaching ignition, mimicking the growth of the O 1*s*/C 1*s* ratio. We must note that after ignition, a similar, unknown peak is detected at 531.6 eV, i.e. 0.5 eV away from the O_{Subs} emission of the poisoned phase. A different species than O_{Subs} seems more likely than such shift of O_{Subs} right after ignition. O_{Subs} vanishes after the ligth-off of the reaction, hence we have called this stage “Transient”.

The existence of the O_{Subs} feature in the O 1*s* region seems clear, but its nature is not evident. Transient regimes [27, 31, 58, 131, 126, 210, 211] with additional species and surface roughening [46, 47] were already observed for other Pt substrates during the CO oxidation. Our transient stage appears only right before ignition and coexists with a remarkable amount of CO on the surface (~0.2 ML). There is a significant amount of CO_2, likely due to the low pumping speed of the setup, since the Pt surface is slightly active prior to ignition and CO_2 accumulates in the chamber. Only T_T and T_B are distinguished in the C 1*s*, hence the peak at 532.1 eV is not CO adsorbed at steps, which appears at a similar binding energy [63]. Chemisorbed O in hollow fcc sites is also discarded [52]. Hence, we resorted to theoretical calculations in order to characterize this unknown species.

For the input of the theory we took into account that CO molecules adsorbed on $\mathrm{T_B}$ sites desorb earlier than those at $\mathrm{T_T}$ positions [55]. Therefore, one would expected a relatively open layer of $\mathrm{T_T}$-CO on the surface close to ignition. To account for this situation, we only considered that the $\mathrm{T_T}$ sites are occupied by CO, leading to a (2×2)-$\mathrm{T_T}$, 0.25 ML superstructure. Several different structural models were considered for the theoretic investigations, combining the (2×2)-$\mathrm{T_T}$ arrangement with coadsorbed O in hollow fcc and subsurface sites. The bare subsurface O was also tested. All the details of the theoretical calculations are presented in [188]. We will limit the description to the experiments and its analysis but will not describe the computational details. These were performed by C. García-Fernández and D. Sánchez-Portal (Materials Physics Center, San Sebastián). For each of the structures (see Appendix B3), they calculated the formation energy (E_{for}), the O 1s core level position for both the CO molecule and O atom [E_B^{CO} and E_B^O, both compared to the experimental value of $\mathrm{T_T}$ (532.7 eV)] and, finally, the CO adsorption energy variation ($\Delta E_{ad}^{\mathrm{CO}}$), as compared to that of the (2×2)-$\mathrm{T_T}$ reference. The results are summarized in Table 3.1.

The first structure that will be discussed is a 0.25 ML layer of CO in $\mathrm{T_T}$ positions with a coadsorbed 0.25 ML structure with oxygen atoms anchored at hollow fcc sites (CO-O$_{fcc}$). Even though this structure has the lowest formation energy E_{for}, and hence should be the most stable situation, the O binding energy is calculated to be $E_B^O = 530.3$ eV, far away from our experimental one. Another reasonable possibility would be coadsorbed subsurface O, which has been postulated before in several metals [162, 212–215], including Pt [84, 85, 216, 217]. A further argumentation for such a subsurface configuration is that in Pt [30, 95, 218], Rh [170, 171] and Pd [219] oxides are formed as trilayer surface oxides, on which O atoms incorporate beneath the topmost metal surface. For these reasons we also considered O incorporation below the (111) terraces. The CO-O$_{sub}$ structure depicted in the middle panel of Figure 3.5c) consists on $\mathrm{T_T}$-CO molecules coadsorbed with O atoms occupying hcp hollow sites below the (111) surface [84, 85]. It features one shared Pt atom between the O and the CO. The formation of this structure lowers the CO adsorption energy by around 0.3 eV, bringing it to values close to that of the steps [220], which would explain the simultaneous CO desorption from steps and terraces. It is noteworthy that this configuration lifts some of the Pt atoms, resembling the surface roughening proposed by McCrea *et al.* [46, 47], and also the surface oxide described by Miller and coworkers on Pt(111) [30]. Regrettably, E_B^O is again far from the value observed experimentally.

Another structural combination comprises $\mathrm{T_T}$-CO and subsurface hcp O in a way that none of the Pt surface atoms are shared by the CO and the O (CO-O_{sub}*). Even though E_B^O matches that extracted experimentally, it increases the adsorption energy of the CO, hence it does not explain the simultaneous ignition. If the amount of subsurface O is doubled and both tetrahedral sites are occupied (CO-2O_{sub}), the situation improves in the sense that the formation of this structure becomes more favourable and the CO adsorption energy decreases even more, explaining the simultaneous ignition. The drawback of this simulated structure is that the calculated O 1s core level position does not fit to the experiment.

Structure	Θ_{CO}/Θ_O [ML]	O site	E_{for} [eV]	E_B^O [eV]	E_B^{CO} [eV]	$\Delta E_{ad}^{\mathrm{CO}}$ [eV]
CO only	0.25/0.00	-	-1.65	-	532.7	0
CO-O_{fcc}	0.25/0.25	fcc	-2.93	530.3	532.8	+0.10
CO-O_{sub}	0.25/0.25	tetra	-1.27	531.3	532.8	-0.31
CO-O_{sub}*	0.25/0.25	tetra	-0.74	532.1	532.9	+0.22
CO-2O_{sub}	0.25/0.50	tetra	-1.32	531.0	532.8	-0.48
O_{sub} only	0.00/0.25	tetra	+0.68	532.0	-	+0.68

Table 3.1: DFT calculations of several CO-O structures at Pt(111). Formation energy (E_{for}), O 1s position for CO (E_B^{CO}) and oxygen (E_B^O), and CO adsorption energy variation ($\Delta E_{ad}^{\mathrm{CO}}$) determined for a number of pure and mixed CO and O structures on Pt(111). CO-O_{sub} is sketched in the middle panel of Figure 3.5c), while all of them are reported in Appendix B3.

To conclude, theoretical calculations suggest that oxygen, $\mathrm{O_{Subs}}$, could lower the adsorption energy of coadsorbed CO molecules anchored at the terraces. This would bring it up towards values similar to those of CO adsorbed at steps, and hence explaining the symmetric ignition of the reaction. Nonetheless, we did not succeed into reproducing both the experimental core level and the decrease of adsorption energy at the same time. This may be related to the complexity of the system, since we are only considering simple structures in order to ease the computations. There is also the possibility of $\mathrm{O_{Subs}}$ being an uncharacterized surface oxide. Additional theoretical calculations could shed light into this transient regime, although such computations are usually complex and require a large amount of time.

3.4 Step doubling during the transient stage

We have proposed that the (111) terraces accommodate subsurface oxygen (O_{Subs}) right before the CO ignition. In this Section we will investigate the chemical species involved in this transient stage at the stepped surfaces available in the c-Pt(111) sample, paying special attention to O_{Subs}. In order to do so, we mapped the curved surface (α-scan) at 350 K (poisoned stage) and 550 K (close to CO ignition, transient stage) at a 1:6 CO:O_2 gas ratio and a total pressure of 0.7 mbar. Relevant O 1s spectra are shown in Figure 3.6, and they were taken right before the C 1s region discussed in Section 3.2. Complete O 1s α-scans can be seen in Appendix B4. The behaviour of B-type vicinals is the same as for A-stepped surfaces. However, since the former steps feature additional species at large α, we will only discuss A-type vicinals in this Section to focus on such species.

In Figure 3.6a) we sketch the O 1s at the (111) plane and different A-type vicinals. There, the evolution from 350 to 550 K is analyzed together with the peak fits for the high temperature measurement. As mentioned in Section 3.3, the leading contribution at 532.5 eV at the position of the (111) plane shifts with the temperature, which we postulate confirms the existence of O_{Subs}. The fitting routine that we used before to extract O_{Subs} is no longer valid at the stepped surfaces, since the broad T_T and S_T contributions lie very close to each other in the O 1s region [63]. This prevented us from resolving T_T and S_T, hence we were forced to consider a single photoemission peak (T_T+S_T) in the O 1s fitting routine at the stepped surfaces. Therefore, we decided to use peaks with fixed energy (small variations were permitted) for O_{Subs} and CO anchored at T_B sites (532.1 and 530.9 eV, respectively). The combined feature (T_T+S_T) was allowed to shift towards lower binding at increasing α, due to the growth of S_T at lower binding energy [63]. An additional peak at 529.6 eV is perceived at $\alpha > +5°$, which we relate to atomic O [52] at the steps ($O_{D\text{-}S}$, see later).

The aforementioned fitting procedure yields the expected decrease of CO adsorbed at T_B positions with α. However, those at (T_T+S_T) sites features a complex behaviour at highly stepped planes, since both T_T and S_T suffer from PED effects. The progress of the different ChemCO species with α was already discussed in Section 3.2 at the very same conditions (the O 1s region was acquired immediately before as the C 1s), hence we shall focus on the nature of the O-related species at the stepped surfaces prior to the CO ignition. The intensity of the oxygen atoms anchored at O_{Subs} and $O_{D\text{-}S}$ positions as a function of the vicinal angle [see Figure 3.6b)] clearly reflects the terrace character of the former and step character of the latter.

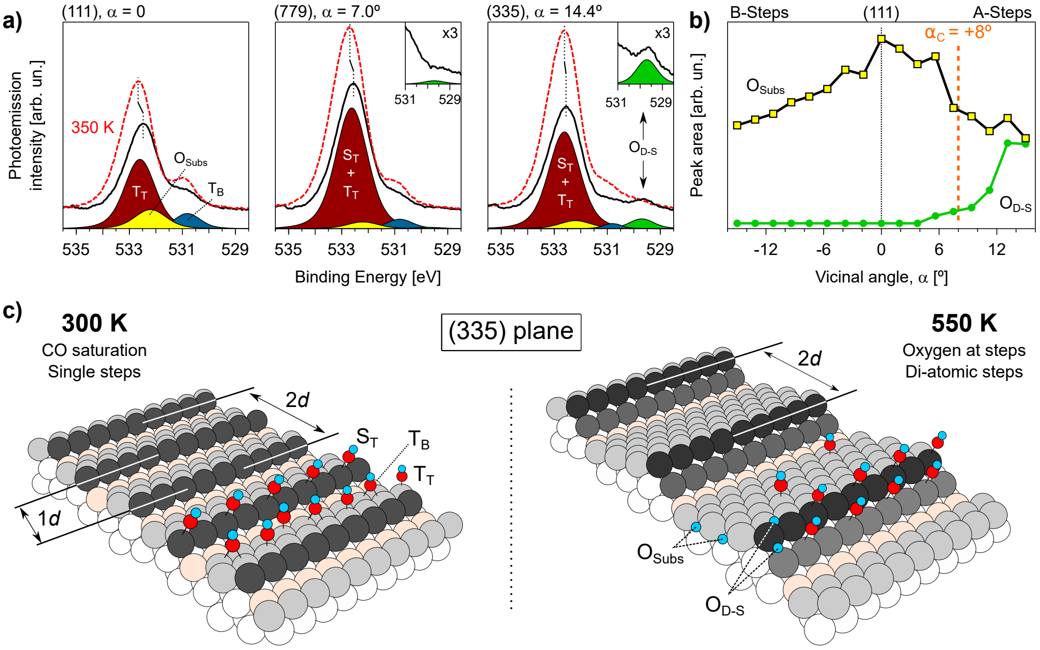

Figure 3.6: Step doubling at vicinal Pt surfaces.
a) Selected fitted spectra at 550 K (transient stage) at different α across A-type Pt stepped surfaces, acquired though surface maps at a 1:6 CO:O_2 gas ratio, 0.7 mbar of total pressure (see Appendix B4). Low temperature scans (350 K, poisoned stage) are included as red dashed lines to emphasize the spectrum shift as the ignition approaches and O_{Subs} arises. Note that the displacement is less marked at the stepped surfaces. The feature around 532.5 eV corresponds to CO anchored at sites at the (111) plane, while it is a combination of CO adsorbed at T_T and S_T positions at the vicinal surfaces and, accordingly, shifts towards lower binding energies as compared to the peak at the (111) plane [63]. Insets at stepped surfaces are added to emphasize the $O_{D\text{-}S}$ peak. **b)** Evolution of oxygen species (O_{Subs} and $O_{D\text{-}S}$) as a function of α. A dashed, orange line is included in order to mirror the break of slope observed in Figure 3.3. **c)** Sketch of monoatomic (left, 300 K, UHV CO saturation) and diatomic (right, 550 K, transient stage) steps on a (335) surface, illustrating the step doubling effect discussed in the text. Terrace-Top, Step-Top and Terrace-Bridge CO molecules are denoted as T_T, S_T and T_B, while O_{Subs} and $O_{D\text{-}S}$ correspond to oxygen below the topmost layer of the surface and atomic O anchored at the diatomic step, respectively.

Only a small amount of $O_{\text{D-S}}$ is observed at 550 K, increasing with α. The position of $O_{\text{D-S}}$ (529.6 eV) resembles atomic O chemisorbed in hollow fcc sites in Pt(111) [52], although its increase with α clearly indicates that it is anchored close to the step edge. Oxygen adsorption at S_B sites was reported before for A-type Pt surfaces [97, 106, 221]. This is expected, since O adsorbs in bridge sites at Pt(110) [222], exhibiting a photoemission peak centered close to 530 eV [40, 130, 223]. Since the nature of $O_{\text{D-S}}$ is not completely clear, we sketch both possibilities in Figure 3.6c).

Regarding O_{Subs}, the shift with the temperature of the large peak at 532.5 eV in the O 1s spectrum is smaller when stepped surfaces are considered [see vertical lines of Figure 3.6a)]. For these reasons, we believe that O_{Subs} is located only beneath the (111) terraces, and hence its decay with α is not an artifact of the fitting procedure.

One interesting phenomenon may be observed. $O_{\text{D-S}}$ emerges around $\alpha =°$, roughly at the same vicinal angle at which the decay of Terrace-CO turns less marked [C 1s analysis, see Figure 3.3b)]. Both effects seem to be correlated: above a critical vicinal angle α_C, Terrace-CO diminish in a less marked pace while the step species $O_{\text{D-S}}$ commences to steadily grow. Although this suggest a complex behaviour, all can be put together if step doubling is considered. This has been reported in several vicinal surfaces upon minor O_2 dosages [102, 224, 225], large CO pressures [70] and during the active stage of the CO oxidation in Pt [144].

A (335) surface ($\alpha = 14.4° > \alpha_C$) with single steps has one step (dark grey), one understep (ligth orange) and two terrace (light grey) rows in the distance between one step [1d, see Figure 3.6c)]. Therefore, these are doubled if the distance between two steps (2d) is considered. However, if a (335) plane with double steps is examined, the transition from mono- to di-atomic steps leads to the increase of one terrace row in expenses of an understep row in the same 2d distance. This is illustrated in Figure 3.6c). A (335) surface with single atomic steps has 2 terrace and 2 subsurface rows per 2d distance, while double-steps have 5 terrace and one understep row in the same 2d area. In both cases, the two step rows per 2d are retained. Hence, this larger room allows for more terrace species to chemisorb, explaining the mild decrease of the slope on the Terrace-CO perceived for Figure 3.3b) at 550 K above α_C. Finally, we did not observe additional O species on the B-side during this α-scan, although they may contribute to the spectra of both types of Pt vicinals if the O_2 content increases, as sketched in Figure 3.2.

3.5 Active stage at stepped surfaces

After discussing in detail the nature of the poisoned stage in the previous sections, we shall now explore the active stage of the reaction found after ignition. This phase is characterized by a large CO_2 production rate and an O-covered surface. After acquiring the α-scans presented earlier in this Chapter, we slowly increased the temperature to 595 K. Here, the signal related to ChemCO vanished at the same time as the CO_2 turnover significantly increased, marking the light-off of the reaction. Following the α-scan approach, we mapped the surface by monitoring both the O 1s and C 1s regions, as shown in Figure 3.7. Only $CO_{2(g)}$ contributes to the C 1s region, since the reaction has ignited. Additional α-scans under other experimental conditions are shown in Appendices B5 and B6, reflecting a variable composition of steps and terraces depending on the experiment parameters.

The entire O 1s α-scan is shown in Figure 3.7a). The two dashed white lines enclose different areas of the O 1s region: gas phase (>534 eV), oxides (534-530 eV) and chemisorbed (<530 eV) contributions. Regarding the gases, only the $O_{2(g)}$ doublet (around 537 and 538 eV, 1.1 eV splitting) and the $CO_{2(g)}$ triplet (535 eV) are detected. No $CO_{(g)}$ is perceived (536.5 eV) [38], since the reaction is O_2-rich and all CO surrounding the crystal reacts to form CO_2 (mass-transfer limit). One interesting behaviour, nicely reflected by the α-scan, is the variable position of all gas phase peaks across the curved surface. Such change may be easily explained in terms of different work-function of the facets, as discussed by Schiller *et al.* [206].

In Figure 3.7b) we show characteristic spectra at the (553), (111) and (223) surfaces, respectively featuring B-steps, terraces and A-steps. The spectrum at the center, the (111) surface, features two well-resolved peaks. The one at 529.6 eV corresponds to chemisorbed O at the follow fcc position of the terraces, O_{Terr} [52, 118]. However, the assessment of the additional peak is not trivial. Its energy (531.4 eV) exceeds 530 eV, hence it must be an oxide (denser O phase). It is clear that it is not PtO_2 (530.2 eV) [226], and 1D oxides at terraces (530.7 eV) are also discarded [25]. To our knowledge, only a peak at the very same binding energy, assigned to PtO, was observed after a reactive sputtering preparation [93]. We could not perform additional experiments to further delve into the nature of this feature, hence we will label this uncharacterized species as “Oxide”.

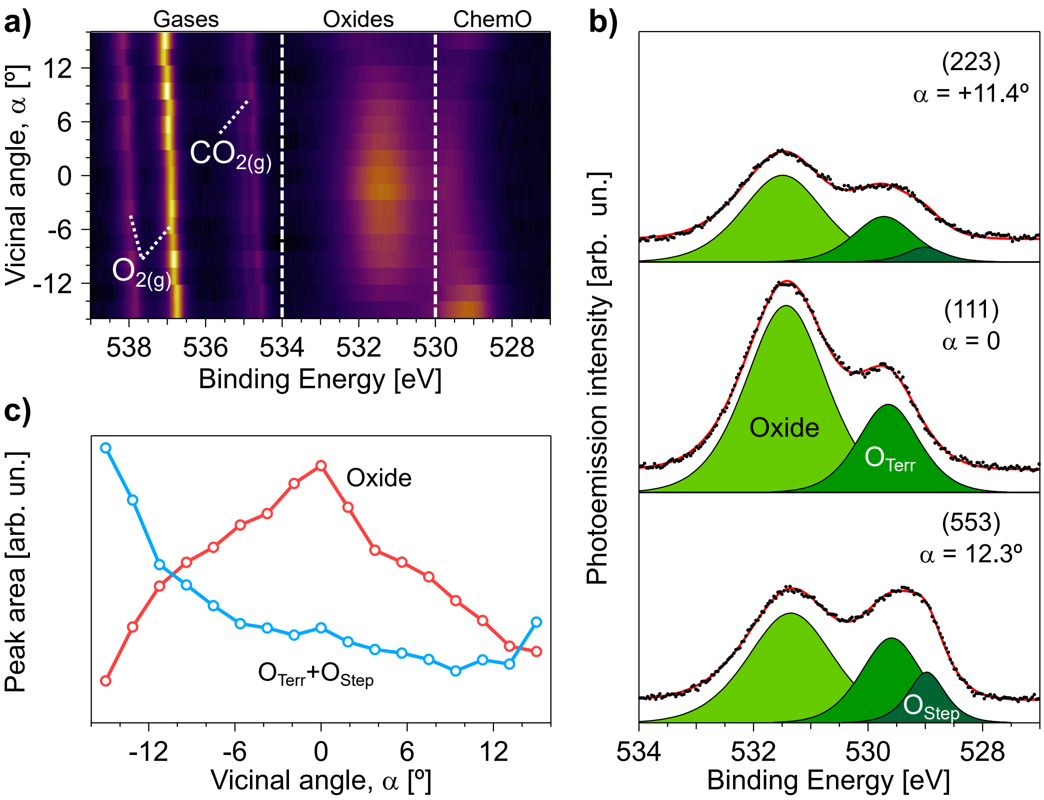

Figure 3.7: O 1*s* α-scan during the active stage.
a) O 1*s* intensity scan across the curved surface during the active stage of the CO oxidation. Different species are identified according to their binding energy, i.e. chemisorbed O (<530 eV), oxides (534-530 eV) and gases (>534 eV). **b)** Selected spectra at relevant surfaces, namely the (553), (111) and (223) planes at the top, center and bottom panels, respectively. **c)** Evolution of oxygen species as a function of α, as extracted from the fit of all spectra shown in a). O_{Terr} and O_{Step} refer to atomic O anchored at terraces in hollow sites and at steps in an unknown position, while Oxide refers to an uncharacterized oxide located at the terraces, respectively. Experiments were undertaken at 595 K under a 1:6 CO:O_2 gas mixture at a total pressure of 0.7 mbar, using photons of 650 eV. $CO_{2(g)}$ and $O_{2(g)}$ in a) refer to the photoemission peaks of such molecules.

The stepped (223) and (553) surfaces are respectively shown in the top and bottom panels of Figure 3.7b). First of all, both Oxide and O_{Terr} decrease at both. Therefore, we can suggest a terrace-nature of the Oxide contribution. The decay of O_{Terr} is strong at the (223) surface but much smaller at the (553) plane, revealing asymmetries between A- and B-type steps. An additional peak at 528.9 eV may be distinguished, labelled as O_{Step}. We will observe the same small peak for kinked Pt vicinal surfaces (see Subsection 4.1.4). The energy position of O_{Step} points towards an atomic O species, yet we mentioned earlier in Section 3.4 that O anchored at bridge and hollow sites near the step edge should also exhibit a peak close to 530 eV. Ogawa *et al.* [227] reported that O could also anchor to the square steps in four-fold hollow positions, but clearly not in the understep region. Due to its large shift as compared to O_{Terr}, we suspect to have O adsorption on these square sites. This is reasonable for $\{100\}$ microfacets, although it is not likely for $\{111\}$ single steps, which may indicate that the B-stepped surfaces are reconstructed.

In Figure 3.7c) we sketch the evolution of Oxide and chemisorbed O (O_{Terr}+O_{Step}) as a function of α. The former decreases with the step density, whereas ChemO decreases or increases depending on the step type. While the species of the active stage are similar at different conditions, their evolution with the step density may vary significantly depending on them (see Appendices B5 and B6). Therefore, it is difficult to extract a clear trend.

To end with this Chapter, we must mention that the study of the active stage of the CO oxidation is not the main topic of this Thesis, and hence it is just preliminary. It is likely that the Pt vicinals [143, 144], if not Pt(111) itself, reconstruct, explaining the variety of behaviours as a function of the step density observed of each of the species. In addition, the bibliography on the Pt oxidation is vast, and several works contradict each other (Subsection 1.3.2). Complementary structure-sensitive experiments, such as surface X-ray diffraction [175] or high-pressure scanning-tunneling microscopy [25], in addition to theoretical calculations [130], could shed light into this problem.

Summary of the c-Pt(111) experiments

In this first experimental Chapter, we explored the CO oxidation on A- and B-type Pt vicinal surfaces up to $\alpha = \pm 15°$. Preliminary experiments undertaken in UHV allowed us to quantify the saturation layer: top and bridge CO molecules dominate the terrace adsorption, while top positions are the preferred adsorption sites at the steps. A residual adsorption in bridge sites at $\{100\}$ steps was also observed. Applying the W-model to our data after CO saturation permitted to derive the effective width of the steps, which gives an idea of the average area of influence of the step inside terraces. The values obtained from the fit were larger compared to the geometric distance between Pt rows, reflecting how the step influence extends towards the lower terrace. A-steps typically feature a lower terrace coverage than its B-type analogous, although both share a similar CO coverage of 0.5 molecules per step atom after CO saturation.

Regarding the CO oxidation experiments, both PLIF and NAP-XPS revealed a surprising simultaneous ignition of A- and B-type Pt vicinals. The C $1s$ mapping at different temperatures prior to the light-off showed a partial depletion of terraces while the steps remained CO-saturated. Since the terraces are partially empty, O_2 can stick, dissociate and start the reaction there. A profound analysis of the O $1s$ and C $1s$ regions during a slow heating ramp at the (111) plane pointed to the existence of an additional oxygen species, since the ratio (O $1s$/C $1s$) increased when approaching the ignition. With the aid of theoretical calculations, we postulated that such species corresponds to subsurface O beneath the (111) terraces, although the precise atomic arrangement is not completely clear from the theory. Nevertheless, such subsurface O would decrease the adsorption energy of coadsorbed CO, explaining the simultaneous ignition of terraces and straight steps observed for Pt. In stepped surfaces, minor amounts of O at $\alpha > 8°$ were perceived just prior to the CO ignition. The steady growth of such O was parallel to a slower decay of terrace-CO species roughly above the same step density. We suspect that this O may cause step doubling at large step densities, which explains the slower decay of terrace-CO at $\alpha > 8°$.

We also studied the active stage of the CO oxidation, whose composition at steps and terraces was found remarkably variable. We detected chemisorbed oxygen in hollow position at terraces, and possibly with fourfold coordination at the steps. We also observed an uncharacterized oxide, maximum at the (111) terraces and markedly decreasing with α, suggesting that it builds up at the Pt(111) terraces. However, additional α-scans of the active stage at different experimental conditions reveal that the relative oxidation of steps and terraces significantly varies with the CO:O_2 gas ratio.

Chapter 4

CO oxidation on Pt kinked surfaces

This Chapter deals with CO oxidation experiments carried out on a curved Pt sample featuring kinked steps. In this Pt crystal, the cylinder curvature is not anymore parallel to the $[1\bar{1}0]$ direction, but perpendicular to it and parallel along the $[1\bar{2}1]$ direction. Unlike the curved samples with straight A- and B-steps, the curved surface of this sample is not symmetric with respect to the [111] direction. It neither features A- or B-steps as for the c-Pt(111) sample described earlier, but kinked steps. The center of the crystal is chosen in a way that the (111) surface is shifted to one edge, covering a ±19.5° angular range around that (645) surface. We will call this crystal k-Pt(645). As sketched in Figure 4.1, a variable density of kinked steps along its curved surface is achieved. This sample spans a total vicinal angle of $\Delta\alpha = 28°$ from the (111) plane located at one side of the crystal, enabling to reach the densely kinked (312) surfaces (2-atom-wide terraces) at the other edge. See Section 2.1 for more details on kinked surfaces. The cleaning routine and sample characterization are described in Appendices C and C1.

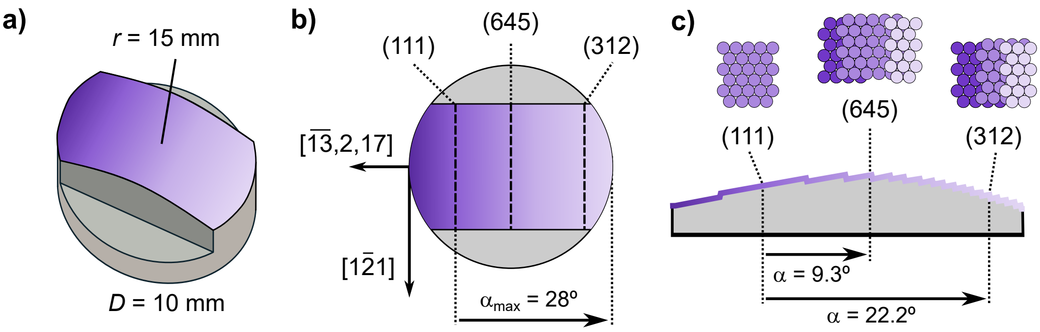

Figure 4.1: Description of the curved k-Pt(645) sample.
a) Model of the curved k-Pt(645) crystal, indicating the radius of curvature r and sample diameter D. **b)** Top view of the sample, with positions of selected surfaces and the maximum vicinal angle α_{max} that can be probed using this crystal. The crystallographic directions perpendicular and parallel to the cylinder axis, namely the $[\overline{13},2,17]$ and $[1\bar{2}1]$, respectively, are also included. **c)** Lateral view of the crystal, indicating the location and vicinal angles α of the (645) and (312) surfaces across its curved surface. Insets with atomic models for the (111), (645) and (312) planes are also included.

4.1 CO and O_2 adsorption in UHV conditions

In order to characterize the CO layer of the poisoned stage and oxygen species of the active stage of the CO oxidation, we performed UHV reference experiments. We exposed the sample to CO and O_2 in separate experiments and measured by XPS the surface chemical species across the curved surface. These measurements were carried out at SuperESCA beamlime at Elettra synchrotron. The experimental procedures are presented in Appendix C.

4.1.1 CO uptake experiments at kinked planes

We first studied the CO adsorption hierarchy at the kinked Pt vicinals. Individual uptake experiments were performed at the (111), (645) and (312) surfaces. These surfaces were separately exposed to $1 \cdot 10^{-9}$ mbar CO at 300 K while continuously recording the C 1s region. Additional information, such as coverage calibration, is given in Appendix C.

The experiment starts at the (111) plane (Figure 4.2, left panels), in order to compare with earlier reports on the CO adsorption on Pt(111). Shortly after CO exposure [Figure 4.2d)], a peak at 286.7 eV appears. It is attributed to CO anchored atop Pt atoms at terraces (Terrace-Top, T_T) [55]. Later and at a slower rate, another feature at 286.0 eV develops, which corresponds to CO adsorbed at terrace bridge sites (Terrace-Bridge, T_B) [55, 72, 228]. The evolution of both CO species is shown in [Figure 4.2g)]. While the T_T-CO intensity steadily grows until saturation at around 0.8 L, the adsorption at T_B sites is slower and seems not to be saturated after the highest dose used here (3 L CO). Our results agree well with a preceding report on the CO adsorption on Pt(111) at 200 K [55]. A residual amount of graphitic carbon ("C") was observed, increasing with time and hence with beam exposure.

The center column of Figure 4.2 illustrates the same experiment for the kinked (645) plane ($\alpha = 9.3°$). As seen in Figure 4.2e), a peak at 286.4 eV emerges prior to any other features. Similarly to close-packed Pt vicinals [63, 67], and in agreement with earlier reports on kinked Pt surfaces [68], we attribute this peak to CO adsorbed in top positions at the kinked edge (Step-Top, S_T). At higher CO exposures, adsorption at T_T and T_B sites is easily perceived. As depicted in Figure 4.2h), S_T-CO markedly slows down at around 0.15 L CO, point at which CO starts to adsorb also at T_T sites. Mimicking the (111) plane uptake, the population of T_T positions is followed closely by that at T_B sites. T_T-CO grows faster than T_B-CO, and stops at around 0.5 L CO. However, T_B-CO continues to increase at a quite reduced rate up to 0.7 L CO. At the highest exposure of this experiment (1 L CO), the surface is not saturated. A residual "C" contribution was also found, although not as pronounced as on the (111) surface.

Finally, the CO adsorption on the clean (312) surface ($\alpha = 22.2°$) will be analyzed (Figure 4.2, right column). As depicted in Figure 4.2f), S_T-CO rises right after introducing CO to the chamber, followed again by the adsorption at T_T sites. The evolution of individual CO species during the uptake at the (312) plane is shown in Figure 4.2i). S_T-CO saturates at around 0.6 L CO, in contrast to T_T-CO, which does not saturate at 1 L CO. The increase in the saturation dose of CO adsorbed at S_T sites is simply explained by its larger step density as compared to the (645) plane. For the same reason, the effective terrace length of the (312) surface is reduced with respect to the (645) plane. Accordingly, the coverage of T_T-CO and T_B-CO steadily decreases at the (645) and (312) plane. At the latter, the coverage of T_T-CO is smallest, and T_B is not even observed. This matches early studies on the CO adsorption by electron energy-loss spectroscopy on the very same surface [68] and by XPS on the "fully" kinked Pt(201) surface ($\alpha = 39.2°$) [229].

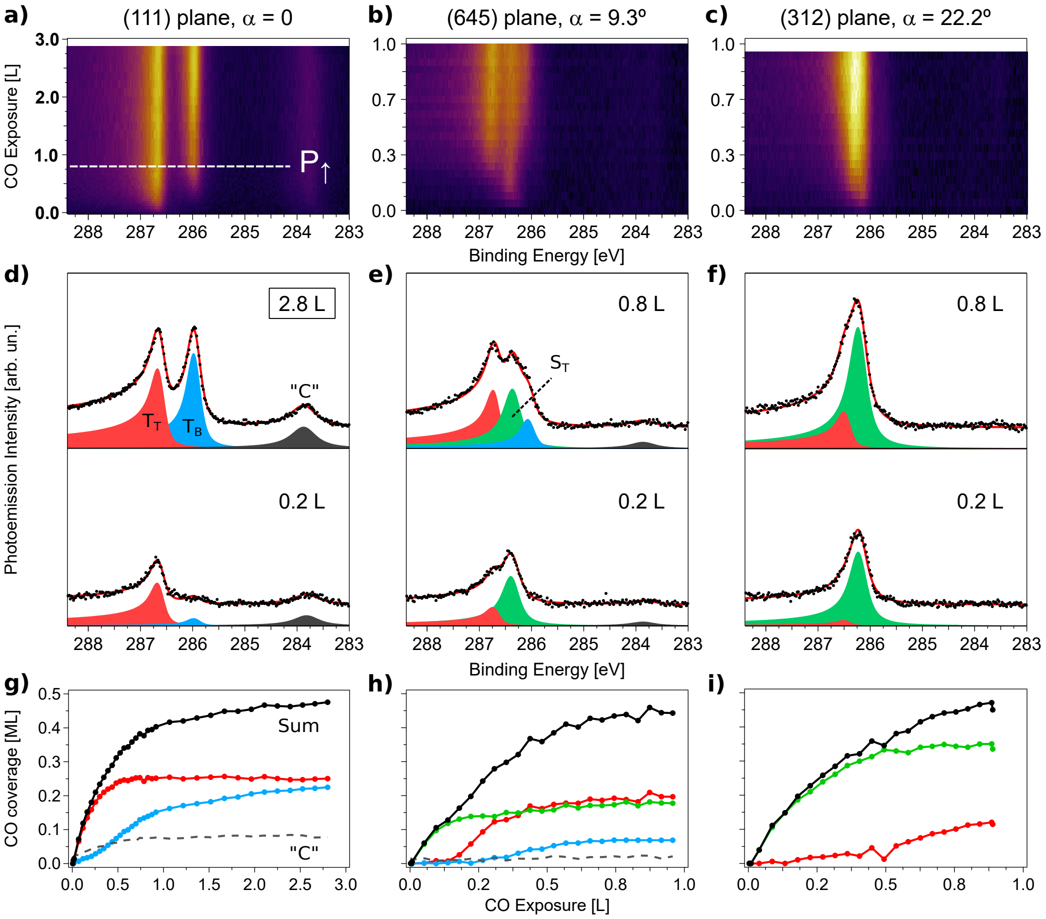

Figure 4.2: CO uptakes experiments at relevant surfaces.
a-c) Color plots of the CO uptakes at the (111), (645) and (312) surfaces, respectively. In the (111) plane, $P_{\uparrow}$ indicates a pressure increase from $1 \cdot 10^{-9}$ to $1 \cdot 10^{-8}$ mbar CO, in order to speed up the process; the other two experiments were carried out at constant pressure of $1 \cdot 10^{-9}$ mbar CO. Note the different scale in a) and b,c). **d-f)** Characteristic fitted spectra at low (top) and high (bottom) CO exposures for each plane. **g-i)** Coverage evolution of each CO species as a function of CO exposure. T_T, T_B and S_T stand for CO adsorbed as Terrace-Top, Terrace-Bridge and Step-Top sites, as sketched in Figure 4.4. The dashed black lines represent the graphitic carbon ("C") contribution, while the solid black line corresponds to the total CO coverage. The measurements were taken at a photon energy of 370 eV at room temperature.

After the joint analysis of the three uptake experiments of Figure 4.2, the CO adsorption sequence can be easily derived as $S_T \to T_T \to T_B$. This matches early reports on densely kinked Pt vicinal surfaces, where CO was found to adsorb at kinks prior to terraces [68, 229]. On the other hand, the preferential chemisorption of CO on T_T sites over T_B positions is also expected [55]. This sequence also agrees well with previous studies on close-packed Pt, Rh and Ni stepped surfaces, where CO adsorbs first on step edges rather than on terraces [63–67, 152, 186, 230, 231]. S_T-CO prevails over T_T-CO on sticking probability, and also on coverage at high α, while T_B positions are always the last occupied sites with the lowest coverage.

4.1.2 CO desorption from selected kinked surfaces

Another important point in the CO experiments is the reverse process to the above described adsorption, the desorption of CO. To gain helpful insights into the CO desorption, a fundamental step during the CO oxidation, we investigated such phenomenon in UHV conditions. More details on the experiments are given in Appendix C. Briefly, CO-saturated surfaces, namely the (111), (645) and (312) planes, were heated (constant heating rate of 5 K/min) while continuously recording XPS. The experiments were carried out at a photon energy of 650 eV to also probe the O 1*s* region. We show the O 1s spectra in Appendix C2, where no O species arising from CO cracking at high temperatures were found.

As in previous discussions, the well-documented (111) plane was used as a reference (left column of Figure 4.3) [56, 61, 117, 232]. As seen in Figures 4.3d,g), T_B starts to desorb right after starting the heating ramp, and vanishes at around 390 K. However, T_T remains rather stable until 320 K and then starts to decrease as well. It completely desorbs at around 430 K, approximately 40 K higher than T_B. Earlier desorption of CO anchored at T_B positions rather than at T_T sites is the expected [56, 117, 233]. The graphitic “C” peak grows during the desorption experiments acquired at the three surfaces. We shall discuss this effect at the end of the Section.

At the (645) surface (center column of Figure 4.3), CO was found to adsorb at the step edge (S_T) in addition to the two positions at terraces (T_T and T_B). Similarly to the (111) plane, the first species to desorb is T_B-CO. It completely vanishes at 360 K, followed by T_T-CO at around 400 K. However, as seen in Figure 4.3h), S_T-CO has not completely desorbed at 480 K. This is expected and illustrates the larger adsorption energy of CO adsorbed at steps as compared to its terraces analogous [63, 65, 67].

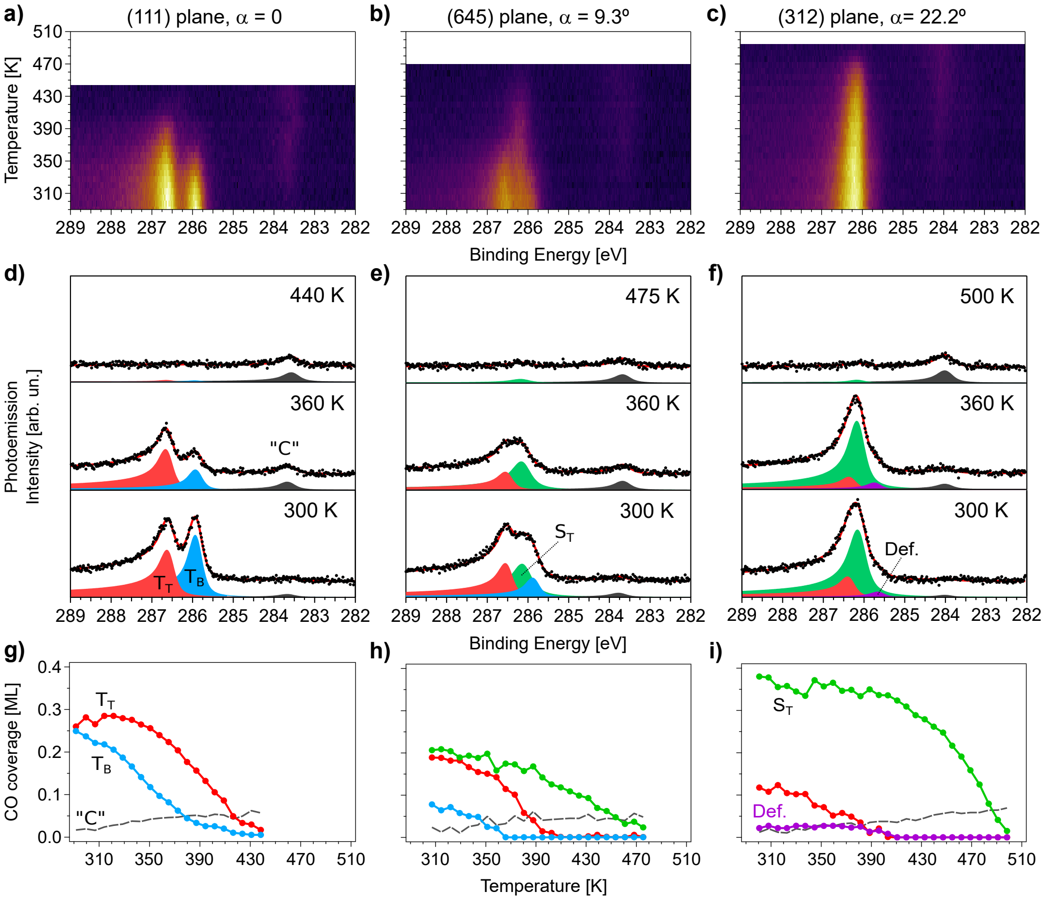

Figure 4.3: CO desorption experiments at relevant surfaces.
a-c) Photoemission intensity plots of the C 1*s* region during a heating ramp at CO-saturated the (111), (645) and (312) surfaces, respectively. The surfaces were exposed to 10 L CO in order to ensure saturation. **d-f)** Selected fitted spectra at the (111), (645) and (312) planes at the start (300 K), middle (360 K) and end (440, 475 and 500 K, respectively) of each desorption experiment. **g-i)** Coverage evolution as a function of temperature of individual CO species, extracted from the fit of all spectra shown in a-c). CO adsorption as Terrace-Top, Terrace-Bridge and Step-Top are denoted as $\mathrm{T_T}$, $\mathrm{T_B}$ and $\mathrm{S_T}$, while graphitic carbon is denoted as “C”. CO chemisorbed at defect sites at the (312) surface is colored in purple. CO adsorption at defects of the (312) surface is colored in purple. The experiments were carried out at a photon energy of 650 eV.

We finished the experiment at the CO-saturated (312) surface (right column of Figure 4.3). The main contribution now is S_T-CO, while the peak related to CO adsorbed at T_T sites is remarkably smaller in this plane, since the terraces are significantly narrow. There is an additional feature initially attributed to CO anchored at T_B sites. However, its position at the (312) plane (285.75 eV) is different from that observed at the (111) surface (285.93 eV), indicating that bridge sites could have different lattice strain within the tiny and odd (312) terraces [207], or it could be that this peak corresponds to CO adsorbed at defects [63]. Upon heating, T_T-CO starts to decrease prior to the feature at 285.75 eV. Additionally, this latter contribution remains almost constant with temperature until desorption. This reveals differences with CO molecules adsorbed at T_B sites on large (111) terraces, as the latter would readily start to desorb rapidly after increasing the temperature above room temperature [55], therefore we postulate that the peak at 285.75 eV is related to CO adsorbed at defects. It can be seen in Figure 4.3i) that CO anchored at both T_T and defect sites sites desorb at 390 K. However, S_T does so at 500 K, reflecting again a larger desorption temperature of CO adsorbed at steps as compared to terraces.

The three experiments confirms the following trend for desorption temperatures: $T_B \rightarrow T_T \rightarrow S_T$. It is exactly the opposite as the adsorption sequence derived in Subsection 4.1.1, as one would expect. Both the uptake and desorption experiments support that the adsorption energy of CO adsorbed at kinks is larger than that at terraces: impinging CO molecules would adsorb first on kinks in the low coverage regime, and they will desorb from them only after the CO from the terraces has almost vanished. Accordingly, such bigger desorption temperature is of relevance to the CO oxidation ignition in NAP experiments on these vicinal surfaces, as it could promote, e.g., the CO-poisoning of the kinks and cause the terraces to ignite earlier than them during the chemical reaction.

It is easily seen in Figure 4.3 that the amount of “C” increased during the three desorption experiments. However, it is not possible to confirm that this effect is promoted by the heating itself of by the intense photon beam impinging the surface. Nonetheless, CO anchored at T_B sites was found to dissociate under the intense synchrotron photon beam in other measurements during these experiments (not shown). Therefore, a new experiment moving the sample would be necessary in order to completely distinguish between beam-assisted CO dissociation and thermal CO cracking.

4.1.3 C 1s α-scan after CO saturation

Next we characterize the CO species at saturation in order to understand the CO-poisoning layer found during reaction conditions. In order to do so, the C 1s was mapped across the curved surface after dosing 0.25 and 10 L CO at 300 K. The O 1s data has been relocated to Appendix C3 in order to ease the discussion, and the C 1s α-scan after the 0.25 L CO is not shown.

We will focus on the C 1s α-scan acquired after CO saturation [10 L CO dose, Figure 4.4a)], since it is the most relevant data to assess the CO poisoning. The C 1s α-scan reveals the changes as a function of vicinal angle expected from the uptake and desorption experiments. The saturation spectra of the (111) surface is depicted in Figure 4.4b). Two peaks are clearly distinguished, corresponding to CO molecules anchored at T_T (Terrace-Top, 286.7 eV) and T_B (Terrace-Bridge, 286.0 eV) positions [52, 55] [see Figure 4.4g)]. Small peaks ascribed to vibrational excitations of T_T- and T_B-CO molecules were also perceived in the photoemission spectra [234–236]. As described in Appendix C, they were added to the fitting routine to finely evaluate the spectra. The small peak at 285.7 eV will be discussed later.

The spectra at the (645) and (312) planes after CO saturation are shown in Figures 4.4c,d), respectively. A new feature appears at 286.3 eV in the (645) plane and dominates the spectrum at the (312) surface spectra. As mentioned before, it is attributed to CO anchored at S_T sites (Step-Top) at the kinked arrays [63, 67]. On one side, both T_T- and T_B-CO steadily decrease at the (645) and (312) surfaces as compared to the (111) plane, reflecting the fact that the terraces narrow with the vicinal angle α. On one hand, S_T-CO is larger at the (312) plane as compared to the (645) surface, as the step density for the latter is higher. However, a closer look to the spectra reveals that two features can actually be resolved, which we attribute to CO adsorbed on top of kink Pt atoms with coordination 6 (S_{T6}, first kink row, 286.17 eV) and 8 (S_{T8}, second kink row, 286.34 eV), as sketched in Figure 4.4g). The CO adsorption at bridge sites at the steps (S_B) was not considered, since it appears at a rather different energy [67].

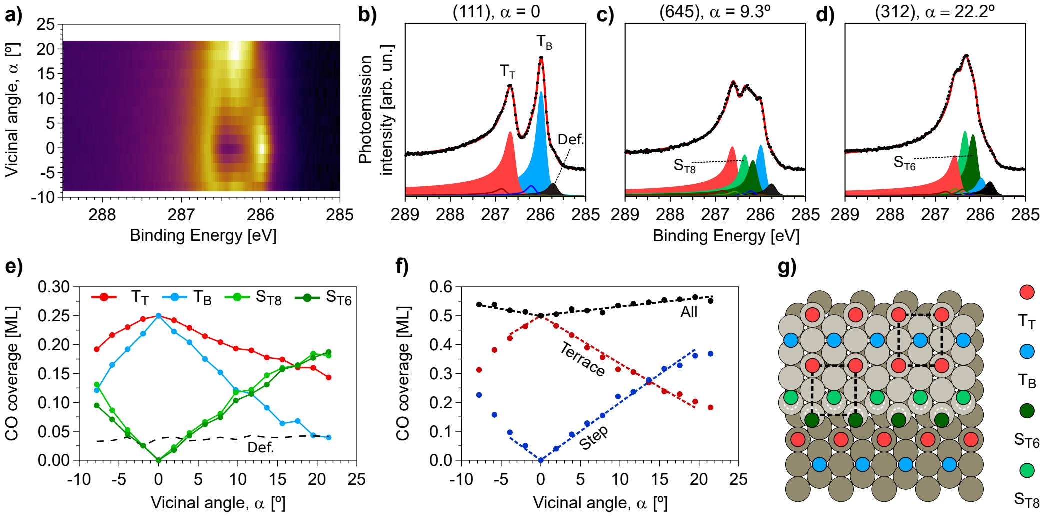

Figure 4.4: C 1*s* α-scan at CO saturation at 300 K.
a) C 1*s* intensity color plot across the curved k-Pt(645) crystal after exposure to 10 L CO at 300 K. Photoemission spectra were recorded at 90 K and at a photon energy of 370 eV. **b-d)** Selected spectra at the (111), (645) and (312) surfaces, respectively, together with their corresponding fits. CO coverage variation of **e)** individual and **f)** total CO species as a function of α, extracted from the fit of all spectra shown in a). **g)** CO adsorption structure around a fully kinked step (see text). CO adsorbed at defects was not included in this sketch. CO adsorption as Terrace-Top, Terrace-Bridge and Step-Top on Pt kink atoms (with coordination 8 and 6) are denoted as T_T, T_B, S_{T8} and S_{T6}, respectively. The black peaks of b-c) and the black dashed line of e) are ascribed to CO adsorbed at defects.

Finally, the feature at 285.8 eV is quite similar in all three spectra, for which we believe that this peak is related to CO adsorbed at defects. The position of the contribution matches an earlier report on Pt(553) [67]. Defects are concomitant to all crystalline samples [61, 122, 208, 209], and one would tentatively assume that they are homogeneously distributed across the sample. In fact we observe that the emission around 285.8 eV is virtually constant across the spectra of the whole α-scan, further supporting the defect-nature of such peak. We show this in Figure 4.4e). Extra CO species, such as CO anchored at terrace-hollow or step-bridge sites, exhibit peaks at similar binding energies [63, 67, 237]. We cannot resolve any additional peaks, hence we will treat this contribution as CO adsorbed at defects. Its adsorption position is not clear, and it is probably a combination of several geometries.

The curved surface was also probed by LEED after the 10 L CO dosage, as shown in Appendix C1. At the (111) plane, the expected $c(4\times2)$ pattern was clearly observed [53], which we used as a reference for coverage calibration (see Appendix C). However, the stepped surfaces showed no further diffraction spots than those arising from ordered monoatomic step arrays, hence no step doubling is expected [238]. This also suggests a random occupation of preferred CO adsorption sites inside the (111) terraces, similarly to B-type but contrary to A-type Pt vicinals [67].

The coverage variation of individual CO species as a function of α at saturation is shown in Figure 4.4e). In contrast to $\mathrm{S_{T8}}$, $\mathrm{S_{T6}}$ and $\mathrm{T_B}$, which exhibit an almost constant energy all over the α-scan (286.34, 286.17 and 285.98 eV, respectively), $\mathrm{T_T}$ smoothly shifted from 286.67 eV at the (111) plane to 286.56 eV at the (312) surface. These subtle variations on the position of $\mathrm{T_T}$ with increasing α are ascribed to a release of the terrace stress (i.e. a decrease in terrace strain) as the step density grows, as reported before for close-packed Pt vicinal surfaces [207].

A closer look to Figure 4.4e) further probes that both Step-CO species ($\mathrm{S_{T8}}$ and $\mathrm{S_{T6}}$) rise with α at an almost identical rate, indicating a similar coverage at the stepped edges. Although $\mathrm{T_T}$- and $\mathrm{T_B}$-CO decrease with the step density, it is clear that CO anchored at $\mathrm{T_T}$ sites does so at a slower rate. Therefore CO adsorption near the kinked step is more favourable in $\mathrm{T_T}$ sites rather than at $\mathrm{T_B}$ positions. Such scenario is quite similar to that observed for close-packed A-steps in Pt, where $\mathrm{T_B}$ decays faster than $\mathrm{T_T}$ at increasing α (see Section 3.2).

To end with, the saturation coverage of CO at terraces, steps and in total as a function of α angle is presented in Figure 4.4f). These results are of upmost importance, as they will permit to evaluate the CO saturation structure on steps in UHV, and compare it to the CO poisoning layer observed during the CO oxidation at the very same stepped surfaces. The constant amount of CO adsorbed at defects was excluded from the analysis below.

The absolute CO coverage is found to slightly increase with the step density at kinked Pt surfaces, in contrast to other Pt, Rh and Pd vicinals featuring straight A- and B-steps [186–188]. In order to investigate the saturation structure at kinked surfaces, we applied the W-model (Subsection 2.1.1) to the evolution of the the total terrace- and Step-CO coverages with α. Briefly to remember, it describes how the coverage at terraces and steps behave as a function of the step density, allowing to extract the effective step size at kinked surfaces (W, region of influence of the step at neighbouring terraces). It also gives information on the coverage at a flat surface [Θ_T^0, surface with no steps, i.e. the (111) plane] and the W-region [Θ_S^0, surface with no terraces].

We started by fitting the Terrace-CO evolution with α [$\Theta_T(\alpha)$] to Equation 2.2. On one hand, we obtained $\Theta_T^0 = 0.5$ ML, i.e. the CO saturation coverage of Pt(111) [53]. On the other hand, the fit yielded an effective extension of the step $W = 4.3$ Å. As mentioned earlier, this W-region accounts for both the step edge atoms and the area of influence (understep region) in the lower terrace. The distance between atomic rows in the perpendicular direction of the kinked step ($a_{\|}$ for kinked surfaces, see Figure 2.2) is 2.77 Å for Pt. W corresponds then to approximately $1.5 \cdot a_{\|}$, hence the kinked steps imaginary extend 50% of the distance of an atomic row in the understep region. W here is larger than its analogous in close-packed Pt steps (3.2 Å, see Section 3.2), illustrating how the kinked steps have a larger effect on the lower terraces as compared to the straight arrays.

The evolution of the CO anchored at the kinks with α [$\Theta_S(\alpha)$] can be fitted to Equation 2.3 to yield the product $W \cdot \Theta_S^0$. Since we know W, we can easily extract Θ_S^0. By multiplying Θ_S^0 by $W/a_{\|}$ (see Subsection 2.1.1), a value of 1.1 CO molecules per kinked row was obtained. This roughly indicates that most of the kinked edge atoms are covered by CO, mimicking Ni(100) vicinals [231]. This means that the step coverage in kinks is remarkably higher than that of other A- and B-type surfaces [67, 186, 187].

With this information, we suggest the CO saturation structure around kinked arrays shown in Figure 4.4g) to highlight the large step CO coverage. No evidence of ordered CO structures is observed in the LEED (Appendix C1). In our proposed structure, CO sticks to all kinked atoms to create a coverage of one molecule per Pt kinked atom. Additionally, CO adsorbs in T_T sites near the kinks and blocks the T_B positions, hence explaining the stronger decay with α of T_B-CO rather than T_T-CO. Since the CO density is larger at the kinks as compared to the terraces, this allows to counterbalance the decay with α of terrace-CO coverage with the growth of kink-CO, which results in the minute increase of the total coverage with α. CO molecules would be slightly displaced from pure S_T sites in order to decrease the intermolecular repulsion of closely packed adsorbates, resembling the $c(4\times2)$-4CO structure developed at terraces [see black dashed lines in Figure 4.4g)]. Note that there is no occupation of S_B sites at the kinks.

Both $\Theta_T(\alpha)$ and $\Theta_S(\alpha)$ fit well to the W-model at $\alpha < 18°$, yet at higher α the linear change does not hold anymore. Note that the model assumes that the local coverage of steps and terraces does not change with the step density. This may be incorrect at highly stepped vicinal surfaces, such as the (312) plane (2-atom-wide terraces) where steps are close to each other and step-step and intermolecular interactions intensify. Although step doubling was not observed by LEED, the change in slope at $\alpha > 18°$ may also be a signature of *disordered* diatomic steps [188].

4.1.4 O 1s α-scan after O_2 saturation

To end with the UHV characterization of the k-Pt(645) sample, we exposed the crystal to O_2 in order to investigate the O chemisorption and Pt oxidation. The following experiments were performed at room temperature, since adsorption of residual gases was observed at 90 K temperature (see Appendix C4). The fitting procedure is detailed in Appendix C.

The O 1s spectrum after dosing 50 L O_2 at the (111) plane depicted in the top panel of Figure 4.5a). It contains a single, asymmetric peak at 529.7 eV, which corresponds to chemisorbed atomic O in fcc hollow sites (ChemO) [118]. ChemO is likely arranged in a 0.25 ML, $p(2\times2)$-O superstructure [52, 73], since low pressure doses of O_2 at room temperature are not sufficient for developing denser oxygen phases in Pt(111) (see Subsection 1.3.2). Therefore, we used the spectrum at the (111) plane for coverage calibration.

We also probed the (645) and (312) planes following the O_2 dose [middle and bottom panels of Figure 4.5a)]. The peak observed at 529.7 eV at the (111) plane shifts towards 529.6 and 529.5 eV at the (645) and (312) surfaces, respectively and grows with the kink density. At the (111) plane, this feature corresponds to ChemO, i.e. O adsorbed in the hollow fcc position *at terraces*, therefore it should reduce its intensity with the kink density. Instead, we observe its growth and a shift towards lower binding energy with α. This suggests the existence of an unresolved O species at the kinks, possibly at hollow sites near the kinked edge due to its similar binding energy. Therefore, we postulate that the feature ChemO corresponds to O anchored in hollow sites at terraces and kink sites. O adsorption at kinks is very efficient [68, 111], hence explaining the increase of ChemO with α. However, we must not discard O adsorption in bridge sites at the {100} microfacet [222], for which a peak around 530 eV was reported [40, 130, 223].

Two new small contributions appear at 528.8 and 530.7 eV after the O_2 dosage at the stepped surfaces. They are bigger on the densely stepped (312) plane rather than at the intermediate (645) surface, reflecting their step nature. On one side, the peak at 530.7 eV ("Oxide") is possibly the 1D oxide reported by Wang *et al.* at Pt(332) [96], although more experiments are needed to confirm this. On the other side, the feature at 528.8 eV (O_K) corresponds to chemisorbed O at kinks. As mentioned above, adsorption in hollow sites at terraces and bridge sites at the {100} microfacet are not alike, since they should exhibit a peak at around 530 eV. Therefore, the remaining alternative is O adsorption at the four-fold square sites at the {100} microfacet of the steps. The transition from three-fold to four-fold increases the O coordination, hence a significant shift towards lower binding energy is expected [239], further supporting our assessment.

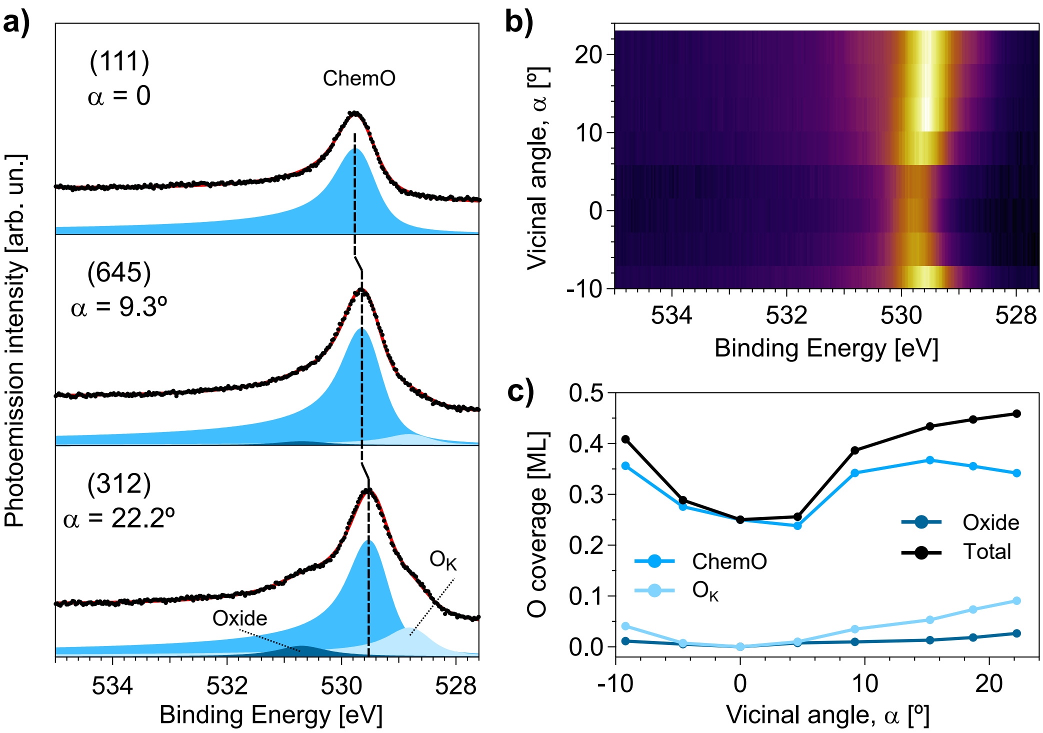

Figure 4.5: O 1*s* α-scan after dosing 50 L O_2 at 300 K.
a) Selected fitted spectra at the (111), (645) and (312) surfaces, respectively. They were extracted from the O 1*s* α-scan shown in **b)**, acquired after an O_2 dose of 50 L. **c)** Coverage variation as a function of α for the individual and total O species, extracted from the fit of all spectra shown in b). ChemO, Oxide and O_K denote hollow chemisorbed O, a step oxide and chemisorbed O at the kinked edges, possibly at square sites. Experiments were carried out at a photon energy of 650 eV at 300 K.

Individual spectra of the α-scan [Figures 4.5b)] were fitted to obtain the evolution of each of the peaks with α, as shown in Figure 4.5c). ChemO is the only contribution at $\alpha = 0$, while both O_K and Oxide steadily grow at $|\alpha| > 0$. As a combination of terrace and step species, ChemO features a complex behaviour that results in a coverage plateau at $\alpha > 10°$, since the growth and decay of the step and terrace components counterbalance each other. Mimicking O chemisorption experiments on Pt(332) [96], almost the double amount of O was observed at $\alpha = 22°$ if compared to the (111) plane, which could translate into a different catalytic activity. Faceting was observed for the “fully” kinked Pt(201) plane [145] and close-packed Pt(997) [102] after O_2 exposure, hence we should not discard such effect here. LEED investigations could not be carried out to confirm such a faceting.

4.2 CO oxidation at kinked vicinal surfaces

After the investigation of the CO and O_2 chemisorption on kinked surfaces presented earlier, we next explore the CO oxidation reaction on such surfaces in the mbar range. The experiments discussed below have been carried our at Lund University (Sweden, PLIF) and at NSLS-II synchrotron (USA, NAP-XPS). Following previous guidelines, a detailed description of the experimental procedures is presented in Appendix C.

4.2.1 Simultaneous ignition of kinked vicinal surfaces

Similarly as before, we first explore the CO ignition with PLIF to simultaneously check for possible asymmetries in the ligth-off across the sample. Such technique is described in Section 2.3. We exposed the sample to a total flow and pressure of 100 ml/min and 150 mbar, respectively, with a gas ratio of 4:4:92 CO:O_2:Ar. The results are shown in Figure 4.6. The temperature was increased from 510 to 680 K during 400 s (heating slope of 25.5 K/min).

Figure 4.6a) shows PLIF images at different temperatures under the gas mixture described above. Almost no $CO_{2(g)}$ production is observed at 600 K (bottom panel), since the surface is in the poisoned stage and tentatively covered by CO. However, a sizeable $CO_{2(g)}$ cloud appears at 638 K (middle panel), which indicates that the reaction is slowly initiating. The surface transitions towards the active stage around 640 K simultaneously across the curved surface. As seen in the top panel of Figure 4.6a), the whole surface is active at 643 K. Mimicking the close-packed steps (Chapter 3), Pt kinked vicinals ignite at the same time as the (111) plane. Furthermore, we performed additional PLIF experiments not included in this Thesis on another curved Pt with the (331) at the center. This crystal allows to compare B-type vicinals from the (111) plane ($\alpha = 0$) up to the (110) surface ($\alpha = 35.3°$). Surprisingly, the same symmetric CO ignition was observed in this crystal. Therefore, we postulate that the ignition of Pt vicinals does not depend significantly on the step density. Again such a behaviour contrasts with the Pd case, where B-steps ignite earlier than its A-type analogous [203].

We also monitored the CO_2 using a Quadrupole Mass Spectrometer (QMS) located in the outlet of the chamber. It mimics the behaviour described above: there is no CO_2 turnover at low temperature (570 K), until the CO_2 production explodes around 635 K. We must note two effects here. One may have noticed that the CO_2 signal in the QMS ignites around 5 K earlier than in PLIF. This is caused by an error in the interpolation of the temperature for each of the PLIF images which we did not correct here.

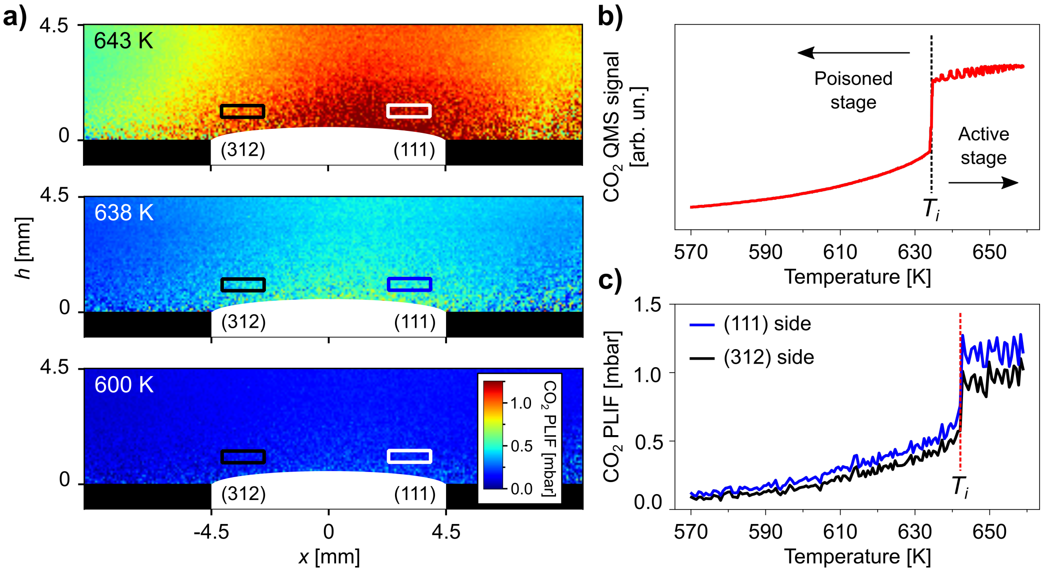

Figure 4.6: PLIF measurements acquired under a 1:1 CO:O$_2$ ratio. **a)** PLIF snapshots at the indicated temperatures under a 4:4:92 CO:O$_2$:Ar gas mixture. The total flow and pressure were 100 ml/min and 150 mbar, respectively, while the heating slope was 25.5 K/min. **b)** CO$_2$ signal (mass 44) in the QMS located in the exhaust. **c)** CO$_2$ PLIF signal at the (111) plane (blue and white rectangles) and (312) surface (black rectangle) positions of the k-Pt(645) crystal, as extracted from the integration of the rectangles shown in a). The dashed lines in b,c) indicate the ignition temperature T_i.

It is worth to mention that we noticed oscillations in the CO$_2$ QMS signal right after the ignition of the reaction. Oscillations of the surface composition have been observed before in Pt [44, 115], hence they seem an appropriate explanation of the behavior observed in the CO$_2$ QMS signal. There could be also a malfunction of the experimental setup, but it is unlikely since the oscillations were only observed just after the light-off.

The integrated intensities above the positions of the (111) and (312) surfaces are shown in Figure 4.6c). The ignition occurs at 640 K simultaneously at both sides, confirming the symmetric ignition of the CO oxidation at Pt vicinals. However, the CO$_2$ production is slightly larger at the (111) side than at the (312) position. This could be expected, since CO anchored at terraces is reported to react faster with O than its analogous at steps and kinks [136–139]. In addition, Pt(557) is known to ignite at a slightly higher temperature than Pt(111) [47], although such an earlier light-off was not observed in our experiments (see Chapter 3). Additional measurements are planned to further investigate this phenomenon, since the laser was not stable enough and hence the data quality is not optimal for such faint differences.

4.2.2 CO oxidation hysteresis cycles

After exploring the ignition of the CO oxidation by PLIF, NAP-XPS experiments will be discussed. We focus now on the evolution of surface species, namely graphitic carbon ("C"), chemisorbed CO (ChemCO) and O-species (O/Pt) as function of the temperature at different surfaces, namely the (111), (645) and (735) planes with $\alpha = 0$, 9.3 and 18.1°, respectively. We will properly analyze the evolution of individual step and terrace species during the CO oxidation in the next sections and focus now on the nature of the ignition. Example spectra during the heating ramp are shown in Appendix C5.

The clean k-Pt(645) sample was exposed to a 0.7 mbar, 1:1 $CO:O_2$ gas mixture at 300 K. We increased the temperature to 400 K in order to speed up the experiment, and then we subsequently heated in 10 K steps while monitoring the aforementioned planes at each temperature. A variety of peaks are rapidly detected in both the O 1s and C 1s regions, as shown in Figure 4.7. Contributions related to ChemCO appear around 531-532.5 and 286-287 eV [24, 38], together with a complex feature at 284 eV related to different graphitic "C" species [132, 240]. Furthermore, the gas phase contributions of CO (290.2 and 536.7 eV) and O_2 (537.2 and 538.8 eV) are perceived [38]. No CO_2 production is observed, neither in the XPS nor the QMS located in the second pumping stage of the analyzer [45].

Additional heating of the crystal caused a slight but noticeable decrease of the ChemCO peaks, accompanied by a remarkable increase of the "C" component around 284 eV. This illustrates how some of the CO starts to dissociate (or crack) on the surface due to the relatively high temperature and intense photon beam. This appears to be more pronounced at the (645) plane, where the amount of "C" is largest. The "C" peaks continue to smoothly grow until they suddenly start to vanish at 450 K at the stepped surfaces, while one more heating step (460 K) was required to remove it from the (111) plane. The amount of "C" on the surface depends on both the CO dissociation and the "C" oxidation. If we compare two different surfaces with the same reactivity towards "C" burning but a different CO dissociation rate, the surface with a faster CO cracking will have a bigger amount of "C". If the CO dissociation is similar for these two imaginary surfaces, the one with a faster "C" oxidation rate will have less "C", since it will be consumed faster. The terraces are less active towards the CO cracking [46], hence if the "C" stays longer on the (111) plane this may indicate that the steps are more active towards the "C" burning [46].

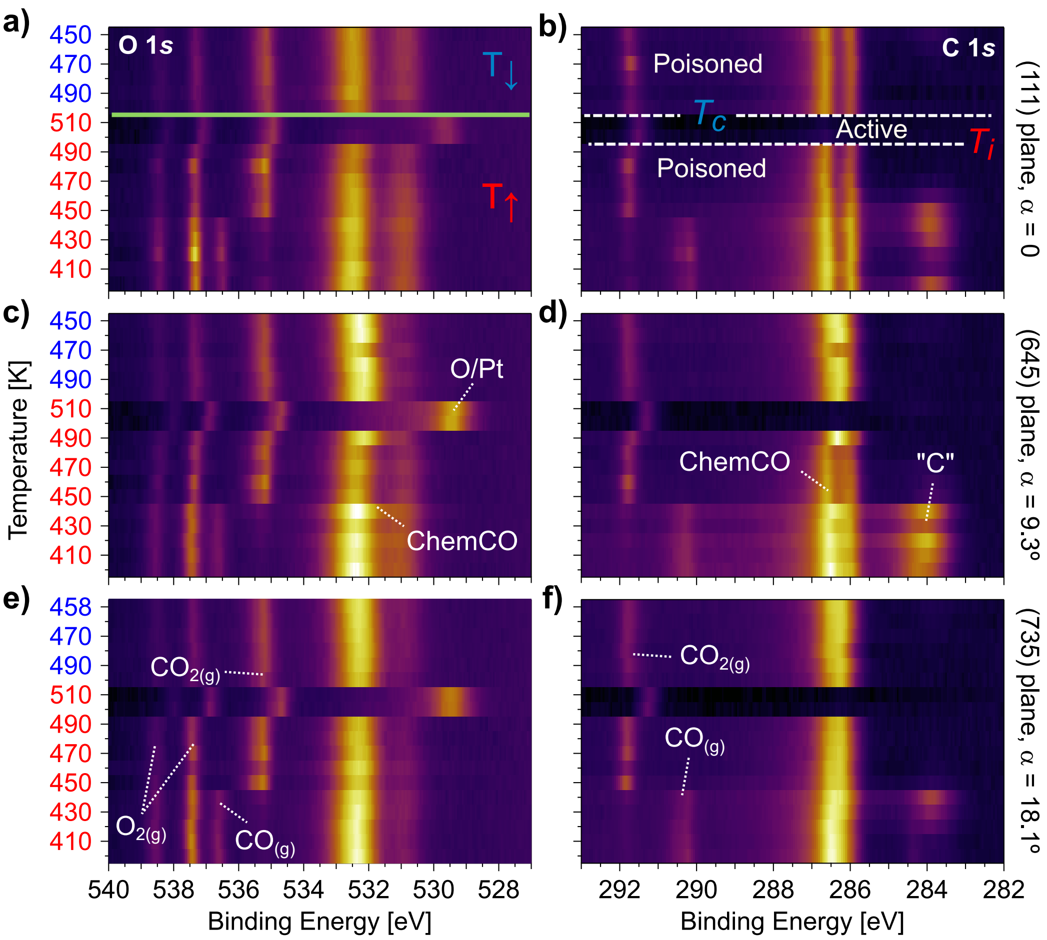

Figure 4.7: Temperature ramps at relevant surfaces.
O 1*s* (left column) and C 1*s* (right column) intensity color plots as a function of sample temperature at the **a,b)** (111), **c,d)** (645) and **e,f)** (735) planes, respectively. Red temperature labels indicate heating, while blue ones designate cooling. The green solid line in a) separates the heating ($T_{\uparrow}$) from the cooling ($T_{\downarrow}$) cycles. T_i and T_c refer to the ignition and cooling of the CO oxidation, whereas O/Pt, ChemCO and “C” stand for oxygen-Pt species, chemisorbed CO and graphitic carbon on the surface, respectively. The spectra were acquired at a photon energy of 650 eV under a 0.7 mbar, 1:1 CO:O_2 gas mixture. The average heating and cooling slope were 13 and -9 K/h, respectively

At a slightly higher temperature than that of the “C” burning, the signal from $CO_{(g)}$ completely disappears in both the XPS and the RGA (not shown). In addition, a new contribution ascribed to $CO_{2(g)}$ arises at 535.2 and 291.6 eV in the O 1s and C 1s, revealing a significant CO_2 production. ChemCO is still observed on the surface, pointing towards the fact that it is not the sample that is active but the Pt filament that was used to heat the sample. This filament is at higher temperatures as compared to the sample, hence it will ignite and consume CO and O_2 before the ignition of the k-Pt(645) sample. This situation will be further discussed in Appendix C.

Further heating of the sample after the “C” burning ($T > 460$ K) yields a considerable decrease of the ChemCO signal in the three surfaces. We continued to increase the temperature in 10 K steps, and once the temperature was raised to 500 K, all ChemCO vanished on the three surfaces. Only the $CO_{2(g)}$ contribution was observed in the C 1s region. This illustrates how the ignition of the CO oxidation is simultaneous in kinked Pt vicinal surfaces, mimicking the the PLIF experiments discussed above and the A- and B-type Pt vicinals (see Chapter 3). Therefore, the ligth-off at these conditions occurs at $T_i = 500$ K disregarding the kink density up to $\alpha = 18.1°$.

A closer look to the O 1s region after ignition reveals new O species (O/Pt in Figure 4.7) at the three different planes. It is easily seen that these O/Pt species are larger at the kinked surfaces rather than at the (111) plane, although we shall discuss the nature of the active stage in Subsection 4.2.6. It is noteworthy that all detected gas phase peaks shifted around 0.35 eV towards lower binding energies after the ligth-off of the reaction. This is caused by a different work-function of the surfaces during the poisoned (CO-covered) and active (O-covered) stages of the CO oxidation [38, 40].

To end with, the surface was also cooled in order to study the quenching of the CO oxidation. The (111), (645) and (753) planes were monitored while subsequently decreasing the temperature also in 10 K steps. All probed surfaces were found to deactivate at the same time right after decreasing the temperature to 500 K, establishing $T_i = T_c = 500$ K. Although T_i and T_c are usually separated in O_2-rich conditions (see Appendix B2), this difference appears to be small for a 1:1 CO:O_2 gas ratio mixture. One should take into account that the Pt filament used for heating is altering the CO:O_2 ratio, and also that the temperature step is relatively big (10 K).

It is noteworthy that the spectrum at 490 K for the (645) surface does not seem to follow the tendency observed in any other heating ramp presented throughout this Thesis. The significant increase of the ChemCO intensity at both the O 1s and C 1s exclusively at the (645) plane only at 490 K is more likely an artifact related to a miss-positioning on a scratch on the sample, rather than a real feature.

4.2.3 Poisoned stage: C 1*s* temperature evolution

We have established that the CO ignition is simultaneous at all investigated kinked Pt vicinals. We will now study the CO-poisoning layer across these surfaces. The results discussed below are very similar to those of the A- and B-type Pt vicinals (see Section 3.2), hence they will be only briefly discussed. Peak fitting and coverage calibration are explained in Appendix C.

To begin with, the k-Pt(645) sample was exposed to 0.1 mbar CO at 300 K to characterize the CO adsorption at higher pressures. The full α-scan is shown in Figure 4.8a). Under the aforementioned conditions Pt(111) is know to develop a $(\sqrt{19} \times \sqrt{19})$R23.4°-13CO superstructure ("$\sqrt{19}$-13CO") composed of 7 Terrace-Top (T_T) and 6 Terrace-Bridge (T_B) CO molecules [24]. This structure is defined by two main peaks ascribed to CO adsorbed at T_T (286.6 eV) and T_B (286.0 eV) sites, as shown in Figure 4.8d) and as reported by Toyoshima *et al.* [24]. An additional feature was found at 287.2 eV, which is attributed to locally denser T_T molecules (T_T*) [67]. Its area was added to that of T_T for the coverage calculations. Furthermore, small peaks attributed to CO molecules in the gas phase $CO_{(g)}$ are located at 290.1 eV. The emissions in the 283.5-284.5 eV region are ascribed to different graphitic "C" species adsorbed on the surface [241]. Their evolution with temperature and α is described in Appendix C7 to ease the text here.

We show in Figure 4.8d) the photoemission spectra at the kinked (645) and (312) surfaces at NAP conditions with only 0.1 mbar CO at room temperature. As discussed in Section 4.1, the new component at 286.3 eV is attributed CO adsorbed atop Pt kinked atoms (Step-Top, S_T). As expected, S_T grows while T_B, T_T (and hence T_T*) decay at larger α, as the step density is higher and the terraces narrow.

Next, the clean sample was exposed to a 0.5 mbar, 1:1 CO:O_2 gas mixture at 300 K. No CO_2 production was observed at this temperature, hence we increased the temperature to vacate surface sites and start the reaction. Different α-scans of the poisoned stage were acquired at 430 and 490 K, namely far from and close to the CO ignition. Individual CO species evolve with α as described for the 0.1 mbar CO reference experiment, therefore a further discussion is not necessary.

The progress of the (111) surface is shown in the top panels of Figures 4.8d-f). When the surface is exposed to 0.1 mbar CO at room temperature, the $\sqrt{19}$-13CO structure develops and the surface occupancy reaches its maximum coverage. However, after adding O_2 to the gas mixture and heat, the CO adsorbed at both T_T and T_B sites starts to decrease, and CO desorption takes place. This behaviour was already observed for c-Pt(111) sample of Section 3.2, hence it shall not be discussed in further detail again.

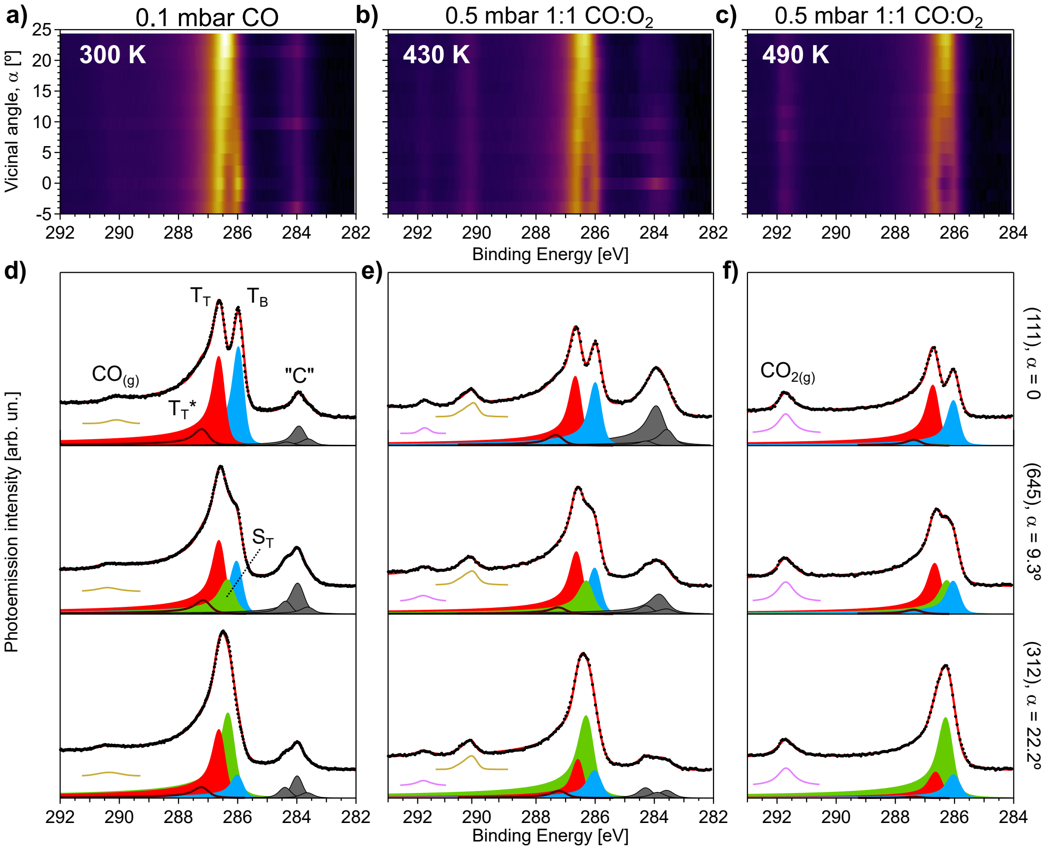

Figure 4.8: C 1*s* region evolution prior to the CO ignition. **a-c)** C 1*s* α-scans of a completely poisoned surface at 300 K (0.1 mbar CO only), and low activity but still poisoned surfaces at 430 and 490 K (1:1 CO:O$_2$), respectively. **d-f)** Selected fitted spectra at the (111), (645) and (312) surfaces at the top, middle and bottom rows, respectively. T$_T$, T$_B$, T$_T$* stand for Terrace-Top, Terrace-Bridge and locally denser Terrace-Top CO chemisorbed molecules, whereas "C" refers to graphitic carbon on the surface. The measurements were acquired at a photon energy of 650 eV.

The different spectra acquired at the (645) and (312) planes under reaction conditions are depicted in the middle and bottom panels of Figures 4.8d-f), respectively. As mentioned already, at 430 K the Terrace-CO contribution at these surfaces has decrease at 430 K as compared to the data acquired at 0.1 mbar CO at room temperature for both surfaces. This effect is even stronger at 490 K, since CO anchored at terraces progressively desorbs. However, the CO adsorbed at S$_T$ sites remains on the surface. Therefore, and mimicking close-packed Pt surfaces explored in Chapter 3, the kinks remain CO-saturated while the terraces are progressively depleted of CO until the simultaneous CO ignition across kinked Pt vicinals.

4.2.4 Poisoned stage: O 1*s* temperature evolution

Similarly to close-packed Pt vicinals, the terraces become CO-depleted while the CO anchored at kinks remains mostly unaltered prior to the CO ignition. We now explore the O 1*s* in order to check for additional O species that may arise during the simultaneous CO ignition. These O 1*s* measurements were acquired right after the C 1*s* presented in the previous region, hence the experimental conditions are the same. We have discussed in Appendix C3 how PhotoElectron Diffraction (PED) effects make it difficult to analyze the O 1*s* region in a quantitative way. Therefore the C 1*s* region is more suitable to properly inspect the CO chemisorption. However, we must rely on the O 1*s* in order to directly detect additional O species, such as subsurface oxygen (O_{Subs}). Peak fitting and coverage calibration are detailed in Appendix C.

As discussed in Section 3.3, we suggest that O_{Subs} causes the simultaneous ignition of CO adsorbed at terraces and steps. We shall briefly analyze the CO species before exploring the existence of O_{Subs}. During the CO chemisorption experiment [0.1 mbar CO, 300 K, Figures 4.9a,d)], features related to CO adsorbed at T_T and T_B sites are detected at 532.6 and 530.9 eV at the (111) surface [52]. A comparison with the spectra at the (645) and (312) planes reveals a steady decrease of T_B-CO, since the terraces narrow as α increases. This behaviour is exactly the same as observed for the C 1*s* spectra. In parallel, the peak at 532.6 eV progressively shifts towards lower binding energy. This is illustrated in Figures 4.9d), and it is related to the emission of CO adsorbed at S_T positions, which appears at slightly lower binding energy than T_T-CO [63]. We are not able to separate the peaks related to CO anchored at T_T and S_T sites, since their energy is quite similar and they are significantly wide. We hence considered a single feature (T_T+S_T) away from the (111) surface to ease the fitting procedure. (T_T+S_T) increases with the step density, since (*i*) PED effects arise and (*ii*) the decay with α of CO adsorbed at T_T sites is counterbalanced by the growth S_T-CO. A small contribution of $CO_{(g)}$ is detected around 536.5 eV [38, 40].

The sample was then exposed to reaction conditions (pressure of 0.5 mbar, 1:1 CO:O_2 gas ratio mixture) and heated to 430 K. In addition to the contribution of $CO_{(g)}$ at 536.5 eV, we may also easily detect a doublet related to $O_{2(g)}$ (537.4 and 538.5 eV) [38], since both CO and O_2 were introduced into the chamber. A closer look to the XPS gas phase features of the α-scans acquired at 430 K [and also at 490 K, see Figures 4.9b,c)] reveals subtle shifts on the peak position, which are ascribed to the different work-functions of each of the vicinal surfaces [206].

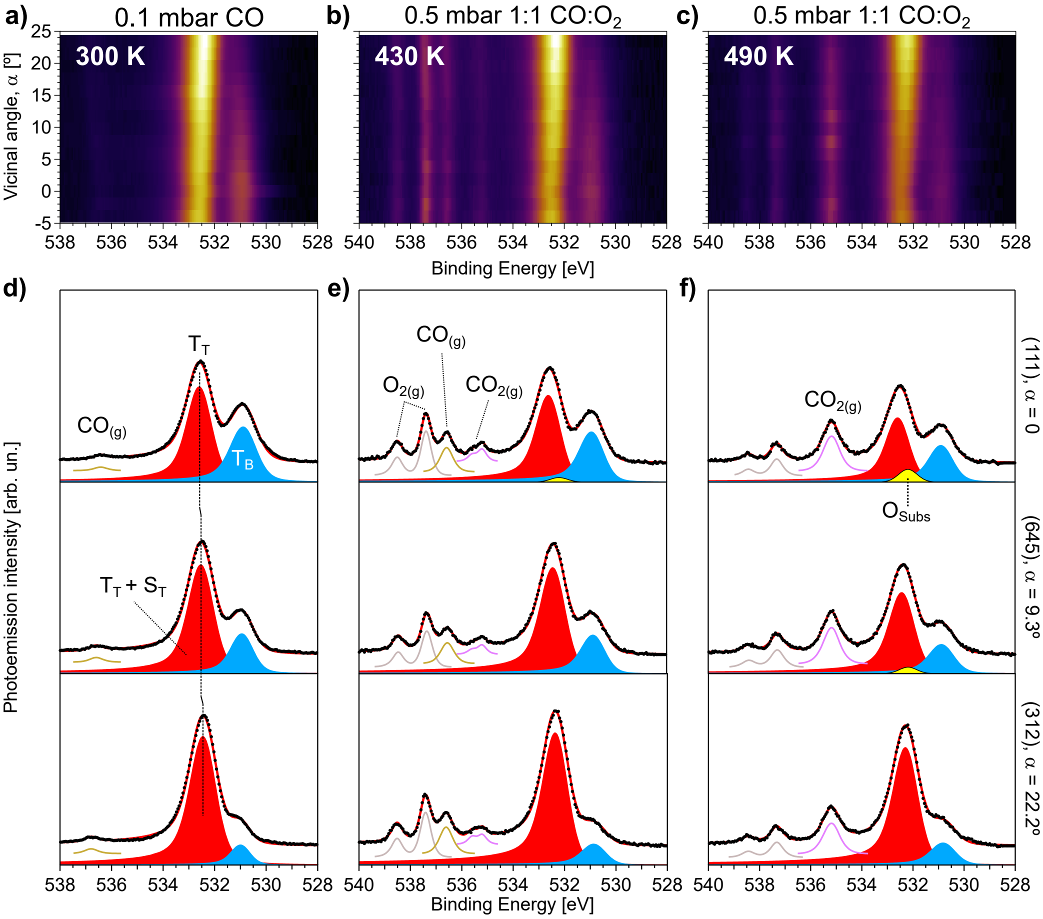

Figure 4.9: O 1*s* α-scans during the poisoned stage.
a-c) O 1*s* α-scans during exposure to 0.1 mbar CO (reference experiment) at 300 K, and during reaction conditions (pressure of 0.5 mbar, 1:1 CO:O_2 gas ratio, still poisoned surface) at 430 and 490 K, respectively. Selected fitted spectra at relevant surfaces, namely the (111), (645) and (312) planes, are shown in **d-f)** at the indicated conditions. T_T, T_B, S_T stand for CO adsorbed in Terrace-Top, Terrace-Bridge and Step-Top sites, while O_{Subs} refers to subsurface oxygen. All spectra were acquired at 650 eV.

A comparison of the spectra at the (111) at 300 K (0.1 mbar CO) and at 430 K (0.5 mbar, 1:1 CO:O_2 gas ratio mixture) reveals that CO adsorbed at terraces starts to leave the surface. This effect is stronger if we consider the spectra acquired at 490 K. However, the decrease of the O 1*s* peaks with the temperature is less marked for the (645) and (312) planes. The situation is again similar as that extracted from the analysis of the C 1*s* region: CO anchored at steps does not leave the surface until right before ignition, and even in that case their decrease is minute.

Even though we are still in the poisoned stage, at 430 K it is already possible to distinguish the peak associated to gas phase $CO_{2(g)}$ (535 eV) [40]. We cannot rule out a low CO_2 production from the sample itself. Nevertheless, we attribute most of the $CO_{2(g)}$ production to the Pt filament used for heating. As discussed in Appendix C, this Pt filament consumes a fraction of both $CO_{(g)}$ and $O_{2(g)}$ to yield $CO_{2(g)}$, hence the small $CO_{2(g)}$ build up prior to the sample ignition. As the temperature (and additionally the time) increases, the Pt filament produces more $CO_{2(g)}$ and accordingly its signal grows. In parallel, that of the $O_{2(g)}$ decays significantly and $CO_{(g)}$ vanishes. Due to the low pumping speed of the set up, the produced $CO_{2(g)}$ is not pumped away quickly, and in parallel both the consumed $CO_{(g)}$ and $O_{2(g)}$ are not introduced as fast as consumed. This explains the significant growth of the $CO_{2(g)}$ and the decay of $CO_{(g)}$ and $O_{2(g)}$ with temperature and time.

Both the O 1s and C 1s regions reflect that terraces are depleted of CO prior to the simultaneous ignition of stepped and flat surfaces. Within this scenario, O_2 molecules can dissociatively adsorb on the terraces and form additional oxygen species. Although no clear signature of ChemO is found around 530 eV [30, 118], the existence of O_{Subs} (532.1 eV) at the (111) surface can be detected. The peak exhibited by CO adsorbed at T_T sites (532.6 eV) will shift towards lower binding energy as O_{Subs} accumulates, hence we can use this displacement to track O_{Subs}. The shift of the peak at 532.6 eV is better seen during experiments with higher O_2 content, although it is difficult to notice if the partial O_2 pressure decreases (see Appendix C5). This may indicate that at lower $O_{2(g)}$ pressures less O incorporates below the surface, as one would expect. If the position of T_T-CO is constrained and no O_{Subs} is introduced in the line fitting routine, its outcome is not satisfactory.

As a comment, we performed a CO desorption cycle in UHV conditions at a CO-saturated (111) plane. As shown in Appendix C2, the peak ascribed to CO adsorbed at T_T sites does not shift during the desorption cycle. This indicates that its change in position during reaction conditions as the CO ignition approaches is tentatively related to the CO oxidation process itself.

In order to properly extract the O_{Subs} contribution at the (111) surface, the position of the emission of CO molecules adsorbed at T_T sites in the O 1s was determined from the reference spectra taken at room temperature under reaction conditions shown in Appendix C6. At 300 K, the surface is covered by a dense CO layer [24] that quenches the O_2 adsorption [58], so no O_{Subs} should exist. Hence, we can constrain the position of T_T-CO at higher temperatures to be the same as that of 300 K. The fitting procedures then requires an additional emission at 532.1 eV (O_{Subs}), as done for the c-Pt(111) experiment in Chapter 3. We extracted the photoemission intensity of O_{Subs} by applying this routine to the spectra at different temperatures.

Applying the method described above yields a small O_{Subs} peak at the (111) surface at 430 K, which significantly increases once the sample is further heated to 490 K [see Figures 4.9e-f)]. This is the expected: the terraces become partially CO-depleted and more O can incorporate under the surface. Nonetheless, the existence of O_{Subs} can only be measured properly at the (111) plane. The T_T-CO peak at the stepped surfaces is observed to shift towards the position of S_T-CO (532.3 eV) at increasing temperature, as T_T-CO (532.6 eV) will smoothly desorb while S_T-CO remains on the surface. Therefore, it is challenging to distinguish whether this shift occurs due to the growth of O_{Subs} or the desorption of T_T-CO at the vicinal planes. In order to roughly derive O_{Subs} from the fitting, we extracted the position of (T_T+S_T) at each α from the scan acquired under 0.1 mbar CO at 300 K while keeping O_{Subs} at 532.1 eV. A small shift (±50 meV) was allowed to enhance the fit and account for the desorption of CO adsorbed at T_T sites. A progressive shift of (T_T+S_T) towards lower binding energy with α is observed, since the binding energy of S_T-CO is lower than T_T-CO. A significant decay of O_{Subs} was observed as the step density increases, matching our previous observations and confirming that the feature at 532.1 eV is anchored at the terraces (see Section 3.4).

Although no O_{Subs} was found at the (645) plane at 430 K during reaction conditions, a significant amount was perceived at 490 K. This is expected, since the CO from the terraces desorbs and allows for more oxygen to incorporate below the surface. Nevertheless, no O_{Subs} was observed at any temperature at the densely stepped (312) surface, since O_{Subs} corresponds to oxygen below the terraces, and those of the (312) plane are extremely narrow. For increasing step densities it becomes specially difficult to extract O_{Subs} from O 1*s* spectra, since the (T_T+S_T) feature significantly increases with α due to PED effects (see Appendix C3).

4.2.5 Chemical species during the poisoned stage

The evolution of CO species (terrace, step and total) and subsurface oxygen O_{Subs} at different temperatures and α is sketched in in Figure 4.10. The coverages were extracted from the systematic fit of the α-scans undertaken at 0.1 mbar CO at 300 K, and at 430, 460 and 490 K under reaction conditions (pressure of 0.5 mbar, 1:1 CO:O_2 gas ratio). The α-scan at 460 K was not shown in Figure 4.10. The C 1*s* was used for the quantification of CO species, while the analysis of O_{Subs} was deduced entirely from the analysis of the O 1*s* region. Details on the coverage calibration are given in Appendix C.

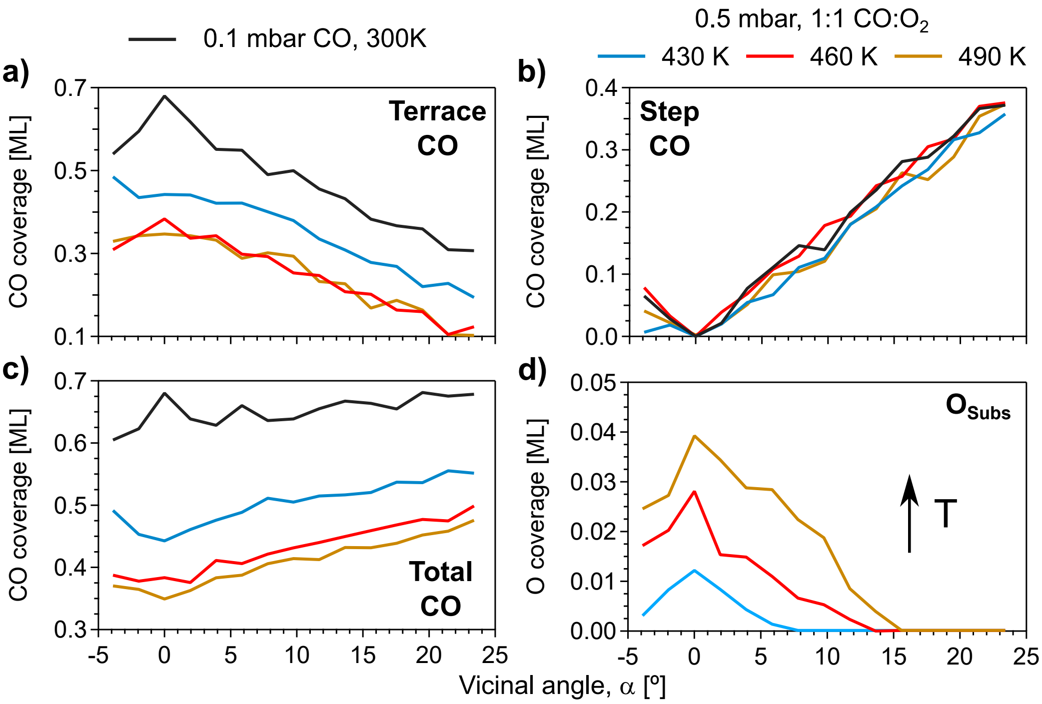

Figure 4.10: Evolution of species during the poisoned stage. **a)** Terrace-CO, **b)** Step-CO, **c)** Total-CO (Terrace+Step) and **d)** O_{Subs} as a function of α at the different conditions indicated in the Figure. These α-scans are shown in Figures 4.8 and 4.9, with the exception of that of 460 K. Coverages of a-c) were obtained from the C 1*s*, although O_{Subs} was derived from the O 1*s*.

The evolution of Terrace-CO (T_T+T_B) with the step density under the different experimental conditions described above is shown in Figure 4.10a). The maximum Terrace-CO coverage is achieved at the (111) surface at 0.1 mbar CO and 300 K, corresponding to the $\sqrt{19}$-13CO, 0.68 ML superstructure [24, 58]. As expected, it rapidly decays as α increases, since the terraces narrow. The NAP Terrace-CO coverage exceeds that observed at UHV saturation (Subsection 4.1.3), reflecting that higher CO pressures can produce larger *terrace* coverages than those achieved under UHV conditions. The same was observed for the c-Rh(111) sample (Chapter 5). Once the sample is submitted to reaction conditions (pressure of 0.5 mbar, 1:1 CO:O_2 gas mixture) and increased temperatures, the expected decay in the overall amount of Terrace-CO is observed. Surprisingly, there is no significant change between 460 and 490 K in the Terrace-CO coverage evolution as a function of α, indicating that the surface may be close to light-off.

The progress of Step-CO with α and temperature is shown in Figure 4.10b). As expected, the amount of CO anchored at steps increases with α, i.e. the step density. As pointed out before, it is clear that within experimental errors, there is no significant change in the Step-CO with the temperature. This confirms that the CO ignition on kinked Pt surfaces also proceeds via the desorption of Terrace-CO while the steps remain saturated. This resembles the situation observed for A- and B-type Pt steps discussed in Chapter 3. In addition, the Step-CO coverages are quite similar to those obtained after exposure to 10 L CO, as shown in Subsection 4.1.3. This proves that only the steps retain the saturation coverage from UHV to NAP, as we proposed earlier. It also indicates that poisoning at the steps is too strong in the present Pt case, and contradicts the usual believe that vicinal surfaces are more reactive compared to high symmetry planes.

The evolution of the Total-CO coverage with temperature and α is depicted in Figure 4.10c). Kinks remain CO-saturated while Terrace-CO progressive desorbs, hence the overall amount of adsorbed CO decays at larger temperatures around the (111) plane. However, it grows with α at higher temperatures since CO does not desorb from the densely-coadsorbed kinks until the ignition is close.

The progress of O_{Subs} at the different conditions mentioned above is shown in Figure 4.10d). Note that no O_{Subs} is observed in the 0.1 mbar CO experiment, since no O_2 was introduced in the chamber. It is clearly seen that O_{Subs} incorporates below the terraces, since it follows a similar decay as Terrace-CO with α. Hence, O_{Subs} accommodates under the terraces in both close-packed (Section 3.4) and kinked Pt vicinals. Its intensity increases with the temperature, since more CO desorbs from the terraces, allowing O to incorporate underneath these CO-depleted terraces. Accordingly, no O_{Subs} is detected at $\alpha > 7°$ at 430 K, but it is detected up to $\alpha = 13°$ and $\alpha = 15°$ at 460 and 490 K, respectively. This reveals that narrower terraces can also accommodate O_{Subs} once the CO adsorbed on them gets reduced.

Since we observed no breaks in the Terrace-CO coverage curve as a function of α, we suggest that no apparent step doubling occurs at the kinked surfaces. One would maybe expect higher tendency of kinked arrays to form double steps, but the coverage curves shown in Figure 4.10 do not suggest such a scenario. One reason for this possible lack of step doubling could be the CO:O_2 ratio, since A-and B-type Pt vicinal surfaces are know to form double steps if the O_2 content of the gas mixture is rich [144]. In our case the gas mixture is just slightly O_2-rich, which may quench the doubling of the steps. Nonetheless, additional experiments are mandatory to further investigate the geometric structure of the kinked Pt surfaces.

4.2.6 Active stage across kinked surfaces

We will now discuss the chemical species found above the ignition, i.e. during the active stage of the CO oxidation. We did not detect any significant peaks in the C 1*s* region during the active stage with the exception of $CO_{2(g)}$. However, new contributions appear in the O 1*s* region. The aim of this Section is to investigate these O-related species at steps and terraces. Details on the peak fitting and coverage calibration are given in Appendix C.

First, the sample was exposed to 0.4 mbar O_2 at 300 K to characterize the bare Pt oxidation at kinked surfaces. In Figure 4.11a) we show the O 1*s* spectra at the (111), (645), (423) and (312) planes. Similarly to the UHV experiments of Subsection 4.1.4, the main contribution at the (111) surface is an asymmetric peak at 529.8 eV, which is ascribed to chemisorbed O in fcc hollow sites (ChemO) [55]. Furthermore, another two smaller contributions are detected. The feature located at 530.5 eV is attributed to the 1D oxide stripes reported by Miller *et al.* [30]. A similar peak was observed in the UHV experiment carried out after a 50 L O_2 dose (saturation), which was attributed to a similar 1D oxide. In that case, however, this peak was associated to a step feature [96], since it increased with α. The fact that we observe it now at the (111) plane at high O_2 pressure reflects how the chemical species in UHV and NAP may differ. This situation again reinforces the need of catalytic studies conducted at (or near) *operando* conditions. The peak at 532.5 eV observed at the (111) slightly grows with the step density while shifting towards the position of surface oxide clusters reported by Held *et al.* in Pt(531) (532.2 eV) [114], indicating that both species could be similar. The shift with the step density may be related, e.g., to similar Pt oxides at terraces and steps. Another possibility are changes in the strain of the surface, as was reported for CO adsorbed on Pt vicinal surfaces [207]. We will later discuss the nature of this feature.

The spectra taken at the (645) and (312) surfaces during the O_2 exposure are shown in the middle and bottom panels of Figure 4.11b). ChemO rises in both spectra, more markedly on the densely stepped (312) plane, while shifting towards lower binding energy at larger step density. As we discussed earlier, this reflects that ChemO is a combination of step and terrace hollow species, unresolved in the spectrum. The feature at 530.5 eV also increases with α, confirming how this component is favoured at the steps [96]. No shift in the position was observed. As discussed in Subsection 4.1.4, the peak at 528.4 eV in both spectra is possibly related to oxygen chemisorbed at square sites at the kinked arrays, hence the name O_K.

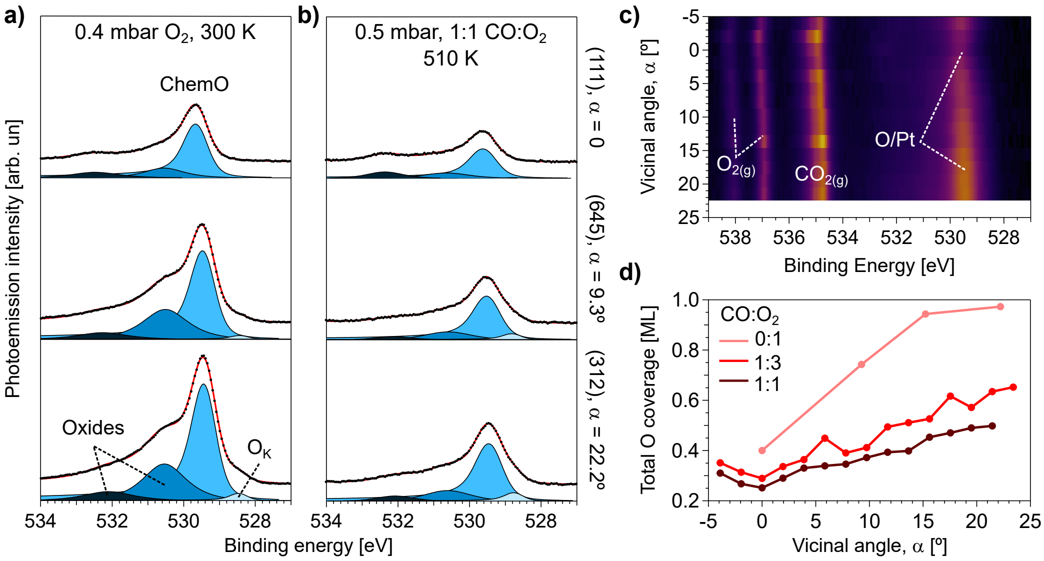

Figure 4.11: O $1s$ evolution across the oxidized k-Pt(645) surface. Individual O $1s$ fitted spectra for **a)** a reference experiment acquired in 0.4 mbar O_2 at 300 K and **b)** during the active stage of the CO oxidation at 510 K (total pressure of 0.5 mbar, 1:1 CO:O_2 gas ratio). The complete α-scan at the latter conditions is shown in **c)**, including the gas phase peaks that where excluded for cleanliness in a) and b). **d)** Total oxygen coverage at different conditions. 0:1 and 1:1 corresponds to the conditions of a) and b), respectively, while 1:3 corresponds to a different α-scan of the active stage of the CO oxidation acquired at a pressure of 0.5 mbar and 1:3 CO:O_2 gas ratio (see Appendix C8). ChemO and O_K stand for chemisorbed O at hollow fcc positions (at terraces and kinks) and square sites (exclusively at kinks). Oxides refer to uncharacterized Pt oxides. The measurements were acquired at a photon energy of 650 eV.

After the analysis of the reference experiment with O_2 only, in the following we will discuss the chemical species observed during the active stage of the CO oxidation. Starting from the experiment in the previous Section (poisoned stage in a 1:1 CO:O_2 gas mixture at 0.5 mbar of total pressure), we further heated the sample until we observed the ignition at 510 K. Afterwards, the k-Pt(645) sample was scanned following the α-scan approach. The α-scan at 1:1 CO:O_2 ratio conditions is shown in Figures 4.11b,c), while another α-scan of the active stage acquired in 1:3 CO:O_2 ratio conditions is illustrated in Appendix C8. The chemical species are the same as those observed at the reference experiment with O_2. The exception is the emission at 532.2 eV that behaves differently. We will discuss its nature with the step density at both α-scans at the end of this Section.

At reaction conditions, both ChemO and the oxide at 530.5 eV have decreased substantially as compared to the reference experiment carried out with pure O_2. A possible explanation for this would be connected to a higher reactivity of both species species as compared to O_K and the other oxide ($\approx$ 532 eV). The intensity of O_K is larger compared to the O_2 reference experiment. Our interpretation for this observation is the following: The dense O phase at the steps (530.5 eV) is reduced by impinging CO molecules. Then some of the remaining oxygen atoms from the steps can come back to a lower oxidation state (less dense phase) such as O_K, causing the observed O_K intensity to increase.

The peak around 532.5 eV increases at the (645) plane if compared to the (111) surface, and then decreases at the (312) plane. This is a rather complex behaviour, and it is possibly related to the existence of different Pt oxide species at terraces and steps that we cannot resolve. The peak also shifts with the step density towards lower biding energy (0.4 eV), further supporting this hypothesis. This behaviour is different as compared to the reference experiment, where a clear growth of the oxygen peak intensity with the step density is observed. Nevertheless, it is difficult to further delve into the characteristics of this species without any structural analysis. Our photoemission data cannot provide more information about this oxide. Its binding energy above 532 eV resembles the O_{Subs} species discussed earlier. Another possibility would be that the uncharacterized oxide is indeed a surface oxide similar to that described by Held and coworkers [114]. In addition, we have observed a small amount of CO in the C $1s$ region. Since CO adsorbed at top sites at terraces and steps exhibit photoemission peaks at similar energies, the peak that we observe at this energy may in fact be a combination of different CO and Pt oxides species at both terraces and steps. Further experiments would be required to provide a better assessment.

To end with, we sketch the total oxygen coverage at the different O-covered surfaces in Figure 4.11d), namely the reference experiment (0.4 mbar O_2, 300 K) and the α-scans of the active stage of the reaction at 1:1 (0.5 mbar, 510 K) and 1:3 (0.5 mbar, 470 K, see Appendix C8) CO:O_2 gas ratio. The maximum amount of O is found during the experiment with only O_2, and then the total O coverage decreases with increasing CO partial pressure. This is the expected, since a larger amount of CO reduces the oxygen species. In addition, the amount of O increases significantly with the step density in the three different sets of experiments. This is also expected, since Pt steps are known to enhance the O chemisorption and Pt oxidation [96].

Summary of the k-Pt(645) experiments

The CO oxidation on kinked Pt vicinal surfaces up to $\alpha = 28°$ has been discussed in this Chapter. First of all, CO and O_2 chemisorption experiments were performed under UHV conditions in order to fully characterize the chemical species and adsorption sites at this rather unexplored family of Pt surfaces. Afterwards, PLIF and NAP-XPS measurements were conducted at millibar pressures. We aimed at exploring possible differences in the ignition of the CO oxidation reaction between kinked and flat surfaces, and also at studying the different chemical species at steps and terraces during the poisoned and active stage of the aforementioned reaction.

To begin with, UHV experiments suggest a high CO coverage of the kinked arrays after saturation. Such a scenario of densely CO-covered kinks causes the overall CO coverage to slightly increase with the step density. This contradicts the reports regarding close-packed vicinals of other late transition metals, such as Pt, Pd and Rh, where the coverage decreases with α. Furthermore, due to the excellent quality of the XPS data, two different top step CO species were detected at the vicinal surfaces, corresponding to CO adsorbed in the first and second atomic rows of the kinked step. CO molecules on kinks mimic those at A- and B-type steps, uptake and desorption experiments confirm that the adsorption energy of CO is larger at the steps, since CO binds preferentially to them in the low coverage regime and desorbs from terraces prior to kinks as the surfaces are heated.

Concerning the O_2 adsorption, no oxide formation was detected on the (111) plane, since the only observed feature was related to the well characterized $p(2\times2)$-O structure formed by chemisorbed oxygen in the hollow fcc position at terraces. Nonetheless, new chemical species were found at the kinked vicinal surfaces, ascribed to three- and four-fold chemisorbed O at the kinks, together with a minor amount of an oxide located at the kinked edges, most likely similar to the 1D oxide stripes observed in close-packed Pt steps. In addition, the total oxygen coverage largely increases with the kink density, again similarly as their analogous A- and B-type straight steps.

Both PLIF and NAP-XPS experiments on the CO oxidation revealed that all facets of the k-Pt(645) crystal ignite at the same temperature, mirroring the simultaneous light-off observed for the A- and B-type vicinals of the c-Pt(111) sample discussed in the previous chapter. Furthermore, NAP-XPS data unveils a similar ignition process: while the step arrays remain CO-saturated prior to the CO light-off, the terraces progressively become CO-depleted as the temperature increases. This permits some O_2 to dissociatively adsorb on the terraces and accumulate below the surface, forming a subsurface O complex (O_{Subs}) that we believe causes the simultaneous ignition of both flat terraces and steps. Through α-scans we evaluated the evolution of O_{Subs} with α. We confirmed that O_{Subs} is anchored below the (111) terraces, since it markedly decays with the step density. As the ignition approaches, more O_{Subs} accumulates below the terraces and it is observed at larger step densities, since the CO-depletion is stronger at the vicinal surfaces as the ignition approaches.

Once the surface is active and the CO_2 production reaches its maximum, O species dominate the O 1*s* spectra. Only a scarce amount of CO is observed in the C 1*s* region. Resembling UHV experiments, the amount of oxygen markedly increases with the step density and the terraces become narrower. Similar oxygen species are found on the surface, in addition to a new uncharacterized oxide. We carried out experiments at different CO:O_2 ratios. The maximum O coverage was observed during a reference experiment with O_2 only. The oxygen coverage decreases for increasing CO in the gas mixture. In addition, the minimum O coverage was observed at the (111) plane, significantly growing with the step density.

Chapter 5

CO oxidation on Rh(111) vicinals with A- and B-steps

In this Chapter we will describe a set of CO oxidation experiments using a Rh curved crystal [c-Rh(111)]. As shown in Figure 2.4, the sample features the (111) surface at the center of the crystal, and an increasing density of steps at either A- or B-type close-packed vicinals as one departs from the center. A- and B-stepped surfaces up to the (223) and (553) planes are available across the curved surface of this crystal, featuring {100}- and {111}-oriented microfacets and $\alpha = +11.4°$ and $-12.3°$, respectively.

5.1 UHV studies on the CO chemisorption

We first explored the CO adsorption in UHV conditions, in order to have a proper reference for the characterization of the CO poisoning layer during the CO oxidation experiments. We already published these results in Ref. [186]. The experimental procedures and the characterization of the clean surface are described in detail in Appendices C and D1, respectively.

5.1.1 CO uptake experiments at selected surfaces

The CO adsorption sequence was explored at different Rh planes at room temperature. Namely, we probed the (111), (223) and (553) planes, which feature flat terraces, A- and B-type close-packed steps, respectively. Separate uptake experiments were performed at the aforementioned surfaces, as shown in Figure 5.1. Larger CO doses were not required to evaluate the adsorption hierarchy, hence the experiments were stopped after exposure to 1 L CO in order to minimize the CO cracking.

To begin with, we dosed $1{\cdot}10^{-9}$ mbar CO into the chamber while probing the well-documented (111) plane. The full uptake experiment is shown in Figure 5.1b). Right after dosing the CO [Figure 5.1e)], a single peak at 286.0 eV is readily observed, which we attribute to CO adsorbed at top positions of Rh atoms at the terraces (Terrace-Top, T_T). Another peak develops at 285.4 eV at larger CO exposures, ascribed to CO anchored at terrace hollow sites (Terrace-Hollow, T_H) [148, 151]. A satellite arising from vibrational excitations of T_T can be detected [236]. We did not perceive vibrational contributions related to CO adsorbed at T_H sites or at the steps. In Figure 5.1h) we show the full uptake experiment at the (111) plane. The CO occupation at T_H positions is significantly smaller than at T_T sites at the end of the uptake experiment. The evolution of both species as a function of CO exposure reveals that while CO anchored at T_T sites has reached almost saturation, CO chemisorbed in T_H positions is still increasing. Therefore, one would expect that the $(\sqrt{3} \times \sqrt{3})\mathrm{R}30^\circ$ structure adopted by T_T-CO is saturated at the end of the uptake experiment. Our experimental findings agree with previous reports on the CO chemisorption on Rh(111) [148, 151].

The same uptake experiments were carried out at the (223) and (553) planes, as shown in Figures 5.1a,c). A new common peak rises at 285.7 eV at the low exposure regime [Figures 5.1d,f)], which is ascribed to CO adsorbed on top sites at the step edge (Step-Top, S_T) [152, 155]. The emission from CO adsorbed at S_T sites is the first peak that emerges at the (223) surface, while at the (553) both S_T and T_T peaks start to develop from the beginning. The scenario at the (223) surface mirrors that of close-packed stepped surfaces of Pt, Pd or Ni, where the adsorption of CO at the step edges is preferential at low coverage [67, 63, 187, 207, 231, 242]. The evolution of individual CO species for both surfaces is shown in Figures 5.1g,i). The population at S_T sites readily saturates at around 0.3 L CO in both surfaces, while T_T-CO does not reach saturation at the end of the uptake experiments. CO adsorption at T_T sites continues to steadily grow during the experiment, yet slower than at the (111) plane, since the terraces are narrower.

CO sticks at the aforementioned T_H sites (285.4 eV) faster and at lower CO exposures at the (223) plane as compared to the (111) and (553) surfaces. Surprisingly, the photoemission intensity at this binding energy after the 1 L CO dose is larger compared to the (111) surface. This reveals that an additional step species may contribute to the emission at 285.4 eV, since the intensity of terrace species should decrease with the step density. In fact, CO adsorption at bridge positions at the steps (Step-Bridge, S_B) was observed previously on Rh(553) at a similar energy [152]. This suggests that this peak is a combination of CO anchored at T_H and S_B sites at the stepped planes. Accordingly, we relabelled such feature as (T_H+S_B) at the vicinal surfaces.

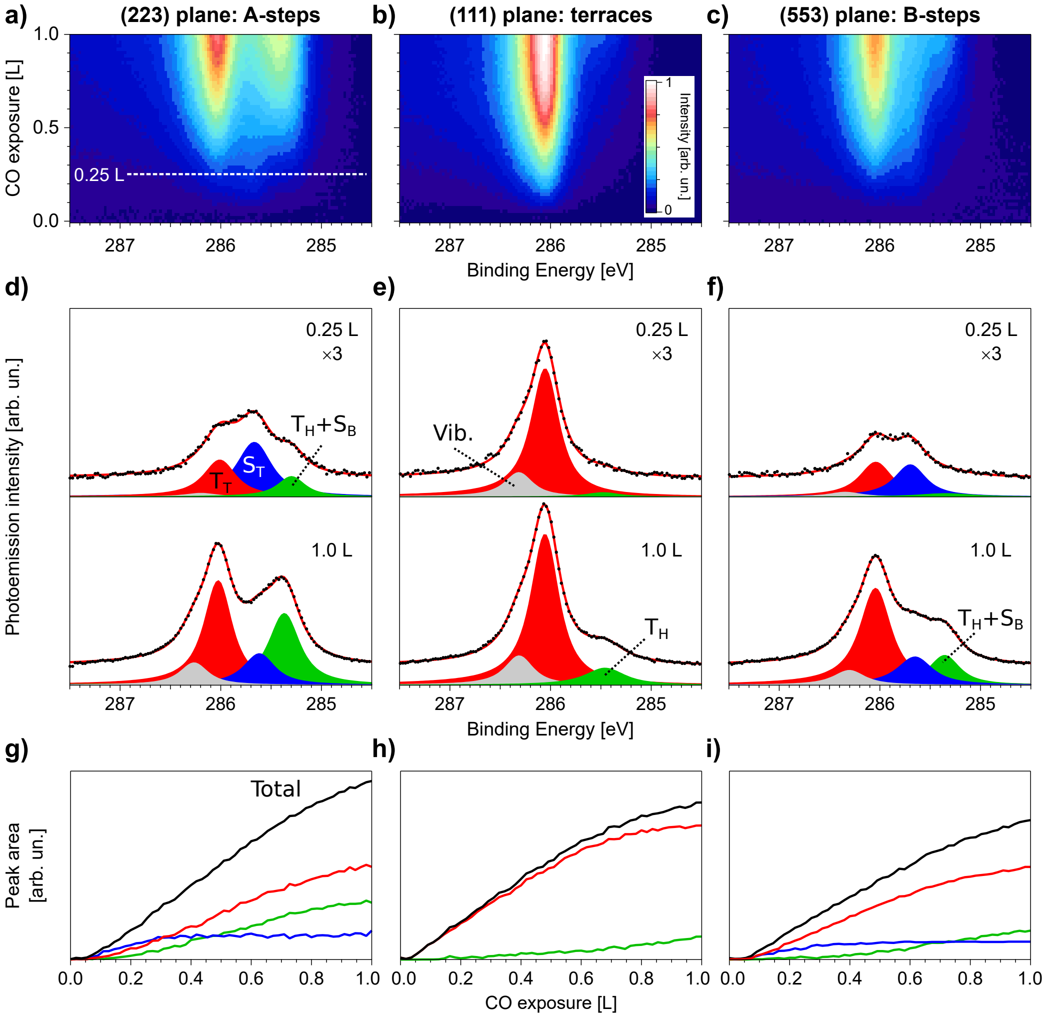

Figure 5.1: CO uptake experiments at relevant Rh surfaces. **a-c)** C 1*s* intensity color plots for separate CO uptake experiments acquired at the (223), (111) and (553) surfaces, respectively. These were performed under $1{\cdot}10^{-9}$ mbar CO during 1330 s. **d-f)** Selected spectra after dosing 0.25 L CO (top) and 1.0 L CO (bottom), together with their corresponding fits. **g-i)** Peak area evolution of CO species as a function of the CO exposure, as extracted from the systematic fit of all spectrum shown in a-c). $\mathrm{T_T}$, $\mathrm{T_H}$, $\mathrm{S_T}$, and $\mathrm{S_B}$ stand for CO adsorbed in Terrace-Top, Terrace-Bridge, Step-Top and Step-Bridge sites, being the black solid lines of j-l) the total sum of each of the aforementioned components. The photoemission experiments were acquired at 300 K using a photon energy of 390 eV.

The CO adsorption sequence can be derived as follow: $\mathrm{S_T}\rightarrow\mathrm{T_T}\rightarrow(\mathrm{S_B}+\mathrm{T_H})$. Although adsorption in $\mathrm{S_B}$ sites is preferred over $\mathrm{T_H}$ [152, 155], we cannot confirm this with our experiments. The total CO area after the 1 L CO dose is illustrated with black lines in Figure 5.1g-i). Even though the adsorption is preferential at the stepped edges, the intensity is larger on the (111) surface as compared to the stepped planes at the low exposure regime (< 0.5 L CO). However, the CO intensity follows the (223)>(111)>(553) sequence at the end of the experiment. The coverage conversion is not straightforward due to PhotoElectron Diffraction effects (PED, see Appendix D) and unresolved features in the spectra, hence it was excluded from this analysis.

5.1.2 Scan of the unsaturated curved surface

In a different set of experiments, and in order to delve into the CO chemisorption at stepped surfaces, we acquired an α-scan across the curved surface after exposing the clean sample to 1 L CO [Figure 5.2a)]. Selected fitted spectra for relevant surfaces are shown in Figure 5.2b).

The evolution of individual species across the curved surface shown in Figure 5.2c) better illustrates the behaviour of the CO adsorption at steps and terraces. The maximum amount of CO adsorbed at $\mathrm{T_T}$ sites is observed at $\alpha = 0$ [i.e. (111) plane], since the terraces are largest there. The average terrace width decreases as the step density increases, hence $\mathrm{T_T}$-CO decays with α. For the same reason, CO chemisorption in $\mathrm{S_T}$ positions is almost negligible at the (111) surface, and then grows with α. The $(\mathrm{T_H} + \mathrm{S_B})$ peak features a more complex behaviour, as it is a combination of terrace and step species. Its intensity at the (111) plane corresponds entirely to CO anchored to $\mathrm{T_H}$ sites, although its rise with the step density is caused by the emission of $\mathrm{S_B}$-CO, which counterbalances the decay of $\mathrm{T_H}$-CO. Furthermore, PED effects may arise [148, 151], making an exact analysis challenging. As noted before, both $\mathrm{S_T}$ and $(\mathrm{T_H}+\mathrm{S_B})$ are slightly larger at the A-side of the crystal, revealing a more efficient chemisorption at these vicinals.

After converting the photoemission intensity to coverage (see Appendix D), we applied the W-model described in Subsection 2.1.1 to the coverage evolution of each of the CO adsorption sites with the step density. However, we cannot distinguish CO adsorbed at $\mathrm{T_H}$ and $\mathrm{S_B}$ sites. Therefore, in order to obtain the effective step size W we supposed that only the evolution of $\mathrm{T_T}$-CO with α $[\Theta_{T_T}(\alpha)]$ contributes to the terrace-CO coverage variation with α $[\Theta_T(\alpha)]$. Small errors around the (111) plane may arise, since $\Theta_T(\alpha)$ corresponds to $\Theta_{T_T}(\alpha)+\Theta_{T_H}(\alpha)$. However, CO adsorption in $\mathrm{T_H}$ positions is likely to decrease dramatically with the step density [187]. Therefore, $\Theta_{T_H}(\alpha)$ will be negligible at large α, hence $\Theta_{T_T}(\alpha) \approx \Theta_T(\alpha)$.

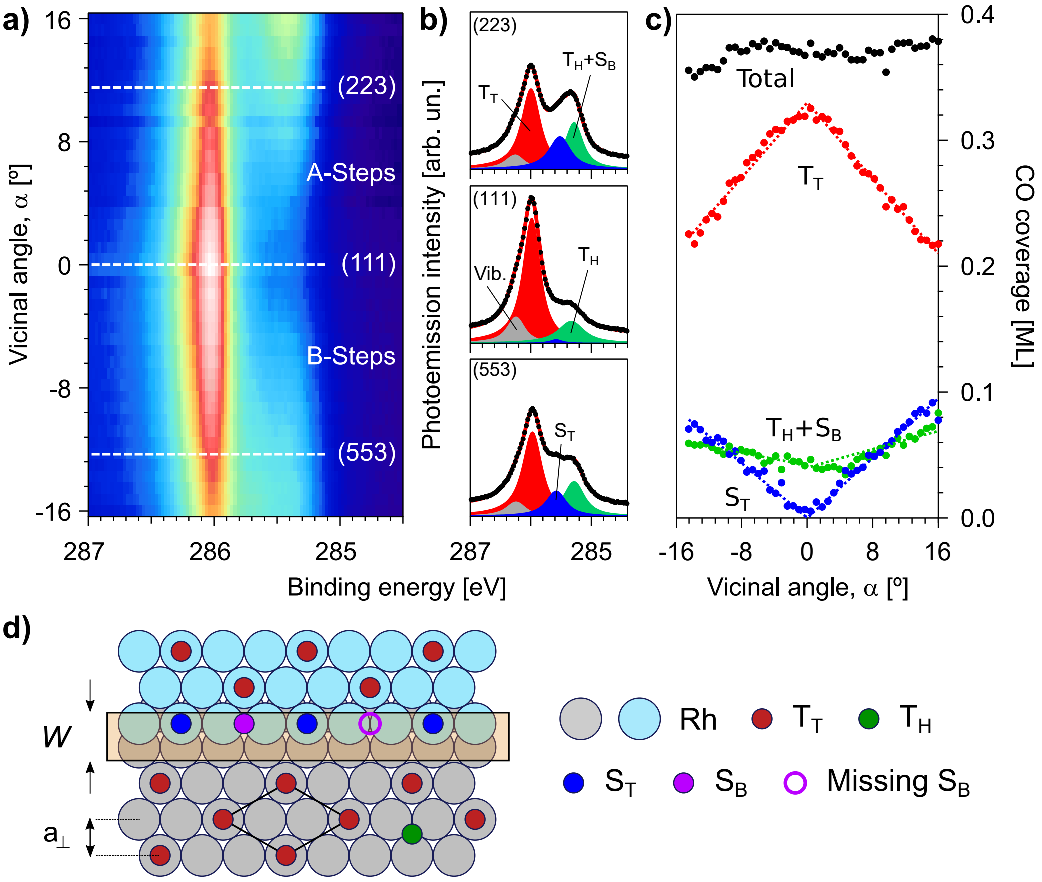

Figure 5.2: C 1s α-scan after dosing 1 L CO.
a) C 1s intensity map across the c-Rh(111) curved surface after a 1 L CO dose at 300 K, with **b)** fitted spectra at relevant surfaces. **c)** Coverage variation of individual and total CO species as a function of α. Dotted lines represent the fit to the W-model described in Appendix D. **d)** CO adsorption model at the low CO dose on an A-type close-packed step, as deduced from the coverage analysis presented in the main text. W (2.85 Å) and $a_\perp$ (2.34 Å) in d) stand for the effective step size and the distance between atomic rows in Rh(111), respectively, while the solid black line represents the $(\sqrt{3}\times\sqrt{3})$R30° superstructure developed by CO molecules anchored at T_T positions at low coverage [148, 151]. The photoemission experiments were acquired using a photon energy of 390 eV.

If we assume that $\Theta_{T_T}(\alpha) \approx \Theta_T(\alpha)$, we can put the latter into Equation 2.2 in order to derive the effective step width W, resulting in $W = 2.9$ Å for both step types. A comparison with the width of an atomic row in Rh close-packed vicinals ($a_\perp$, 2.34 Å) reveals that the effective step size only extends approximately 1/5 of an atomic row into the understep region of the lower terraces, which remain CO-depleted [Figure 5.2d)]. Θ^0_T can also be extracted from this fit. Since we supposed $\Theta_{T_T}(\alpha) \approx \Theta_T(\alpha)$, in this particular case $\Theta^0_{T_T} = \Theta^0_T$. $\Theta^0_{T_T}$, corresponding to the $\mathrm{T_T}$-CO coverage at the (111) plane. We determined a value close to 1/3 ML, indicating that $\mathrm{T_T}$-CO molecules form the $(\sqrt{3} \times \sqrt{3})$R30° superstructure [148, 151].

Fitting the variation of $\mathrm{S_T}$-CO with α [$\Theta_{S_T}(\alpha)$, see Figure 5.2c)] to Equation 2.3 yields the product $W \cdot \Theta^0_{S_T}$. Since we know W, we can derive $\Theta^0_{S_T}$, the $\mathrm{S_T}$-CO coverage at the W-region. As we discussed in Subsection 2.1.1, multiplying $\Theta^0_{S_T}$ by $W/a_\perp$ allows to extract the number of CO molecules per step row. A value of $\approx 1/3$ CO molecules per step row for both A- and B-steps is obtained, hence CO molecules are anchored to $\mathrm{S_T}$ sites in 1 out of 3 Rh step atoms.

Finally, the ($\mathrm{T_H}$+$\mathrm{S_B}$) feature is a combination of terrace and step species. Since we cannot resolve the individual features, we fit its evolution with α to Equation D1, which accounts for both $\Theta_{S_B}(\alpha)$ and $\Theta_{T_H}(\alpha)$ at the same time. Since $\Theta^0_{T_H}$ equals to the coverage of a fully flat surface, we can extract its value (0.04 ML) from the coverage of CO anchored at $\mathrm{T_H}$ sites at the (111) plane, where $\alpha = 0$. The only variable left to fit is then $\Theta^0_{S_B}$, from which values of 0.18 and 0.13 CO molecules per step row are obtained for the A- and B-type steps after the conversion. This value is roughly 1/6, revealing that 1 out 6 of the Rh step atoms are covered by CO molecules in $\mathrm{S_B}$ sites, half of those at $\mathrm{S_T}$ positions. Therefore, approximately half of the step atoms are occupied by CO molecules in $\mathrm{S_T}$ and $\mathrm{S_B}$ sites $(1/3 + 1/6 = 1/2)$ *before CO saturation*. As discussed in Appendix D, a correction factor was applied to the ($\mathrm{T_H}$+$\mathrm{S_B}$) peak, hence the coverage of $\mathrm{S_B}$-CO may be underestimated.

Following the guides described above, we propose the model sketched in Figure 5.2d) for CO-covered Rh stepped surfaces with 1 L dose, near saturation. As discussed previously, the (111) terraces feature $(\sqrt{3}\times\sqrt{3})$R30° domains of $\mathrm{T_T}$, and the CO at $\mathrm{T_H}$ positions is residual. At the step edges, 1/3 of the atoms are covered by CO molecules located in $\mathrm{S_T}$ geometry, while only 1 out of 2 available $\mathrm{S_B}$ sites may also be occupied by CO.

5.1.3 CO saturation and dissociation

In order to explore the CO saturation, we monitored the C 1*s* region at the (111), (223) and (553) surfaces after dosing 0.25, 1 and 12 L CO, as shown in Figure 5.3a). A closer look to the spectra of the (111) plane shows no change between the 1 and 12 L CO dose for T_T-CO (286.0 eV). As discussed in the literature, the formation of the (2×2)-3CO saturation superstructure requires the coverage of T_T sites to decrease (from 1/3 to 1/4 ML), hence there are no direct signs of the formation of the (2×2)-3CO arrangement [148, 151]. However, CO anchored at T_H sites (285.4 eV) significantly grows after the 12 L dose. A total coverage of 0.57 ML (0.33 ML T_T + 0.24 ML T_H) is obtained at 300 K from the fit of the (111) plane spectra, matching the Rh(111) CO saturation at 300 K coverage reported by Beutler *et al.* [151]. We propose an intermediate stage at terraces between the (2×2)-3CO and the $(\sqrt{3} \times \sqrt{3})$R30°-CO superstructures, as sketched in Figure 5.3b). At this relatively high CO coverage, CO molecules will start to populate T_H sites in addition to T_T positions. However, the XPS reveals that the 0.33 ML of T_T-CO are retained. Hence, we suggest that the population of T_H sites causes the displacement of some CO molecules anchored at T_T sites towards the position of the (2×2) lattice, but maintaining the 1/3 ML of T_T-CO.

For both stepped surfaces, the feature (T_H+S_B) around 285.5 eV is the only one that increases significantly after the 12 L CO dose. For the (223) plane, coverage values of 0.24, 0.12 and 0.07 ML are obtained for CO adsorbed at T_T, (T_H+S_B) and S_T positions, respectively. However, the coverages for the (553) surface of T_T and (T_H+S_B) sites increase to 0.31 and 0.19 ML, while that of S_T decreases to 0.05 ML. Mimicking the dissimilarities reported for A- and B-type Pt vicinals [67], we attribute these asymmetries to the particular configuration of {100} and {111} microfacets.

A model for the CO chemisorption in Rh(223) is proposed in Figure 5.3b). As derived in Subsection 5.1.2, there is one S_T-CO per three Rh atoms. This leaves 2 out of 3 Rh step atoms free and room for only one S_B-CO molecule to adsorb between these Rh atoms. *Before CO saturation*, only 1 out of 2 of these S_B sites was covered by CO (see Figure 5.2), hence it is reasonable to suppose that both sites are covered *after saturation*. This corresponds to 1 S_B-CO molecule per 3 Rh step atoms, yielding a CO saturation coverage of 2/3 ML per step row (1/3 ML S_T-CO + 1/3 ML S_B-CO). Nevertheless, it appears than the ratio of S_B-CO per S_T-CO is larger at the (553) surface at saturation, since the coverage of S_T-CO is slightly smaller as compared to the (223) plane. Other stepped surfaces, such as Pd(111) vicinals and Pt(553), feature 0.5 ML of CO molecules per step row, while this coverage can increase to 1 at Ni(100) vicinals [63, 187, 231]

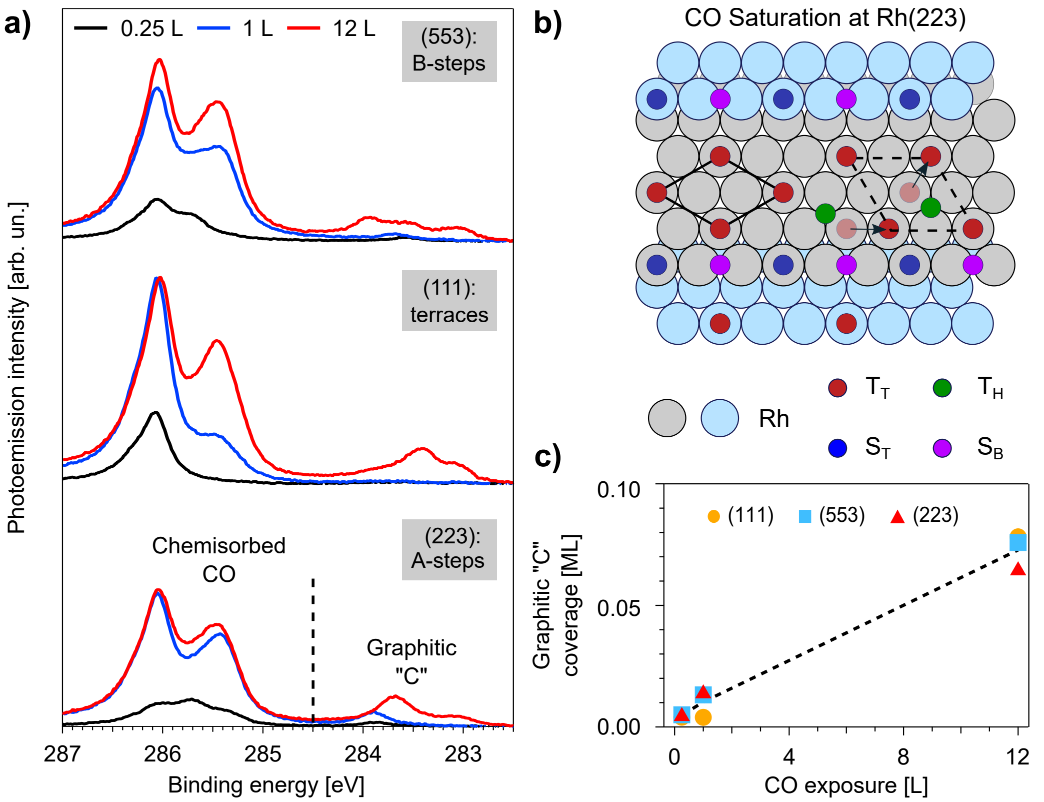

Figure 5.3: C 1*s* evolution at increasing CO dose.
a) Individual spectra at the (553), (111) and (223) surfaces at the low (0.25 L, black), intermediate (1 L, blue) and saturation (12 L, red) CO doses. **b)** Rh(223) CO saturation model at 300 K, as derived from the coverage analysis. As sketched in the dashed black rhombus, T_H molecules are added within the $(\sqrt{3} \times \sqrt{3})R30^\circ$ unit cell (solid black rhombus), increasing the terrace coverage by forming (2×2)-3CO domains. T_T, T_H, S_T, and S_B designate CO anchored to Terrace-Top, Terrace-Bridge, Step-Top and Step-Bridge sites, respectively. **c)** Graphitic carbon ("C") coverage at the three CO doses at each of the surfaces, extracted from the fits of the spectra shown a). A linear fit is included to illustrate the dependence on the CO dose.

To end with, different graphitic carbon species ("C") are observed around 284 eV in Figure 5.3a). Our findings agree with previous experiments [152, 156, 195, 243, 244], and contradict others [148, 151, 236, 245]. However, there is no apparent step-enhanced CO dissociation, since the total "C" coverage shown in Figure 5.3c), is similar at the three surfaces. Therefore, our data suggest that the total amount of "C" does not depend on the step density, as claimed elsewhere [246, 247], but on the total CO exposure. Likely, the CO cracking is determined by factors external to the sample, such as the photon beam or residual hydrocarbons of the chamber.

5.2 CO oxidation on close-packed Rh vicinals

After studying the CO species at flat and stepped Rh surfaces, we can now explore the CO oxidation under NAP conditions with an adequate reference. Additionally, and mimicking the case of Pt, we employed PLIF measurements to study the ignition of the CO oxidation, and NAP-XPS experiments to investigate the chemical species at the different stages of the reaction. Most of the experiments were performed at NSLS-II synchrotron (New York, USA), although complementary measurements were carried also out at ALBA synchrotron (Barcelona, Spain). Details on the experimental procedures and analysis are again given in Appendix D.

5.2.1 Asymmetric ignition of Rh vicinals

As a first approach, we performed PLIF measurements (see Section 2.3) on the c-Rh(111) sample, since we can simultaneously probe the CO_2 production across the whole curved sample and easily detect asymmetries on the ignition [203]. We exposed the clean c-Rh(111) sample to a 4:4:92 CO:O_2:Ar gas mixture, reaching a total flow and pressure of 100 ml/min and 150 mbar, respectively. Subsequently, the sample was heated while continuously recording PLIF images. No CO_2 PLIF signal is observed at low temperature, since the sample is covered/poisoned by CO [bottom panel of Figure 5.4a), 520 K]. The CO_2 signal observed in the Quadrupole Mass Spectrometer [QMS, Figure 5.4b), located in the outlet of the chamber] is also small. Just a small bump appears at 500 K, possibly arising from graphitic "C" burning.

The CO_2 production steadily increases until the temperature reaches 525 K. At this temperature, a large CO_2 cloud appears on the B-side of the crystal in the PLIF snapshots [middle panel of Figure 5.4a), 525 K], which progressively expands towards the A-side. This indicates that the light-off temperature is lower in the B-side of the crystal and the ignition is asymmetric. Such behaviour is similar to that of close-packed Pd vicinals [203], and it radically differs from the simultaneous ignition in Pt vicinal surfaces (Chapter 3 and Ref. [188]). After further increase of the temperature we observe the full ignition of the whole sample at 530 K [top panel of Figure 5.4a)]. As extracted from the data, the B-side of the sample ignites around 5 K earlier than the other edge, again similar to the delay observed for Pd [203].

The cooling of the reaction, i.e. the passage from active to poisoned stage, was also investigated by PLIF. As discussed in Appendix D2, the cooling temperature T_c is also asymmetric: the B-steps have a lower cooling temperature T_c than its A-type analogous. Therefore, the cooling mimics the ignition, as one would naively expect.

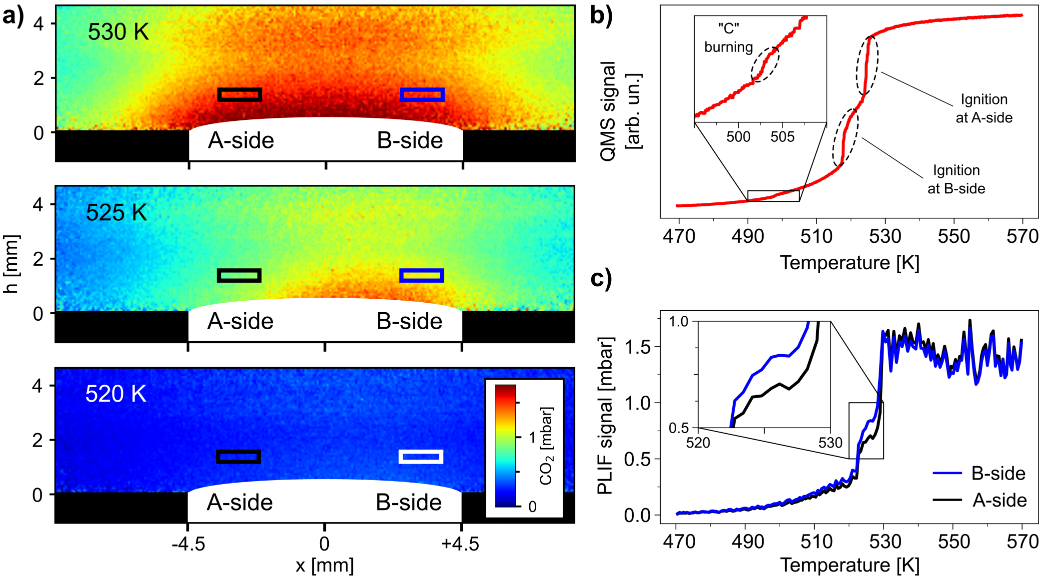

Figure 5.4: PLIF measurements in a 1:1 CO:O_2 gas ratio mixture. **a)** PLIF snapshots acquired at selected temperatures under a 4:4:92 CO:O_2:Ar gas mixture. The total flow and pressure were 100 ml/min and 150 mbar, respectively, while the heating slope was 0.21 K/s. **b)** CO_2 signal in the QMS (mass 44) located in the outlet of the chamber. **c)** CO_2 PLIF signal at the right (B-steps, blue and white) and left (A-steps, black) sides of the c-Rh(111) sample. The two rectangles mark the integration regions from which each of the curves in c) were derived. Insets were added in b) and c) in order to emphasize the "C" burning and the A-B asymmetry during the ignition, respectively.

In Figure 5.4c) we show the integrated CO_2 PLIF at the regions above the A- and B-sides of the crystal. The intensity markedly increases around 525 K at both sides. The onset shows again the earlier ignition at the B-edge, although a small variation is also found at the A-side due to the diffusion of the CO_2 cloud from the B-side. The behavior is reversed 5 K above, where the A-side exhibits a steeper jump as compared to the B-side. This observation is a clear proof of the lateral limits of the approach (curved surfaces and PLIF) to properly account for the gas phase at local facets.

Interestingly, a comparison between Figures 5.4b) and c) reveals that the two different bumps in the QMS CO_2 signal correspond to the ignition of each of the sides of the sample observed by PLIF. With this information, we explored the dependence of the ignition temperatures at each of the sides ($T_{i,A}$ and $T_{i,B}$) as a function of the CO:O_2 ratio. The results are shown in Figure 5.5a), showing the growth of the ignition temperatures with the CO:O_2 gas ratio [39]. The QMS also reveals significant variations of the difference between ignition temperatures ($T_{i,A} - T_{i,B}$) as the CO:O_2 ratio changes, as shown in Figure 5.5b). While the minimum difference is observed at 1:1 conditions (expressed in terms of total pressure), it steadily increases with either the amount of O_2 or CO in the gas mixture.

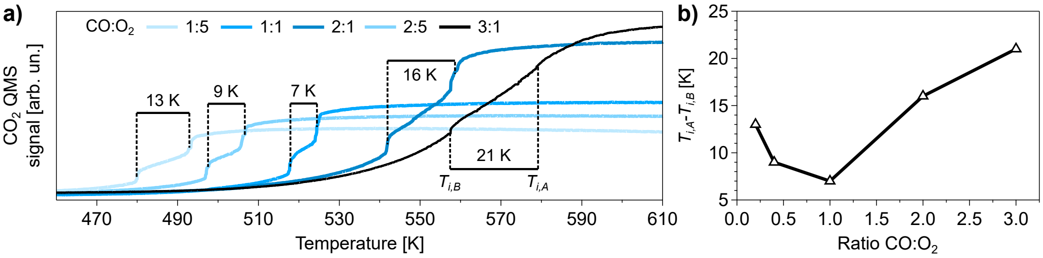

Figure 5.5: Variability of T_i as a function of the CO:O_2 ratio. **a)** QMS CO_2 signal (mass 44) during heating cycles acquired at different CO:O_2 ratios. The total pressure and flow were kept at 150 mbar and 100 ml/min, while changing the CO and O_2 flows as indicated in the legend. Ar was added as a carrier gas to reach the aforementioned conditions. **b)** Difference between the ignition temperature at the A- and B- sides of the crystal, $T_{i,A} - T_{i,B}$, as a function of the CO:O_2 ratio. The experiments were carried out with a heating slope of 0.21 K/s.

While the two transitions are easily distinguished in O_2-rich conditions, they become less pronounced as the CO content increases, and they are hardly distinguished at 3:1 CO:O_2 ratio. In fact, PLIF experiments at the latter conditions (not shown) reveal the expected parallelism: the CO_2 cloud is more blurry and the A-B difference is less defined. We attribute such effect to a stronger CO-poisoning across the whole sample, which decreases the A-B asymmetry observed under O_2-rich conditions, or even to the formation of facets under this CO-rich atmosphere [175]. Since the CO-poisoning weakens as the O_2 content grows, the asymmetry is still well-defined, as we observe.

5.2.2 Chemical species prior to the CO ignition

PLIF measurements revealed an asymmetric ligth-off of the CO oxidation at Rh vicinals. We then performed NAP-XPS experiments (see Section 2.2) in order to investigate the surface species at Rh vicinals during such asymmetric ignition. The c-Rh(111) sample was exposed to a 0.7 mbar, 1:4 $CO:O_2$ gas mixture (O_2-rich) and heated in order to trigger the reaction. O 1*s* and C 1*s* spectra were acquired at the positions of the (111), (223) and (553) surfaces at different conditions, as shown in Figure 5.6. Details regarding the fitting procedure and the coverage calibration are given in Appendix D.

Prior to any CO oxidation experiments, we measured the aforementioned surfaces under 0.1 mbar CO at 300 K in order to have a reference for CO coverage calibration. Two peaks clearly dominate both spectra in the (111) plane [bottom panels of Figure 5.6b)], which are attributed to CO molecules in Terrace-Top (T_T, 532.4 and 286.1 eV) and Terrace-Hollow (T_H, 530.8 and 285.5 eV) sites [148, 151, 174]. After fitting the spectra, we obtained a T_H/T_T ratio close to 2 in the O 1*s* (2.02) and C 1*s* (2.03 for both 650 and 400 eV of photon energy), indicating that the 0.75 ML, (2×2)-3CO superstructure is developed [148, 151]. Accordingly, the spectra at the (111) plane at 0.1 mbar CO, 300 K was used for coverage calibration of the other spectra.

The stepped (223) and (553) surfaces were also probed in the pure CO atmosphere, as shown in the bottom panels of Figures 5.6a,c). They feature A- and B-steps, with square {100} and triangular {111} microfacets, respectively. Similarly to Pt [63], we cannot resolve the emission from CO adsorbed at steps in the O 1*s* (only a subtle shift of the peaks was detected), hence we will focus on the C 1*s* region for now. Two new contributions arise in the C 1*s*. One of them is ascribed to CO molecules anchored atop Rh atoms in the stepped arrays (Step-Top, S_T, 285.8 eV), while the other corresponds to CO adsorbed in bridge sites at the steps (Step-Bridge, S_B, 285.4 eV) [152]. The step-CO coverages agree with those presented in the UHV characterization of the curved sample, i.e. 1 S_T and 1 S_B molecules per 3 Rh edge atom (2/3 CO molecules per Rh step row, see Figure 5.3). However, the coverage of CO molecules anchored at the terraces at these vicinals is larger as compared to the UHV experiments. This is the expected, since the relatively high CO pressure induced the formation of the 0.75 ML, (2×2)-3CO superstructure at room temperature at the (111) plane, although it was not developed at the same temperature under UHV conditions. The same increase of the terrace-CO coverage with the CO pressure was observed for the k-Pt(645) sample (see Subsection 4.2.5).

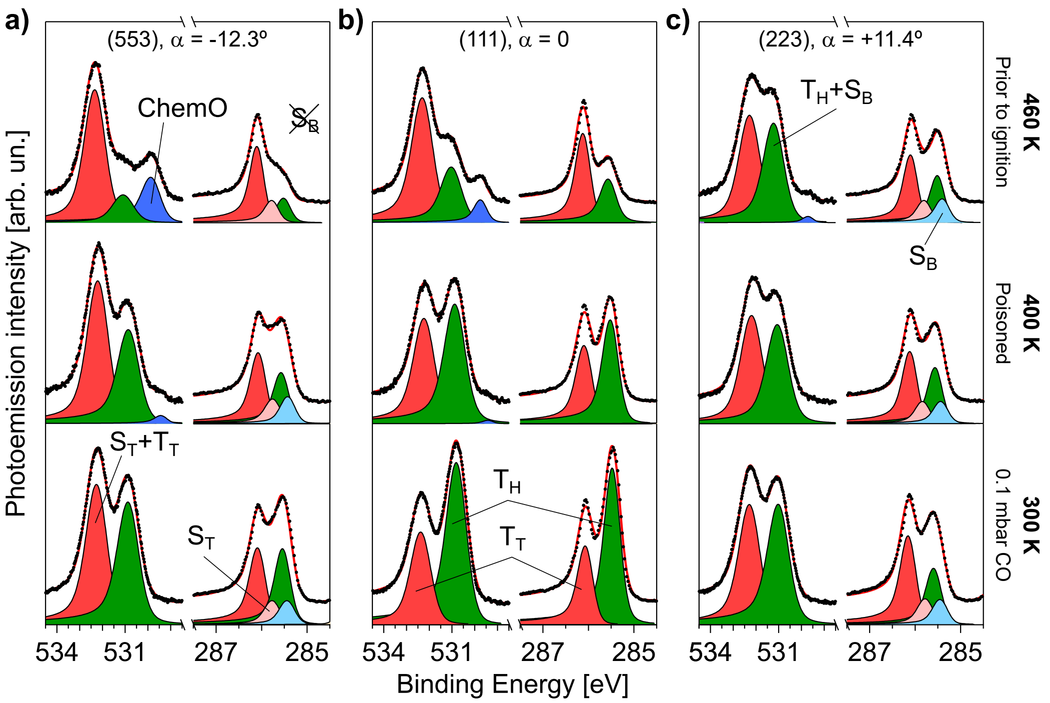

Figure 5.6: Evolution of selected Rh surfaces during ignition. O 1*s* and C 1*s* acquired at the **a)** (553), **b)** (111) and **c)** (223) surfaces at different conditions. The bottom row corresponds to a reference experiment undertaken at 0.1 mbar CO at 300 K, while the spectra at the middle and top rows were acquired at a total pressure of 0.7 mbar in a 1:4 CO:O_2 gas mixture at 400 K (poisoned stage) and 460 K (pre-ignition stage, see text), respectively. T_T, T_H, S_T and S_B stand for CO molecules anchored in Terrace-Top, Terrace-Hollow, Step-Top and Step-Bridge sites, as sketched in Figure 5.3. Additionally, ChemO refers to chemisorbed atomic oxygen in the hollow fcc position [157, 169]. Step and terrace emission cannot be resolved in the O 1*s*, hence the features are re-labelled as T_T+S_T and T_H+S_B. The photon energy of the O 1*s* and C 1*s* region were 650 and 400 eV, respectively.

We also observed a striking increase of T_T-CO as one departs from the (111) plane. We attribute this to a transition between the (2×2)-3CO [1/4 ML T_T] to the $(\sqrt{3} \times \sqrt{3})$R30°-CO [1/3 ML T_T] at the terraces [148, 151]. The CO adsorption at T_H sites would become highly unstable as the step density rises [187]. Hence, CO molecules can rearrange themselves in T_T sites as α increases and T_H-CO decreases. They would tentatively form $(\sqrt{3} \times \sqrt{3})$R30°-CO patches on the surface, increasing the T_T-CO coverage. The coverage of T_T-CO decreases as T_H-CO adsorbs [148, 151], hence one would expect the opposite behaviour as CO leaves T_H sites.

Afterwards, we added O_2 to the chamber (total pressure of 0.7 mbar, 1:4 CO:O_2 gas ratio) and started heating the sample. We observed a huge cracking of CO adsorbed at T_H sites, as discussed in Appendix D3. Further heating caused the oxidation of most of the “C” and the recovery of T_H. Nevertheless, since we were no longer at 300 K, the desorption of T_H had already started and the initial values of the reference experiments could not be reached again. No CO_2 production was detected, excluding the “C” oxidation as a relevant reaction pathway *under these conditions*.

The temperature was further increased until the majority of the “C” disappeared from the surface at around 400 K. Individual spectra at this temperature are depicted in the middle row of Figure 5.6. If compared to the reference experiment at 300 K, a slight decrease of T_H-CO is observed. This effect is more pronounced at the (111) plane rather than at the stepped surfaces, since the maximum of CO adsorbed at T_H positions is found at the former surface. The intensity of T_T-CO increases mildly with α due to the formation of $(\sqrt{3} \times \sqrt{3})R30^\circ$ domains as T_H-CO desorbs, as mentioned earlier. No change is observed for CO adsorbed at neither S_T nor S_B sites, indicating that the step saturation coverage developed at 300 K (and hence UHV) is preserved also at 400 K. Minor amounts of atomic O chemisorbed at terrace hollow fcc sites (ChemO) can be perceived at the (111) surface at around 529.8 eV [157, 169]. The latter grows larger at the (553) plane at a similar energy [161] (529.9 eV in this case), pointing towards additional O adsorption close to the {111} edge. Such peak is absent in the (223) surface. No $CO_{2(g)}$ production was detected, hence we continued the heating ramp.

At around 460 K, both $CO_{(g)}$ and $O_{2(g)}$ started to steadily decrease in both the RGA and XPS (not shown), while the $CO_{2(g)}$ signal smoothly increased. We are therefore in a regime were the CO_2 turnover has not reached its maximum. At this stage we investigated in more detail the (111), (223) and (553) surfaces, as shown in the top row of Figure 5.6. Due to the strong asymmetry, a complete α-scan was taken that is further explained in Appendix D4, together with additional data to illustrate the composition variability of the Rh vicinals just before ignition. The $CO_{2(g)}$ signal was roughly half of its maximum, for which we call this *pre-ignition stage*. At slightly higher temperatures the maximum CO_2 production was achieved and most of the CO vanished from the surface. This mark the transition towards the active stage, which shall be discussed in the next Section.

A closer look to the spectra at the (223) plane at 460 K reveals minor changes in both the O 1*s* nor the C 1*s* regions. CO molecules anchored at S_T and S_B sites remain unaltered, whilst the terrace components mildly decrease and a minute amount of ChemO appears. The scenario is slightly different for the (111) surface. To remember, the amount of CO at T_T sites shortly increases with temperature due to the formation of $(\sqrt{3} \times \sqrt{3})R30^\circ$ domains, since CO adsorbed at T_H sites has decreases dramatically and the surface is now more open. This situation of partially empty (111) terraces (CO occupation of ≈0.4 ML at 460 K *vs* 0.75 ML at 300 K) would permit O_2 molecules to impinge, dissociate and react with coadsorbed CO at neighbouring sites. In fact, a growing amount of ChemO is detected at the (111) plane, larger than at 400 K, illustrating the partial CO-depletion and oxygen chemisorption at the terraces.

Notwithstanding, the strongest changes are observed at Rh(553). The C 1*s* reveals that, in addition to the great decrease of T_H, S_B has totally vanished from the spectra. Furthermore, a large amount of ChemO has simultaneously appeared in the O 1*s*. One observes a strong asymmetry between A-B Rh vicinals during the ignition of the CO oxidation: while A-steps remain CO-saturated, a large fraction of adsorption sites at the B-steps are CO-depleted during the pre-ignition stage. In other words, A-steps remain CO-poisoned while B-type steps are partially empty, enabling O_2 molecules to dissociatively adsorb. Therefore, we postulate that the asymmetric ignition of the CO oxidation at A-B Rh vicinals is caused by this partial CO-depletion at B-steps, allowing the reaction to start at a lower temperature as compared to A-steps. This provides a reasonable explanation of the asymmetric ignition observed in the PLIF experiments, probing the usefulness of the combined NAP-XPS and PLIF approach that we follow.

5.2.3 Active stage of the CO oxidation

Right after heating to 470 K, the surface evolved from the pre-ignition stage to the active stage, where almost all CO has vanished from the surface and the CO_2 turnover reaches its maximum. The surface composition of the active stage was mapped through α-scans at several temperatures, namely 470, 510, and 570 K, observing significant differences between the surfaces and temperatures. Again, special attention has been paid to the (223), (553), and (111) surfaces close to the borders and the center of the crystal. Here we will focus on the O 1*s* spectra to study the Rh oxidation. The C 1*s* data during the active stage is discussed in Appendix D5.

The O 1s spectra at the (111) plane at 470 K [Figure 5.7d), middle panel] consist on two well defined peaks at 532.2 and 529.6 eV, attributed to CO adsorbed at T_T sites and ChemO, respectively. As compared to the (111) spectra at 460 K [Figure 5.6b)], T_T-CO has vanished significantly while the contribution from ChemO has grown markedly. This indicates that the surface is covered mostly by oxygen species during the active stage. We want to remark the coexistence of CO and ChemO during the active stage at the Rh surfaces, similarly to Pd surfaces [206] and both contrasting with the Pt case [188], where CO and ChemO never coexist once the surface has ignited. The feature "Oxide" detected around 531 eV will be addressed later.

A similar situation is observed at the (553) surface [Figure 5.7d), bottom panel]. In this surface, both contributions (T_T-CO and ChemO) are slightly smaller if compared to the (111) plane. This decrease with the step density confirms their terrace nature. Nonetheless, we cannot discard some O adsorption at the stepped arrays since the peak is broader as compared to that of the (111) plane, pointing towards unresolved species in the O 1s region.

Two large peaks at 530 and 529 eV dominate the spectra of the (223) plane [top panel of Figure 5.7d)], confirming the formation of the (9×9) surface oxide [169]. The formation of this oxide has been shown to be accompanied with a surface restructuring into Rh(111) and Rh(11$\bar{1}$) facets in Rh(553) [175]. For this reason a faceting of the whole A-side vicinal part has to be supposed. Furthermore, a contribution at 533.2 eV is detected only on the A-side of the crystal, growing larger with the density of A-steps. We attribute such species to carbonates/carboxyls [243] anchored at the A-steps (Carb), as extracted from the C 1s analysis (see Appendix D5). Another possibility would be CO adsorbed on the (9×9) oxide, since CO adsorbed on Pd_5O_4 exhibits a peak above 533 eV [248]. Nevertheless, CO does not adsorb on the (9×9) Rh oxide, hence this situation must be discarded [169].

The peak around 530 eV shifts towards higher binding as the density of both A- and B-type steps increases [see Figure 5.7a)]. An explanation for this is not clear. Variations on the position due to an irregular strain at the stepped surfaces [207] or an unresolved species seem the most likely situation, since a change in the interaction CO-O should not alter significantly the position of the peaks, at least at Rh(111) terraces/facets [157]. The sample was further heated to 510 K in order to desorb the terrace CO and promote the formation of a "pure" active stage, i.e. without any CO on the surface. The results are shown in the panels of Figures 5.7b) and e).

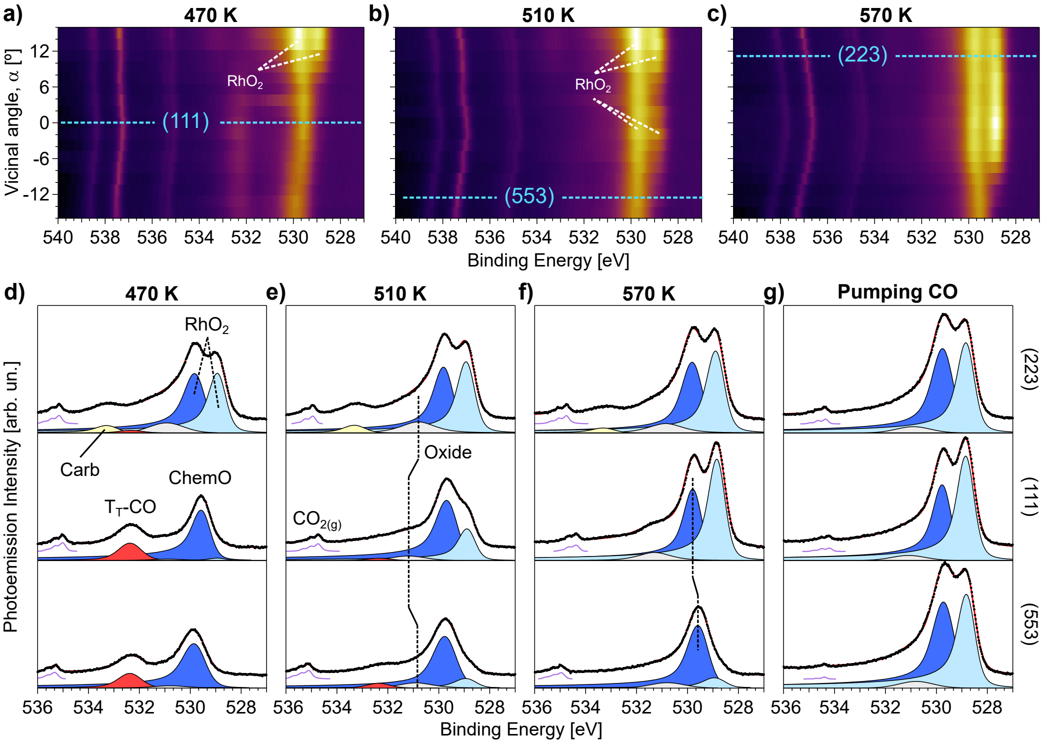

Figure 5.7: O 1*s* temperature evolution across the curved surface. **a-c)** O 1*s* α-scans acquired at 470, 510 ad 570 K under a 1:4 CO:O_2, 0.7 mbar gas mixture. **d-f)** Individual fitted spectra of the (223), (111) and (553) surfaces at each of the temperatures, and **g)** while pumping away the CO at 570 K. ChemO, RhO_2 and Oxide stand for chemisorbed atomic O in fcc sites, the (9×9) surface oxide and an uncharacterized Rh oxide. Terrace-Top CO molecules, carbonate/carboxyl species and gas phase CO_2 are denoted as T_T, Carb and $CO_{2(g)}$. Vertical dashed lines are included in e,f) to illustrate the shift of Oxide and ChemO/RhO_2 with α, respectively. The photon energy was 650 eV.

The (223) surface is virtually the same: the RhO_2 trilayer grows slightly, while the carbonates remain on the surface and T_T-CO finally disappears. At the (111) plane, however, one can detect a slight increase of the peak at 529 eV, indicating that Rh(111) terraces/facets also start to develop the trilayers at 510 K. The ratio between the peaks at 530 and 529 eV at the (111) plane differs from 1, indicating that the terraces are partially covered by a mixture of ChemO and the (9×9) oxide, since a full RhO_2 trilayer would give rise to a 1:1 ratio between the features at 530 and 529 eV [169].

Most of CO adsorbed at T_T sites has vanished from the (111) plane at 510 K, although a significant amount of it is detected at the (553) plane [middle and bottom panels of Figure 5.7e)]. Therefore, T_T-CO increases with α, as better seen at the C 1s region (see Appendix D5). Terrace species should decrease with α, hence the increase of T_T-CO at the (553) plane as compared to the (111) surface is striking. However, we have to take into account that at 510 K the (111) plane is also oxidized forming RhO_2 trilayers. If one compares the α-scans acquired at 510 K for the O 1s [Figure 5.7b)] and C 1s [Figure D5b)] regions, the behaviour of RhO_2 trilayers and T_T-CO is inverse. The decay of the trilayers with α is parallel to the growth of T_T-CO with the step density and, once no RhO_2 is observed, T_T-CO decreases with α as a regular terrace species. The surfaces near the (111) plane at $\alpha = 0$ feature the (9×9) oxide, on which CO is known not to adsorb [169]. Hence, the CO adsorption is quenched at these surfaces and its intensity close to the (111) surface is lower as compared to 460 K, where no trilayers are observed. However, no (9×9) oxide is observed around the (553) plane. Therefore, CO can still adsorb at T_T sites at these surfaces, hence it grows in intensity with α. When the RhO_2 trilayers disappear at large α at the B-side of the crystal, T_T-CO starts to decrease as a regular terrace CO species.

The last map across the curved surface was acquired at 570 K. It is shown in Figures 5.7c) and f). CO-related peaks are no longer observed on the surface. Again, at the (223) plane only a subtle increase of the RhO_2 peaks is observed, together with a minor decrease of Carb, indicating that the latter is desorbing, decomposing and/or reacting with the oxygen.

The RhO_2 trilayers are now fully developed in most of the Rh surfaces, since its two O 1s features prevail over the other components at $+15 > \alpha > -4°$. At $-4 > \alpha > -8°$, the peak at 530 eV markedly decreases while the one at 529 eV rapidly vanishes at increasing step density, indicating that the surface is transitioning from a pure O-Rh-O trilayer to a pure chemisorbed O phase. As sketched in Figure 5.7f), a slight shift of the peak at 530 eV is observed through this passage, revealing that the interfacial oxygen of the trilayer and ChemO may have a subtle difference in the energy. Only ChemO latter is observed at $\alpha < -8°$, which may indicate that the B-side is more reactive towards the CO oxidation, since the formation of the trilayer is known to be quenched if the CO oxidation is sufficiently faster, for example in CO excess [49, 171]. In fact, there were no signs of the development of the (9×9) oxide in other measurements with lower O_2 content (Appendix D6).

Lastly, we closed only the CO leak valve and measure the three characteristic surfaces of the c-Rh(111) sample at 570 K, as shown in Figure 5.7g). While the (223) and (111) surfaces do not change significantly after closing the CO leak valve, the two peaks of the RhO_2 trilayer are easily perceived now at the (553) plane. Therefore, we postulate that formation of the surface oxide at the B-side of the crystal (and possibly its faceting [175]) was not observed at lower temperature due to a faster reduction by CO as compared to the A-side. This tentatively refers to a larger reactivity of the {111} microfacets over the {100} steps for the CO oxidation. On one hand, Klikovits *et al.* compared the bare oxidation of A- and B-type Rh close-packed steps. For A-steps, the step oxidation develops a closed structure, while for B-steps the structure is defective (i.e. open) [249]. One would then expect a larger reactivity of the B-steps oxide, similarly as we postulate. On the other hand, Gustafson and coworkers affirmed that "*specific Rh crystal planes exposed during catalysis will not directly influence the reactivity*" [168]. However, our results confirm that at the very same experimental conditions, A- and B-steps behave radically different, both during the CO ignition and during the active stage of the CO oxidation.

To end with, we will asses the nature of the "Oxide" contribution at around 531 eV. No reports exist to our knowledge on such photoemission peak, although its larger binding energy as compared to the features of RhO_2 may point towards Rh_2O_3 [163], or maybe impurities arising due to the long time that the crystal has been at high temperatures. The contribution at 531 eV has a pronounced shift with α [see Figure 5.7e)], it is less resolved at the stepped surfaces and its evolution with α is different at each of the α-scans. All of these features may point to several, unresolved oxides and/or impurities at the each of the planes.

Summary of the c-Rh(111) experiments

The CO oxidation on close-packed Rh stepped surfaces was explored in the $\alpha \pm 15^\circ$ range around the (111) plane. UHV adsorption experiments were performed to explore the CO chemisorption at steps prior to and at CO saturation. Such an analysis is necessary in order to characterize the poisoning layer of the CO oxidation experiments. To continue with, PLIF and NAP-XPS measurements were employed to explore the ignition of the aforementioned reaction, and the latter was also used to probe the chemical species during the different stages of the CO oxidation.

The UHV experiments revealed a preferential adsorption of CO molecules at steps for A-type vicinal surfaces, while terrace and steps were simultaneously populated by CO molecules in the B-type vicinals. After a 12 L CO dose, we observed a saturation structure of both A- and B-type steps of one Step-Top (S_T) and one Step-Bridge (S_B) CO molecules per 3 Rh edge atoms, for a total coverage of 2/3 CO molecules per step Rh atom. However, the terrace saturation was 0.57 ML, far from the low temperature saturation value. Therefore, the 0.75 ML, (2×2)-3CO superstructure was not developed at 300 K. Finally, a minute CO cracking was also detected. However, this process seems to be more dependent on the CO dosage than step dependent.

PLIF measurements revealed that, contrary to Pt and similarly to Pd, the B-side of the crystal ignites earlier while heating and quenches later during cooling cycles than its A-type analogous, which may naively point to a larger reactivity of the triangular {111} steps over their squared {100} twins. Hence we discovered an asymmetric ignition of the CO oxidation on Rh vicinals. The ignition of the reaction heavily depends on the CO:O_2 ratio, and so does the A-B asymmetry: large CO or O_2 excess leads to an increase of the difference between the ignition of {100} and {111} facets. Nonetheless, an increase on the CO content of the gas mixture caused the ignition to be less defined in both the RGA and the PLIF measurements, tentatively due to a CO-poisoning that is more difficult to overcome. A further possibility for this observation is a complete faceting of the surface giving rise to a completely different arrangement of the surface atoms.

Photoemission data confirmed that exposure to large CO pressures increases the terrace coverage, where the (2×2)-3CO superstructure is developed. Nonetheless, the saturation structure described above for the steps remains unaltered. The sample was heated while probing the (223), (111) and (553) surfaces in order to explore the species involved in the asymmetric ignition. While the (223) plane evolved substantially only after ignition, the (553) and (111) planes showed significant changes during the heating ramps.

As CO molecules from T_H sites desorb with increasing temperature, a small amount of chemisorbed atomic oxygen (ChemO) accumulate at the CO-depleted terraces of the (111) plane. Nonetheless, the most distinguished behaviour was that of the B-steps: just before the ignition of the crystal, most of the T_H sites and all of the CO molecules anchored at S_B spots have vanished from the surface, on which a large amount of ChemO is now observed. Hence, we postulate that the early ignition observed by PLIF on the B-side of the crystal is caused by the partially empty {111} microfacets of the B-steps, which allow O_2 to stick, dissociate and react to produce CO_2 earlier than its A-type, CO-poisoned analogous.

Further increase of the temperature caused the ignition of the whole sample. Most of the CO molecules have vanished from the surface, which is now covered by several oxygen species. At low temperature (470 K), both the (111) and (553) planes feature a large amount of ChemO, together with a small amount of Terrace-Top CO molecules. However, the (223) surface is largely oxidized forming the O-Rh-O trilayers (surface oxide) at the top of the surface. Also on the A-side vicinals only, two different C 1*s* peaks were observed for increasing α that were attributed to carbonates/carboxyls anchored exclusively to the {100} microfacets.

The RhO_2 (9×9) trilayers started to develop also at the (111) terraces as the sample reaches 510 K. At this temperature, a residual amount of CO molecules at T_T positions endure near the (111) plane. Its adsorption is triggered by the increasing (9×9) surface oxide. The B-side of the crystal remained with chemisorbed oxygen. No RhO_2 formation was observed, even after heating the sample to 570 K. The O-Rh-O trilayers dominate most the curved sample at this latter temperature, since only densely B-stepped surfaces remain with only ChemO. Nonetheless, after closing the CO leak valve at 570 K, the trilayer peaks rapidly appeared at the (553) surface, homogeneously covering the curved crystal. Therefore, one would tentatively affirm that the CO oxidation is faster on the {111} steps, since these Rh surfaces are not fully oxidized until the CO is removed from the chamber. Finally, an uncharacterized and residual peak around 531 eV was observed for all surfaces, which we attribute to a combination of an unknown Rh oxide and impurities.

Chapter 6

Concluding remarks

Throughout this Thesis, we have studied the ignition and nature of the poisoned stage of the CO oxidation, and also briefly the species of its active stage. We made use of curved crystals, which allowed us to investigate the unexplored large family of stepped surfaces vicinals to Rh(111) and Pt(111).

Curved Pt samples with A- and B-steps [c-Pt(111)] and kinks [k-Pt(645)] showed a surprising behaviour. In separate PLIF experiments, we observed that the (111) plane and each of the stepped surfaces ignited at the very same temperature, revealing a simultaneous in all investigated Pt(111) vicinals. Additional NAP-XPS experiments showed that CO adsorbed at terraces steadily desorbs as the temperature increases under reaction conditions. However, CO anchored at the straight steps and kinks remains on the surface while heating, and only a minute desorption is perceived just before the ignition of the CO oxidation.

In this scenario of partially CO-depleted terraces, we performed a slow and precise CO ignition cycle at Pt(111). A significant shift in the O $1s$ CO peak was detected during the heating cycle, not perceived under UHV conditions. Using the spectra at low temperature as a reference, we derived the existence of an additional oxygen feature hidden by the CO emission peak. In order to do so, we supposed that (*i*) no additional species contributed to the spectra and (*ii*) there was no shift of the CO-related peak with the temperature. Under these constrains, we extracted the evolution of a new peak that slowly increases with the temperature, significantly rises prior to ignition, and vanishes afterwards. Also just before ignition, we observed signatures of step doubling in the A-side of the c-Pt(111) sample, which were not observed for the k-Pt(645) crystal.

We resorted to theoretical DFT calculations to investigate this uncharacterized, transient peak arising just before the ignition. They suggest that subsurface oxygen could accommodate under the relatively CO-depleted terraces, lifting some of the Pt atoms. It would also increase the adsorption energy of the remaining CO molecules anchored at terraces, bringing it up to values similar to those of CO adsorbed at steps, hence explaining the symmetric ignition of flat and stepped surfaces.

We briefly explored the active stage of the reaction for both c-Pt(111) and k-Pt(645). For the later, we found that the amount of oxygen markedly increases with the step density. This is the expected trend, since steps are oxidized easier than the (111) terraces. However, at larger O_2 partial pressures the amount of oxygen was observed to decrease with the density of steps for the c-Pt(111) sample. This points towards the oxidation of the terraces as the O_2 content increases, which is hindered at lower O_2 pressures due to kinetic limitations. In addition to chemisorbed oxygen, we observed the formation of several oxides at steps and terraces, which we could not further identify.

In the PLIF experiments conducted on the c-Rh(111) sample we observed an asymmetric CO ignition. Similarly to Pd, in Rh the B-type steps ignite at lower temperature than the A-steps. However, the measurements suggest that the asymmetry of the ignition goes away if the CO partial pressure is increased, while it is still well-defined under O_2-rich conditions.

NAP-XPS experiments confirmed the A-B asymmetry prior to the ignition. Just before the ignition, the A-steps remain CO-saturated, and only a small decrease of the intensity of the Terrace-CO peaks is observed. A significant decay (> 50 %) of CO adsorbed in hollow sites at terraces is observed at the (111) plane, and also at the (553) surface that features B-steps. But more importantly, at this latter plane the peak corresponding to CO adsorbed in bridge sites at the steps vanished just before the ignition, indicating that the B-steps are partially CO-depleted. In parallel, a simultaneous increase in the CO_2 production was observed in the mass spectrometer, and a large amount of chemisorbed O appeared in the NAP-XPS. Therefore, we postulate the following as the reason for the asymmetric ignition. On one hand, the O_2 cannot adsorb at the CO-saturated A-steps, and hence the CO_2 production is hindered. On the other hand, the B-steps have free sites due to the earlier desorption of CO at bridge positions, hence providing empty space for O_2 to adsorb, dissociate and start the reaction at the very same temperature at which the A-steps are saturated.

The A- and B-type steps and the (111) plane also behave different during the active stage of the CO oxidation. The A-side of the c-Rh(111) sample readily forms a RhO_2 trilayer after transitioning to the active stage, which is known not to be reactive towards the CO oxidation. RhO_2 trilayers do not form on the (111) plane until the temperature is further increased, revealing that the (111) surface is not oxidized at low temperature, likely having a remarkable reactivity towards the CO_2 production. However, no RhO_2 formation was observed at the B-side of the crystal unless the CO flow into the chamber was stopped. This reflects that the B-steps are not oxidized in the presence of a sizeable amount of CO in the chamber. Therefore, we believe that the B-steps are more reactive towards the CO oxidation than the A-steps, since the CO oxidation is faster on the B-side of the crystal, as no RhO_2 is observed during reaction conditions.

Combining PLIF, NAP-XPS and curved crystals is a powerful approach. Currently, we are applying the same strategy to study the ethylene epoxidation, CO_2 dissociation and hydrogenation and NO dissociation and reduction, using curved Ag, Cu and Rh crystals, respectively. NAP-XPS can provide the essential spectroscopic signatures of the catalyst surface along with the gas phase, yet we lack a structural characterization technique, which could provide the complete picture of the catalytic reaction.

Appendices

Appendix A: introduction

A1 Reaction mechanisms on a surface

Two gasses, $A_{(g)}$ and $B_{(g)}$, that react on a surface to yield a desorbing product, $C_{(g)}$, may do so in several ways [9, 250]. A surface reaction is typically classified as a Langmuir-Hinshelwood [13, 14] or Mars-van Krevelen [17, 18] process. Nevertheless, two other possibilities are possible, namely the Eley-Rideal [15, 16] and the Harris-Kasemo [251]. As sketched in Figure A1:

- A **Langmuir-Hinshelwood** [LH, Figure A1a)] process consists on the adsorption of both $A_{(g)}$ and $B_{(g)}$ (bimolecular reaction) on free sites on the surface (*), forming a chemisorbed state on the surface (A*, B*). These two molecules/atoms may collide, and a fraction will form the product C*, which is still adsorbed. The last step comprises the product desorption as $C_{(g)}$, usually promptly after its formation.

- The **Eley-Rideal** [ER, Figure A1b)] mechanism shares the same initial step, yet only one of the reactants, for instance $A_{(g)}$, is adsorbed on the surface. After the chemisorption, the other reactant, $B_{(g)}$, collides in an adequate way with A* to form C*, which readily desorbs.

- A **Mars-van Krevelen** [MvK, Figure A1c)] reaction is similar to the ER process. The initial adsorption of $A_{(g)}$ forms a compound on the catalyst surface, such as an oxide. Impinging $B_{(g)}$ can then collide at a certain site of the compound, retrieve one of its A* elements. The product C* will form, and eventually desorb. Simultaneously, the missing A* will be readily replaced with a new element of $A_{(g)}$.

- The **Harris-Kasemo** [HK, Figure A1d)] pathway resembles the LH process, since both reactants are coadsorbed on the surface. However, one of them may develop what is called a "hot atom" (or molecule), A': adsorbed particles with an excess of kinetic energy, moving across surface sites on the catalyst [7]. This reactive A' can collide with B* to form C*, which will again leave the surface as $C_{(g)}$.

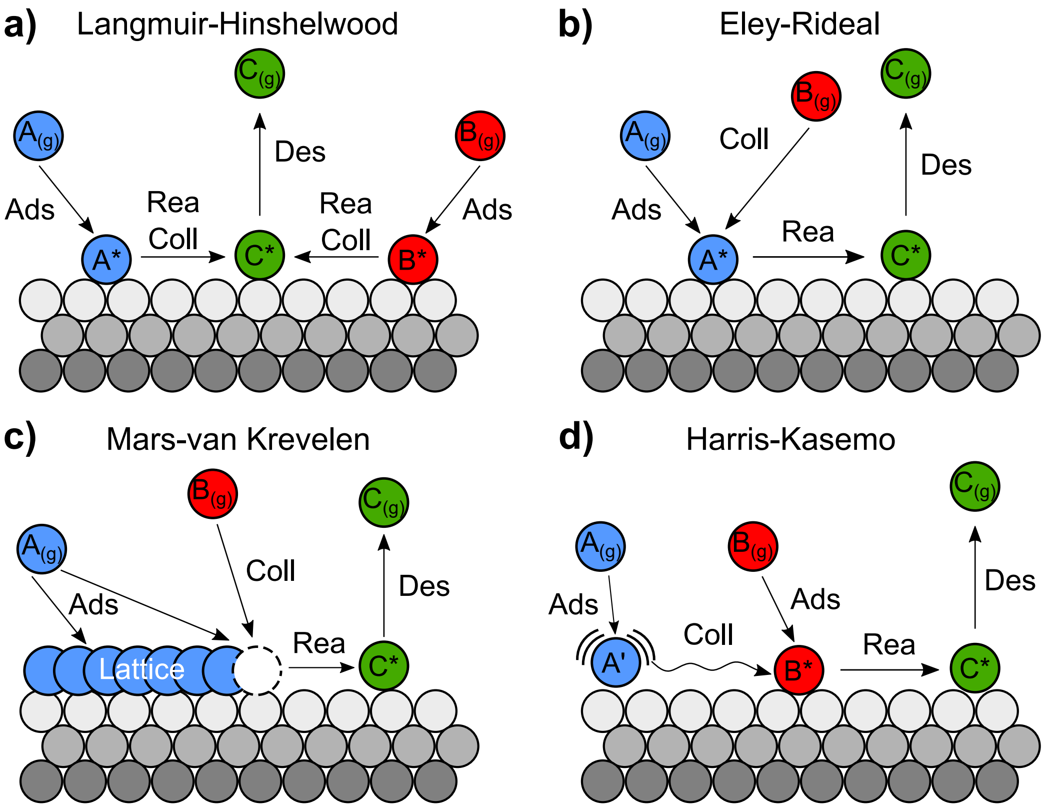

Figure A1: Relevant mechanisms for gas-surface reactions. **a)** Langmuir-Hinshelwood mechanism, on which two reactants ($A_{(g)}$, $B_{(g)}$) adsorb in parallel (A*, B*), collide and react to form the adsorbed product C*. In all mechanisms described below, C* promptly desorbs as $C_{(g)}$. **b)** Eley-Rideal process, in which a gas reactant $B_{(g)}$ collides with an already adsorbed reactant A* to form C*. **c)** Mars-van Krevelen pathway. First, the reactant $A_{(g)}$ chemisorbs on the surface forming a compound, e.g., an oxide. Later, $B_{(g)}$ collides with this compound, removing one constituent to form the product C. The consumed A* element is readily renewed by $A_{(g)}$. **d)** The Harris-Kasemo reaction involves the adsorption of $A_{(g)}$ and $B_{(g)}$. However, while one of them develops the chemisorbed state B*, the other is weakly adsorbed in the form of a hot particle A'. Due to its extra energy, the reactive A' moves fast around the surface until it collides and reacts with B*, yielding C*. The labels Ads, Coll, Rea and Des refer to adsorption, collision, reaction and desorption, respectively, which may not be isolated events.

A2 Review of Pt bibliography

There is a vast bibliography about the interaction of CO, O_2 and CO+O_2 with Pt. Relevant references are classified on Table 1.

Table 1: Relevant bibliography on the CO oxidation on Pt

	Pt(111)
CO adsorption	[24, 52–59, 61, 72, 208, 228, 237, 252–254]
O_2 adsorption	[30, 43, 71, 73, 74, 78–81, 83–85, 88, 90, 97, 103, 105–107] [120, 133, 182, 216, 218, 221, 226, 255–266]
CO oxidation	[38, 44, 46, 47, 89, 116–119, 122–125, 141, 199, 211, 267]
	Pt(110)
CO adsorption	[53, 59]
O_2 adsorption	[86, 87, 182, 257, 268]
CO oxidation	[19, 27, 31, 41, 44, 115, 128–130, 132]
	Curved surfaces, nanoparticles, wires and films
CO adsorption	[207]
O_2 adsorption	[91–95, 269–273]
CO oxidation	[123, 126, 127, 130, 134, 180, 188, 210, 274, 275]

A-steps	CO adsorption	O_2 adsorption	CO oxidation
(113)	-	[182]	[276]
(112)	[59, 65, 66]	[105, 182, 258]	[136, 140]
(335)	[64, 65]	[98, 99, 106, 277, 278]	[137, 139]
(223)	[67]	[108]	-
(557)	[69, 70]	[89, 100, 103, 110]	[46, 47, 135]
(997)	-	[100, 101, 279]	[144]

B-steps	CO adsorption	O_2 adsorption	CO oxidation
(331)	-	[182]	-
(221)	-	[99, 258]	-
(553)	[62, 63, 67]	[106, 108, 277]	-
(332)	[70]	[96, 257, 268]	[141, 142]
(779)	-	[280, 281]	[143]

Kinks	CO adsorption	O_2 adsorption	CO oxidation
(201)	[59]	-	[211, 145]
(513)	-	[114]	-
(312)	[68]	[111, 112]	[138]

A3 Properties of A-, B- and kinked steps

Further notes complementing those of Section 2.1, are presented here to better describe the relation between step density, vicinal angle and terrace length for each type of steps. The variety of surfaces described in Table 2 is intended to be used as a reference for the surfaces mentioned in the text.

As an example, a (112) surface is sketched at the top of Figure A2. The Miller (hkl) indexes describe both a plane parallel to the "macroscopic" surface, and a vector perpendicular to it (referred to as [hkl]). The (111) plane runs parallel to the flat terraces, while for the (112) it does so across the outermost step edge. The angle spanned between two planes (or *surfaces*) is the same as that defined by its two perpendicular vectors, hence the angle between two surfaces can be derived by simply applying the scalar product. Since we have defined the vicinal angle α with respect to the flat (111) plane, we can just apply the aforementioned relation to easily calculate α.

Nevertheless, α is just the angle between two planes: it does not give any surface information by itself. We need to relate it to significant magnitudes of our surface, as described in Figure A2. Lets suppose that the (112) plane features monoatomic steps of a given height, h. Defining a as the face-centered cubic (*fcc*) lattice constant of our metal, and doing some simple trigonometry, one can derive that $h = a\sqrt{3}/3$ for (111) steps. We may also define another two concepts, the terrace length, l, and the distance between steps, d. Note that while l is parallel to the (111) plane, d is so to the surface we are considering, in this case the (112). Since d and l are respectively perpendicular to the [112] and [111] directions, the angle between them is also α. Hence, we may write a triangle formed by h, l, d and α, as sketched in Figure A2a). After applying trigonometric relations one may obtain:

$$sin(\alpha) = \frac{h}{d} \tag{A1}$$

$$d^{-1} = \frac{sin(\alpha)}{h} \tag{A2}$$

While d is a distance, its inverse d^{-1} is related to the frequency at which steps appear in space, i.e. step density. Therefore, we can now easily relate α with d^{-1} to describe a vicinal surface.

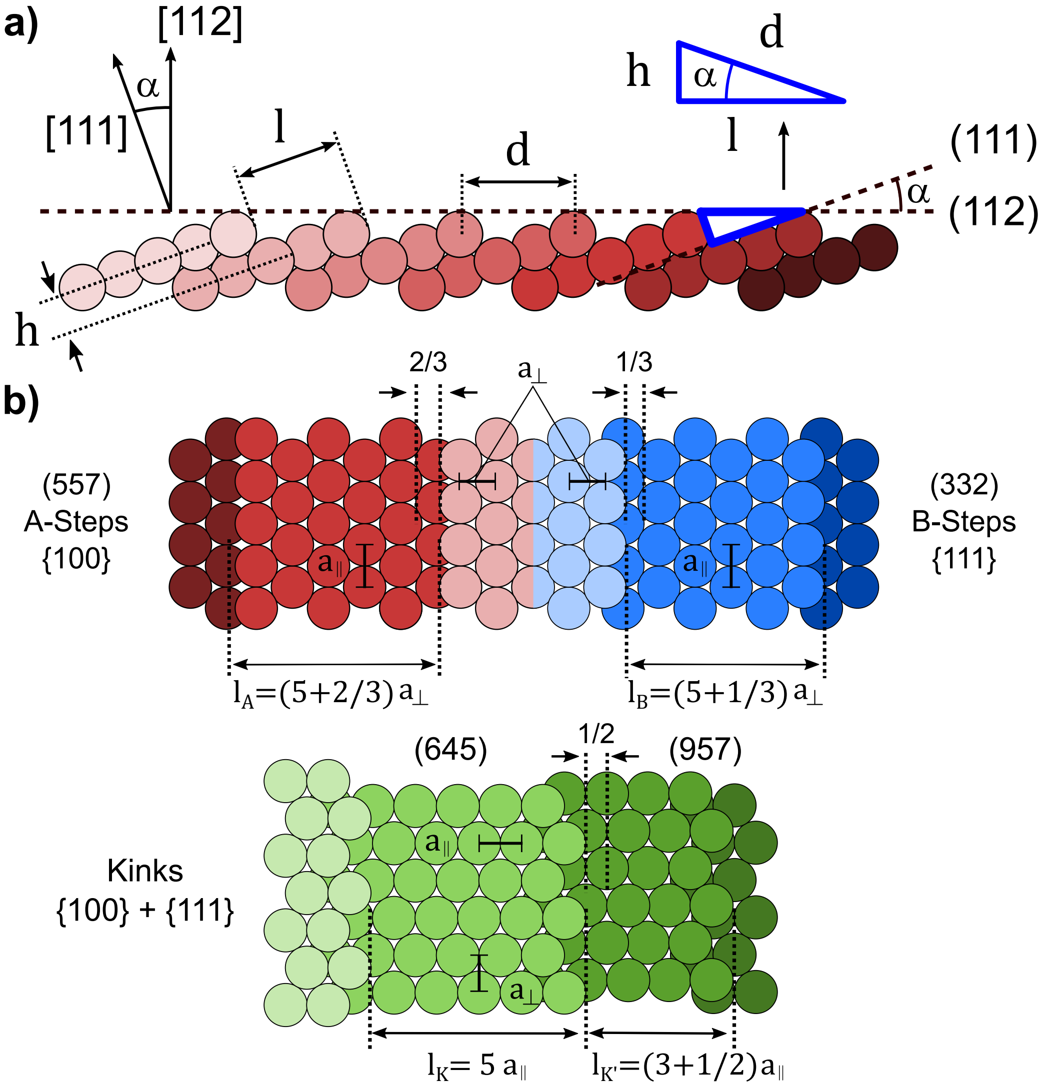

Figure A2: Relevant properties of (111) vicinals.
a) Lateral sketch of an ideal (112) surface, showing the terrace length, distance between steps, step height and vicinal angle (l,d,h and α, respectively). (111) and (112) planes and [111] and [112] directions are depicted. **b)** Illustrations of terrace length l for A- and B- (red and blue, exposing 2/3 and 1/3 of one atomic row $a_\perp$) and kinked steps (green, exposing 1/2 atomic row $a_\parallel$). See Section 2.1 for a profound discussion on the nature of each of the steps.

Another equation that emerges from the triangle is:

$$tan(\alpha) = \frac{h}{l} \tag{A3}$$

enabling to relate the α (and hence d^{-1}) with the terrace length. l can be easily deduced from the corresponding structural model of each vicinal surface, therefore we will describe each vicinal with respect to l. From them, we will derive d^{-1}, α and Miller indexes. In order to do so, we shall define two distances, $a_\perp$ and $a_\|$. They are illustrated at the center and bottom rows of Figure A2 and they correspond to the inter-atomic distance between rows in the perpendicular ($a_\perp = a\frac{\sqrt{3}}{2\sqrt{2}}$) and parallel ($a_\| = a\frac{\sqrt{2}}{2}$) vectors of a close-packed step. Note that since $a_\perp$ and $a_\|$ are defined using a straight step as a reference, they are rotated 90° at the kinked surfaces. Let us discuss each step-type individually:

- **A-steps**: its terraces are separated by square, $\{100\}$ microfacets, hence 2/3 of the understep atomic row are visible. The terrace length corresponds to the number of fully exposed atoms m [$m = 5$ in the case of the (557)] plus 2/3, all multiplied by the interatomic distance $a_\perp$, hence $l_A = (m + 2/3)a_\perp$.

- **B-steps**: the terraces in these surfaces are divided by triangular, $\{111\}$ microfacets, exhibiting 1/3 of the understep atomic row. In this case, the terrace length equals m [$m = 5$ in the case of the (332)] plus 1/3, all multiplied by $a_\perp$, therefore $l_B = (m + 1/3)a_\perp$.

- **Kinks**: the terraces are separated by alternate $\{111\}$ and $\{100\}$ microfacets, i.e. $\{31\bar{1}\}$ microfacets [68]. Due to the unique configuration of these steps, m can take values in 1/2 intervals, since adding one atomic row only increases the terrace length by 0.5 times the interatomic row distance, which in this case is $a_\|$ (these surfaces are 90° rotated with the close-packed arrays). The terrace length is simply defined as $l_K = m \cdot a_\|$ or $l_K = (m + 1/2)a_\|$.

Knowing l and m, and applying the previous equations, one can easily describe a vicinal plane. This is shown in Table 2, for which h values for Pt and Rh of 2.26 and 2.21 Å, i.e. monoatomic steps, were considered. The Miller indices for A-, B- and kinked surfaces are obtained as $(m, m, m + 2)$, $(m + 1, m + 1, m - 1)$ and $[(m + 1, m - 1, m)]$, respectively.

Table 2: Selected (111) vicinals with pertinent magnitudes.

A-steps $(m,m,m+2)$

m	(h,k,l)	$l_A/a_\perp$	Vicinal angle, α [°]	d_{Pt}^{-1} [Å^{-1}]	d_{Rh}^{-1} [Å^{-1}]
1	(1,1,3)	1+2/3	29,45	0,218	0,223
2	(1,1,2)	2+2/3	19,47	0,147	0,151
3	(3,3,5)	3+2/3	14,42	0,110	0,113
4	(2,2,3)	4+2/3	11,42	0,088	0,090
5	(5,5,7)	5+2/3	9,45	0,073	0,074
6	(3,3,4)	6+2/3	8,05	0,062	0,063
8	(4,4,5)	8+2/3	6,21	0,048	0,049

B-steps $(m+1,m+1,m\text{-}1)$

m	(h,k,l)	$l_B/a_\perp$	Vicinal angle, α [°]	d_{Pt}^{-1} [Å^{-1}]	d_{Rh}^{-1} [Å^{-1}]
1	(1,1,0)	1+1/3	35,26	0,255	0,261
2	(3,3,1)	2+1/3	22,00	0,166	0,170
3	(2,2,1)	3+1/3	15,79	0,120	0,123
4	(5,5,3)	4+1/3	12,28	0,094	0,096
5	(3,3,2)	5+1/3	10,03	0,077	0,079
6	(7,7,5)	6*1/3	8,47	0,065	0,067
8	(9,9,7)	8+1/3	6,46	0,050	0,051

Kinks 2[(m+1,m-1,m)]

m	(h,k,l)	$l_K/a_\parallel$	Vicinal angle, α [°]	d_{Pt}^{-1} [Å^{-1}]	d_{Rh}^{-1} [Å^{-1}]
1	(2,0,1)	1,0	39,23	0,255	0,261
1,5	(5,1,3)	1,5	28,56	0,202	0,207
2	(3,1,2)	2,0	22,21	0,166	0,170
2,5	(7,3,5)	2,5	18,09	0,140	0,143
3	(4,2,3)	3,0	15,23	0,120	0,123
3,5	(9,5,7)	3,5	13,13	0,106	0,108
4	(5,3,4)	4,0	11,54	0,094	0,096
4,5	(11,7,9)	4,5	10,28	0,085	0,087
5	(6,4,5)	5,0	9,27	0,077	0,079
5.5	(13,9,11)	5,5	8,44	0,071	0,072
6	(7,5,6)	6,0	7,749	0,065	0,067
7	(8,6,7)	7,0	6,653	0,056	0,058
8	(9,7,8)	8,0	5,828	0,050	0,051

A4 General aspects of XPS

In this appendix we will deal with more general aspects of the X-ray photoemission (XPS) technique. XPS is based on the photoelectric effect discovered by Hertz in 1887 [282] and later explained by Einstein in 1905 [283]. Impinging photons on a material can release electrons if the energy of the light is larger than a material specific constant called work function (ϕ): the minimum energy required to eject an electron from a certain material. If one is able to analyze the amount of electrons as a function of their kinetic energy E_k, it will be noted that there are strong intensity variations, corresponding to element-specific excitations of inner electrons. The device to do the detection is called electron analyzer. Inside this analyzer the electron will gain some energy, the work function of the material from which the analyzer is made (ϕ_A). Since sample and detector are electronically connected, their Fermi levels are aligned. This finally leads to the photoemission equation given already in Equation 2.4 as $E_k = h\nu - \phi_A - E_B$, being $h\nu$ the energy of impinging photons, and E_B the binding energy of the excited electronic level. Due to the described Fermi level connection of sample and analyzer, the sample work function ϕ_S does not play any role in Equation 2.4 [284].

Nowadays, a HemiSpherical Analyzer (HSA) is typically used to monitor the intensity of the photoelectrons as a function of their energy; details about their operation can be found in the second Chapter of Ref. [194] and the web page of common manufactures [285, 286]. Briefly, the HSA comprises two different hemispheres separated by a gap, in order to allow electrons to travel [194]. The trajectory of the negatively charged electrons inside the HSA can be tuned by controlling the voltage applied between the outer and inner hemispheres of the electron analyzer. After a proper calibration of the spectrometer, one can correlate the kinetic energy of the incoming electron to the voltage applied between both hemispheres. Only the electrons with a certain energy can travel between the hemispheres, while electrons of a smaller (higher) energy will collide on the inner (outer) hemisphere not reaching the detector. Hence, we can count the number of electrons arriving to the detector as a function of their kinetic energy by ramping the voltages at both hemispheres, and in this way obtain an electron spectrum. The counting itself is done by an electron multiplier to increase the signal to noise ratio. This can be either achieved with one or several channeltrons or with a channel electron multiplier, the latter one allowing allowing to significantly increase the number of photoelectrons detected [287]. Since the electrons leave the sample with a remarkable velocity, they are slowed down prior to the HSA by a set of lenses. A correction factor is then applied by the detector to calibrate the E_K scale.

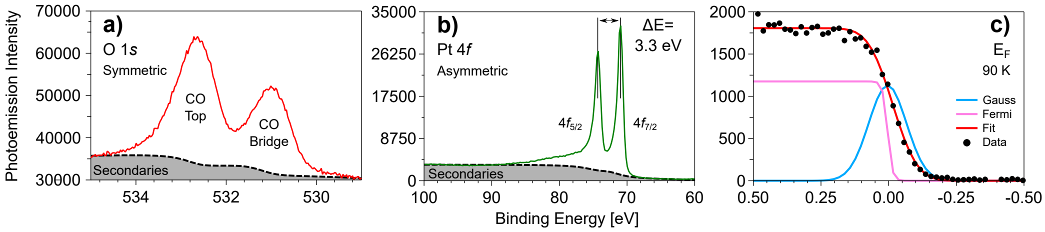

Figure A3: General features of photoemission spectra. **a)** O 1s region after exposing a Pt(111) surface to 10 L CO, showing two symmetric peaks related to CO adsorbed in top and bridge sites. **b)** Pt 4f scan of a Pt(111) sample after cleaning, with two distinct components arising due to the spin-orbit coupling of the 4f levels. **c)** Fermi level acquired at 90 K on Pt(111), showing the Fermi and Gauss components used for extracting the overall resolution.

Three different spectra are sketched in Figure A3 in order to discuss some common, important properties of photoemission spectra. Several features have to be taken into account:

- **Background**. This encompasses the additional intensity, apart from the lines themselves, that contributes to the spectrum (light grey areas in Figure A3). Inelastic scattering *with the metal lattice* is a frequent event in escaping photoelectrons, causing them to loose a portion of their energy [194]. Hence, they will be detected at higher higher E_B (lower E_K) as compared to that of the the main peak. These scattered (or *secondary*) electrons give rise to the characteristic shape of the so-called Shirley background [288].
- **Shape of the peaks**. A closer look to the spectra of Figures A3a,b) reveals that their peaks are remarkably different. On one hand, the intensity of the O 1s lines decays a few eV above their maximum: they are *symmetric* functions, whose broadness is determined by the *width* of the peak. On the other hand, the Pt 4f peaks extend several eV at the larger binding energy side. Due to this characteristic tail at lower kinetic energy, they are called *asymmetric*.
  - A symmetric photoemission peak follows a Lorentz distribution [191], although it has to be convoluted with a Gauss profile to take into account the broadening of the peaks due to the experimental resolution (see below). For simplicity, a Voigt profile (linear combination of lorentzian and gaussian) is then used.

  - The asymmetry arises due to the interaction of valence band electrons with the holes left on the sample (electron-hole pairs), giving rise to their easily detectable shape. The coupling with electron-hole pairs causes the photoelectron to lose energy, increasing the intensity at larger binding energies. Their photoemission intensity decays as the interaction energy increases [191], intuitively due to the inability of electrons to leave the sample if they are strongly attached to the hole. These peaks are usually referred to as *metallic*, as they are the typical lineshape for metals.

- **Spin-orbit splitting**. The Pt $4f$ spectrum is shown in Figure A3b), consisting of two emissions (a doublet). They are labelled as $4f_{7/2}$ and $4f_{5/2}$, with higher and lower intensity/E_K, respectively. This is the so-called spin-orbit or *j-j* interaction: the electron has a certain angular momentum, and the same applies for all electron levels with orbital quantum number $l \leq 1$ (p, d, f shells). Hence, there will be an interaction between the spin moment of the electron and that of the orbital, breaking the degeneration. This will give rise to two well-defined orbital levels, detected as two different photoemission peaks. It is noteworthy that every additional feature, such as losses, in the higher-intensity part *must also appear* in the lower-intensity region, since the levels are splitted. The intensity ratio (orbital-specific) and energy difference (both orbital- and element-specific, ΔE) between the orbitals was tabulated by Moulder *et al.* [289].

- **Resolution and Fermi level**. In Figure A3c) we sketch a Fermi edge measured for a temperature of 90 K. A Fermi-Dirac function at the aforementioned temperature cannot provide a reasonable fit to the data: the function is broadened. The sole act of measuring cannot be separated from the "error" of the experiment itself, which follows a normal (gaussian) distribution. That "error" results from the energetic broadening due to the experimental resolution of the measurement caused by (i) the linewidth of the photon beam and (ii) the energy resolution of the analyzer. As a result the thermally broaden Fermi-Dirac function has to be convoluted by a Gaussian function characteristic for this experimental resolution [191]. This same Gausian function has to be used later to convolute the above mentioned peak profiles in order to fit either the gas induced peaks or the metal substrate ones.

Appendix B: c-Pt(111)

Experimental methods

- **Sample cleaning and characterization.** The c-Pt(111) sample is described in Figure 2.4. Briefly, in this curved crystal vicinal angles up to ±15° can be explored, hence the (553) and (223) surfaces may be reached close to the two edges. Standard vacuum techniques are employed for cleaning the sample, namely Ar^+ sputtering at 1 kV ion energy, annealing at 1000 K in $5 \cdot 10^{-8}$ mbar O_2 and final flashes to 1100 K. The cleanliness was checked by XPS and LEED. The latter showed the splitting pattern presented in [207].

- **Photoemission experiments.** CO chemisorption experiments were performed in UHV at the I311 beamline of the Max II synchrotron (Sweden) [290], in normal emission and grazing incidence geometries.

  NAP-XPS CO oxidation experiments were conducted at the 23-ID-2 beamline of the NSLS-II synchrotron in New York (USA) [200, 291], also at normal emission geometry but at 50° incidence. CO and O_2 (purity $> 99.98\%$, Matheson) were dosed into the chamber using high precision leak valves. The pressure was monitored using a hot cathode ion gauge ($p < 10^{-5}$ mbar) or a capacitance manometer ($p > 10^{-5}$ mbar), while the temperature of the sample was monitored using a K-type thermocouple located between the sample and the heater. A pyrolitic boron nitride heater was employed, unless else noted. The gases close to the sample were monitored using a mass spectrometer located in the second differential pumping stage of the analyzer [45].

- **Photoemission peak analysis.** The peak fitting was performed using the CasaXPS software [292]. Doniac-Šunjić lineshapes convoluted with a Gaussian profile were considered for the C 1*s* peak fitting [293], adding a Shirley-type background [288]. T_T was remarkably more asymmetric than the other CO features, which shared a similar value. Step species (S_T and S_B) were broader than the other ChemCO contributions, while T_T was slightly wider than T_B.

With respect to the vibrational contributions of $\mathrm{T_T}$ sites [63, 67, 236], they were constrained to have the same peak parameters (width, asymmetry...), binding energy distance to $\mathrm{T_T}$ and height ratio derived at the (111) plane at the spectra obtained at other α. Their area was added to that of $\mathrm{T_T}$ for the coverage calibration. We added two vibrational features at 0.3 eV and at 0.6 eV distance to the main $\mathrm{T_T}$ emission. Similar contributions contributions corresponding to satellites of other CO species were not perceived.

The O 1s peaks could be reasonably fitted with symmetric Voigt profiles, hence we did not considered Doniac-Šunjić lineshapes.

- **UHV coverage calibration.** We assumed CO coverage saturation at the (111) plane after the 10 L CO dose, leading to a 0.5 ML, $c(4 \times 2)$ superstructure [52, 53], with CO molecules in $\mathrm{T_T}$ and $\mathrm{T_B}$ positions equally coating the surface [55]. Since PhotoElectron Diffraction (PED) features may arise [252, 294–297], and as discussed by Kinne *et al.* [55], a correction needs to be applied to $\mathrm{T_B}$ so it has the same coverage as $\mathrm{T_T}$ at the (111) plane. In our case, this correction factor was 1.4. After correcting the intensity variation of bridge species ($\mathrm{T_B}$ and $\mathrm{S_B}$) as a function of α, the intensity of the individual species at each of the points of the α-scan was converted to coverage knowing that the intensity of $\mathrm{T_T}$ at the (111) plane equals 0.25 ML.

- **NAP coverage calibration.** We have discussed in Section 3.2 how the CO anchored at steps remains virtually unaltered as the temperature increases during a CO oxidation experiment. Hence, it seems adequate to assume that the steps of the vicinal surfaces feature the same coverage in UHV and in NAP conditions. In fact, we have observed this phenomenon during the experiments of Chapters 4 and 5: at low temperature, far away from ignition, the step coverage at Pt and Rh vicinals is retained from UHV to NAP. Therefore, we decided to use the step coverage in UHV to calibrate those of the NAP measurements. We fitted the variation with α of the step-CO photoemission intensity [$I(\alpha)$] during the CO oxidation essays at 350 K and the step UHV saturation coverage [$\Theta_S(\alpha)$] to our W-model (Equation 2.3). Since we are assuming that the coverage in UHV and NAP at 350 K are the same, hence by simply dividing the slope of fit of $I(\alpha)$ by that of $\Theta_S(\alpha)$, one may obtain a factor to convert intensity to coverage during the NAP experiments. In other words, we are forcing the fit of $\Theta_S(\alpha)$ to be the same in UHV and in NAP at 350 K, in order to preserve the step saturation. This fit is sketched with a dashed black line in Figure 3.3b).

B1 Symmetric ignition: C 1*s* analysis

The C 1*s* measurements shown in Figure B1 were acquired right after the O 1*s* region during the heating ramp depicted in Figure 3.2. We will just focus on the ignition of the CO oxidation at different Pt surfaces now; a more profound discussion on the chemical species observed during the poisoned stage is presented elsewhere in Chapter 3.

At a temperature of 515 K, quite below the ignition temperature, only chemisorbed CO (ChemCO, 286.7-285.8 eV) species are observed [55, 63]. The ChemCO intensity steadily decreases with the temperature, reflecting how the ChemCO starts to desorb. Mimicking Figure 3.2, all ChemCO vanishes simultaneously in all surfaces right after heating the sample to 560 K, marking a symmetric ignition at A- and B-type Pt vicinals. The $CO_{(g)}$ signal (doublet at 290.2 eV) is replaced by $CO_{2(g)}$ (291.2 eV) as the ignition approaches, since the reaction is taking place. The shift in its position after the ligth-off is caused by a change of the surface work-function [38].

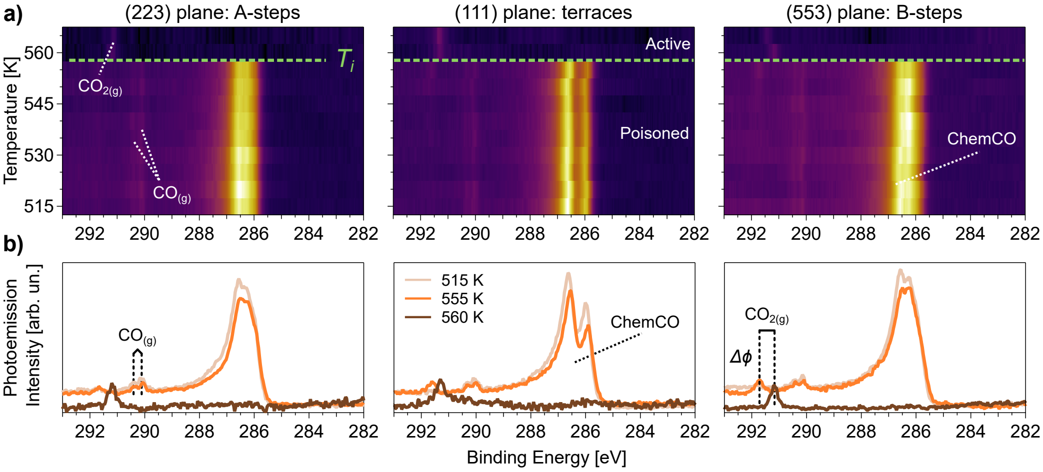

Figure B1: C 1*s* heating ramp at relevant c-Pt(111) positions. **a)** C 1*s* temperature ramp as color plots for the (223) [left], (111) [center] and (553) [right] planes, respectively. **b)** Individual spectra at characteristic temperatures [515 K (light orange), 555 K (orange) and 560 K (brown)] and planes. C 1*s* spectra were acquired at a photon energy of 650 eV under 0.7 mbar, 1:6 $CO:O_2$ ratio gas mixture (average heating slope of 5.5 K/h). They are complementary to those of Figure 3.2. The labels "Active" and "Poisoned" mark each of the stages of the CO oxidation. $\Delta\phi$ reflects the change of the work-function of the surface as it transitions towards the active stage during the ignition [38], which occurs at $T_i = 560$ K.

B2 Hysteresis of the reaction at Pt vicinals

In a different experiment, we studied both the ignition (T_i) and cooling (T_c) of the CO oxidation across Pt close-packed vicinals. We exposed the sample to a 1.0 mbar, 1:4 CO:O_2 gas mixture and subsequently heated the sample in 10 K steps (22.5 K/h in average). As shown in Figure B2, we monitored the (111), (223) and (553) surfaces at each of the temperatures.

This CO oxidation experiment mimics that described in Appendix B1. At low temperature, the surface is covered by ChemCO, and only $CO_{(g)}$ and $O_{2(g)}$ are detected in the gas phase. Further heating yields a progressive decrease of ChemCO, which is simultaneously replaced by O-related species at 575 K at the aforementioned surfaces. This marks the symmetric ignition of the reaction. At this point, $CO_{(g)}$ vanishes, $O_{2(g)}$ decays and $CO_{2(g)}$ abruptly boosts, indicating that the surface has reached the active stage. After heating to 585 K, we started to cool the sample. At 525 K, the reaction quenches in parallel (ChemCO appears and the O/Pt species vanish) again in all three surfaces, marking a simultaneous cooling of the reaction.

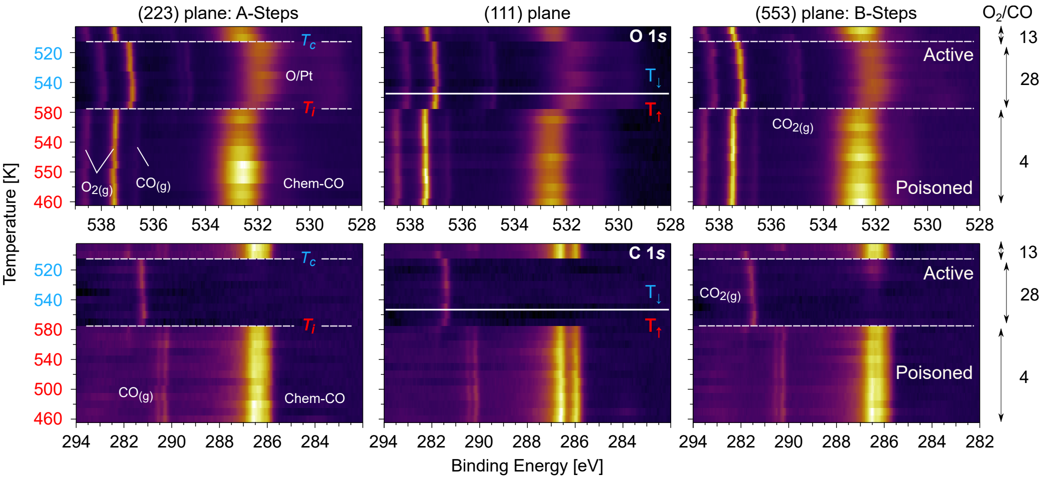

Figure B2: Hysteresis cycles at relevant c-Pt(111) positions. Temperature color plots of the O 1*s* (top row) and C 1*s* (bottom row) regions during a heating (red scale, $T_{\uparrow}$) and cooling (blue scale, $T_{\downarrow}$) cycle. The (223), (111) and (553) surfaces were sequentially monitored at 1.0 mbar, 1:4 CO:O_2 gas ratio, in 10 K steps (22.5 K/h in average). Both T_i and T_c of the reaction occur simultaneously at 575 and 525 K, respectively. As sketched at the right side of the figure, the ratio O_2/CO in the QMS increases during ignition, since the CO is consumed and the reaction reaches mass transfer limit. See Figure 3.2 for additional details.

B3 Structures used for the calculations

Each of the structures presented in Table 3.1 are illustrated in Figure B3. They correspond to:

- **CO - a)**: CO-T_T molecules in a 0.25 ML, (2×2) superstructure.
- **CO-O_{fcc} - b)**: 0.25 ML CO-T_T and 0.25 ML O in hollow fcc positions.
- **CO-O_{sub} - c)**: 0.25 ML CO-T_T and 0.25 ML O in subsurface tetrahedral sites, both sharing a single Pt atom.
- **CO-O_{sub}* - d)**: 0.25 ML CO-T_T and 0.25 ML O in subsurface tetrahedral sites without sharing any Pt atom.
- **CO-2O_{sub} - e)**: 0.25 ML CO-T_T and 0.5 ML O in both subsurface tetrahedral sites.
- **O_{sub} - f)**: 0.25 ML of O on subsurface hcp tetrahedral positions.

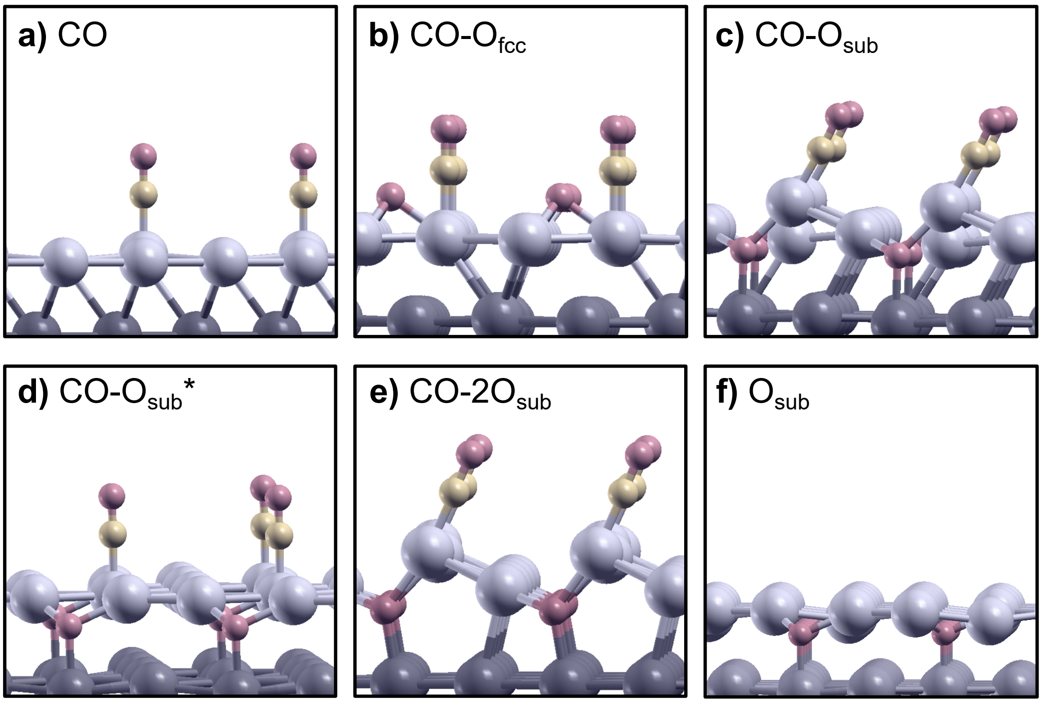

Figure B3: Structures used in the theoretical calculations. Structures considered in the DFT calculations for the characterization of the transient stage of the CO oxidation. See Table 3.1 for further details.

B4 PED effects at Pt vicinal planes

In Figure B4 we show the entire O 1s α-scans acquired simultaneously as those presented in Figure 3.3. A substantial increment of the total intensity with α was observed, which we attribute to enhanced CO-emission due to PED effects. These arise even at the (111) surface, since the $\mathrm{T_T}/\mathrm{T_B}$ ratio after CO saturation is far from the ideal value of 1 [24]. For these reasons between other, we decided to rely on the C 1s for the examination of the CO-poisoning layer. Species arising from CO dissociation are not distinguished in UHV, yet they are residual during CO oxidation conditions due to the high pressures and temperatures.

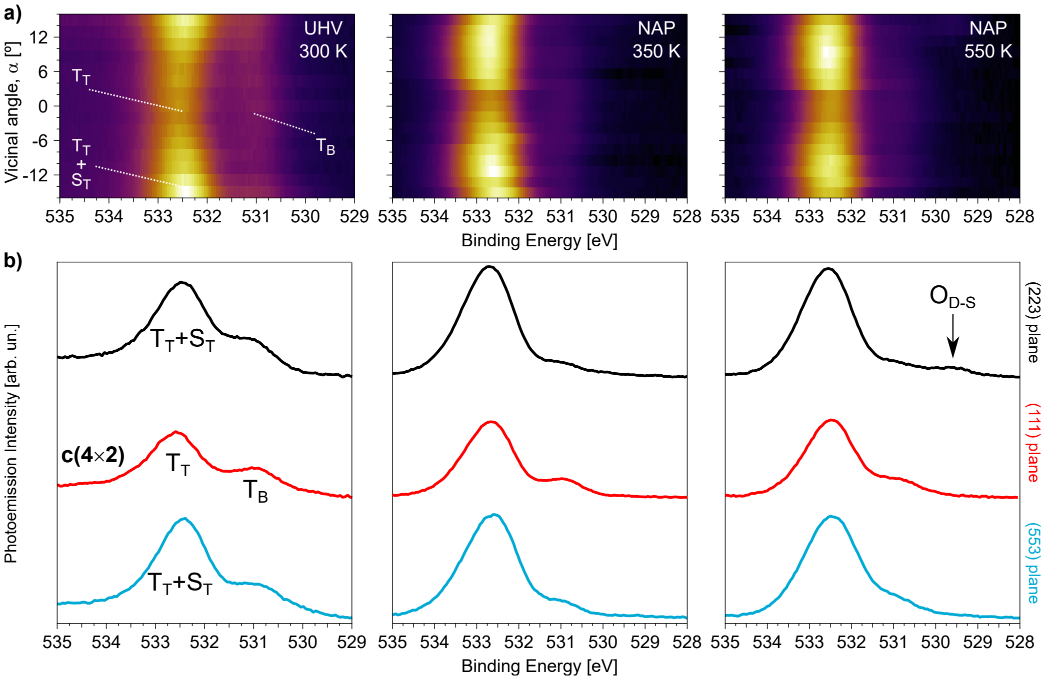

Figure B4: O 1s α-scans of the poisoned stage.
a) Intensity plots of the O 1s α-scans, together with **b)** characteristic spectra at the (223), (111) and (553) surfaces at different experimental conditions. They correspond to exposure to 10 L CO at 300 K (UHV 300 K, left column), and under a 1:6 CO:O_2 gas mixture at 0.7 mbar at 350 K (NAP 350 K, center column) and 550 K (NAP 550 K, right column). Experiments were acquired at 400 eV (UHV) and 650 eV (NAP) of photon energy. $\mathrm{T_T}$, $\mathrm{T_B}$, $\mathrm{S_T}$ and O correspond to Terrace-Top, Terrace-Bridge, Step-Top CO molecules and atomic oxygen anchored to the surface.

B5 O_2 chemisorption reference experiments

In order to have a proper reference for the analysis of the active stage of the reaction, we exposed the sample to 10 L O_2 at 300 K. We subsequently cooled down to 90 K to reduce the vibrational broadening of the peaks. This is a fine approach for the CO experiments, yet it is not as adequate for the O_2, since adsorption from residual gases (mainly CO) was observed. A similar phenomenon was observed during similar experiments conducted on the k-Pt(645) sample (Appendix C4). The complete α-scan and selected fitted spectra after the 10 L dose are shown in Figure B5.

A closer look at the spectra at the (111) plane [Figure B5a), center] reveals a large feature at 529.8 eV, which we readily identify as chemisorbed O in the hollow fcc position, O_{Terr} [52, 118]. In addition, two relatively large contributions are detected at 530.9 and 532.3 eV. As we discussed in Subsection 1.3.2, further oxidation of Pt(111) at 300 K requires strong oxidizers. Therefore, here we believe that contamination (CO, H_2O ...) are responsible for the observation. At low temperature, coadsorbed O and CO would not react, hence contributing to the O 1s region [55, 237]. The small peak around 528 eV, constant across the curved surface, is related to defects, as reported by Kim *et al.* at a similar energy and relative intensity [263].

The bottom panel shows the spectra at the (553) surface obtained after the O_2 dose. The main contribution, O_{Terr}, markedly increases and slightly shifts towards lower binding energy, possibly screening a similar configuration, i.e. hollow O, at the steps. The peak around 530.8 eV increases with the step density, indicating its step-like character. As for the contribution around 532.1 eV, it slightly shifts towards lower binding energy without decreasing its intensity. As we mentioned before, we believed that these two contributions are related to both uncharacterized Pt oxides and adsorption from residual gases from the chamber, namely CO and H_2O.

The situation is more complex at the (223) plane, since several additional peaks can be distinguished. O_{Terr} also increases and shifts, perhaps pointing to a similar hollow O species near the $\{100\}$ steps. The peaks around 531 and 532 eV grow as compared to the (111) plane. This could be expected, since adsorption from contaminants and oxide formation is more likely to occur at steps. In addition, a peak at 529 eV is now clearly distinguished in the photoemission spectra. It increases with α, which indicates that such species is adsorbed close to the step edge (O_{Step}). Since it increases only with the density of $\{100\}$ steps, we suggest that it corresponds to atomic O anchored at four-fold sites at these steps [227]. Another contribution is detected at 530.3 eV, which we attribute to PtO_2 [226, 256].

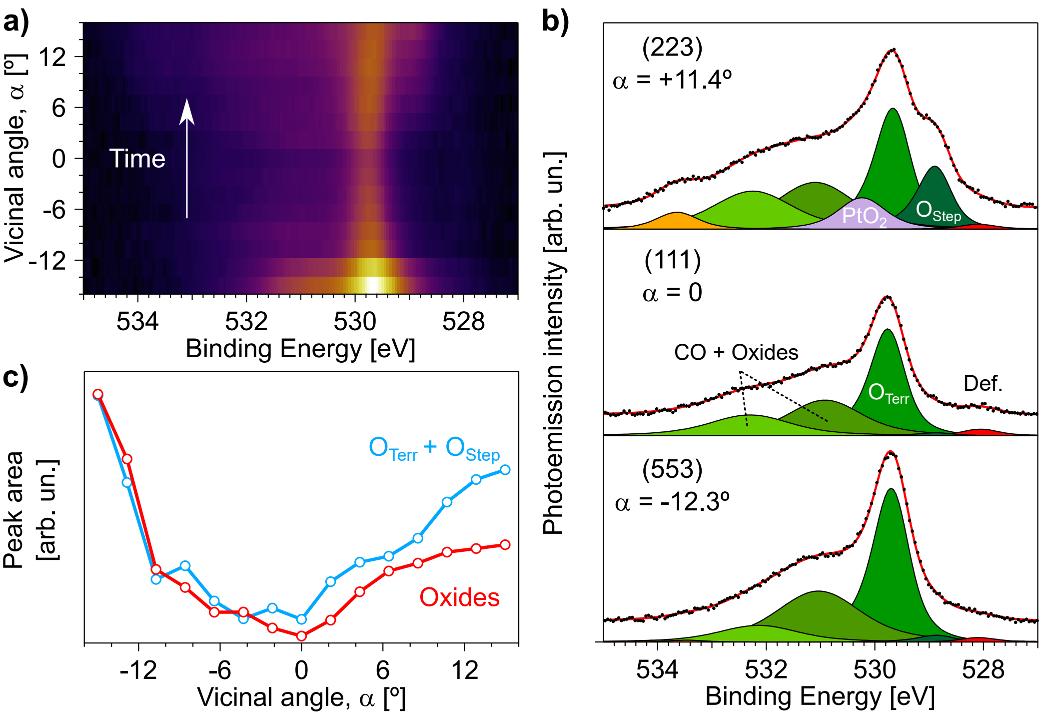

Figure B5: Curvature map after a 10 L O_2 dose at 300 K.
a) Intensity plot of the O 1s α-scan, together with **b)** characteristic spectra at the (223), (111) and (553) surfaces after exposure to 10 L O_2 at room temperature. Spectra were acquired at 90 K and 650 eV of photon energy. **c)** ChemO (O_{Terr}+ O_{Step}) and Oxides (all other contributions) evolution across the curved surface, showing a parallel increase of their intensity with the step density. See text for the description of each of the species and labels. We also indicate the direction (time) at which the scan was taken.

We also detect one additional peak at 533.6 eV. Several possibilities arise: another oxide with a different oxidation state, e.g. , Pt_3O_4 [79], physisorbed O_2 [270] or CO adsorbed on some of the oxides [248] are possible candidates for this contribution, yet we cannot speculate more without additional data. Additional C 1s nor Pt 4f were not acquired, hence we are forced to end the discussion here. It is also important to mentioned that as we reach the end of the α scan (from -15 to +15°), more and more species appear, pointing to adsorption of residual gases on the sample. To conclude, although some of species may be related to contamination, the trend is clear: the amount of oxygen increases with α, in clear contradiction with the α-scan acquired during the active stage discussed in Section 3.5.

B6 Active stage at a 2:3 CO:O_2 ratio

We also scanned the curved surface in a different experiment, in this case under 0.5 mbar, 2:3 CO:O_2 ratio conditions. At this gas mixture, the Pt curved surface ignited at 575 K, hence the curved surface was α-scanned at this temperature. The results are shown below, mimicking the increase in the total O coverage with α observed for the O_2 dosage experiments performed in UHV (see Figure B5). We used a Pt heater for this experiments. Since it consumes gases from the chamber, the lower T_i is expected in spite that the the CO:O_2 ratio is larger.

The spectra at the (111) plane [Figure B6b), center] consists on two well-defined peaks. The smaller one at 529.8 eV corresponds to atomic O adsorbed in hollow fcc sites (O_{Terr}) [52], and the larger one at 531.6 eV is related to an unknown oxide (Oxide). Considering now the stepped surfaces, O_{Terr} increases at the (553) plane, yet decreases at the (223) surface [Figure B6b), right and left, respectively]. However, O_{Step} (atomic O anchored near the steps, possibly on four-fold coordination [227]) rises at the former A-stepped plane, and the combination of them roughly equals that of the other side. A similar ChemO coverage is observed, even though the species are different.

To end with, the Oxide peak markedly grows with α, in clear contradiction to the behaviour described in Section 3.5. Since the structure of this oxide is unclear, it is difficult to speculate about such behaviour. The main difference between the experiments is the CO:O_2 ratio (2:3 here *vs* 1:6 for Section 3.5). We postulate two simple explanations for this difference between experiments. On one side, the gas mixture of the experiments described in Section 3.5 is oxidative, which may enhance the otherwise kinetically limited oxidation of the terraces [79, 110, 120, 256]. Since the space occupied by terraces is generally larger than that of the steps, the oxidation of the terraces would easily explain the decay of Oxide with α. On the other side, the CO:O_2 ratio of the current experiment is closer to be stoichiometric, hence one would expect more reduced terraces at these conditions. The growth of Oxide with α can then be explained by the additional oxidation of steps, very likely since they have a larger tendency to develop oxides [96, 110, 114].

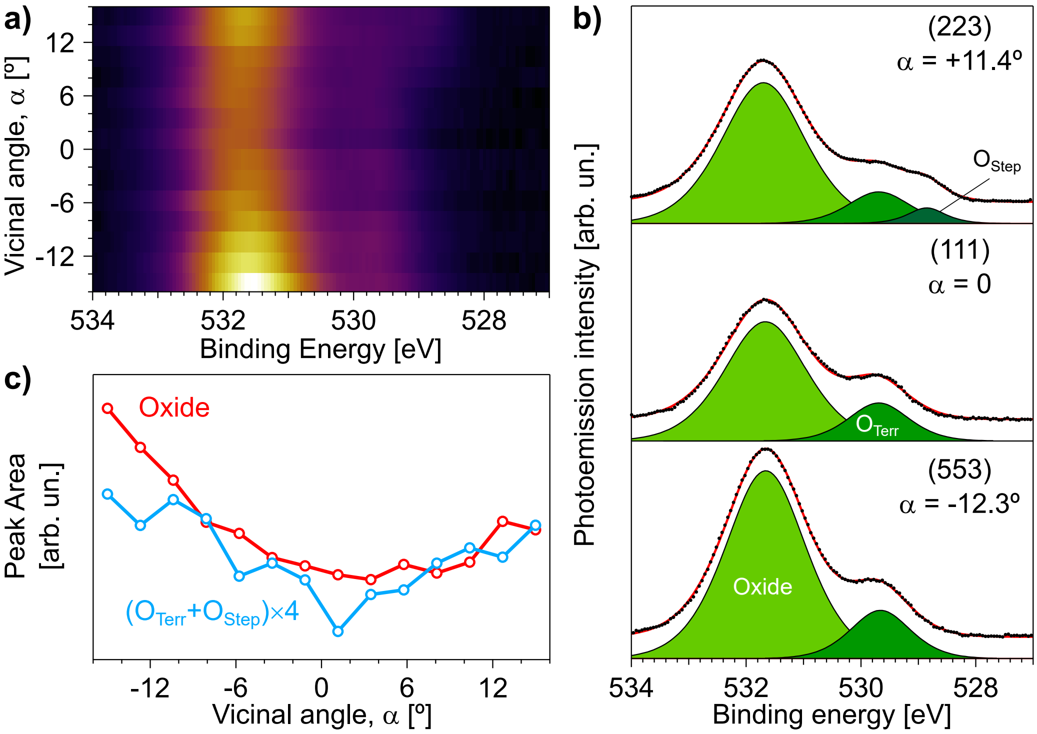

Figure B6: Additional O 1*s* maps during the active stage.
a) O 1*s* α-scan color plot, together with **b)** individual spectra at the (223), (111) and (553) surfaces in a 0.5 mbar, 2:3 CO:O_2 gas mixture at 575 K (active stage). **c)** ChemO ($O_{Terr}+O_{Step}$) and Oxide (all others) evolution across the curved surface, showing a parallel increase of their intensity with the step density. See text for the description of each of the species and labels.

Appendix C: k-Pt(645)

Experimental methods

- **Sample cleaning and characterization.** The k-Pt(6459 sample is described in Figure 4.1. It features the (645) plane at the center of the crystal, while the (111) and (312) surfaces are located at each of the edges of the crystal. The sample was cleaned with several cycles of Ar^+ sputtering (1 kV), O_2 annealing ($1 \cdot 10^{-7}$ mbar, 800 K) and final flashes (950 K) until no contaminants were detected by means of XPS. Where available, the LEED of the sample was checked in order to probe the correct structure of the clean curved surface (see Appendix C1).

- **UHV reference experiments.** Chemisorption measurements were carried out in UHV at the SuperESCA beamline at the Elettra synchrotron in Trieste (Italy) [298] in normal emission geometry. The peak fitting was performed using the *lmfit* package of Python [299]. Doniac-Šunjić lineshapes [293] convoluted with a Gaussian were considered for the peak fitting, unless the opposite is stated. A Shirley-type background was subtracted during the fitting [288].

  Small peaks ascribed to vibrational excitations of CO molecules could be distinguished in the C 1*s* spectra [234–236], hence they were included in the fitting procedure to further improve it. As extracted from the fitting at the (111) surface, such satellites were fixed at 220 meV towards higher binding energy above the position of the main contribution, while the intensity ratio derived was 11.5 % for T_T and 10 % for T_B sites. The other parameters (width, asymmetry...) were constraint to those of the major peak. Their area was added to that of the main feature for quantification. Even though T_T- and T_B-CO yielded similar width values, T_T was markedly more asymmetric (65%) than T_B. Both step-CO peaks have a similar asymmetry as T_B, and they are approximately 20% broader compared to their terrace analogous. The satellites were also included for both S_{T6}- and S_{T8}-CO, using the same intensity ratio for the satellites as for T_T-CO.

- **CO coverage calculation at UHV saturation.** The $c(4\times2)$ superstructure observed at the (111) plane was used as a reference for coverage calibration. It corresponds to a 0.5 ML coverage [53], where both $\mathrm{T_T}$ and $\mathrm{T_B}$ equally coat the surface with 0.25 ML each [52]. As explained by Kinne *et al.* [55], deviations from the theoretical 1:1 $\mathrm{T_T}$:$\mathrm{T_B}$ area ratio in the C 1s can arise due to PED effects, therefore different factors are required in order to properly calculate the coverage of $\mathrm{T_T}$ and $\mathrm{T_B}$. The obtained ratio between $\mathrm{T_T}$ and $\mathrm{T_B}$ at the (111) plane was 0.9, quite close to the theoretical value of 1. Knowing that both $\mathrm{T_T}$ and $\mathrm{T_B}$ have a saturation coverage of 0.25 ML at the (111) plane, two different area-to-coverage factors were defined in order to calculate each coverage curve presented in Figure 4.4e). As top species, we used the same factor for $\mathrm{T_T}$- and $\mathrm{S_T}$-CO.

- **Uptake and desorption measurements.** Both the CO uptake and desorption experiments have lower statistics and resolution (bigger beam slit and analyzer in *fast-scan* mode) as compared to the high-resolution spectra of the α-scans, therefore neither the satellites nor the two different step-CO peaks could be resolved.

  The crystal was annealed after each of the CO uptakes in order to remove the adsorbed CO and prevent the accumulation of graphitic "C". The coverage at the uptake experiments was calculated assuming that the CO adsorption at $\mathrm{T_T}$ sites is saturated at the end of the (111) plane measurement. This coverage corresponds to 0.25 ML [52, 55]. As explained above, a factor needs to be applied to $\mathrm{T_B}$ in order to properly calculate the coverage. Since this correction factor can only be extracted from the spectra of the CO-saturated (111) plane, the same factor obtained above was used, as the photon energy and geometry are the same.

  During the desorption experiments, the photon energy was different from the other CO chemisorption measurements (650 eV to detect additional O species). Hence it is not possible to use the previously obtained coverage calibration factors. Therefore, the initial spectra at the (111) surface was used as calibration. Assuming CO saturation at the beginning of the desorption experiment, the area of CO adsorbed at $\mathrm{T_T}$ and $\mathrm{T_B}$ sites equals 0.25 ML each [55]. Individual area-to-coverage factors were calculated for top ($\mathrm{T_T}$ and $\mathrm{S_T}$) and bridge ($\mathrm{T_B}$) CO species using the areas of $\mathrm{T_T}$ and $\mathrm{T_B}$ at the (111) plane in order to convert the photoemission intensity to coverage. The factor obtained from $\mathrm{T_T}$ was used to calibrate the graphitic "C" coverage.

- **Oxygen exposure.** In the literature, the O 1s peaks are fitted to either symmetric (Gauss, Lorenztian, Voigt) [38, 40, 88, 114, 120, 130, 132, 263] or asymmetric (Doniac-Šunjić, asymmetric Voigt) functions [30, 118, 255]. In our case, several symmetric features were required to properly fit the Pt(111) spectra after the 50 L O_2, similarly as in Ref. [263]. This would indicate the formation of several oxides at the (111) plane at UHV and 300 K, which is unlikely (see Subsection 1.3.2). However, a single Doniac-Šunjić peak convoluted with a Gaussian profile was enough for a proper fitting of the spectrum at the (111) surface (Figure 4.5c), therefore this lineshape was chosen for the ChemO contribution. Since we postulate that O_K is also chemisorbed O, we also chose an asymmetric lineshape for this contribution. The width of both ChemO and O_{Kink} were quite similar, illustrating their similar electronic structure [40].

  Oxide species have larger O density than chemisorbed phases, and by definition have no metallic character. Therefore, the electron-hole excitation losses are quenched, and the asymmetry should disappear, yielding symmetric features in the spectra. The width of the oxide peak around 530.5 eV was almost the double, indicating a larger oxide character [40] compared to ChemO and O_K.

- **High pressure photoemission experiments.** NAP-XPS experiments were performed at the 23-ID-2 beamline of NSLS-II (New York, USA, see Appendix B).

  It is important to mention that the sample at that time was heated using a Pt filament located in the back of the sampleholder. This thin wire is at a higher temperature than the sample. Being from the same catalytic material, this filament itself will ignite the reaction prior to the colder sample. This will consume both $CO_{(g)}$ and $O_{2(g)}$ from the chamber, resulting into a decrease of T_i of the sample due to a lower partial pressure of $CO_{(g)}$ and $O_{2(g)}$. We have sketched this effect in Section 1.2. The CO oxidation experiments described in Chapter 3 were carried out later using an inert boron nitride (BN) heater. These new experiments confirmed that the activity of the surface is low or none if the surface of the sample is CO-covered. For this reason we classify the surface as poisoned if a significant amount of chemisorbed CO is detected. Again, the $CO_{2(g)}$ production observed in both the QMS and NAP-XPS is caused by the reaction onset at the Pt filament, not at the sample itself.

Regarding the fitting procedure of the poisoned stage, ChemCO and graphitic “C” peaks were fitted using asymmetric Doniac-Šunjić lineshapes convoluted with a Gaussian profile [55]. The gas phase contributions were fitted using Voigt functions [38]. The $CO_{(g)}$ was fitted using a single, wide peak during the exposure to 0.1 mbar CO. However, up to three different components were observed in the CO oxidation experiments. CO adsorbed at T_T sites was found to be more asymmetric than T_B-CO. S_T-CO and the satellite T_T* were remarkably wider than the other two CO-related contributions. For the latter, this may indicate that we cannot resolve S_{T6} and S_{T8} in the NAP-XPS experiments. The position of S_T was constant in all probed vicinal surfaces, although a smooth displacement of the T_T, T_T* and T_B features towards the position of S_T was detected at increasing vicinal angle due to a change in the strain of the terraces with α [207].

Considering the fitting routine of the active stage, Doniac-Šunjić lineshapes convoluted with a Gaussian profile were used to fit both ChemO and O_K contributions. Voigt functions were used for the oxides and the gases, since they have no metallic character and therefore its photoemission peaks should be symmetric. The $O_{2(g)}$ was fitted using two peaks at 537.4 and 538.5 eV [38], while up to three different components at 0, +0.2 and +0.4 eV from the position of the main contribution (535.2 eV) were used to properly extract the $CO_{2(g)}$ features. Note that the binding energy of the gas phase peaks shift with the step density across the α-scans [206].

The CO coverages were derived from the C 1s, knowing that the coverage of CO adsorbed at T_T and T_B sites corresponds to those of the $\sqrt{19}$-13CO arrangement in the (111) surface at 0.1 mbar CO at room temperature [24]. Individual area-to-coverage factors were defined for T_T-CO (and hence S_T-CO) and T_B-CO using the spectrum at the (111) plane at 0.1 mbar and 300 K, and where applied to the other spectra of the α-scans to calculate their evolution with the step density and temperature. As for the quantification of O_{Subs}, the area of T_T-CO at 0.1 mbar CO and 300 K (0.37 ML) was used as calibration.

The oxygen coverage during the active stage of the CO oxidation was calibrated assuming a total oxygen coverage of 0.4 ML in the (111) plane at 0.4 mbar O_2 at room temperature (reference experiment), since is the reported value for Pt(111) under 0.7 mbar O_2 at room temperature [30]. Despite the O_2 pressure is smaller in the current experiment, the Pt oxidation is kinetically limited [79, 110, 120, 25], hence the errors using this calibration are negligible.

C1 Clean and CO-covered surface: LEED

The Low Energy Electron Diffraction (LEED) patterns of the curved sample were checked for sample surface orientation and superstructure evaluation. The characteristic hexagonal diffraction pattern corresponding to the (111) fcc terraces was found close to the border of the crystal edge [264]. Away from that point, the LEED pattern reveals a steady split of the LEED spots. This splitting results from the additional lattice related to the ordered steps of the surface [102]. The splitting increases with the step density due to the narrowing of the terraces (and a shorter real lattice constant) [238], becoming very pronounced at the highly stepped (312) plane.

We also checked the LEED after the CO dosing. A sharp $c(4 \times 2)$ diffraction pattern was observed at the (111) plane, rapidly vanishing after electron beam exposure. The kinked surfaces only featured the characteristic splitting of spots due to the increasing step density, hence we conclude that CO molecules do not arrange in an ordered manner at the kinked vicinals and there is no step doubling. However, since the $c(4 \times 2)$ LEED pattern rapidly vanished at the (111) plane, another possibility is that we are disordering the adsorbate structure during the LEED measurement itself.

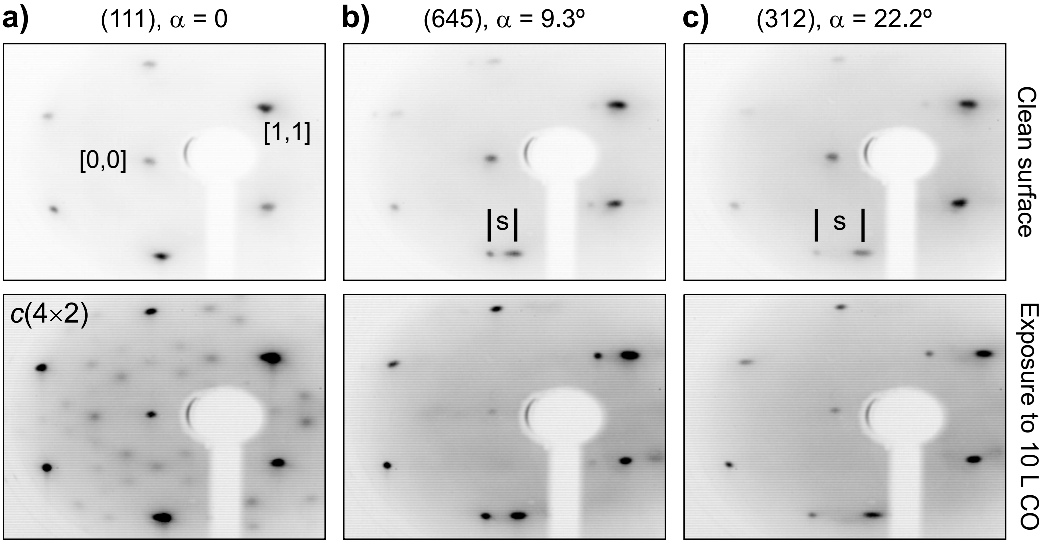

Figure C1: LEED patterns of the clean and CO-covered surfaces. a-c) LEED diffraction images obtained after cleaning the sample (top, 300 K) and after dosing 10 L CO (bottom, 90 K) at the (111), (645) and (312) planes, respectively. The increasing splitting distance of the spots as α increases is labelled as **s**. Positions of the [0,0] and [1,1] spots are also indicated in one LEED image.

C2 O 1*s* evolution during the CO desorption

The O 1*s* region was also recorded during the CO desorption experiments described in Subsection 4.1.2, in order to check for dissociation species and to track shifts of the T_T-CO peak, as observed during temperature ramps under CO oxidation conditions on Pt(111) (see Section 3.3). Therefore, a direct comparison between CO desorption experiments and the heating ramp during the CO oxidation would provide direct evidence on whether this shift is due to new chemical species arising from the reaction or it is concomitant to the desorption itself.

As shown below, no dissociation products were detected in the O 1*s* region in any of the studied surfaces. More importantly, no shift of T_T-CO was found at the (111) plane, indicating that the shift observed during the CO oxidation is not related to the desorption, but to the reaction itself. The peak does shift at the (645) and (312) stepped surfaces at higher temperatures, although this is caused by an earlier desorption of CO anchored at T_T sites (532.6 eV) prior to S_T positions desorption (532.3 eV) [63].

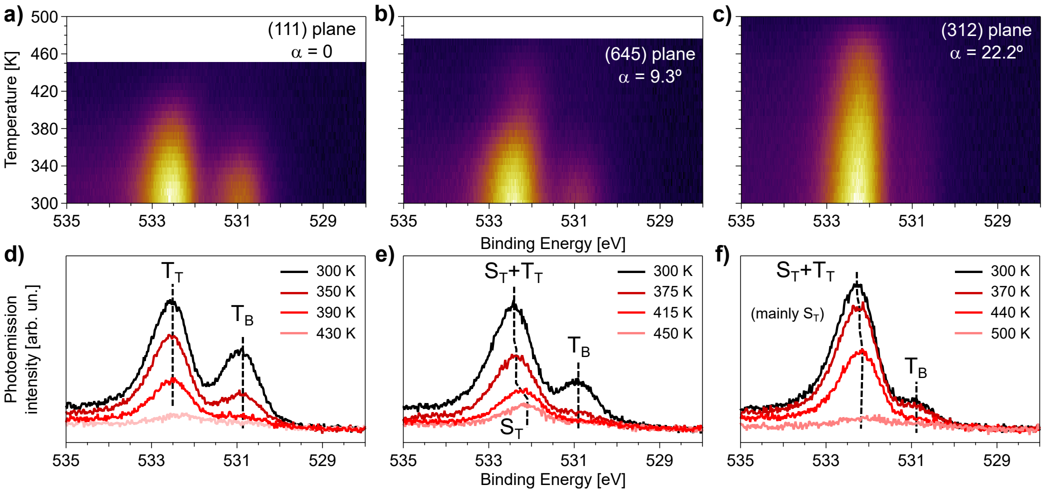

Figure C2: O 1*s* evolution during CO desorption cycles.
a-c) O 1*s* temperature ramps during the CO desorption experiments of Subsection 4.1.2. **d-f)** Separate spectra for the (111), (645) and (312) planes at different temperatures. Dashed black lines indicate the approximate position of peak maximum in order to illustrate the shifts of the peaks. Experiments were carried out at a photon energy of 650 eV and a heating slope of 5 K/min.

C3 O 1s α-scans at low and high CO dose

The O 1s region was also scanned at 650 eV after the exposure to 0.25 and 10 L CO at 300 K. All species are well resolved in the C 1s region (see Figure 4.4), although peaks from CO anchored at $\mathrm{T_T}$ (532.6 eV) and $\mathrm{S_T}$ (532.3 eV) sites are not resolved in the O 1s [63]. The LEED exhibits a $c(4 \times 2)$ pattern at the (111) plane, where $\mathrm{T_T}$ and $\mathrm{T_B}$ should be equally populated. It is clearly seen in Figure C3c) that the ratio between CO adsorbed at $\mathrm{T_B}$ positions (531.0 eV) and at $\mathrm{T_T}$ sites is not 1, reflecting that the O 1s spectrum at the (111) plane suffers from PED effects [24]. A closer look to the α-scans reveals an significant shift with α in the peak around 532.5 eV. This is expected: at low α, the main contribution is $\mathrm{T_T}$-CO. However, once the step density increases, $\mathrm{S_T}$-CO peak intensity builds up while $\mathrm{T_T}$-CO decreases. Both effects cause a shift of the broad O 1s peak towards low.

A substantial increment in the total intensity with α was observed. This effect is also attributed to enhanced O 1s emission due to PED effects and the curved shape of the crystals, and not to such large increase in the total coverage. The same intensity growth with α after CO saturation was observed for close-packed Pt vicinals, as described in Appendix B4.

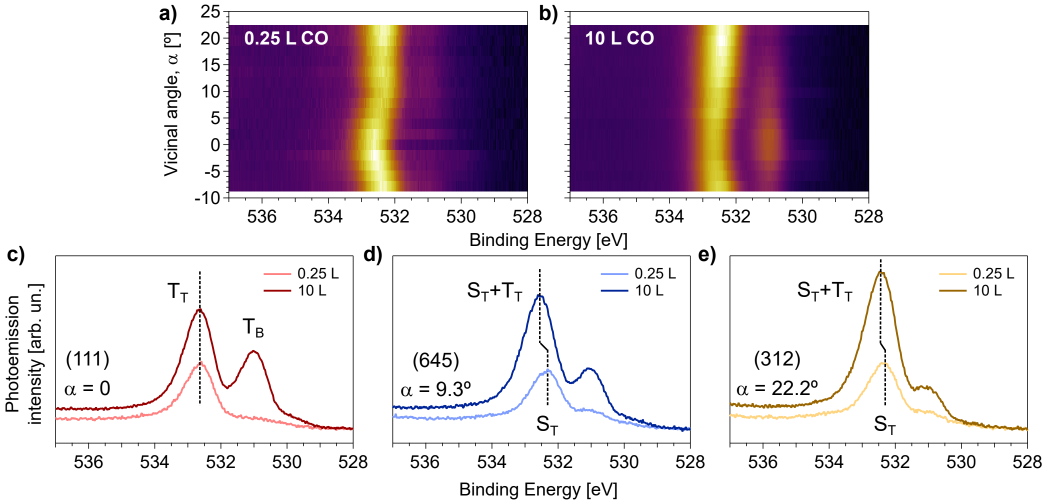

Figure C3: O 1s α-scans for the 0.25 and 10 L CO dose.
a,b) O 1s α-scans at 0.25 and 10 L CO doses, together with **c-e)** individual spectra for the (111), (645) and (312) planes. Vertical lines are added to emphasize the shift at increasing CO dose in the stepped planes. CO adsorbed as Terrace-Top, Terrace-Bridge and Step-Top are denoted by $\mathrm{T_T}$, $\mathrm{S_T}$ and $\mathrm{T_B}$, respectively. The surface was exposed to CO at 300 K, although the spectra were measured at 90 K. The photon energy was 650 eV.

C4 O_2 α-scan at low temperature

In order to study the O_2 adsorption and oxidation of Pt kinked vicinals, we exposed the k-Pt(645) sample to O_2 at 300 K. We subsequently cooled down to 90 K to decrease the thermal broadening of the photoemission peaks while maintaining the structure formed at 300 K. However, some CO adsorption from the residual gases of the chamber was found. This CO will not react with coadsorbed O at this low temperature, but will interfere with the analysis of the O-saturated surfaces. Therefore, it was decided to perform the same experiment on the clean surface at 300 K, as discussed in Subsection 4.1.4. We measured less points across the curved surface to speed up the experiment and to avoid CO sticking to the surface and possibly reacting with the oxygen species. Nonetheless, the tendencies at 90 and 300 K are similar. Both O_K and the oxide peak at 530.8 eV increase with the step density, while ChemO markedly increases with α and shifts towards lower values of binding energy. Therefore, although there is some small amount of CO it does not seem to significantly interact with the coadsorbed O *at low temperature*. It is noteworthy to mention that the initial surface was CO-free, and hence the O_2 saturation dose was reduced to 6 L O_2, as compared to the 50 L O_2 required to saturate the crystal when a small amount of CO was already adsorbed at 300 K.

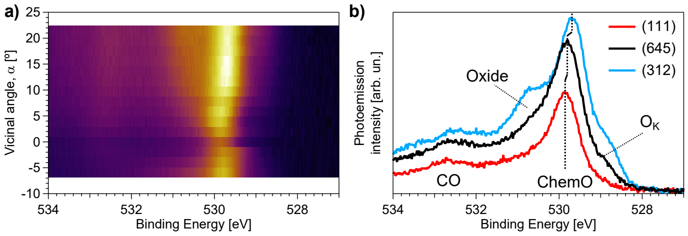

Figure C4: Surface scan for O-saturated sample at 90 K.
a) O 1*s* α-scans after exposure to 6 L O_2 at 300 K and subsequent cooling to 90 K. **b)** Individual O 1*s* photoemission spectra for the (111), (645) and (312) planes. O_K and ChemO allude to chemisorbed O at square sites at the kinks and at hollow sites at steps and terraces, while Oxide and CO stand for an uncharacterized oxide and chemisorbed CO molecules coming from residual gases from the chamber. Refer to Subsection 4.1.4 for more details about the nature of these chemical species. Experiments carried out at a photon energy of 650 eV.

C5 Ignition at different CO:O_2 ratios

We studied the CO ignition at Pt kinked vicinals at two different CO:O_2 gas ratios. In one experiment, we exposed the sample to 0.7 mbar, 1:1 CO:O_2 gas ratio. We heated the sample in 10 K steps while sequentially monitoring three points of the surface, namely the position of the (111), (645) and (735) planes. Here we show individual spectra extracted from the heating cycle discussed in Subsection 4.2.2. Due to a misalignment on the position, the most stepped surface in this experiment was the (735) surface ($\alpha = 18.1°$) and not the (312) plane ($\alpha = 22.2°$), yet the differences between these two surfaces are presumably negligible.

In the other experiment, we exposed the sample to 0.5 mbar, 1:3 CO:O_2 gas ratio conditions (O_2-rich). The sample was heated while sequentially probing the (111), (645) and (312) planes in 10 K increments. A closer look to the ramp at the (645) surface reveals how the large amount of “C” blocks the CO adsorption, since the ChemCO peaks significantly increase once the large “C” contribution vanishes. ChemCO smoothly decreases upon heating, until it simultaneously vanishes at the three probed planes at 460 K. The CO_2 build-up before the sample ignition is probably caused by the hot Pt filament used at that time for heating the sample. Note that T_i is lower in this experiment, since the O_2 content is larger [39].

Below the ignition temperature T_i, the three investigated surfaces are covered by chemisorbed CO (ChemCO) and a remarkable amount of graphitic “C” in the (111) plane and specially the (645) plane. Further heating of the sample induces the vanishing of almost all “C” at 450 K at the (645) surface, although additional heating to 460 K is needed to remove it from the (111) plane. Subsequent heating to 500 K causes the ChemCO to also leave the surfaces. This process takes place now at the same temperature, revealing a simultaneous CO ignition of all kinked vicinals studied in this work. Once the CO has left the surface, new O species (O/Pt) are observed in the spectra. More details on the active stage are given in Subsection 4.2.6.

As discussed in Subsection 4.2.5, the simultaneous light-off of flat and stepped Pt surfaces is ascribed to a subsurface oxygen species arising just prior to the ignition towards the active stage (O_{Subs}). It appears around 532.1 eV in the O 1s region, causing a gentle shift of the T_T-CO feature at 532.6 eV towards lower binding energies, as observed and depicted in the top panel of Figure C5a). Higher O_2 content in the gas mixture would tentatively cause larger amounts of O_{Subs} to accumulate below the surface, hence enhancing the peak shift towards 532.1 eV. As the amount of O_2 is smaller in the 1:1 CO:O_2 experiments, such variation is more difficult to observed there, although it is quite evident in the 1:3 CO:O_2 experiments.

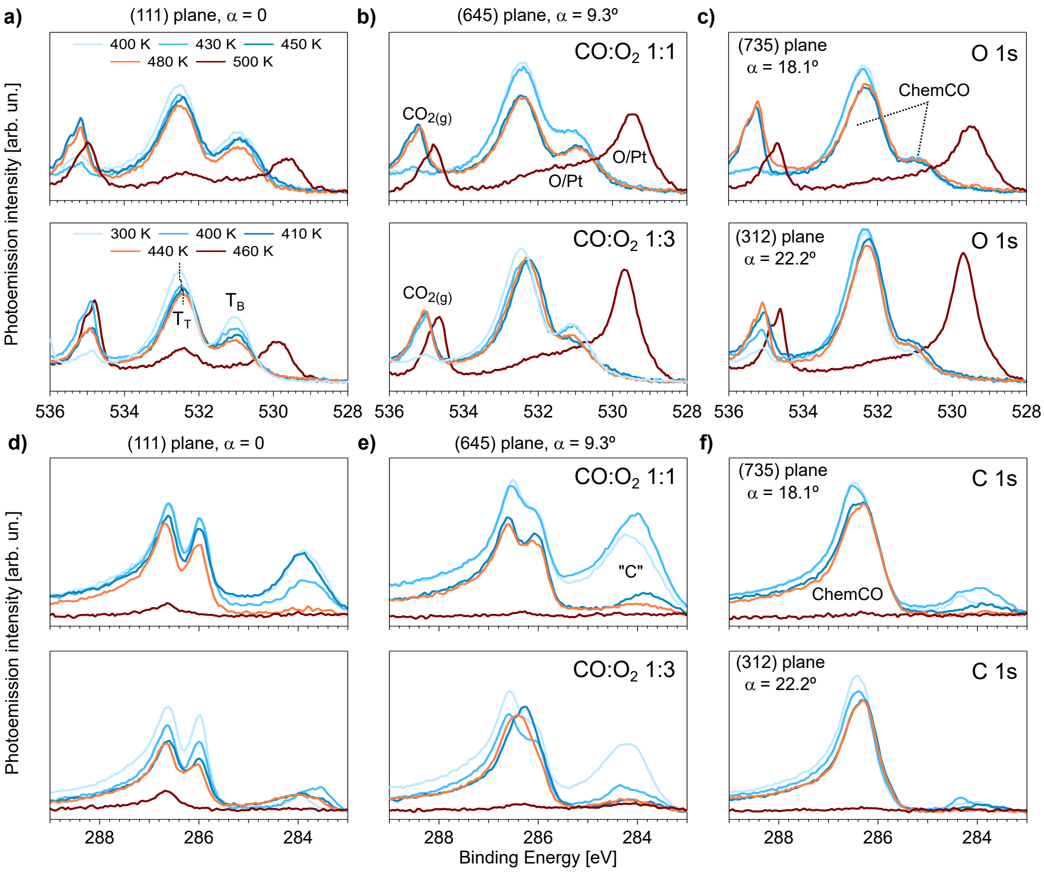

Figure C5: Selected spectra acquired in different CO:O$_2$ ratios. O 1*s* individual spectra at the **a)** (111), **b)** (645) and **c)** (735) or (312) planes, respectively for 1:1 (top, 0.7 mbar of total pressure) and 1:3 (bottom, 0.5 mbar of total pressure) conditions. C 1*s* individual spectra at the **e)** (111), **d)** (645) and **f)** (735) or (312) planes, respectively for 1:1 (top, 0.7 mbar of total pressure) and 1:3 (bottom, 0.5 mbar of total pressure) conditions. O/Pt, ChemCO and "C" allude to Pt-oxygen species, CO and graphitic "C" on the surface, as discussed in Subsection 4.2.2. The measurements were acquired at a photon energy of 650 eV.

C6 Reference spectra at the (111) plane

We acquired C 1*s* and O 1*s* photoemission spectra at the (111) position under reaction conditions at 300 K, in order to properly extract the O_{Subs} peak at higher temperatures during the heating ramps. The surface is not active at such low temperature, therefore neither CO_2 production nor additional oxygen species apart from CO are expected or were observed. Only CO and a small amount of graphitic carbon ("C") are present on the surface, hence these conditions are an optimal reference for extracting the position of T_T-CO at the (111) plane.

The main peaks in both regions (O 1*s*, C 1*s*) are Terrace-Top (T_T, 532.6 and 286.6 eV) and Terrace-Bridge (T_B, 530.9 and 286.0 eV) CO molecules [24], accompanied by a tiny bump related to locally denser T_T-CO (T_T*, 287.3 eV [67]) only detected in the C 1*s*. In addition, smaller peaks ascribed to graphitic "C" adsorbed on the surface are detected around 284 eV, together with the gas phase features of CO (290.2, 290.5 and 535.6 eV) and O_2 (537.4 and 538.5 eV) [38]. As mentioned in Subsection 4.2.5, the position of T_T-CO at the (111) surface was fixed to the here obtained value (532.6 eV) in the O 1*s* fitting procedure at higher temperatures during CO oxidation experiments in order to properly extract the contribution of O_{Subs}.

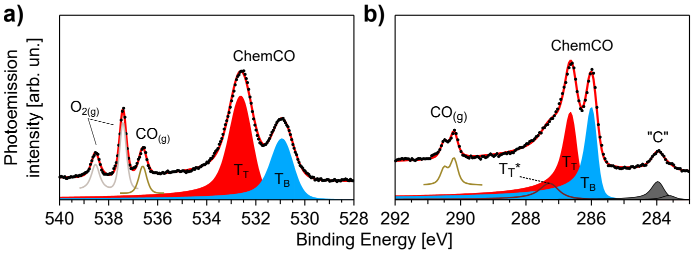

Figure C6: Photoemission spectra at (111) plane at 300 K.
a) O 1*s* and **b)** C 1*s* regions acquired at 300 K under a a pressure of 0.7 mbar in a 1:1 CO:O_2 gas mixture. T_T, T_B and T_T* stand for Terrace-Top, Terrace-Bridge and locally denser T_T CO molecules, while $O_{2(g)}$ and $CO_{2(g)}$ refer to the gas phase contribution of such species. "C" refers to graphitic carbon. The measurements were acquired at a photon energy of 650 eV.

C7 Graphitic "C" at the poisoned stage

We observed a significant amount of graphitic "C" at the different α-scans of the poisoned stage shown in Subsection 4.2.3. The progress of the overall amount of graphitic "C" at each of the conditions across these α-scans is shown in Figure C7, featuring a remarkable variability with the temperature and step density. The maximum amount of "C" is observed at 430 K, and it progressively decreases with the temperature until it completely vanishes at 490 K, establishing a "C" burning temperature between 460 and 490 K.

At 430 K, the "C" area is found maximum at the (111) plane, and steadily decreases with the step density. However, at 460 K the maximum amount of "C" is observed at $\alpha = 10°$, near the (645) plane. This unveils a rather complex behaviour, which depends on several factors. On one side, a fast CO dissociation or slow "C" burning would increase the amount of "C" on the surface. On the other side, if the kinetics of the "C" oxidation are fast or those of the CO cracking are slow, the relative amount of "C" on the surface will decrease. Since close-packed Pt vicinals are known to enhance the CO cracking [46], we suggest that the increase of the "C" intensity at $\alpha < 10°$ corresponds to a faster "C" cracking rate enhanced by the kinked steps. However, the "C" oxidation kinetics are enhanced at $\alpha > 10°$ due to the kinks, hence showing a decrease of the "C" intensity above this α.

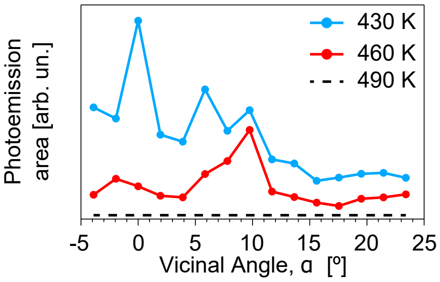

Figure C7: Graphitic "C" evolution at different temperatures. Sum of the area of individual graphitic "C" species, as extracted from the C 1s peak fitting of the α-scans acquired under reaction conditions (total pressure of 0.5 mbar, 1:1 CO:O_2 gas ratio) shown in Subsection 4.2.5. The α-scan acquired 460 K is not shown. The data at 490 K is above the "C" oxidation, and accordingly no "C" is observed anymore on the surface.

C8 Additional α-scan of the active stage

We have discussed the surface composition of the (111), (645) and (312) surfaces during the active stage and during a reference experiment with only O_2. The additional α-scan of the active stage acquired in O_2-rich conditions (total pressure of 0.5 mbar, 1:3 $CO:O_2$ gas ratio), together with selected spectra at relevant surfaces is shown in Figure C8.

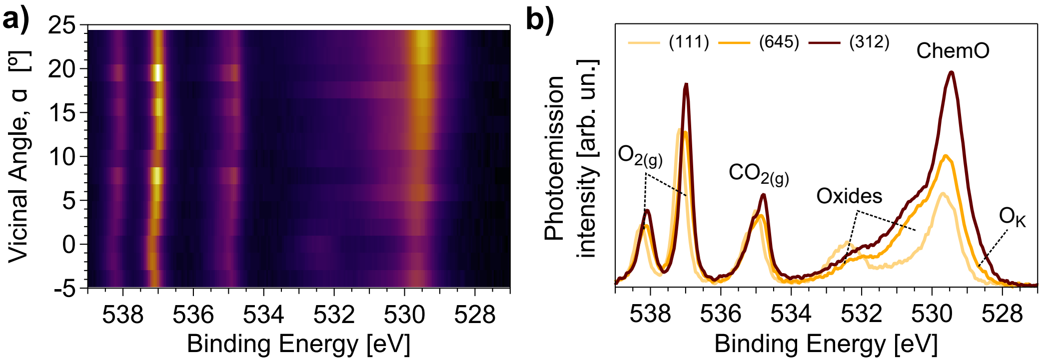

Figure C8: α-scan of the active stage at 1:3 $CO:O_2$ gas ratio. **a)** O 1*s* α-scan acquired at a total pressure of 0.5 mbar in a 1:3 $CO:O_2$ gas ratio. It was acquired at 470 K during the active stage of the CO oxidation. Selected spectra at relevant surfaces are shown in **b)**. As discussed in the main text, ChemO, O_K and Oxides refer to chemisorbed O in fcc sites and at the kinked arrays (possibly in square sites) and uncharacterized Pt oxides, respectively. $CO_{2(g)}$ stands for the photoemission peaks of gas phase CO_2. The measurements were acquired at a photon energy of 650 eV.

Most of the photoemission peaks were found to increase with the step density, indicating that the steps are oxidized easier than at the flat (111) terraces [96]. Additional details on these species are given in Subsection 4.2.6. The main contribution to the spectra is ChemO, markedly increasing with the step density. O_K and the peak at 530.5 eV grow with the step density, indicating that it is favoured at the stepped edges. However, the peak at 532.5 eV is maximum at the (111) plane and decreases with α. A similar feature was observed during bare O_2 exposure, hence we ascribed it to an uncharacterized oxide. However, we perceived a small amount of adsorbed CO during the active stage of the CO oxidation in the C 1s region (not shown), for which we believe this contribution is indeed a combination of a certain uncharacterized oxide and a residual amount of adsorbed CO.

Appendix D: c-Rh(111)

Experimental methods

- **Sample cleaning and characterization.** The c-Rh(111) sample is described in Figure 2.4. Briefly, in this curved crystal vicinal angles up to $\alpha = \pm 15^\circ$ can be explored, hence the (553) and (223) surfaces may be reached close to the two edges. Several cycles of Ar^+ sputtering (1.5 kV), O_2 annealing (500-1200 K) and final flashes (1200 K) were employed for cleaning the sample, until a clean and ordered surface was observed by XPS and LEED (see Appendix D1).

- **Photoemission experiments and peak fitting.** UHV measurements were performed at the I311 beamline of the Max II facility in Lund (Sweden) [290]. C 1*s* and Rh 3*d* core levels were acquired at 300 K in normal emission geometry with photons of 390 eV.

  The main CO oxidation experiments were performed at the 23-ID-2 beamline of NSLS-II synchrotron (USA, see Appendix B). Additional measurements were conducted at the Circe beamline of ALBA facility (Spain), whose details have been reported elsewhere [201].

  The peak fitting of the UHV experiments was carried out using the CasaXPS software [292], while that of the NAP-XPS spectra was performed using a homemade script with Python's *lmfit* package [299]. Doniac-Šunjić lineshapes convoluted with a Gaussian profile were considered for the peak fitting [293] adding a Shirley background [288].

  Regarding the fitting procedure of the CO-related peaks in the C 1*s* and UHV, the (T_H+S_B)-CO contribution was remarkably wider than the other CO-related peaks, since it is a combination of two different species. The vibrational satellite of T_T was constrained to have the same parameters (asymmetry, width...) as the main peak, and its area was added to that of T_T-CO for coverage calibration.

In NAP conditions, the width of the individual CO species contributions was similar. Their asymmetry was also alike, however it decreased following $\mathrm{T_T \rightarrow T_H \rightarrow S_T \rightarrow S_B}$. In the O 1$s$ region, both ($\mathrm{T_T+S_T}$) and ($\mathrm{T_H+S_B}$) features broaden and shift with the step density, since the individual components cannot be resolved.

In the fittings of the O 1s region during the active stage, the $\mathrm{RhO_2}$ peaks were constrained to have the same width, although the asymmetry of the component at 530 eV was smaller [169]. The other contributions were significantly less asymmetric and broader in the O 1s region, and they were sharper and more asymmetric in the C 1s.

- **Coverage calculations.** The 1/3 ML, $(\sqrt{3}\times\sqrt{3})\mathrm{R}30^\circ$ superstructure developed by CO adsorbed at $\mathrm{T_T}$ sites at the (111) plane was used as a coverage calibration for the UHV experiments. The 0.75 ML, (2×2)-3CO saturation structure was not observed at 300 K. The latter is formed upon CO saturation at 100 K, and consists of $\mathrm{1T_T+2T_H}$ CO molecules per unit cell. Since PED effects arise, the experimental ratio $\mathrm{T_H/T_T}$ increases to 3 at 390 eV. Therefore, disregarding geometric factors, one can straightforwardly deduce a intensity ratio-to-coverage correction factor of 2/3 to achieve the right ratio at 390 eV [148, 151]. Since $\mathrm{T_H}$ and $\mathrm{S_B}$ cannot be resolved, the aforementioned factor was applied to $(\mathrm{T_H+S_B})(\alpha)$, hence the coverage of CO adsorbed at $\mathrm{S_B}$ sites may be underestimated.

  The $\mathrm{T_H/T_T}$ ratio was 2 during the CO chemisorption experiments after exposure to 0.1 mbar CO at 300 K at the (111) plane. It then seems reasonable to expect that the CO molecules are arranged forming the 0.75 ML, (2×2)-3CO superstructure, thus we used this structure for calibration. An intensity-to-coverage factor was extracted from the spectra at the (111) plane, which was later applied to each of the other spectra to calculate the CO coverage of each of the species.

- **Adsorption model.** As we could not distinguish $\mathrm{T_H}$ and $\mathrm{S_B}$ in the C 1s region, fitting the coverage evolution with α to the W-model is not straightforward. While $\Theta_{T_T}(\alpha)$ and $\Theta_{S_T}(\alpha)$ follow the equations described in Subsection 2.1.1, $\Theta_{T_H+S_B}(\alpha)$ is a combination of $\Theta_{T_H}(\alpha)$ and $\Theta_{S_B}(\alpha)$, hence the sum of both has to be considered.

$$\Theta_{T_H+S_B}(\alpha) = \underbrace{\Theta^0_{T_H}\left[1 - W_S\frac{|\sin\alpha|}{h}\right]}_{\Theta_{T_H}(\alpha)} + \underbrace{\Theta^0_{S_B}\cdot W_S\frac{|\sin\alpha|}{h}}_{\Theta_{S_B}(\alpha)} \tag{D1}$$

D1 α-scans of the clean c-Rh(111) surface

We characterized the c-Rh(111) sample with LEED after the cleaning routine. Figure D1a) shows the LEED α-scan of the clean c-Rh(111) sample, together with single images of relevant surfaces. We have rotated the sample in order to better distinguish the [1,0] LEED spot. The six-fold diffraction pattern characteristic of the (111) plane is observed at the center. As expected, as one moves away from the center, the step density increases and the spots split [102, 300]. The splitting distance smoothly increases with the vicinal angle α since the terraces narrow, hence confirming the correct distribution of step density across the curved surface [238].

We also mapped the Rh $3d_{5/2}$ region across the clean c-Rh(111), as shown in Figure D1b). Two peaks are observed at the (111) plane, related to bulk ($\mathrm{Rh_B}$, 307.2 eV) and terrace ($\mathrm{Rh_T}$, 306.7 eV) Rh atoms. An additional small feature can be detected at the stepped surfaces, steadily increasing with α, which we ascribe to Rh step atoms ($\mathrm{Rh_S}$, 306.5 eV). $\mathrm{Rh_T}$ decays as $\mathrm{Rh_S}$ rises, since the growth of steps is detrimental to the physical space occupied by terraces. Here we neglected the understep component located between the $\mathrm{Rh_B}$ and $\mathrm{Rh_T}$ peaks, since it is smaller than the $\mathrm{Rh_S}$ emission [301].

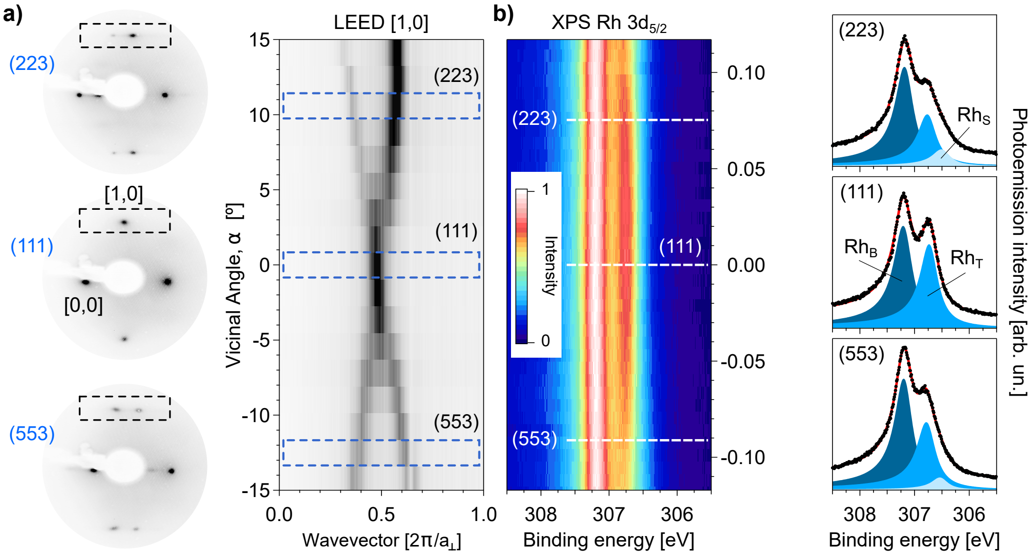

Figure D1: Surface scans for the clean c-Rh(111) sample.
a,b) LEED [1,0] (E = 77 eV) and Rh $3d_{5/2}$ (E = 390 eV) separate α-scans across the curved surface of the clean c-Rh(111) sample at 300 K. Individual images and photoemission spectra, together with fits for the latter, are shown for relevant surfaces in each of the α-scans. $\mathrm{Rh_B}$, $\mathrm{Rh_S}$ and $\mathrm{Rh_T}$ stand for emission arising from bulk, step and terrace Rh atoms, respectively.

D2 Cooling of the CO oxidation

During the PLIF experiments, we exposed the clean c-Rh(111) sample to a 4:4:92 CO:O_2:Ar gas mixture at a total flow of 100 ml/min, reaching a total pressure of 150 mbar. After finishing the heating ramp described in Subsection 5.2.1, the sample was kept at 630 K during 200 s, and was subsequently cooled down to 420 K. The experiment is depicted in Figure D2, showing the opposite trend of Figure 5.4 since we are now exploring the cooling of the CO oxidation. At high temperature [530 K, Figure D2a)], the whole sample is active. However, as the temperature decreases, the A-side deactivates while the B-side is still active (500 K). If the sample is further cooled, the whole sample transitions to the poisoned stage and the CO_2 production can no longer be observed (470 K). Therefore, the cooling of the CO oxidation in A-B Rh vicinals is also asymmetric. The CO_2 signals evolution in the QMS and PLIF are shown in Figures D2b,c), mimicking the behaviour described above.

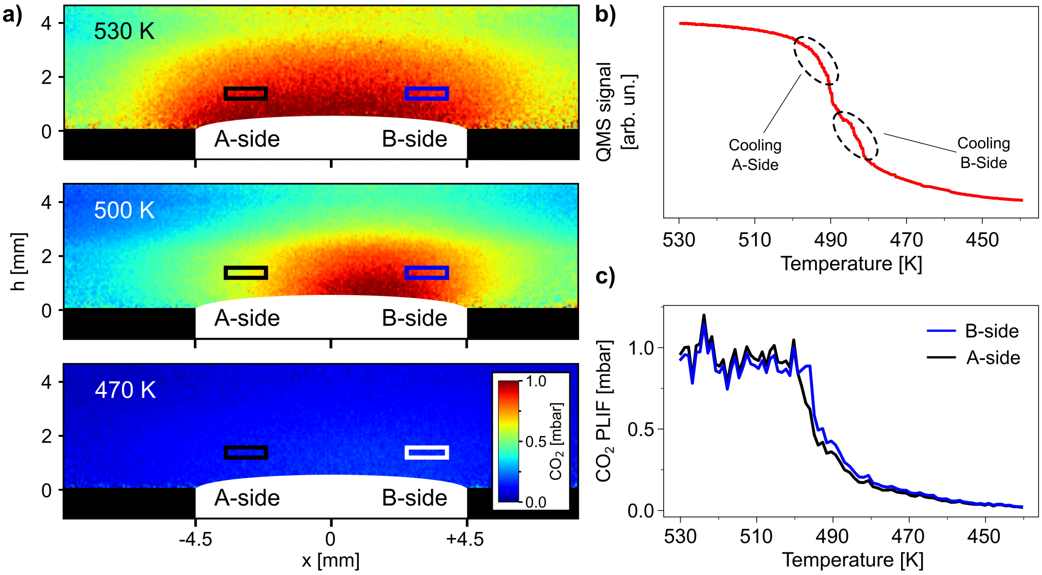

Figure D2: PLIF cooling cycle in a 1:1 CO:O_2 gas ratio.
a) PLIF snapshots acquired at selected temperatures under a 150 mbar, 4:4:92 CO:O_2:Ar gas mixture at a total flow of 100 ml/min. CO_2 signals at the **b)** QMS (mass 44) and **c)** PLIF during the cooling cycle. The right (B-side, white and blue) and left (A-side, black) curves of c) were extracted from the integration of all images in the regions sketched with rectangles in a). The cooling slope was 2.6 K/min.

D3 CO cracking during the heating ramps

As advanced in the main text, we observed a remarkable dissociation of CO adsorbed at T_H sites during the ignition cycles. Here we will explain this observation in detail. For this purpose separate temperature ramps at (111) and (223) positions across the curved crystal during CO oxidation experiments are shown in Figure D3. Such experiments correspond to additional measurements undertaken at ALBA synchrotron, for which the total pressure was 1.5 mbar and the CO:O_2 pressure ratio was 1. Although not shown here, the same preferential dissociation of T_H-CO was observed in the experiments carried out at NSLS-II facility described in Subsection 5.2.2. No $CO_{2(g)}$ production was observed after the “C” burning in any of the aforementioned measurements, ruling out the graphitic “C” oxidation as a relevant pathway for CO_2 production at these conditions.

At the beginning of the heating ramp, the amount of CO molecules chemisorbed at T_H positions (285.5 eV) starts to decrease while the graphitic carbon contributions (“C”, around 284 eV) significantly grow. This indicates that the CO is cracking, maybe with the assistance of the intense photon beam impinging the sample. Nevertheless, the contribution from “C” rapidly decreases once the temperature is further increased since it is being oxidized by the O_2 gas inside the chamber. As a consequence the empty T_H positions can be occupied again by CO molecules. A rapid comparison between Figures D3a,c) reveals that “C” is found at even higher temperature at the (223) surface than at the (111).

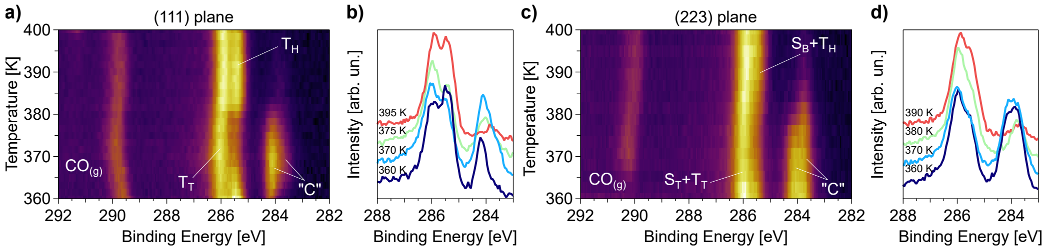

Figure D3: T_H-CO dissociation at the (111) and (223) surfaces. a,c) Color plot of temperature ramps acquired in separate experiments at the (111) and (223) planes submitted to a 1.5 mbar, 1:1 CO:O_2 gas ratio mixture. **b,d)** Individual C 1*s* spectra at the indicated temperatures for each of the surfaces. Following the main text, T_T, T_H, S_T and S_B refer to CO molecules in Terrace-Top, Terrace-Hollow, Step-Top and Step-Bridge sites, respectively. Furthermore, graphitic carbon on the surface and gas phase CO are labelled as “C” and $CO_{(g)}$. The experiments were undertaken with a photon energy of 650 eV at ALBA synchrotron.

D4 Variability of the pre-ignition stage

At a given temperature, Rh B-type steps can be CO-depleted and O-covered while A-type vicinals are still CO-saturated, as observed in heating ramps at both experimental runs at NSLS-II and ALBA. On one hand, the NSLS-II experiments [1:4 $CO:O_2$ gas ratio, Figures D4a,d)] show a linearly decreasing (increasing) ChemO (T_H+S_B) from the B-side towards the A-side. On the other hand, in the ALBA measurements [1:1 $CO:O_2$ gas ratio, Figures D4b,c,e)]), both ChemO and T_H+S_B are virtually constant at $\alpha < 0$ (B-side), while ChemO grows and T_H+S_B decays at $\alpha > 0$ (A-side). In addition, the relative amount of ChemO is larger on the (111) surface if compared to the NSLS-II data, which point towards more oxidized terraces in the ALBA experiments. Therefore, A-B asymmetries observed prior to the full ignition depend on the $CO:O_2$ ratio.

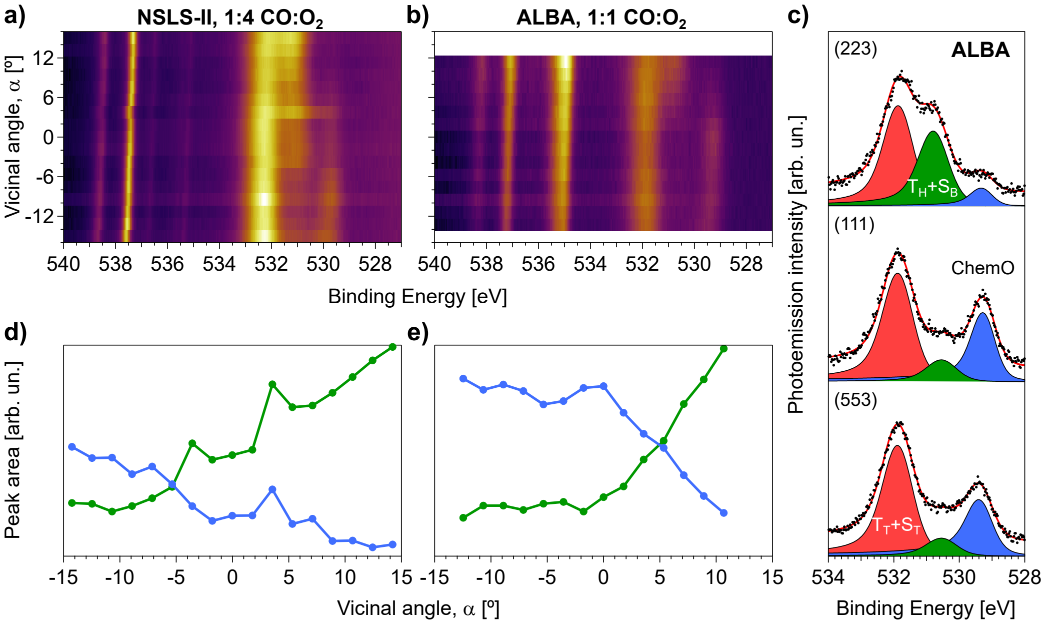

Figure D4: Asymmetries prior to ignition at different $CO:O_2$ ratios. **a,b)** O 1s α-scans acquired under a 0.7 mbar, 1:4 $CO:O_2$ gas mixture at 460 K (650 eV, NSLS-II, see Figure 5.6) and a 1 mbar, 1:1 $CO:O_2$ gas mixture at 420 K (670 eV, ALBA), with fitted spectra for the former shown in **c)**. **d,e)** Peak area evolution as a function of the vicinal angle in each of the curvature maps for T_H+S_B and ChemO, as extracted from the individual fit of all the spectra shown in a,b). T_T, S_T, T_H, S_B stand for Terrace-Top, Step-Top, Terrace-Hollow and Step-Bridge CO molecules, while ChemO refers to chemisorbed O in hollow fcc sites.

D5 C 1*s* analysis during the active stage

We also acquired the C 1*s* region during the active stage of the CO oxidation. The spectra are shown in Figure D5, and they were taken right after the O 1*s* spectra presented in Subsection 5.2.3. The results are similar to those derived by the O 1*s* analysis, with the addition that two different carbonate/carboxyl features at high binding energy are detected in the C 1*s* region.

First of all, we want to remind that the reaction has reached mass-transfer limit and no CO is detected in the gas phase anymore. Only a doublet related to $CO_{2(g)}$ is distinguished between 291 and 290 eV. As discussed previously, the gas phase peaks shift during the α-scan since the work-function is not homogeneous across the curved surface [206]. At 470 K, a significant amount of CO molecules adsorbed at T_T sites is observed around 286 eV, although it is remarkably smaller than that of the (111) surface at 460 K, prior to the sample ignition (Figure 5.6). As a terrace species, it decreases with the step density, slowly on the B-side and much stronger on the A-part of the c-Rh(111) sample. Simultaneously on the latter, two well-defined contributions grow with α, indicating that such species are anchored exclusively at A-steps. Their binding energy is typical of carbonate/carboxyl species [243], we therefore denominate them shortly as “Carb”. As extracted from the O 1*s*, the A-side of the crystal is largely oxidized forming RhO_2 trilayers. Therefore another possibility would be that these features arise from CO adsorbed on metallic areas close to the RhO_2 trilayers. A similar peak was observed in the C 1*s* after dosing CO on a Pd_5O_4 surface [248]. Adsorbed CO on the surface oxide [169] and adsorbed CO_2 are also unlikely [302].

The temperature was increased to 510 K, and the curved surface was scanned again. No substantial change is observed at the (223) surface, although both the (111) and the (553) spectra evolve significantly. A large amount of CO molecules have desorbed from the latter surfaces, yet the maximum amount of CO adsorbed at T_T sites is now at the (553) surface. This is a remarkable behaviour, since T_T-CO should decrease with the step density. Nonetheless, a simple explanation arises after the analysis of the O 1*s* region: the terraces are now partially oxidized as well, forming the RhO_2 trilayers, on which the CO adsorption is hindered [169]. Since the (553) surface features only ChemO, the ability of CO molecules to stick to the surface is not quenched and the amount of CO at T_T positions increases. Hence, the CO adsorption is quenched close to the (111) surface. However, no (9×9) oxide is observed around the (553) plane. Therefore, CO can still adsorb at T_T sites at these surfaces, hence it grows in intensity with α. When the RhO_2 trilayers disappear at large α at the B-side of the crystal, T_T-CO starts to decrease as a regular terrace CO species.

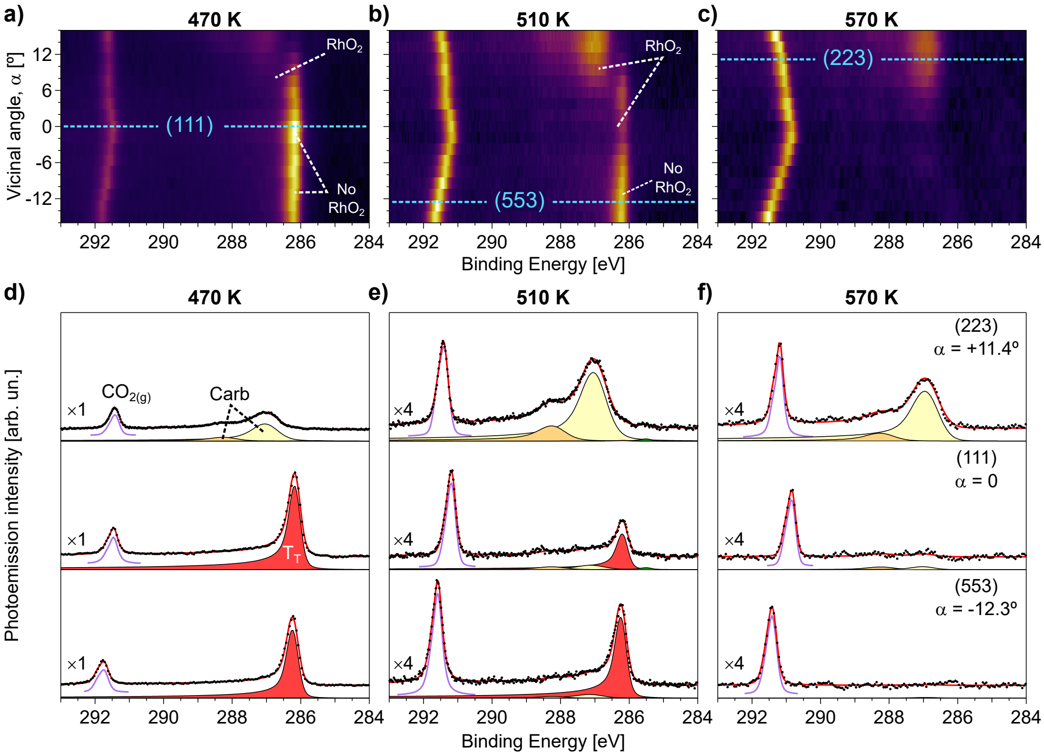

Figure D5: C 1s evolution with the α during the active stage. **a-c)** C 1s α-scans acquired under a 0.7 mbar, 1:4 CO:O$_2$ gas mixture at 470, 510 ad 570 K. Notes are added in order to emphasize the existence of the RhO$_2$ trilayers at selected surfaces, as extracted from the O 1s analysis of Figure 5.7. **d-f)** Individual fitted spectra for the (223), (111) and (553) surfaces [top, middle and bottom panels, respectively] at each of the indicated temperatures. Following previous guidelines, T$_\mathrm{T}$, Carb and CO$_{2(g)}$ stand for Terrace-Top CO molecules, two different carbonate/carboxyl species and the contribution from gas phase CO$_2$. The experiments were undertaken with a photon energy of 650 eV.

Finally, after reaching 570 K, chemisorbed CO is hardly detectable at any of the surfaces. Only the features related to CO$_{2(g)}$ and both Carb peaks are present on the C 1s region. The latter have slightly decreased, indicating that their desorption, decomposition and/or reaction had started.

D6 Oxidation of the Rh surfaces

During the NAP experiments in ALBA we first investigated the oxidation of the Rh surfaces. In order to do so, we exposed the clean c-Rh(111) to 1 mbar O_2 at 410 K and acquired spectrum at several points across the curved surface. The full α-scan is shown in Figure D6a), while selected spectra at relevant surfaces, namely the (111), (223) and (553) planes, are shown in Figure D6b). Two peaks around 529 and 530 eV, characteristic of the RhO_2 trilayer, are easily observed homogeneous in the whole α-scan. This indicates that the (9×9) surface oxide is formed on all facets of the sample, as discussed in Subsection 1.4.2.

We also explored the active stage of the CO oxidation in the NAP experiments conducted at ALBA. We exposed the sample to a 1 mbar, 1:1 $CO{:}O_2$ gas ratio mixture, and heated the sample until we observed ignition at 580 K. The O 1s region at the (111), (223) and (553) surfaces is shown in Figure D6c), clearly showing a single feature between 529 and 530 eV the O 1*s* region (and a small amount of adsorbed CO at 532 eV). This reveals that there is no RhO_2 formation at these conditions. However, we did observe the RhO_2 formation during the active stage of the CO oxidation in the experiments of NSLS-II (Subsection 5.2.3, 1:4 $CO{:}O_2$ gas ratio). This large difference between the 1:1 (ALBA) and 1:4 (NSLS-II) $CO{:}O_2$ ratios is expected, and it reflects how the formation of the trilayers is quenched if the CO oxidation kinetics are faster than those of the Rh oxidation.

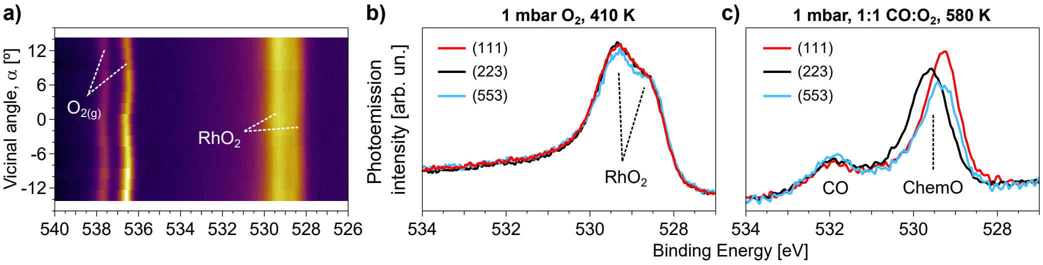

Figure D6: O-covered Rh surfaces during the ALBA experiments. **a)** O 1*s* α-scan acquired under 1 mbar O_2 at 410 K, with selected spectra at the (111), (223) and (553) planes shown in **b)**. **c)** Relevant surfaces under a 1:1 $CO{:}O_2$, 1 mbar, gas mixture at 580 K, during the active stage of the CO oxidation. Adsorbed CO molecules, chemisorbed O and the trilayer surface oxide are denoted as CO, ChemO and RhO_2, respectively. The photon energy of these experiments was 670 eV.

Bibliography

[1] P. Atkins et al., *Atkins' Physical Chemistry* (Oxford University Press, Oxford, United Kingdom, 2018), pp. 395, 741–744.

[2] I. Langmuir, "The mechanism of the catalytic action of platinum in the reactions $2CO + O_2 = 2CO_2$ and $2H_2 + O_2 = 2H_2O$", Transactions of the Faraday Society **17**, 621 (1922).

[3] D. L. Nelson et al., *Lehninger Principles of Biochemistry*, Eighth (W.H. Freeman & Company, New York, United States, 2021).

[4] *Lets talk science: catalytic converters*, `https://letstalkscience.ca/educational-resources/stem-in-context/catalytic-converters`, Accessed: 2021-08-13.

[5] *Scientif american: make elephant toothpaste*, `https://www.scientificamerican.com/article/make-elephant-toothpaste/`, Accessed: 2021-11-08.

[6] *Nobel prize in chemistry, 2007*, `https://www.nobelprize.org/prizes/chemistry/2007/summary/`, Accessed: 2021-08-04.

[7] G. Ertl, *Reactions at Solid Surfaces* (John Wiley & Sons, Inc., Hoboken, NJ, USA, 2009), pp. 1, 21, 51, 60–63, 103, 109–111.

[8] P. A. Bagot, "Fundamental surface science studies of automobile exhaust catalysis", Materials Science and Technology **20**, 679–694 (2004).

[9] G. Ertl, "Reactions at well-defined surfaces", Surface Science **299-300**, 742–754 (1994).

[10] D. E. Hooks et al., "Epitaxy and molecular organization on solid substrates", Advanced Materials **13**, 227–241 (2001).

[11] J. K. Nørskov et al., "The nature of the active site in heterogeneous metal catalysis", Chemical Society Reviews **37**, 2163 (2008).

[12] G. Rothenberg, *Catalysis: Concepts and Green Applications*, Vol. 22, 7 (Wiley, 2008), pp. 65, 78.

[13] I. Langmuir, "Part II.—"Heterogeneous reactions. Chemical reactions on surfaces", Trans. Faraday Soc. **17**, 607–620 (1922).

[14] C. N. Hinshelwood, *The kinetics of chemical change* (The Clarendon press, Oxford, 1940).

[15] D. Eley et al., "Parahydrogen conversion on tungsten", Nature **146**, 401–402 (1940).

[16] D. Eley, "The catalytic activation of hydrogen", Advances in Catalysis **1**, 157–199 (1948).

[17] P. Mars et al., "Oxidations carried out by means of vanadium oxide catalysts", Chemical Engineering Science **3**, 41–59 (1954).

[18] C. Doornkamp et al., "The universal character of the Mars and Van Krevelen mechanism", Journal of Molecular Catalysis A: Chemical **162**, 19–32 (2000).

[19] B. L. Hendriksen et al., "Looking at heterogeneous catalysis at atmospheric pressure using tunnel vision", Topics in Catalysis **36**, 43–54 (2005).

[20] D. Esposito, "Mind the gap", Nature Catalysis **1**, 807–808 (2018).

[21] S. Blomberg et al., "In Situ X-Ray Photoelectron Spectroscopy of Model Catalysts: At the Edge of the Gap", Physical Review Letters **110**, 117601 (2013).

[22] S. Blomberg et al., "Bridging the Pressure Gap in CO Oxidation", ACS Catalysis **11**, 9128–9135 (2021).

[23] J. Dou et al., "Operando chemistry of catalyst surfaces during catalysis", Chemical Society Reviews **46**, 2001–2027 (2017).

[24] R. Toyoshima et al., "A high-pressure-induced dense CO overlayer on a Pt(111) surface: A chemical analysis using in situ near ambient pressure XPS", Physical Chemistry Chemical Physics **16**, 23564–23567 (2014).

[25] M. A. van Spronsen et al., "Observing the oxidation of platinum", Nature Communications **8**, 429 (2017).

[26] F. Gao et al., "CO Oxidation on Pt-Group Metals from Ultrahigh Vacuum to Near Atmospheric Pressures. 2. Palladium and Platinum", The Journal of Physical Chemistry C **113**, 174–181 (2009).

[27] F. Gao et al., "CO Oxidation on Pt-Group Metals from Ultrahigh Vacuum to Near Atmospheric Pressures. 1. Rhodium", Journal of Physical Chemistry C **113**, 182–192 (2009).

[28] J. A. Martín-Gago et al., *El nanomundo en tus manos* (Critica, Barcelona, Spain, 2014), p. 213.

[29] J. Y. Park et al., *Bridging materials and pressure gaps in surface science and heterogeneous catalysis* (Springer New York, New York, NY, 2014), pp. 3–17.

[30] D. J. Miller et al., "Oxidation of Pt(111) under Near-Ambient Conditions", Physical Review Letters **107**, 195502 (2011).

[31] F. Gao et al., "CO oxidation trends on Pt-group metals from ultrahigh vacuum to near atmospheric pressures: A combined in situ PM-IRAS and reaction kinetics study", Surface Science **603**, 65–70 (2009).

[32] C. J. Kliewer et al., "Pyrrole Hydrogenation over Rh(111) and Pt(111) Single-Crystal Surfaces and Hydrogenation Promotion Mediated by 1-Methylpyrrole: A Kinetic and Sum-Frequency Generation Vibrational Spectroscopy Study", The Journal of Physical Chemistry C **112**, 11373–11378 (2008).

[33] J. Gustafson et al., "High-Energy Surface X-ray Diffraction for Fast Surface Structure Determination", Science **343**, 758 (2014).

[34] K. Roy et al., "Ambient Pressure Photoelectron Spectroscopy: Opportunities in Catalysis from Solids to Liquids and Introducing Time Resolution", ChemCatChem **10**, 666–682 (2018).

[35] J. Zetterberg et al., "An *in situ* set up for the detection of CO_2 from catalytic CO oxidation by using planar laser-induced fluorescence", Review of Scientific Instruments **83**, 053104 (2012).

[36] H. J. Freund et al., "CO oxidation as a prototypical reaction for heterogeneous processes", Angewandte Chemie - International Edition **50**, 10064–10094 (2011).

[37] K. Qadir et al., "Intrinsic Relation between Catalytic Activity of CO Oxidation on Ru Nanoparticles and Ru Oxides Uncovered with Ambient Pressure XPS", Nano Letters **12**, PMID: 23067327, 5761–5768 (2012).

[38] N. Johansson et al., "Ambient pressure phase transitions over Ir(111): at the onset of CO oxidation", Journal of Physics: Condensed Matter **29**, 444002 (2017).

[39] J. Gustafson et al., "The Role of Oxides in Catalytic CO Oxidation over Rhodium and Palladium", ACS Catalysis **8**, 4438–4445 (2018).

[40] Y. Yu et al., "Chemical states of surface oxygen during CO oxidation on Pt(110) surface revealed by ambient pressure XPS", Journal of Physics: Condensed Matter **29**, 464001 (2017).

[41] T. Engel et al., “Elementary Steps in the Catalytic Oxidation of Carbon Monoxide on Platinum Metals”, in *Advances in catalysis*, Vol. 28, C (1979), pp. 1–78.

[42] Prof. Henrik Grönbeck, private communication. The main reason that CO dominates the surface at low temperatures is that O_2 requires two sites to adsorb, while CO only needs one. Given the adsorbate-adsorbate interaction, one site should not be understood as one surface atom, but instead more than one atom. This results in the end in a surface that is CO poisoned at low temperatures, where the rate constant for CO desorption is lower than that of adsorption. An additional fact is that the sticking coefficient The main reason that CO dominates the surface at low temperatures is that O_2 requires two sites to adsorb, while CO only needs one. Given the adsorbate-adsorbate interaction, one site should not be understood as one atom but instead somewhat more than one atom. This results in the end in a surface that is CO poisoned at low temperatures where the rate constant for desorption is lower than that of adsorption. An addition fact is that the sticking coefficient of O_2 is smaller than that of CO, which is close to one. On the other hand, the reaction barrier is about 1 eV, while the CO desorption energy is 1.4 eV on Pt(111). This means that once CO starts to desorb, the CO oxidation reaction is fast and all CO will be consumed, changing the CO coverage from high to close to zero.

[43] B. Shan et al., “CO-Coverage-Dependent Oxygen Dissociation on Pt(111) Surface”, The Journal of Physical Chemistry C **113**, 710–715 (2009).

[44] R. M. Eiswirth et al., “Nonlinear dynamics in the CO-oxidation on Pt single crystal surfaces”, Applied Physics A Solids and Surfaces **51**, 79–90 (1990).

[45] As discussed in Section 2.2, a small aperture is placed close to the sample in NAP-XPS in order to collect the photoelectrons without loosing much intensity due to gas-phase scattering. The gas close to the sample also enters via this hole towards the differential pumping stage of the analyzer. Hence, placing a QMS in one of these stages allows to selectively probe the gas phase near the surface.

[46] K. McCrea et al., “Surface structure sensitivity of high-pressure CO dissociation on Pt(557), Pt(100) and Pt(111) using sum frequency generation surface vibrational spectroscopy”, Surface Science **494**, 238–250 (2001).

[47] K. R. McCrea et al., “The role of carbon deposition from CO dissociation on platinum crystal surfaces during catalytic CO oxidation: Effects on turnover rate, ignition temperature, and vibrational spectra”, Journal of Physical Chemistry B **106**, 10854–10863 (2002).

[48]M. Smartt Bell, *Lavoisier in the Year One: The Birth of a New Science in an Age of Revolution* (W. W. Norton & Company, New York, USA, 2006), p. 59.

[49]J. Gustafson et al., "A high pressure x-ray photoelectron spectroscopy study of CO oxidation over Rh(100)", Journal of Physics Condensed Matter **26**, 055003 (2014).

[50]E. Lundgren et al., "Novel in Situ Techniques for Studies of Model Catalysts", Accounts of Chemical Research **50**, 2326–2333 (2017).

[51]G. Ertl et al., "Chemisorption of CO on the Pt(111) surface", Surface Science **64**, 393–410 (1977).

[52]O. Björneholm et al., "Overlayer structure from adsorbate and substrate core level binding energy shifts: CO, CCH_3 and O on Pt(111)", Surface Science **315**, L983–L989 (1994).

[53]P. Norton et al., "Absolute coverages of CO and O on Pt(111); Comparison of saturation CO coverages on Pt(100), (110) and (111) surfaces", Surface Science **122**, L593–L600 (1982).

[54]H. J. Yang et al., "STM investigation of CO ordering on Pt(111): From an isolated molecule to high-coverage superstructures", Journal of Physical Chemistry C **117**, 16429–16437 (2013).

[55]M. Kinne et al., "Kinetic parameters of CO adsorbed on Pt(111) studied by in situ high resolution x-ray photoelectron spectroscopy", Journal of Chemical Physics **117**, 10852–10859 (2002).

[56]H. Froitzheim et al., "The kinetics of the adsorption and desorption of the system CO/Pt(111) derived from high resolution TREELS", Surface Science **211-212**, 837–843 (1989).

[57]S. R. Longwitz et al., "High-coverage structures of carbon monoxide adsorbed on Pt(111) studied by high-pressure scanning tunneling microscopy", Journal of Physical Chemistry B **108**, 14497–14502 (2004).

[58]J. Kim et al., "In Situ Observation of Competitive CO and O_2 Adsorption on the Pt(111) Surface Using Near-Ambient Pressure Scanning Tunneling Microscopy", The Journal of Physical Chemistry C **122**, 6246–6254 (2018).

[59]R. McCabe et al., "Binding states of CO on single crystal planes of Pt", Surface Science **66**, 101–124 (1977).

[60]N. Bosio et al., "Sensitivity of Monte Carlo Simulations to Linear Scaling Relations", Journal of Physical Chemistry C **124**, 11952–11959 (2020).

[61] H. Hopster et al., “Adsorption of CO on Pt(111) and Pt 6(111) × (111) studied by high resolution electron energy loss spectroscopy and thermal desorption spectroscopy”, Surface Science **77**, 109–117 (1978).

[62] R. Brandt et al., “The arrangement of CO adsorbed on a Pt(533) surface”, Chemical Physics Letters **221**, 219–223 (1994).

[63] B. Tränkenschuh et al., “A site-selective in situ study of CO adsorption and desorption on Pt(355)”, Journal of Chemical Physics **124**, 1–10 (2006).

[64] J. S. Luo et al., “CO Adsorption Site Occupation on Pt(335) - a Quantitative Investigation Using TPD and EELS”, Surf. Sci. **274**, 53–62 (1992).

[65] J. Xu et al., “Terrace width effect on adsorbate vibrations: a comparison of Pt(335) and Pt(112) for chemisorption of CO”, Surface Science **327**, 193–201 (1995).

[66] S. C. Creighan et al., “The adsorption of CO on the stepped Pt{211} surface: A comparison of theory and experiment”, Catalysis Letters **88**, 39–45 (2003).

[67] B. Tränkenschuh et al., “The dissimilar twins - a comparative, site-selective in situ study of CO adsorption and desorption on Pt(322) and Pt(355)”, Surface Science **601**, 1108–1117 (2007).

[68] M. R. McClellan et al., “Carbon monoxide adsorption on the kinked Pt(321) surface”, Surface Science **112**, 63–77 (1981).

[69] J. Kim et al., “Thermal Evolution and Instability of CO-Induced Platinum Clusters on the Pt(557) Surface at Ambient Pressure”, Journal of the American Chemical Society **138**, 1110–1113 (2016).

[70] F. Tao et al., “Supporting Online Material for ”Break-up of Stepped Pt Catalyst Surfaces by High CO Coverage””, Science (New York, N.Y.) **327**, 850 (2010).

[71] J. L. Gland et al., “Oxygen interactions with the Pt(111) surface”, Surface Science **95**, 587–602 (1980).

[72] H. Steininger et al., “On the adsorption of CO on Pt(111)”, Surface Science **123**, 264–282 (1982).

[73] C. Puglia et al., “Physisorbed, chemisorbed and dissociated O_2 on Pt (111) studied by different core level spectroscopy methods”, Surface science **342**, 119–133 (1995).

[74] N. Materer et al., “Reliability of detailed LEED structural analyses: Pt(111) and Pt(111)-$p(2{\times}2)$-O”, Surface Science **325**, 207–222 (1995).

[75] K. Mortensen et al., “Adsorption position of oxygen on the Pt(111) surface”, Surface Science **220**, L701–L708 (1989).

[76] U. Starke et al., “A low-energy electron diffraction study of oxygen, water and ice adsorption on Pt(111)”, Surface Science **287-288**, 432–437 (1993).

[77] J. Wintterlin et al., “Existence of a ”Hot” Atom Mechanism for the Dissociation of O_2 on Pt(111)”, Phys. Rev. Lett. **77**, 123–126 (1996).

[78] C. Ellinger et al., “Atmospheric pressure oxidation of Pt(111)”, Journal of Physics: Condensed Matter **20**, 184013 (2008).

[79] J. F. Weaver et al., “Oxidation of Pt(111) by gas-phase oxygen atoms”, Surface Science **592**, 83–103 (2005).

[80] N. A. Saliba et al., “Oxidation of Pt (111) by ozone ($\mathrm{O_3}$) under UHV conditions”, Surface Science **419**, 79–88 (1999).

[81] D. I. Jerdev et al., “Evidence for slow oxygen exchange between multiple adsorption sites at high oxygen coverages on Pt(111)”, Surface Science **498**, L91–L96 (2002).

[82] R. Bradley Shumbera et al., “The transition from surface to bulk oxide growth on Pt(100): Precursor-mediated kinetics”, Surface Science **601**, 4809–4816 (2007).

[83] S. P. Devarajan et al., “STM study of high-coverage structures of atomic oxygen on Pt(111): $p(2\times1)$ and Pt oxide chain structures”, Surface Science **602**, 3116–3124 (2008).

[84] P. Légaré, “Interaction of oxygen with the Pt(111) surface in wide conditions range. A DFT-based thermodynamical simulation”, Surface Science **580**, 137–144 (2005).

[85] J. M. Hawkins et al., “Density functional theory study of the initial oxidation of the Pt(111) surface”, Physical Review B **79**, 125434 (2009).

[86] W. X. Li et al., “Oxidation of Pt(110)”, Physical Review Letters **93**, 146104 (2004).

[87] T. M. Pedersen et al., “Structure and activity of oxidized Pt(110) and α-$\mathrm{PtO_2}$”, Physical Chemistry Chemical Physics **8**, 1566 (2006).

[88] C. R. Parkinson et al., “Reaction of atomic oxygen with a Pt(111) surface: Chemical and structural determination using XPS, CAICISS and LEED”, Surface Science **545**, 19–33 (2003).

[89] P. Légaré et al., “On the interaction of $\mathrm{O_2}$ with Pt(111) and Pt(557) surfaces: core-level shift study using conventional and synchrotron radiation sources”, Surface Science **198**, 69–78 (1988).

[90] D. H. Parker et al., “Study of high coverages of atomic oxygen on the Pt(111) surface”, Surface Science **217**, 489–510 (1989).

[91] N. Seriani et al., “Catalytic Oxidation Activity of Pt_3O_4 Surfaces and Thin Films”, The Journal of Physical Chemistry B **110**, 14860–14869 (2006).

[92] C. R. Aita et al., “Sputter deposition of platinum films in argon/oxygen and neon/oxygen discharges”, Journal of Applied Physics **56**, 958–963 (1984).

[93] M. Hecq et al., “Sputtering deposition, XPS and X-ray diffraction characterization of oxygen-platinum compounds”, Journal of The Less-Common Metals **64**, 25–37 (1979).

[94] J. R. McBride et al., “Growth and characterization of reactively sputtered thin-film platinum oxides”, Journal of Applied Physics **69**, 1596–1604 (1991).

[95] J. F. Weaver, “Surface Chemistry of Late Transition Metal Oxides”, Chemical Reviews **113**, 4164–4215 (2013).

[96] J. G. Wang et al., “One-dimensional PtO_2 at Pt steps Formation and reaction with CO”, Physical Review Letters **95**, 256102 (2005).

[97] P. J. Feibelman et al., “O Binding Sites on Stepped Pt(111) Surfaces”, Physical Review Letters **77**, 2257–2260 (1996).

[98] A. Rar et al., “Desorption and dissociation of oxygen admolecules on a stepped platinum (533) surface”, Surface Science **318**, 89–96 (1994).

[99] H. Wang et al., “Adsorption and dissociation of oxygen on Pt(335)”, Surface Science **372**, 267–278 (1997).

[100] B. Lang et al., “Low energy electron diffraction studies of chemisorbed gases on stepped surfaces of platinum”, Surface Science **30**, 454–474 (1972).

[101] E. Hahn et al., “Orientational instability of vicinal Pt surfaces close to (111)”, Physical Review Letters **72**, 3378–3381 (1994).

[102] G. Comsa et al., “He-beam scattering study of the dynamics of oxygen induced reconstruction of the Pt(997) surface”, Surface Science **119**, 159–171 (1982).

[103] G. Lindauer et al., “On the interaction of oxygen with Pt single crystals; LEED study of step coalescence”, Surface Science **126**, 301–306 (1983).

[104] G. Maire et al., “Characterization of surface structure dependence for interactions of oxygen with well-defined platinum surfaces”, Surface Science **80**, 238–244 (1979).

[105] A. Winkler et al., “Kinetics and energetics of oxygen adsorption on Pt(111) and Pt(112)- A comparison of flat and stepped surfaces”, Surface Science **201**, 419–443 (1988).

[106] L. Jacobse et al., “The molecular dynamics of adsorption and dissociation of O_2 on Pt(553)”, Journal of Chemical Physics **143**, `10.1063/1.4923006` (2015).

[107] P. J. Feibelman et al., “Vibrations of O on stepped Pt(111)”, Physical Review B - Condensed Matter and Materials Physics **58**, 2179–2184 (1998).

[108] J. Bandlow et al., “Oxidation of stepped Pt(111) studied by x-ray photoelectron spectroscopy and density functional theory”, Physical Review B **83**, 174107 (2011).

[109] S. Günther et al., “In situ X-ray photoelectron spectroscopy of catalytic ammonia oxidation over a Pt(533) surface”, Journal of Physical Chemistry C **112**, 15382–15393 (2008).

[110] Z. Zhu et al., “Formation of nanometer-sized surface platinum oxide clusters on a stepped Pt(557) single crystal surface induced by oxygen: A high-pressure STM and ambient-pressure XPS study”, Nano Letters **12**, 1491–1497 (2012).

[111] M. R. Mcclellan et al., “Oxygen Adsorption on the Kinked Pt(321) Surface”, Studies in Surface Science and Catalysis **14**, 213–218 (1983).

[112] M. R. McClellan et al., “Molecular and atomic oxygen adsorption on the kinked Pt(321) surface”, Surface Science **124**, 188–208 (1983).

[113] Y. Iwasawa et al., “The reactions of carbon monoxide at coordinatively unsaturated sites on a platinum surface”, Chemical Physics Letters **44**, 468–470 (1976).

[114] G. Held et al., “Effect of Oxygen Adsorption on the Chiral Pt{531} Surface”, The Journal of Physical Chemistry B **109**, 6159–6163 (2005).

[115] G. Ertl, “Oscillatory Kinetics and Spatio-Temporal Self-Organization in Reactions at Solid Surfaces”, Science **254**, 1750–1755 (1991).

[116] C. T. Campbell et al., “A molecular beam study of the catalytic oxidation of CO on a Pt(111) surface”, The Journal of Chemical Physics **73**, 5862–5873 (1980).

[117] J. L. Gland et al., “Vibrational characterization of carbon monoxide oxidation on the Pt(111) surface”, Surface Science **151**, 260–270 (1985).

[118] M. Kinne et al., “Kinetics of the CO oxidation reaction on Pt(111) studied by in situ high-resolution x-ray photoelectron spectroscopy”, The Journal of Chemical Physics **120**, 7113–7122 (2004).

[119] J. Wintterlin et al., “Atomic and Macroscopic Reaction Rates of a Surface-Catalyzed Reaction”, Science **278**, 1931–1934 (1997).

[120] D. Fantauzzi et al., “Growth of Stable Surface Oxides on Pt(111) at Near-Ambient Pressures”, Angewandte Chemie - International Edition **56**, 2594–2598 (2017).

[121] R. Colen et al., “Oxidation of CO on Pt(111) at intermediate pressures”, Surface Science **408**, 310–316 (1998).

[122] X. Su et al., “High-Pressure CO Oxidation on Pt(111) Monitored with Infrared-Visible Sum Frequency Generation (SFG)”, Journal of the American Chemical Society **119**, 3994–4000 (1997).

[123] D. Miller et al., “Different reactivity of the various platinum oxides and chemisorbed oxygen in CO oxidation on Pt(111)”, Journal of the American Chemical Society **136**, 6340–6347 (2014).

[124] S. Krick Calderón et al., “CO oxidation on Pt(111) at near ambient pressures”, The Journal of Chemical Physics **144**, 044706 (2016).

[125] A. Farkas et al., “High Pressure Carbon Monoxide Oxidation over Platinum (111)”, The Journal of Physical Chemistry C **117**, 9932–9942 (2013).

[126] E. M. Alayon et al., “On highly active partially oxidized platinum in carbon monoxide oxidation over supported platinum catalysts”, Journal of Catalysis **263**, 228–238 (2009).

[127] R. Vakili et al., “Understanding the CO Oxidation on Pt Nanoparticles Supported on MOFs by Operando XPS”, ChemCatChem **10**, 4238–4242 (2018).

[128] B. L. Hendriksen et al., “CO Oxidation on Pt(110): Scanning Tunneling Microscopy Inside a High-Pressure Flow Reactor”, Physical Review Letters **89**, 2–5 (2002).

[129] M. D. Ackermann et al., “Structure and reactivity of surface oxides on Pt(110) during catalytic CO oxidation”, Physical Review Letters **95**, 1–4 (2005).

[130] D. R. Butcher et al., “In situ oxidation study of Pt(110) and its interaction with CO”, Journal of the American Chemical Society **133**, 20319–20325 (2011).

[131] S. M. McClure et al., “New insights into catalytic CO oxidation on Pt-group metals at elevated pressures”, Chemical Physics Letters **469**, 1–13 (2009).

[132] J.-Y. Chung et al., “In-situ study of the catalytic oxidation of CO on a Pt(110) surface using ambient pressure X-ray photoelectron spectroscopy”, Surface Science **603**, L35–L38 (2009).

[133] D. L. Bashlakov et al., “Subsurface Oxygen on Pt(111) and Its Reactivity for CO Oxidation”, Catalysis Letters **142**, 1–6 (2012).

[134] H. Hopster et al., “Catalytic oxidation of carbon monoxide on stepped platinum(111) surfaces”, Journal of Catalysis **46**, 37–48 (1977).

[135] Y. Ohno et al., “Angular distribution of desorbing carbon dioxide produced in two processes on a stepped platinum (557) surface”, Surface Science **382**, 221–230 (1997).

[136] A. Szabó et al., “Oxidation of CO by oxygen on a stepped platinum surface: Identification of the reaction site”, The Journal of Chemical Physics **96**, 6191–6202 (1992).

[137] J. Xu et al., “Direct spectroscopic observation of the reactive catalytic site for CO oxidation on Pt(335)”, The Journal of Chemical Physics **97**, 5250–5252 (1992).

[138] J. L. Gland et al., “Carbon monoxide oxidation on the kinked Pt(321) surface”, The Journal of Chemical Physics **79**, 6349–6356 (1983).

[139] J. Xu et al., “Catalytic oxidation of CO on Pt(335): A study of the active site”, The Journal of Chemical Physics **99**, 725–732 (1993).

[140] T. Matsushima et al., “Reaction sites for carbon monoxide oxidation on a stepped platinum (112) surface: a spatial distribution study of product desorption”, Surface Science **293**, 145–151 (1993).

[141] J. Neugebohren et al., “Velocity-resolved kinetics of site-specific carbon monoxide oxidation on platinum surfaces”, Nature **558**, 280–283 (2018).

[142] L. Zhou et al., “Origin of Thermal and Hyperthermal CO_2 from CO Oxidation on Pt Surfaces: The Role of Post-Transition-State Dynamics, Active Sites, and Chemisorbed CO_2”, Angewandte Chemie - International Edition **58**, 6916–6920 (2019).

[143] O. Balmes et al., “Generation of surface steps on Pt(977) induced by the catalytic oxidation of CO”, Journal of Catalysis **309**, 33–37 (2014).

[144] O. Balmes et al., “Diatomic Steps in Pt(997) Surfaces Are Better Catalysts than Monatomic Steps for the CO Oxidation Reaction near Atmospheric Pressure”, ACS Catalysis **6**, 1285–1291 (2016).

[145] M. Sander et al., “Microfacetting of Pt(210) induced by oxygen adsorption and by catalytic CO oxidation”, Surface Science **271**, 159–169 (1992).

[146] L. H. Dubois et al., "The chemisorption of CO and CO_2 on Rh(111) studied by high resolution electron energy loss spectroscopy", Surface Science **91**, 514–532 (1980).

[147] M. Van Hove et al., "The structure of Rh(111)(2×2)-3CO from LEED intensities: Simultaneous bridge and near-top adsorption in a distorted compact hexagonal CO overlayer", Surface Science **129**, 482–506 (1983).

[148] A. Beutler et al., "On the adsorption sites for CO on the Rh(111) single crystal surface", Surface Science **371**, 381–389 (1997).

[149] M. Gierer et al., "Structural reanalysis of the Rh(111)+$(\sqrt{3} \times \sqrt{3})R30°$-CO and Rh (111) + (2×2)-3CO phases using automated tensor LEED", Surface Science **391**, 176–182 (1997).

[150] E. Lundgren et al., "Surface X-ray-diffraction study of the Rh(111) (2x2)-3CO structure", Physical Review B **59**, 5876–5880 (1999).

[151] A. Beutler et al., "Coverage- and temperature-dependent site occupancy of carbon monoxide on Rh(111) studied by high-resolution core-level photoemission", Surface Science **396**, 117–136 (1998).

[152] A. Stroppa et al., "Adsorption and dissociation of CO on bare and Ni-decorated stepped Rh(553) Surfaces", The Journal of Physical Chemistry C **113**, 942–949 (2009).

[153] L. A. DeLouise et al., "Carbon monoxide adsorption and desorption on Rh{111} and Rh{331} surfaces", Surface Science **138**, 417–431 (1984).

[154] L. A. DeLouise et al., "Characterization of CO binding sites on Rh{111} and Rh{331} surfaces by XPS and LEED: Comparison to EELS results", Surface Science **147**, 252–262 (1984).

[155] H. P. Koch et al., "A RAIRS, TPD, and DFT Study of Carbon Monoxide Adsorption on Stepped Rh(553)", The Journal of Physical Chemistry C **112**, 806–812 (2008).

[156] M. Rebholz et al., "Adsorption and dissociation of CO on Rh(210)", Surface Science **259**, L797–L803 (1991).

[157] A. J. Jaworowski et al., "Adsorption sites in O and CO coadsorption phases on Rh(111) investigated by high-resolution core-level photoemission", Surface Science **431**, 33–41 (1999).

[158] M. V. Ganduglia-Pirovano et al., "Oxygen-induced Rh $3d_{5/2}$ surface core-level shifts on Rh(111)", Physical Review B **63**, 205415 (2001).

[159] L. Köhler et al., "High-coverage oxygen structures on Rh(111): Adsorbate repulsion and site preference is not enough", Physical Review Letters **93**, 1–4 (2004).

[160] J. Gustafson et al., “Self-limited growth of a thin oxide layer on Rh(111)”, Physical Review Letters **92**, 10–13 (2004).

[161] J. Gustafson et al., “Oxygen-induced step bunching and faceting of Rh(553): Experiment and *ab initio* calculations”, Physical Review B **74**, 35401 (2006).

[162] R. G. Farber et al., “Identification of Surface Sites for Low-Temperature Heterogeneously Catalyzed CO Oxidation on Rh(111)”, ACS Catalysis **8**, 11483–11490 (2018).

[163] R. Westerström et al., “Structure and reactivity of a model catalyst alloy under realistic conditions”, Journal of Physics: Condensed Matter **20**, 184018 (2008).

[164] P. Nolte et al., “Shape Changes of Supported Rh Nanoparticles During Oxidation and Reduction Cycles”, Science **321**, 1654–1658 (2008).

[165] J. I. Flege et al., “In situ structural imaging of CO oxidation catalysis on oxidized Rh(111)”, Physical Review B - Condensed Matter and Materials Physics **78**, 10–12 (2008).

[166] C. Dri et al., “Initial oxidation of the Rh(110) surface: Ordered adsorption and surface oxide structures”, Journal of Chemical Physics **125**, `10.1063/1.2345058` (2006).

[167] J. Gustafson et al., “Structure of a thin oxide film on Rh(100)”, Physical Review B - Condensed Matter and Materials Physics **71**, 1–9 (2005).

[168] J. Gustafson et al., “Sensitivity of catalysis to surface structure: The example of CO oxidation on Rh under realistic conditions”, Physical Review B - Condensed Matter and Materials Physics **78**, 1–6 (2008).

[169] E. Lundgren et al., “The surface oxide as a source of oxygen on Rh(111)”, Journal of Electron Spectroscopy and Related Phenomena **144-147**, 367–372 (2005).

[170] J. Gustafson et al., “Structure and catalytic reactivity of Rh oxides”, Catalysis Today **145**, 227–235 (2009).

[171] J. Gustafson et al., “Catalytic activity of the Rh surface oxide: CO oxidation over Rh(111) under realistic conditions”, Journal of Physical Chemistry C **114**, 4580–4583 (2010).

[172] F. Gao et al., “Reaction kinetics and polarization modulation infrared reflection absorption spectroscopy investigations of CO oxidation over planar Pt-group model catalysts”, Langmuir **26**, 16540–16551 (2010).

[173] J. Gustafson et al., "Reply to "Comment on "Catalytic Activity of the Rh Surface Oxide: CO Oxidation over Rh(111) under Realistic Conditions"""", The Journal of Physical Chemistry C **114**, 22372–22373 (2010).

[174] C. Zhang et al., "Steps and catalytic reactions: CO oxidation with preadsorbed O on Rh(553)", Surface Science **715**, `10.1016/j.susc.2021.121928` (2022).

[175] C. Zhang et al., "Faceting of rhodium(553) in realistic reaction mixtures of carbon monoxide and oxygen", Journal of Physical Chemistry C **119**, 11646–11652 (2015).

[176] K. Oura et al., *Surface Science: An Introduction* (Springer Berlin Heidelberg, Berlin, Heidelberg, 2003), pp. 6–12, 214.

[177] T. Lawton et al., "Initial Oxidation of Cu(hkl) Surfaces Vicinal to Cu(111): A High-Throughput Study of Structure Sensitivity", The Journal of Physical Chemistry C **116**, 16054–16062 (2012).

[178] Q. Chen et al., "9 Physical studies of chiral surfaces", Annu. Rep. Prog. Chem., Sect. C: Phys. Chem. **100**, 313–347 (2004).

[179] A. R. Passos et al., "Three-dimensional strain dynamics govern the hysteresis in heterogeneous catalysis", Nature Communications **11**, 4733 (2020).

[180] S. B. Vendelbo et al., "Visualization of oscillatory behaviour of Pt nanoparticles catalysing CO oxidation", Nature Materials **13**, 884–890 (2014).

[181] F. Mittendorfer et al., "Morphology of mesoscopic Rh and Pd nanoparticles under oxidizing conditions", Physical Review B - Condensed Matter and Materials Physics **76**, 8–11 (2007).

[182] N. Seriani et al., "Platinum-group and noble metals under oxidizing conditions", Journal of Physics: Condensed Matter **20**, 184023 (2008).

[183] S. V. Auras et al., "Recent advances in the use of curved single crystal surfaces", Progress in Surface Science **96**, 100627 (2021).

[184] K. Ali et al., "Atomically-precise texturing of hexagonal boron nitride nanostripes", Advanced Science **n/a**, 2101455.

[185] J. E. Ortega et al., "Interplay between structure and electronic states in step arrays explored with curved surfaces", Phys. Rev. B **83**, 085411 (2011).

[186] F. Garcia-Martinez et al., "CO chemisorption on vicinal Rh(111) surfaces studied with a curved crystal", The Journal of Physical Chemistry C **124**, 9305–9313 (2020).

[187] F. Garcia-Martinez et al., “Reduced Carbon Monoxide Saturation Coverage on Vicinal Palladium Surfaces: the Importance of the Adsorption Site”, The Journal of Physical Chemistry Letters, 9508–9515 (2021).

[188] F. Garcia-Martinez et al., “Catalytic Oxidation of CO on a Curved Pt(111) Surface: Simultaneous Ignition at All Facets through a Transient CO-O Complex**”, Angewandte Chemie International Edition **59**, 20037–20043 (2020).

[189] 1981 Physics Nobel Prize web page, `https://www.nobelprize.org/prizes/physics/1981/summary/`, Accessed 17/10/2021.

[190] 1921 Physics Nobel Prize web page, `https://www.nobelprize.org/prizes/physics/1921/summary/`, Accessed 17/10/2021.

[191] S. Hiifner, *Photoelectron Spectroscopy*, Third (Springer-Verlag Berlin Heidelberg, Saarbriicken, Germany, 2003), pp. 4, 7, 39, 40, 62, 65.

[192] Elettra sinchrotrone webpage for photoionization cross sections, `https://vuo.elettra.eu/services/elements/WebElements.html`, Accessed 19/10/2021.

[193] M. Seah et al., “Quantitative Electron Spectroscopy of Surfaces”, Surface And Interface Analysis **1**, 2–11 (1979).

[194] J. F. Watts et al., *An Introduction to Surface Analysis by XPS and AES* (John Wiley & Sons, Ltd, Chichester, UK, 2003), pp. 7, 17, 37, 53, 75.

[195] L. Nguyen et al., “Atomic-Scale Structural Evolution of Rh(110) during Catalysis”, ACS Catalysis **7**, 664–674 (2017).

[196] P. Willmott, *An Introduction to Synchrotron Radiation* (John Wiley and Sons, Ltd, Singapore, 2011).

[197] S. Mobilio et al., *Synchrotron Radiation* (Springer-Verlag Berlin Heidelberg, London, England, 2015).

[198] D. E. Starr et al., “Investigation of solid/vapor interfaces using ambient pressure X-ray photoelectron spectroscopy”, Chemical Society Reviews **42**, 5833–5857 (2013).

[199] J. Schnadt et al., “The new ambient-pressure X-ray photoelectron spectroscopy instrument at MAX-lab”, Journal of Synchrotron Radiation **19**, 701–704 (2012).

[200] R. M. Palomino et al., “New In-Situ and Operando Facilities for Catalysis Science at NSLS-II: The Deployment of Real-Time, Chemical, and Structure-Sensitive X-ray Probes”, Synchrotron Radiation News **30**, 30–37 (2017).

[201] V. Pérez-Dieste et al., "Near ambient pressure XPS at ALBA", Journal of Physics: Conference Series **425**, `10.1088/1742-6596/425/7/072023` (2013).

[202] C. Schlueter et al., "New HAXPES Applications at PETRA III", Synchrotron Radiation News **31**, 29–35 (2018).

[203] S. Blomberg et al., "Strain Dependent Light-off Temperature in Catalysis Revealed by Planar Laser-Induced Fluorescence", ACS Catalysis **7**, 110–114 (2017).

[204] J. Zetterberg et al., "Spatially and temporally resolved gas distributions around heterogeneous catalysts using infrared planar laser-induced fluorescence", Nature Communications **6**, 1–8 (2015).

[205] Johan Zetterberg, private communication. The PLIF spatial resolution depends on both the laser and optics. One one side, the x and y components (image plane) are limited by the detector and imaging optics. On the other side, the z-direction (perpendicular to the picture) is set by the laser size of the laser sheet. The temporal resolution is limited by the repetition rate of the camera, which in this case is 10 Hz.

[206] F. Schiller et al., "Catalytic Oxidation of Carbon Monoxide on a Curved Pd Crystal: Spatial Variation of Active and Poisoning Phases in Stationary Conditions", Journal of the American Chemical Society **140**, 16245–16252 (2018).

[207] A. L. Walter et al., "X-ray photoemission analysis of clean and carbon monoxide-chemisorbed platinum(111) stepped surfaces using a curved crystal", Nature Communications **6**, 8903 (2015).

[208] X. Su et al., "Pressure Dependence (10^{-10} – 700 Torr) of the Vibrational Spectra of Adsorbed CO on Pt(111) Studied by Sum Frequency Generation", Phys. Rev. Lett. **77**, 3858–3860 (1996).

[209] B. Poelsema et al., "Helium scattering and work function investigation of co adsorption on Pt(111) and vicinal surfaces", Surface Science **123**, 152–164 (1982).

[210] M. S. Chen et al., "Highly active surfaces for CO oxidation on Rh, Pd, and Pt", Surface Science **601**, 5326–5331 (2007).

[211] M. Ehsasi et al., "Steady and nonsteady rates of reaction in a heterogeneously catalyzed reaction: Oxidation of CO on platinum, experiments and simulations", The Journal of Chemical Physics **91**, 4949–4960 (1989).

[212] R. G. Farber et al., “Exposure of Pt(553) and Rh(111) to atomic and molecular oxygen: do defects enhance subsurface oxygen formation?”, Journal of Physics: Condensed Matter **29**, 164002 (2017).

[213] A. Böttcher et al., “Formation of subsurface oxygen at Ru(0001)”, Journal of Chemical Physics **110**, 3186–3195 (1999).

[214] M. Fields et al., “Role of Subsurface Oxygen on Cu Surfaces for CO_2 Electrochemical Reduction”, Journal of Physical Chemistry C **122**, 16209–16215 (2018).

[215] Z. Qu et al., “Formation of subsurface oxygen species and its high activity toward CO oxidation over silver catalysts”, Journal of Catalysis **229**, 446–458 (2005).

[216] D. Fantauzzi et al., “Surface Buckling and Subsurface Oxygen: Atomistic Insights into the Surface Oxidation of Pt(111)”, ChemPhysChem **16**, 2797–2802 (2015).

[217] H. Niehus et al., “Surface and subsurface oxygen adsorbed on Pt(111)”, Surface Science **93**, L147–L150 (1980).

[218] S. Hanselman et al., “Thermodynamics of the formation of surface PtO_2 stripes on Pt(111) in the absence of subsurface oxygen”, Physical Chemistry Chemical Physics **22**, 10634–10640 (2020).

[219] M. Shipilin et al., “Step dynamics and oxide formation during CO oxidation over a vicinal Pd surface”, Physical Chemistry Chemical Physics **18**, 20312–20320 (2016).

[220] C. Busó-Rogero et al., “Co oxidation on stepped-pt(111) under electrochemical conditions: insights from theory and experiment”, Phys. Chem. Chem. Phys. **15**, 18671–18677 (2013).

[221] Z. Gu et al., “Absorption of Atomic Oxygen into Subsurfaces of Pt(100) and Pt(111): Density Functional Theory Study”, The Journal of Physical Chemistry C **111**, 9877–9883 (2007).

[222] D. J. Liu et al., “Interactions between oxygen atoms on Pt(100): Implications for ordering during chemisorption and catalysis”, ChemPhysChem **11**, 2174–2181 (2010).

[223] G. Derry et al., “High coverage states of oxygen adsorbed on Pt(100) and Pt(111) surfaces”, Surface Science **140**, 165–180 (1984).

[224] G. Hoogers et al., “Adsorbate-induced step-doubling reconstruction of a vicinal metal surface: oxygen on Rh 332”, Surface Science **286**, 306–316 (1993).

[225] L. Niu et al., “Reconstruction kinetics of a stepped metallic surface: Step doubling and singling of Ni(977) induced by low oxygen coverages”, Surface Science **356**, 144–160 (1996).

[226] M. Peuckert et al., “Characterization of oxidized platinum surfaces by X-ray photoelectron spectroscopy”, Surface Science **145**, 239–259 (1984).

[227] T. Ogawa et al., “Adsorption and diffusion of oxygen atoms on a Pt(211) stepped surface”, Journal of Physical Chemistry C **117**, 9772–9778 (2013).

[228] A. Cudok et al., “Low-temperature adsorption kinetics of CO on Pt(111) derived from nonequilibrium time-resolved electron-energy-loss spectroscopy measurements”, Physical Review B **47**, 13682–13686 (1993).

[229] J. Lang et al., “An XPS study of nitric oxide, carbon monoxide and oxygen adsorption on Pt(210)”, Surface Science **167**, 261–270 (1986).

[230] J. Somers et al., “Nexafs determination of CO orientation on a stepped platinum surface”, Surface Science **183**, 576–590 (1987).

[231] K. Sinniah et al., “Chemisorption on stepped metal surfaces: CO/vicinal Ni(100)”, The Journal of Chemical Physics **98**, 9018–9029 (1993).

[232] C. Campbell et al., “A molecular beam investigation of the interactions of CO with a Pt(111) surface”, Surface Science **107**, 207–219 (1981).

[233] C. Campbell et al., “A molecular beam study of the adsorption and desorption of oxygen from a Pt(111) surface”, Surface Science **107**, 220–236 (1981).

[234] S. Surnev et al., “Co adsorption on pd(111): a high-resolution core level photoemission and electron energy loss spectroscopy study”, Surface Science **470**, 171–185 (2000).

[235] A. Föhlisch et al., “Beyond the chemical shift: vibrationally resolved core-level photoelectron spectra of adsorbed co”, Phys. Rev. Lett. **81**, 1730–1733 (1998).

[236] M. Smedh et al., “Vibrationally resolved C 1s photoemission from CO absorbed on Rh(111): the investigation of a new chemically shifted C 1s component”, Surface Science **491**, 99–114 (2001).

[237] M. Kinne et al., “Coadsorption of D_2O and CO on Pt(111) studied by in situ high-resolution x-ray photoelectron spectroscopy”, Langmuir **20**, 1819–1826 (2004).

[238] M. Ilyn et al., “Step-doubling at Vicinal Ni(111) Surfaces Investigated with a Curved Crystal”, Journal of Physical Chemistry C **121**, 3880–3886 (2017).

[239] A. Baraldi et al., “Real-time X-ray photoelectron spectroscopy of surface reactions”, Surface Science Reports **49**, 169–224 (2003).

[240] D. Q. Yang et al., “Carbon is X-ray photoemission line shape analysis of highly oriented pyrolytic graphite: The influence of structural damage on peak asymmetry”, Langmuir **22**, 860–862 (2006).

[241] B. Eren et al., “Dissociative Carbon Dioxide Adsorption and Morphological Changes on Cu(100) and Cu(111) at Ambient Pressures”, Journal of the American Chemical Society **138**, 8207–8211 (2016).

[242] A. Wille et al., “Low temperature dissociation of CO at reactive step sites of Pd(112)”, Journal of Molecular Structure **695-696**, 345–352 (2004).

[243] A. Tolia et al., “Surface Oxidation of Rhodium at Ambient Pressures as Probed by Surface-Enhanced Raman and X-Ray Photoelectron Spectroscopies”, Journal of Catalysis **150**, 56–70 (1994).

[244] F. B. de Mongeot et al., “Carbon Monoxide Dissociation on Rh Nanopyramids”, Physical Review Letters **97**, 056103 (2006).

[245] F. Strisland et al., “CO adsorption on the Rh(100) surface studied by high resolution photoelectron spectroscopy”, Surface Science **415**, L1020–L1026 (1998).

[246] W. Liu et al., “The surface structure effect on the chemisorption of CO on Rh”, Surface Science **232**, 323–328 (1990).

[247] D. M. Ren et al., “A study of chemisorption behavior of carbon monoxide on rhodium surfaces”, Surface Science **232**, 316–322 (1990).

[248] N. M. Martin et al., “CO Adsorption on Clean and Oxidized Pd(111)”, The Journal of Physical Chemistry C **118**, 1118–1128 (2014).

[249] J. Klikovits et al., “Step-Orientation-Dependent Oxidation: From 1D to 2D Oxides”, Physical Review Letters **101**, 266104 (2008).

[250] C. Becker, *From Langmuir to Ertl: The “Nobel” History of the Surface Science Approach to Heterogeneous Catalysis* (Elsevier, 2018), pp. 99–106.

[251] J. Harris et al., “On precursor mechanisms for surface reactions”, Surface Science Letters **105**, L281–L287 (1981).

[252] G. Nisbet et al., “Structural analysis of Pt(1 1 1)c($\sqrt{3} \times 5$)rect.-CO using photoelectron diffraction”, Surface Science **601**, 1296–1303 (2007).

[253] P. J. Feibelman et al., “The CO/Pt(111) Puzzle”, The Journal of Physical Chemistry B **105**, 4018–4025 (2001).

[254] M. Pedersen et al., “CO on Pt(111): Binding site assignment from the interplay between measured and calculated STM images”, Chemical Physics Letters **299**, 403–409 (1999).

[255] D. J. Miller et al., “Low O_2 dissociation barrier on Pt(111) due to adsorbate-adsorbate interactions”, Journal of Chemical Physics **133**, `10.1063/1.3512618` (2010).

[256] M. A. Van Spronsen et al., “Surface science under reaction conditions: CO oxidation on Pt and Pd model catalysts”, Chemical Society Reviews **46**, 4347–4374 (2017).

[257] M. Salmerón et al., “The structure and stability of surface platinum oxide and of oxides of other noble metals”, Surface Science **112**, 207–228 (1981).

[258] Ž. Šljivančanin et al., “Oxygen dissociation at close-packed Pt terraces, Pt steps, and Ag-covered Pt steps studied with density functional theory”, Surface Science **515**, 235–244 (2002).

[259] H. Steininger et al., “Adsorption of oxygen on Pt(111)”, Surface Science **123**, 1–17 (1982).

[260] J.-S. McEwen et al., “How low can you go? Minimum energy pathways for O_2 dissociation on Pt(111)”, Physical Chemistry Chemical Physics **14**, 16677 (2012).

[261] E. F. Holby et al., “Thermodynamics and hysteresis of oxide formation and removal on platinum (111) surfaces”, Journal of Physical Chemistry C **116**, 9942–9946 (2012).

[262] Q. Fu et al., “A First Principles Study on the Dissociation and Rotation Processes of a Single O 2 Molecule on the Pt(111) Surface”, The Journal of Physical Chemistry C **115**, 6864–6869 (2011).

[263] Y. S. Kim et al., “The study of oxygen molecules on Pt(111) surface with high resolution x-ray photoemission spectroscopy.”, The Journal of chemical physics **133**, 034501 (2010).

[264] S. A. Krasnikov et al., “Self-limited growth of triangular PtO_2 nanoclusters on the Pt(111) surface”, Nanotechnology **21**, 335301 (2010).

[265] Z. Yang et al., “Density functional theory studies on the adsorption, diffusion and dissociation of O_2 on Pt(111)”, Physics Letters, Section A: General, Atomic and Solid State Physics **374**, 4713–4717 (2010).

[266] P. Valentini et al., “Molecular dynamics simulation of O_2 sticking on Pt(111) using the ab initio based ReaxFF reactive force field”, Journal of Chemical Physics **133**, `10.1063/1.3469810` (2010).

[267] M. C. Wheeler et al., “Experimental study of CO oxidation by an atomic oxygen beam on Pt(111), lr(111), and Ru(001)”, Journal of Chemical Physics **108**, 3057–3063 (1998).

[268] W.-X. Li, “Oxidation of platinum surfaces and reaction with carbon monoxide”, Journal of Physics: Condensed Matter **20**, 184022 (2008).

[269] D. Friebel et al., “In situ X-ray probing reveals fingerprints of surface platinum oxide”, Phys. Chem. Chem. Phys. **13**, 262–266 (2011).

[270] M.-C. Jung et al., “X-Ray Photoelectron Spectroscopy Study of Pt-Oxide Thin Films Deposited by Reactive Sputtering Using O_2 /Ar Gas Mixtures”, Japanese Journal of Applied Physics **38**, 4872–4875 (1999).

[271] G. M. Bancroft et al., “ESCA Study of Sputtered Platinum Films”, Analytical Chemistry **47**, 586–588 (1975).

[272] W. D. Westwood et al., “Formation of PtO films by reactive sputtering”, Journal of Applied Physics **45**, 2313–2315 (1974).

[273] T. L. Barr, “An ESCA study of the termination of the passivation of elemental metals”, The Journal of Physical Chemistry **82**, 1801–1810 (1978).

[274] M. Rinnemo et al., “Catalytic ignition in the $CO - O_2$ reaction on platinum: experiment and simulations”, Surface Science **376**, 297–309 (1997).

[275] M. Sander et al., “Spatial coupling between kinetic oscillations on different regions of a cylindrical Pt single crystal”, Vacuum **41**, 272–274 (1990).

[276] T. Yamanaka et al., “An aligned oxidation of carbon monoxide induced by 193 nm irradiation on platinum(113)”, Chemical Physics Letters **264**, 180–185 (1997).

[277] M. J. Van Der Niet et al., “The influence of step geometry on the desorption characteristics of O_2, D_2, and H_2O from stepped Pt surfaces”, Journal of Chemical Physics **132**, `10.1063/1.3407434` (2010).

[278] A. T. Gee et al., “The dynamics of O_2 adsorption on Pt(533): Step mediated molecular chemisorption and dissociation”, The Journal of Chemical Physics **113**, 10333–10343 (2000).

[279] G. Comsa et al., “He-beam scattering study of the dynamics of oxygen induced reconstruction of the Pt(997) surface Par”, Surface Science **119**, 159–171 (1982).

[280] F. Netzer et al., “Adsorption studies on a stepped Pt(111) surface: O_2, CO, C_2H_4, C_2N_2”, Surface Science **74**, 547–567 (1978).

[281] K. Schwaha et al., “The adsorption of oxygen on the stepped Pt(S)-[9(111) × (111)] face”, Surface Science **65**, 277–286 (1977).

[282] H. Hertz, “Ueber einen einfluss des ultravioletten lichtes auf die electrische entladung”, Annalen der Physik **267**, 983–1000 (1887).

[283] A. Einstein, “Über einen die erzeugung und verwandlung des lichtes betreffenden heuristischen gesichtspunkt”, Annalen der Physik **322**, 132–148 (1905).

[284] Calibration of Photoemission Spectra and Work Function Determination, Dr. Rudy Schlaf, `http://rsl.eng.usf.edu/Documents/Tutorials/PEScalibration.pdf`, Accessed 19/10/2021.

[285] Omicron Argus CU analyzer, `https://scientaomicron.com/Downloads/Brochures/ESPEC/Argus_CU_SO_Brochure.pdf`, Accessed 17/10/2021.

[286] Thermo Scientific Alpha110 analyzer, `http://tools.thermofisher.com/content/sfs/brochures/D16093~.pdf`, Accessed 17/10/2021.

[287] SPECS MCD (multi channel detector), `https://www.specs-group.com/nc/specs/products/detail/mcd-detector/`, Accessed 18/10/2021.

[288] D. A. Shirley, “High-resolution x-ray photoemission spectrum of the valence bands of gold”, Physical Review B **5**, 4709–4714 (1972).

[289] J. Moulder et al., *Handbook of X-ray Photoelectron Spectroscopy: A Reference Book of Standard Spectra for Identification and Interpretation of XPS Data* (Physical Electronics Division, Perkin-Elmer Corporation, 1995).

[290] R. Nyholm et al., “Beamline I311 at MAX-LAB: a VUV/soft X-ray undulator beamline for high resolution electron spectroscopy”, Nuclear Instruments and Methods in Physics Research Section A: Accelerators, Spectrometers, Detectors and Associated Equipment **467-468**, 520–524 (2001).

[291] J. P. Simonovis et al., “Enhanced Stability of Pt-Cu Single-Atom Alloy Catalysts: In Situ Characterization of the Pt/Cu(111) Surface in an Ambient Pressure of CO”, The Journal of Physical Chemistry C **122**, 4488–4495 (2018).

[292] C. X. software, `http://www.casaxps.com/`, Accessed 10/05/2020.

[293] S. Doniach et al., “Many-electron singularity i n x-ray photoemission andx-ray line spectra from metals”, J. Phys. C: Solid State Phys. **3**, 285–291 (1970).

[294] F. Bondino et al., “Structural determination of molecules adsorbed in different sites by means of chemical shift photoelectron diffraction: c(4×2)-CO on Pt(111)”, Surface Science **459**, 467–474 (2000).

[295] M. Nowicki et al., “CO adsorption on Pt(110) investigated by X-ray photoelectron diffraction”, Surface Science **478**, 180–192 (2001).

[296] D. A. Wesner et al., “Orientation of adsorbed CO on Pt(111) + K by X-ray photoelectron diffraction”, Physical Review B **33**, 8837–8840 (1986).

[297] D. A. Wesner et al., “Adsorbate orientation on platinum by polar-angle x-ray photoelectron diffraction”, Journal of Vacuum Science & Technology A: Vacuum, Surfaces, and Films **5**, 927–931 (1987).

[298] A. Abrami et al., “Super ESCA: First beamline operating at ELETTRA”, Review of Scientific Instruments **66**, 1618–1620 (1995).

[299] lmfit package, `https://lmfit.github.io/lmfit-py/`, Accessed 12/03/2020.

[300] J. Gland et al., “The adsorption of oxygen on a stepped platinum single crystal surface”, Surface Science **75**, 733–750 (1978).

[301] J. Gustafson et al., “Identification of Step Atoms by High Resolution Core Level Spectroscopy”, Physical Review Letters **91**, 056102 (2003).

[302] J. Kim et al., “How Rh surface breaks CO_2 molecules under ambient pressure”, Nature Communications **11**, `10.1038/s41467-020-19398-1` (2020).